İ.E. ÖNDER

# ASSESSMENT OF SHEET METAL FORMING PROCESSES BY NUMERICAL EXPERIMENTS

İ. ERKAN ÖNDER

METU 2005

MAY 2005

# ASSESSMENT OF SHEET METAL FORMING PROCESSES BY NUMERICAL EXPERIMENTS

A THESIS SUBMITTED TO
THE GRADUATE SCHOOL OF NATURAL AND APPLIED SCIENCES
OF
MIDDLE EAST TECHNICAL UNIVERSITY

BY

İ. ERKAN ÖNDER

IN PARTIAL FULFILLMENT OF THE REQUIREMENTS
FOR
THE DEGREE OF MASTER OF SCIENCE
IN
MECHANICAL ENGINEERING

MAY 2005

Approval of the Graduate School of Natural and Applied Sciences

_____

Prof. Dr. Canan Özgen
Director

I certify that this thesis satisfies all the requirements as a thesis for the degree of Master of Science.

_____

Prof.Dr. Kemal İder
Head of Department

This is to certify that we have read this thesis and that in our opinion it is fully adequate, in scope and quality, as a thesis for the degree of Master of Science.

_____

Prof. Dr. A. Erman Tekkaya
Supervisor

**Examining Committee Members**

| | | |
|---|---|---|
| Prof. Dr. S. Engin Kılıç | (METU, ME) | _____ |
| Prof. Dr. A. Erman Tekkaya | (METU, ME) | _____ |
| Prof. Dr. Levend Parnas | (METU, ME) | _____ |
| Asst. Prof. Dr. Merve Erdal | (METU, ME) | _____ |
| Assoc. Prof. Dr. Hakan Gür | (METU, METE) | _____ |

**I hereby declare that all information in this document has been obtained and presented in accordance with academic rules and ethical conduct. I also declare that, as required by these rules and conduct, I have fully cited and referenced all material and results that are not original to this work.**

İ. Erkan ÖNDER

# ABSTRACT

ASSESSMENT OF SHEET METAL FORMING PROCESSES BY NUMERICAL EXPERIMENTS

Önder, İ. Erkan

M.S., Department of Mechanical Engineering

Supervisor: Prof. Dr. A. Erman Tekkaya

May 2005, 234 pages

Sheet metal forming technologies are challenged especially by the improvements in the automotive industry in the last decades. To fulfill the customer expectations, safety requirements and market competitions, new production technologies have been implemented. This study focuses on the assessment of conventional and new sheet metal forming technologies by performing a systematic analysis. A geometry spectrum consisting of six different circular, elliptic, quad cross-sections are selected for the assessment of conventional deep drawing, hydro-mechanical deep drawing and high-pressure sheet metal forming. Within each cross-section, three different equivalent drawing ratios are used as a variant. More than 200 numerical experiments are performed to predict the forming limits of three competing processes. St14 stainless steel is used as the material throughout the assessment study. The deformation behavior is described by an elasto-plastic material model and all numerical simulations are carried out by using dynamic-explicit commercial finite element code.

The process validation is done by interpreting the strain results of numerical experiment. Therefore, the reliability of predictions in the assessment study highly

depends on the quality of simulations. The precision of numerical experiments are verified by comparing to NUMISHEET benchmarks, analytical formulation, and experiments to increase the assets of the assessment study.

The analyses revealed that depending on the workpiece geometry and dimensional properties certain processes are more preferable for obtaining satisfactory products. The process limits for each process are established based on the analyzed cross-sections of the spectrum. This data is expected to be useful for predicting the formability limits and for selecting the appropriate production process according to a given workpiece geometry.

**Keywords:** Dynamic-explicit FEM, Deep drawing, Hydroforming, Forming limits, Process evaluation

# ÖZ

SAC METAL ŞEKİLLENDİRME İŞLEMLERİNİN DEĞERLENDİRİLMESİ

Önder, İ. Erkan

Yüksek Lisans, Makina Mühendisliği Bölümü

Tez Yöneticisi: Prof. Dr. A. Erman Tekkaya

Mayıs 2005, 234 sayfa

Sac şekillendirme teknolojileri son on yıl içinde özellikle otomotiv endüstrisinin gelişmesi ile çokça talep edilir hale gelmiştir. Müşteri isteklerini, güvenlik gereksinimlerini ve pazar rekabetini karşılamak amacıyla yeni üretim teknolojileri hayata geçirilmiştir. Bu çalışmada sistematik bir analizle yeni ve geleneksel sac şekillendirme teknolojileri değerlendirmeye odaklanmıştır.

Altı farklı dairesel, eliptik ve dörtgen kesit alanlarından oluşan bir geometrik spektrum, geleneksel derin çekme, hidromekanik derin çekme, yüksek basınçla sac şekillendirme işlemlerini değerlendirmek için seçilmiştir. Her bir kesit alanının içinde üç değişik eşdeğer çekme oranı kullanılmıştır. 200'den fazla sayısal deney üç rakip prosesin şekillendirme sınırlarını tahmin etmek amacıyla gerçekleştirilmiştir. Bu değerlendirme çalışması süresince malzeme olarak St14 paslanmaz çeliği kullanılmıştır. Deformasyon davranışı elasto-plastik malzeme modeli tarafından tanımlanmış ve bütün sayısal çözümler bir dinamik-açık ticari sonlu elemanlar kodu kullanılarak hesaplanmıştır.

İşlem doğrulaması sayısal deneyden elde eldilen gerinme sonuçlarının yorumlanmasıyla yapılmıştır. Bu nedenle bu değerlendirme çalışmasındaki

tahminlerin güvenilirliği büyük ölçüde simulasyonların kalitesine bağlıdır. Sayısal deneylerin hassasiyeti NUMISHEET 2002 referansları, analitik formülasyon ve çalışmanın değerini arttıracak deneylerden elde edilmiş sonuçların karşılaştırılmasıyla doğrulanmıştır.

Analizler iş parçasının geometrisine ve boyut özelliklerine bağlı olarak kimi işlemlerin istenilen yeterlilikteki ürünlerin elde edilmesinde daha tercih edilebilir olduğunu göstermiştir. Her bir işlem için analiz edilmiş spektrumun değişik kesit alanları baz alınarak proses limitleri belirlenmiştir. Bu verilerin, şekilllendirme limitlerinin tahmininde ve verilen iş parçasının geometrisine göre uygun üretim işleminin seçiminde çok kullanışlı olacağı beklenmektedir.

**Anahtar Kelimeler:** Dinamik–Açık Sonlu Elemanlar Metodu, Derin Çekme, Hidro Şekillendirme, Şekillendirme Sınırları, İşlem Değerlendirilmesi

**To My Family**

# ACKNOWLEDGMENTS

I would like to express my deepest gratitude and appreciation to my supervisor Prof. Dr.-Ing. A. Erman Tekkaya who inspired, encouraged and supported me at all levels of this study.

I would like to thank to my colleagues Emre Akın and Çağlar Sönmez, whose friendship, support and suggestions made great contributions to this work. I sincerely thank to Ayşegül Altunbaş for spell check, corrections and motivation. I also want to thank Varlık Kılıç and Tahir Fidan for providing me a peaceful working environment.

I send my best wishes to Virtual Metal Forming Laboratory (VMFL) members for their contributions.

In addition, I would like to thank Prof. Dr.-Ing. Matthias Kleiner and my colleagues Michael Trompeter and Alexander Brosius at the institute of Forming Technology and Lightweight Construction (IUL) for their hospitality and cooperation.

Some part of this study was supported by AFP research project with the project number of BAP-2002-03-02-011

Finally, my greatest thanks go to my family who shaped me with their never-ending patience.

# TABLE OF CONTENTS

# CHAPTER 1

# INTRODUCTION

## 1.1 Motivation

Sheet metal forming operations are among the most elegant operations in metal forming. Low cost mass production of high quality sheets and existence of sheet materials with excellent strength-to-weight ratio, cause the sheet metal forming processes to become a highly preferable forming technique [1].

Especially in automotive industry applications, deep drawing and bending are the most frequently employed operations. It is widely utilized for the forming of outer panel and inner profile (Figure 1.1).

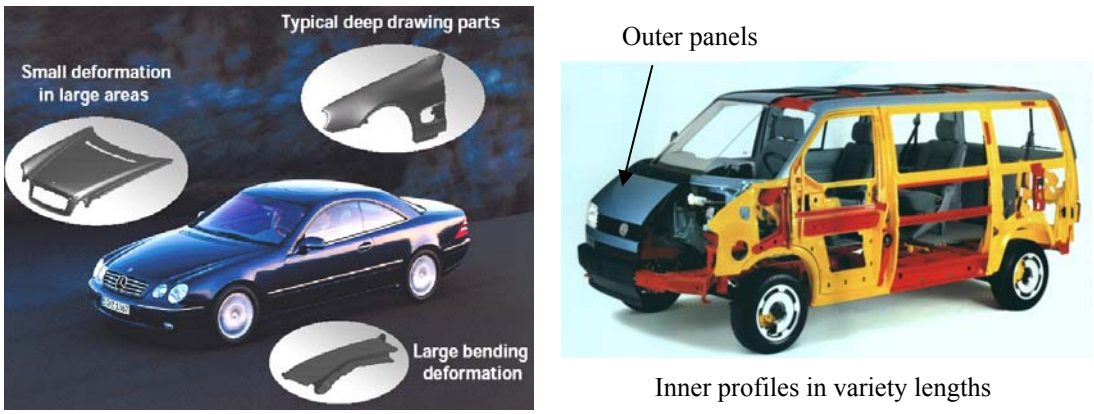


**Figure 1.1** Examples to automotive industry applications [2]

Improvements in the applications and market demands enforce the sheet metal forming industry to implement new forming technologies that are sketched in Figure 1.2. However, this brings the requirement of performing systematic

researches for the determination of formability limits and capability of new technologies.

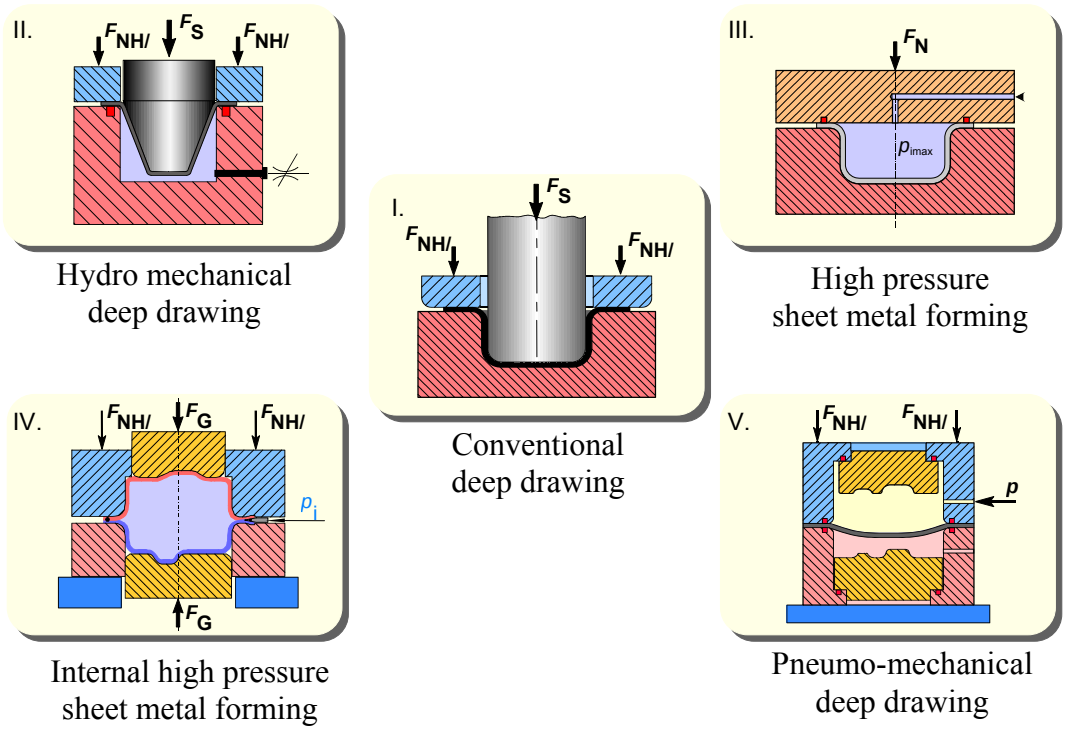


**Figure 1.2** Current deep drawing technologies implemented in sheet metal forming industry [3]

For the manufacture of a specific part, process validation is a key issue, since the improper selection of utilized process yields unsatisfactory results both in quality and in cost effectiveness. Although the methodology of the processes is the same, the tool design, process limitations, and capability of each process are quite different. Therefore, it is very important to know which process is more eligible to manufacture a desired product. Figure 1.3 shows an example to a specific product whose manufacturing by conventional techniques is improper.

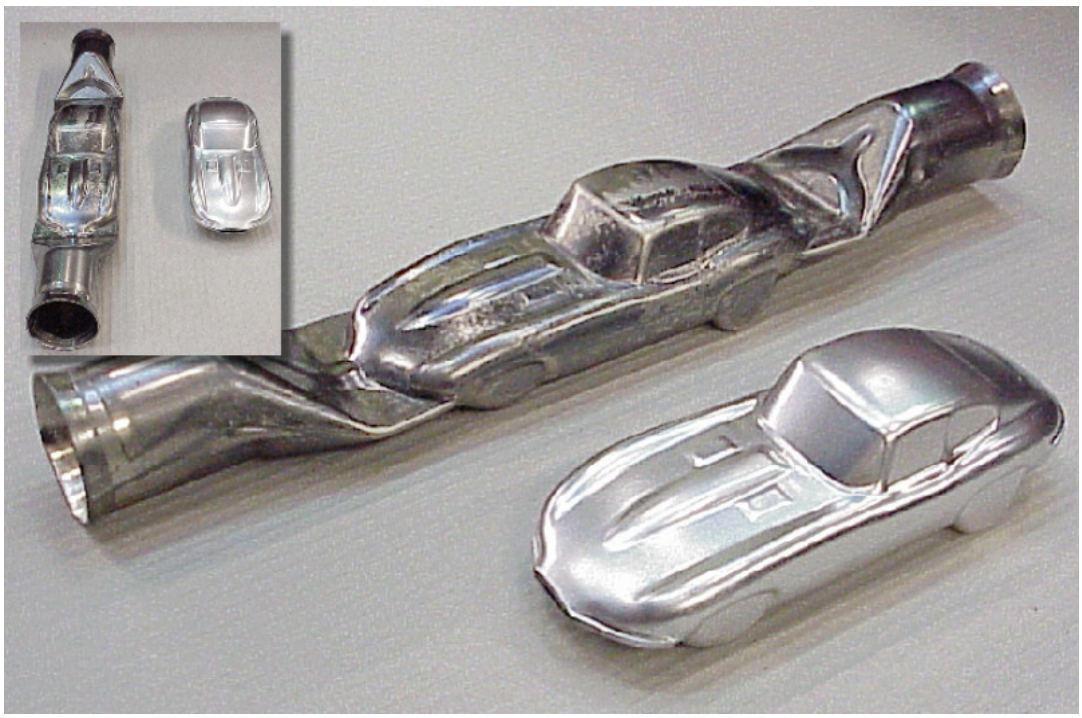

**Figure 1.3** A product (key holder) manufactured by a new forming technology [4]

## 1.2 Aim and scope of this study

Increasing use of new technologies in automotive and aircraft applications requires precise investigation and developments on all aspects of sheet metal forming processes to satisfy the demand by the industry.

This study focuses on the assessment of conventional and new sheet metal forming technologies by performing a systematic analysis. Three competing processes namely conventional deep drawing, hydro-mechanical deep drawing, and high-pressure sheet metal forming will be simulated by numerical experiments to assess the forming capabilities. A geometry spectrum consisting of circular, elliptic and quadrangle cross-sections are selected, and numerous numerical experiments using those geometries will be performed to predict the forming limits. St14 stainless steel will be used as the material throughout the study. The deformation behavior is described by an elasto-plastic material model and all numerical simulations will be carried out by using dynamic-explicit commercial finite element code.

Systematic researches require intensive care in determination of parameters and involve great number of trials. Therefore, the worthiness of the study highly depends on the precision of the result and computational time spent.

To increase the reliability of the study, both the process and numerical parameters will be optimized to achieve a balance between precision and computational time before the assessment study is performed. The influences of each parameter on the simulation results will be observed and optimum parameters will be proposed. Then, the simulations using those parameters will be compared with benchmarks, analytical formulations, and experiments.

In conclusion, it is aimed to predict the forming limits of each metal forming processes and foresee the drawability of sheet material into any specific shape. Finally, the assessment study will be completed by comparing the formability limits of competing processes.

## 1.3 Content of this study

The whole study can be divided into six chapters. In the first chapter, general information about the study will be given. The next chapter is the literature survey, which will include the description of the sheet metal forming processes, material properties of sheet metals and information about simulation methods. Chapter 3 is dedicated to finite element method (FEM) and its theoretical background. In the fourth chapter, numerical and process parameters of simulations are optimized; simulation results of a convention deep drawing are compared with both NUMISHEET 2002 workbench and an analytical formulation. In addition, at the end of the chapter high-pressure sheet metal forming simulation will be confirmed with experiment. In chapter 5, systematic numerical experiments will be performed for the assessment of three sheet metal forming processes, which are conventional deep drawing (DD), hydro-mechanical deep drawing (aquadrawing), and high-pressure sheet metal forming (HBU). The comparison and discussion of the simulation results will be done and

forming limits of competing processes will be predicted. Finally, conclusion will be the content of the last chapter.

# CHAPTER 2

# LITERATURE SURVEY

## 2.1 Introduction

In this chapter, the literature related to the current study will be discussed. First, the process definition of conventional deep drawing and hydroforming is presented. Secondly, anisotropy and formability of sheet metals are examined and possible failure modes are mentioned. At the end of the chapter, development of numerical simulations in metal forming is mentioned.

## 2.2 Conventional deep drawing process

Deep drawing is a process by which a flat sheet of metal is formed into specific shape of geometry. The undeformed sheet, called the blank or workpiece, is placed over the die, and it is pressed into the die cavity using a punch, as shown in Figure 2.1. A blankholder is used to apply pressure to the outer section of the blank called the flange during the forming process and binder is the upper part of the die on which the flange keeps in contact.

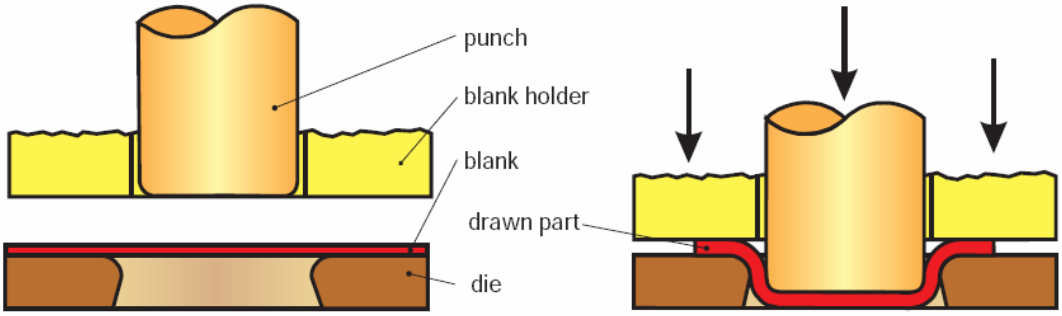


**Figure 2.1** Single-step draw deep drawing with blank holder [1]

Deep drawing is the most well known method of press forming thin sheets, and is used commonly in three-dimensional forming of sheet workpieces. Products that are produced by deep drawing can be seen within many fields, from automobile bodies to household applications and as well as construction auxiliary parts [5]. It is the most suitable sheet metal forming technique for the mass production of simple shaped bodies (Figure 2.2); however, it has some limitations. Even with a good lubrication, limiting drawing ratio, which is defined in Section 2.4, is restricted in the range between 2.0 and 2.3. Also some common failure modes like wrinkling, tearing, necking, poor surface appearance are the other factors that necessitate further developments in drawing processes.

**Figure 2.2** Examples to conventional deep drawing workpieces

## 2.3 Hydroforming

Hydroforming or hydraulic forming has been one of the fundamental sheet metal forming processes for quite a long time, having been developed before pre-World War II. Its applications in the German aircraft industry were still restrained in some specific fields because of particular drawbacks and having relatively less research and practical experience, but since 1990s, it has been attracting increasingly more attention in many industrial fields, especially in the automotive industry [6].

Hydroforming is a kind of soft-tool forming technology. Soft-tool forming technologies include rubberpad forming technology and fluid-tool forming in which the hydroforming belongs. In hydroforming, oil, water or other fluid mediums are used as the punch or the die. Hydroforming has a variety of names: Hydraulic

forming, hydroforming deep drawing, flexible forming, hydrobulging, high-pressure forming, low-pressure forming, and hydro-mechanical deep drawing. However, hydroforming can be used for all situations when fluid pressure is used in the process as an aid; whilst others are usually referred to as a certain specific hydraulic-forming process variation or a process aided with a fluid, respectively. Hydroforming can be classified as the following processes according to its process features:

- Tube Hydroforming
- Hydro-Mechanical Deep Drawing
- High Pressure Sheet Metal Forming

### 2.3.1 Tube Hydroforming

Tube Hydroforming (THF) has been called with many different names depending on the period and country it was used and studied. In Tube hydroforming (Figure 2.3), a fluid medium is taken as the punch and the tube is formed into the desired shape through simultaneous applications of a compressive axial force and an internal pressure, which is usually obtained by various means such as hydraulic, viscous medium, elastomer, polyurethane, etc [7]. The tubular workpiece is finally forced to assume the internal shape of the split die. In this technology, the hydrobulging pressure is comparatively higher than the ones in other hydroforming processes. The process is classified as: (a) low-pressure forming, where the internal pressure is generally smaller than a maximum of 80–100 MPa and the wall thinning is generally less than 5%; and (b) high-pressure forming, where the internal pressure generally reaches a maximum of 690 MPa, the seal technology being critical in high-pressure forming [6].

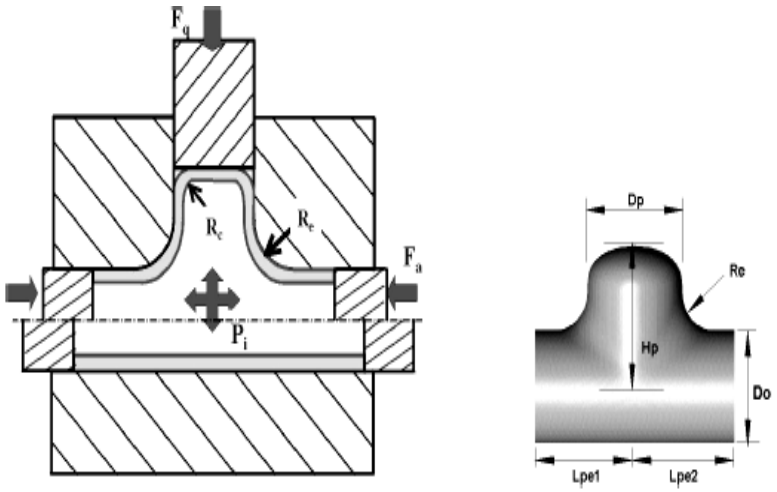


**Figure 2.3** Parameters in typical THF. $F_a$:Axial Force, $F_q$:Counter Force, $P_i$:Internal Pressure, $R_c$:Corner Radius, $R_e$:Fillet Radius, $D_0$:Initial Diameter, $D_p$:Protrusion diameter, $H_p$:Bulge height, $L_p$:Distance between tube edge

Although Tube Hydroforming process has been used in the industry only for more than a decade, developments of the techniques and establishment of the theoretical background goes back to 1940s [7]. Its property to reduce the process steps and overall production cost, as well as to improve the structural stress and stiffness when producing tube-like components, makes itself a competitive alternative to conventional techniques.

### 2.3.2 Hydro-mechanical Deep Drawing

Hydro-mechanical deep-drawing technology was first developed in 1890. However, the real development began after the Second World War. Early research work began mainly in Germany and Japan [8].

Hydro-mechanical deep drawing has various names, e.g. hydromec, aquadraw, fluid former, drawing with counter pressure or hydraulic counter-pressure deep drawing, deep drawing, process with fluid-pressure assisted method, hydraulic forming and even just hydroform or hydroforming, each representing its different features. In fact, the hydro-mechanical deep-drawing process is a kind of soft-tool forming

technology originating from hydroforming technology. Furthermore, the hydro-mechanical deep drawing can be divided into the hydrostatic type and the hydrodynamic type based on the feature of the fluid pressure. In most cases, process is in the hydrostatic state, but there exist some cases, such as explosive forming with fluid as the medium, where the fluid is in the dynamic state [8].

In the hydro-mechanical deep-drawing process, the female die is replaced by fluid medium and the final shape of the workpiece is determined by the punch. Fluid medium is pressurized as the punch penetrates and the counter pressure in the chamber can be controlled by a valve or a pump. The function of the blank holder is almost the same as in the conventional deep drawing. However, the fluid may escape under the blank or O-ring is used for preventing the flow out of the fluid on the flange. Furthermore, with some modification in the setup, the blank is forced into the die cavity filled with fluid by the radial force created around the outside of the blank (Figure 2.4).

The hydro-mechanical deep drawing has some features, which makes itself favorable among the other alternatives. First of all, it has a friction holding effect so that friction forces, produced between the blank and the punch, serve as a part of the forming force. Secondly, it has a resistance reduction effect that reduces the friction resistance between the flange and the die because of the flowing out of the fluid. Finally, it has an initial extension and wrinkle-prevention effect. Vicinity of the die shoulder portion and unsupported regions are subjected to bulging pressure, causing circumferential tensile stresses, which prevents wrinkles to occur and satisfies a more uniform thickness distribution.

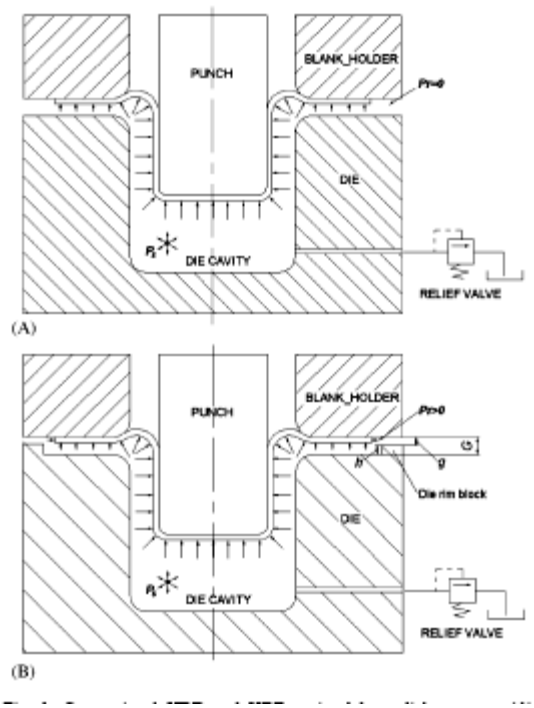


**Figure 2.4** (A) Typical hydro-mechanical deep drawing, (B) Hydro-mechanical deep drawing assisted by radial pressure

### 2.3.3 High Pressure Sheet Metal Forming

High Pressure Sheet Metal Forming (HBU) in fact a free-hydrobulging process where the fluid is functioning as a punch, thus, reducing the tooling and labor cost. It is mostly used for the forming of some special shaped, specific-structured spheroidal shell as well as to produce complex-shaped sheet metal parts. Hydroformed products have been used in automotive, aircraft, and household applications. However, the recent developments of this technology in these respects are mainly activated by the automotive industry.

Most materials formed with conventional methods can be hydroformed. The materials require sufficient elongation properties to allow bending, bulging or stretching without failure.

Compared with conventionally deep drawn parts, hydroformed parts are better in respect of both tolerances and repeatability. HBU can also improve both the quality

and the performance of the products by producing lighter, cheaper, stronger and stiffer parts. The rigid tool half can be made from inexpensive materials [6]. Besides, parts made from blanks of different thickness and materials can be produced using the same tools and also, several parts can be formed in the same press cycle in fluid cell applications. Another advantage is that it has less springback as it is released from the die since the residual stresses are significantly lower.

Hydroforming technology also has some drawbacks or limitations: Cycle time is relatively slow and dies cannot be changed as quickly as conventional dies. In addition, the low production rate limits the manufacture of low volume parts. Furthermore, Hydroforming equipments are generally 30% more expensive than conventional tools. Despite these disadvantages, High Pressure Sheet Metal forming is an unbeatable process for the production of prototype parts.

## 2.4 Drawing Ratio

The drawing ratio, generally speaking, can be defined as the ratio of optimum initial area of the blank to the mean cross-sectional area of die and punch. Maximum drawing ratio is an important numerical value to determine the required number of drawing steps. For cylindrical cup drawing process with circular cross-section, drawing ratio can be defined by the following equation:

$$\beta = \frac{A_0}{A_i} = \sqrt{\frac{\pi r_0^2}{\pi r_i^2}} = \frac{r_0}{r_i} \tag{2.1}$$

where

$A_0$ is initial blank area

$A_i$ is mean cross-sectional area of punch and die

$r_0$ is the initial radius of blank

$r_i$ is the average of punch radius ($r_p$) and die cavity radius ($r_d$)

For non-circular cross-section, equivalent drawing ratio can be defined as the ratio of initial blank area and mean cross-sectional area of punch and die.

The drawing ratio is dependent on many factors like the tool geometry, lubrication conditions, and the amount of blank holding forces, sheet thickness, and material properties (especially the R and n value). The limiting drawing ratio (LDR), which can be reached in a single drawing step, is theoretically calculated by membrane analysis.

## 2.5 Definition of the Anisotropy

Due to their crystallographic structure and the characteristic of the rolling process, sheet metals generally exhibit a significant anisotropy of mechanical properties [9]. The variation of their plastic behavior with direction is assessed by a quantity called Lankford parameter of anisotropy coefficient [10]. This coefficient is usually determined by uniaxial tensile tests on sheet specimens in the form of a strip. The anisotropy coefficient (r) is defined by

$$r = \frac{\varepsilon_2}{\varepsilon_3} \tag{2.2}$$

where $\varepsilon_2$; $\varepsilon_3$ are the strains in the width and thickness directions, respectively

Experiments show that "r" depends on the in-plane direction. If the tensile specimen is cut having its longitudinal axis parallel to the rolling direction, the coefficient $r_{90}$ is obtained. The average of the r-values obtained for different directions in the plane of the sheet metal represents the coefficient of normal anisotropy $r_n$. The coefficient of normal anisotropy is obtained from equation

$$r_n = \frac{r_0 + 2 \cdot r_{45} + r_{90}}{4} \tag{2.3}$$

where

$r_0$ is anisotropy factor in rolling direction (RD)

$r_{45}$ is anisotropy factor in 45° direction relative to RD

$r_{90}$ is anisotropy factor in 90° direction relative to RD

A measure of the variation of normal anisotropy with the angle to the rolling direction is given by the quantity,

$$\Delta r = \frac{r_0 + r_{90} - 2 \cdot r_{45}}{2} \tag{2.4}$$

where

$r_0$ is anisotropy factor in rolling direction (RD)

$r_{45}$ is anisotropy factor in 45° direction relative to RD

$r_{90}$ is anisotropy factor in 90° direction relative to RD

known as planar anisotropy.

## 2.6 Formability of Sheet Metals

At the end of the nineteenth century, due to the development of the sheet forming technology, sheet metal formability became a research topic. Some of the first researchers interested in this field were Bessemer and Parkers, Adamson, Considere and Erichsen [9]. Necking, tearing, wrinkling, bursting, or poor qualities in appearance are the factors that generally define a limit to the deformation in sheet metal forming (Figure 2.5). Figure 2.6 summarizes the parameters that have an effect on the formability of sheet metals.

Furthermore, the influence of various parameters on the formability in deep drawing is presented in Figure 2.7. Methods developed for evaluating the formability of sheet metal may be subdivided into four groups, shown in Figure 2.8.

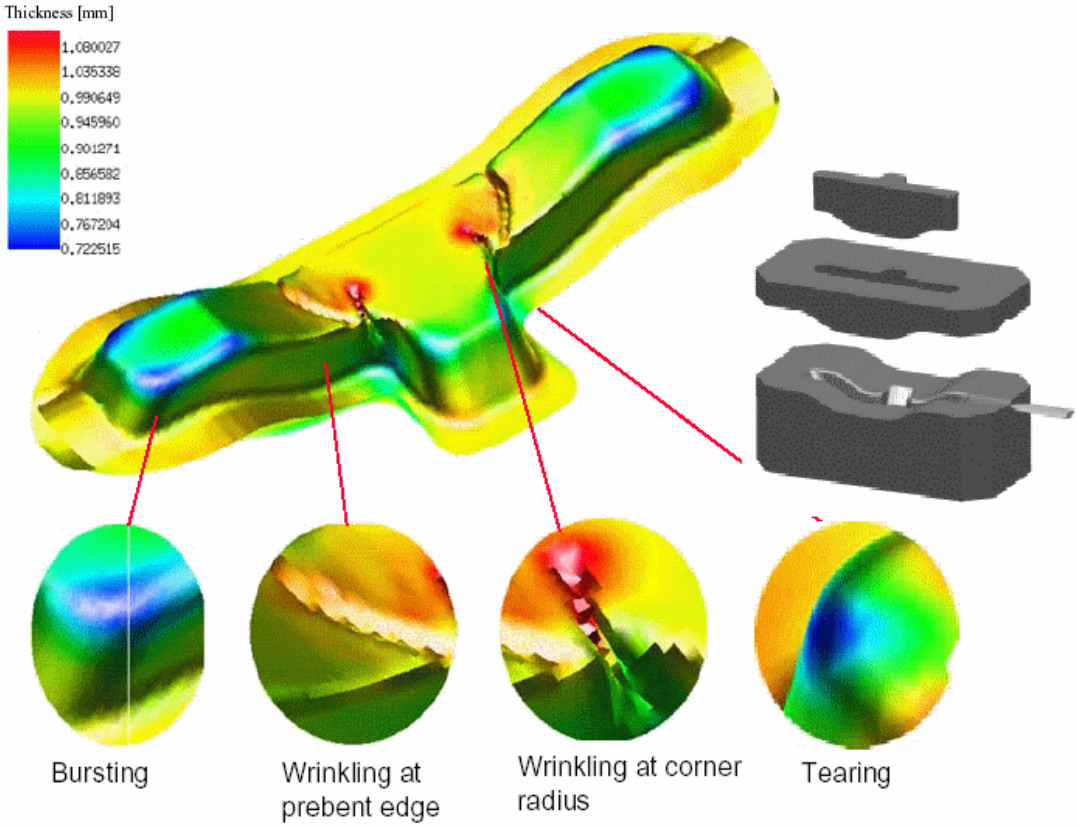


**Figure 2.5** Possible failure modes in sheet metal products

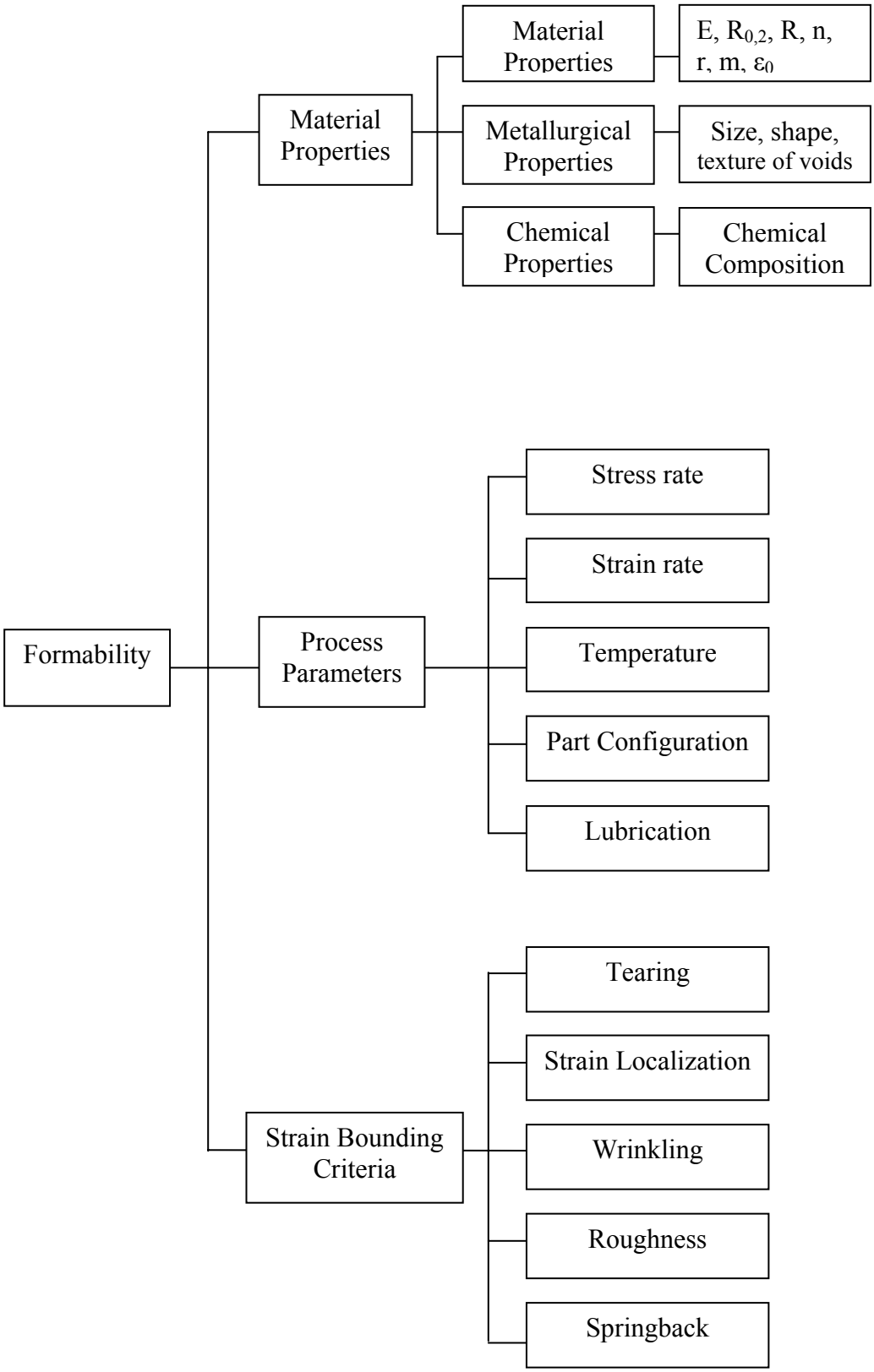


**Figure 2.6** Parameters influencing sheet metal formability

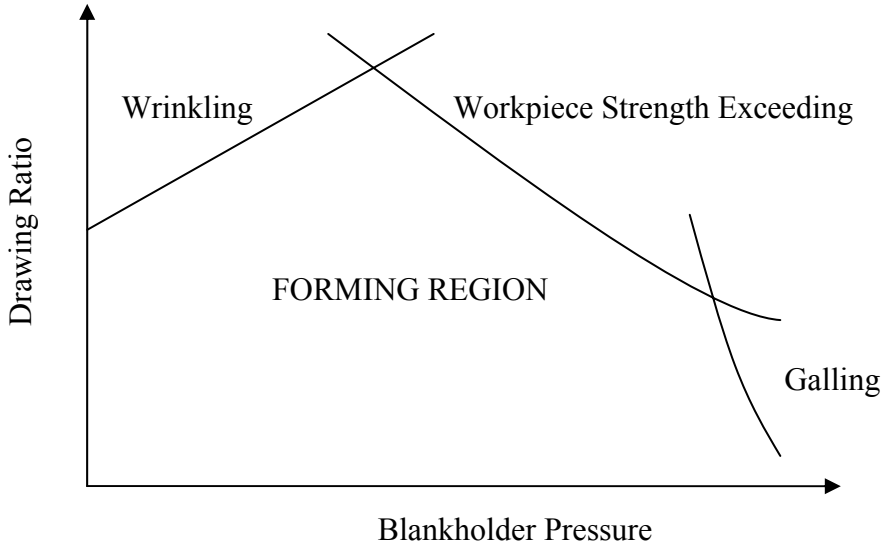


**Figure 2.7** Influence of various parameters on formability in deep-drawing

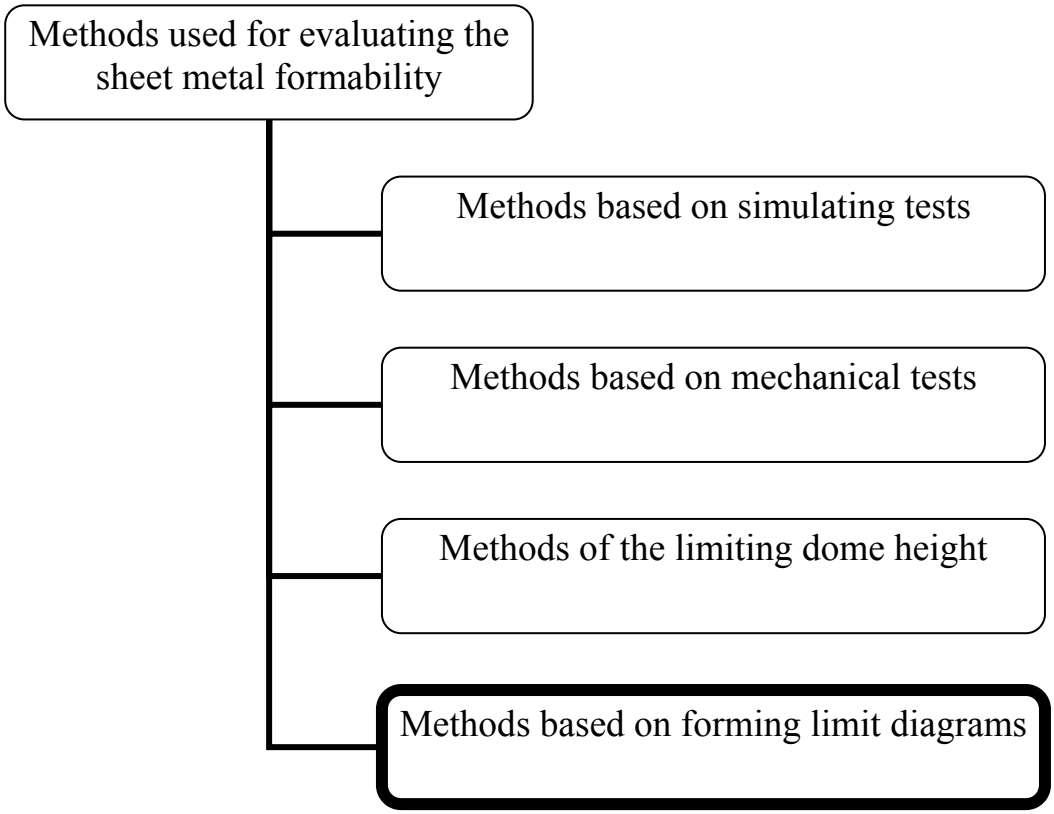


**Figure 2.8** Methods for evaluating sheet metal formability

### 2.6.1 Forming Limit Diagram

Maximum values of principal strains $\varepsilon_1$ and $\varepsilon_2$ can be determined by measuring the strains at fracture on sheet components covered with grids of circles. The research in this field was pioneered by Keeler, based on the observations of Gensamer [9]. During forming, the initial circles of the grid become ellipses. Keeler plotted the maximum principal strain against the minimum principal strain obtained from such ellipses at fracture of parts after biaxial stretching. By this way, a curve limiting the tolerable range is obtained.

Later Goodwin plotted the curve of tension/compression domain by using different mechanical tests. In this case, transverse compression allows obtaining high values of tensile strains like in rolling or wire drawing.

The diagrams of Keeler and Goodwin together give the values of $\varepsilon_1$ and $\varepsilon_2$ at fracture. Those strain values can be used to determine forming limit diagram (FLD) that is seen in Figure 2.9 [9].

Keeler and Goodwin also suggested an empirical formula that was obtained from experimental trials on standard steel test specimens. This curve is only a function of work hardening exponent (n) and thickness (in mm), and it has been used for about twenty years and has yielded numerous successful results. However, it is not verified for the materials whose work hardening exponent is more than 0.21 and steel with a thickness in excess of 5mm. It is also not suitable for aluminum and new steels [11].

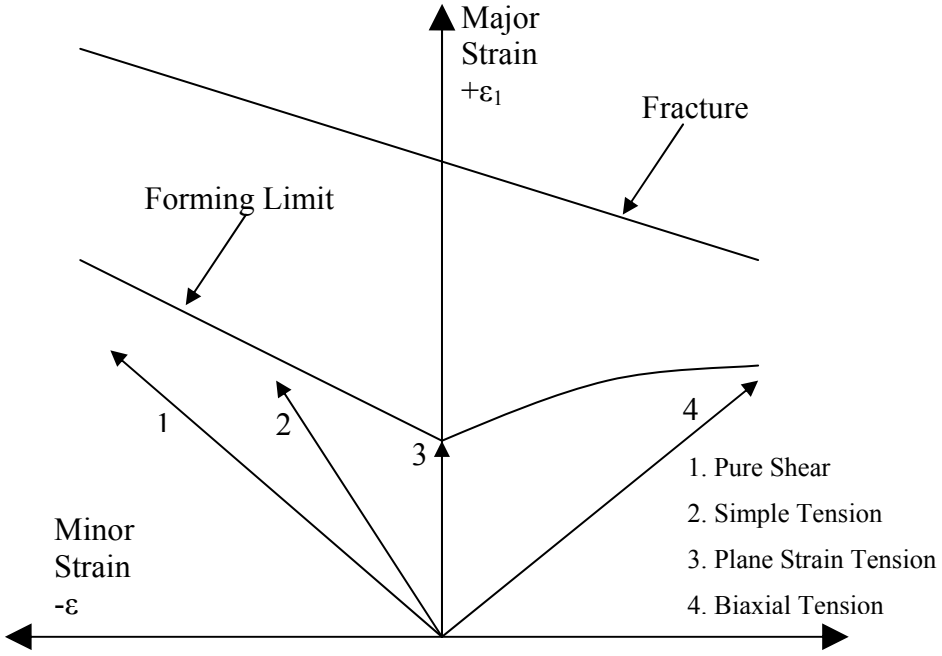


**Figure 2.9** Forming limit diagrams for necking and for fracture

## 2.7 Development of analysis methods in process simulation of metal forming

Analysis methods in process simulation describes all methods by which one or more of the process parameters of a real physical process are tried to predict approximately before its actual happening. It is aimed to manufacture products economically. Therefore, the application of process simulation must always be more economical than the application of the real process.

As seen in Figure 2.10, some analysis methods are developed to predict process parameters in metal forming. These methods can be classified under three subgroups [12]:

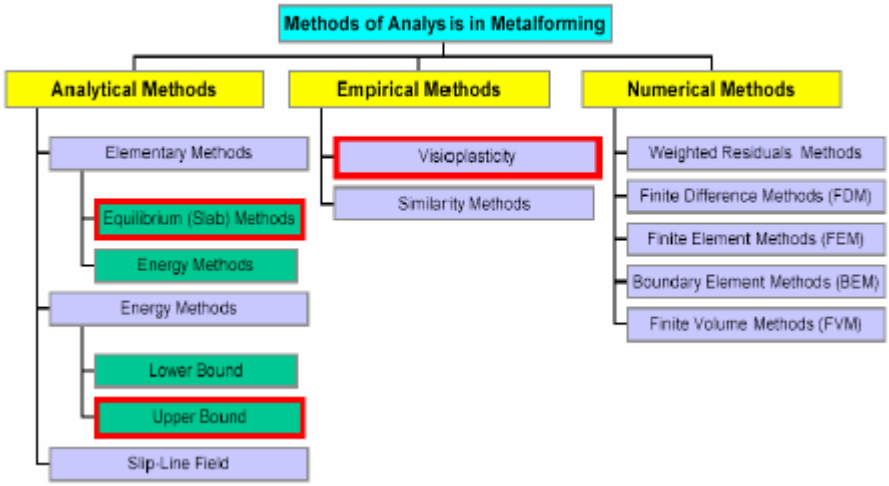


**Figure 2.10** Analysis methods in metal forming [33]

Analytical Methods:

- Elementary Methods (Slab Methods, Energy Methods)
- Energy Methods (Upper Bound, Lower Bound)
- Slip Line Field

Empirical Methods:

- Visioplasticity
- Similarity Methods

Numerical Methods:

- Weighted Residuals Methods
- Finite Difference Methods
- Finite Element Methods
- Boundary Element Methods
- Finite Volume Method

### 2.7.1 Empirical Methods for Process Simulations

Before the efficient employment of computers in process simulation, until approximately 1960, empirical simulation methods were predominately used in the process simulation. Visioplasticity and similarity methods are the most popular empirical simulation methods.

In visioplasticity, the grid that can be formed by mechanical, photomechanical, and electrochemical means, are used to observe the velocity field exits on a symmetry plane after deformation. The workpiece is deformed in one-step and the location of the nodes is compared with the initial locations to determine the displacements (Figure 2.11). The strain rates can be determined if the velocities are known. The stresses and strains are computed by using the strain rates. In addition, the determination of the velocity field in metal forming processes is necessary for the prediction of the total power required.

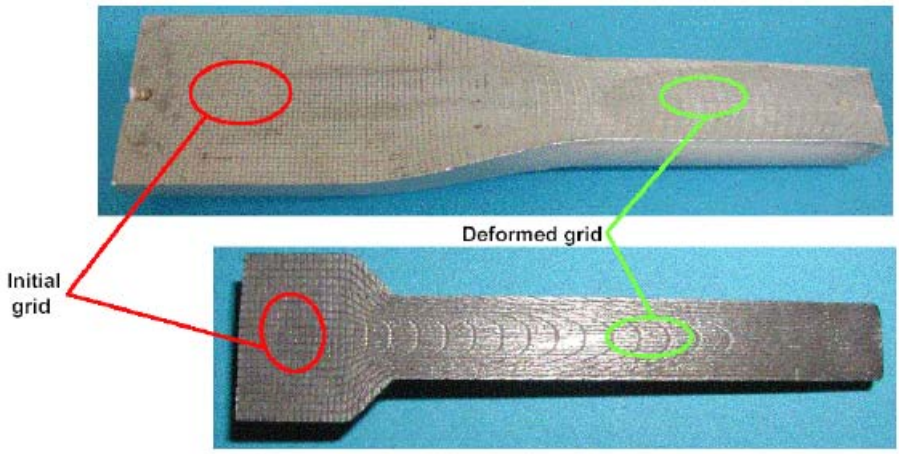


**Figure 2.11** Visioplasticity

A further estimation could be obtained by the similarity method employing spare materials such as waxes, polymers and other materials instead of metallic materials. This method is based on the fact that, the materials mentioned exhibit large similarities with the material characteristic of metals so that it simulates the flow of material quite well. Relatively too small forming forces is adequate since they have much lower yield stresses.

### 2.7.2 Analytical Methods for Process Simulation

Parallel to the empirical analysis methods described above analytical models were used to predict process parameters too. These models are exclusively based on the elementary theory of plasticity. It is characteristic that the formulation is based on a simple analytic algorithm or on a numerically graphic solution like the slip line field. Most popular analytical methods are slab method which requires a force balance on a strip of metal of different thickness, upper bound method that satisfies all the kinematic boundary conditions and lower bound method where the equilibrium equations and all force boundary conditions are satisfied.

### 2.7.3 Numerical Procedures for Process Simulation

Numerical simulation in the field of metal forming is not only a tool which the designer increasingly makes use of, but it is also an indispensable instrument in the research and development stages of the technology of metal forming [9].

The bases of finite element method (FEM) has been established through the effort of Courant, Argyris, Turner *et al,* Clough and Zienkiewicz *et al.* in the years 1940 through 1965. At the end of the sixties, Zienkiewicz has performed the extension of linear approach to non-linear problems for small elasto-plastic deformation. However, the milestone in finite element method is the introduction of the rigid plastic solution method and beginning of two dimensional applications in the universities at the beginning of seventies. The basic study related to the modeling

of large elasto-plastic deformations has been presented by McMeeking and improved by Nategaal, Simo and Taylor with the implementation of large rotations and consistent linearization. After the mid nineties three-dimensional applications of numerical solutions started worldwide in the industry [9].

Attempts of numerical approximate solution of sheet metal forming go back to 1980's. The very first numerical solutions of sheet forming processes have been obtained by finite difference methods (FDM) [13]. These methods are, however, restricted to axisymmetrical problems. In the nineties, attempts have been made to replace FDM with FEM in general three-dimensional deep drawing problems. This is due to the serious drawback of not applying boundary conditions in a general manner as it could be done elegantly in the finite element method, FDM could not be established.

The real break-through of the numerical approximation of sheet metal processes was possible through the application of the finite element method done by Wang and Budianski, Wifi, Gotoh and Ishise [9]. In those applications, they used either elasto-plastic or rigid plastic material law and element types were membrane or continuum. Up to this point, all studies are static implicit or static explicit type.

The dynamic explicit methods have their roots in the study of Belytschko and Mullen in 1977. After that, further improvements of numerical procedures in sheet metal forming have continued with the incorporation of viscous effects, replacement of drawbeads with artificial forces, thermo-mechanically coupled modeling.

Developments in the sheet metal forming simulation by the finite element method started roughly 5 to 6 years later than the bulk forming simulation. This is due to the basic differences given in Table 2.1 [9] between these processes.

**Table 2.1** Comparison of sheet metal forming and bulk metal forming [9]

| | **Sheet Metal Forming** | **Bulk Metal Forming** |
|---|---|---|
| **Workpiece Geometry** | Plane Structured<br>S/V α 1/t, t≈1 | Balance<br>S/V α 1/a, a>>1 |
| **Material Behavior** | Normal (Planar) anisotropy | Bauschinger effect |
| **Deformation Kinematics** | (very) large displacements but moderate strains | large displacements and (very) large strains |
| | instabilities (necking, wrinkling, etc.) | almost no instability mode |
| **Process Features** | Cold | Cold / warm / hot |
| | Workpiece failure | Die and workpiece failure |
| | Spring-back critical | Spring-back not critical |
| | Residual stresses critical | Residual stresses critical |
| **Finite Element Solution** | Always elasto-plastic | Rigid / visco-rigid / elasto-plastic |
| | Shell (membrane) elements | Continuum elements |
| | Isothermal | Thermo-mechanically coupling |
| | Basically explicit | Implicit |
| | Remeshing due to inhomogeneous deformation and geometric description accuracy | Remeshing due to large elemental distortions |

# CHAPTER 3

# REVIEW OF FINITE ELEMENT METHOD

## 3.1 Introduction

The finite element method (FEM) is a numerical technique by which differential equations are solved approximately up to a selected degree of accuracy [9].

In FEM, the behavior of a continuum, which is normally impossible to determine exactly, is approximated by idealization. For this purpose, the shape and behavior of the continuum is redefined by a mesh which is composed of finite collection of sub-domains called finite elements and nodal points where the values of the function (displacements) and its derivatives (velocity and acceleration) are specified.

Furthermore, the relationship between the unknown displacement and known forces at the nodes are determined with a formulation, which can be either *linear* as in Eq. (3.1), where the structural stiffness is independent of displacement, or a *non-linear formulation* as in Eq. (3.2), where the structural stiffness is dependent on displacement.

$$\{F\} = [k] \cdot \{u\} \tag{3.1}$$

$$\{F\} = [k\{u\}] \cdot \{u\} \tag{3.2}$$

where

*F* is force vector

*k* is the stiffness matrix

*u* is the displacement vector

The sources of nonlinearity in the finite element analysis can be classified as material nonlinearity, contact nonlinearity and geometric nonlinearity. Metal forming simulations are non-linear problems and they should be solved by using non-linear formulation.

The number and density of mesh depends on the requirements of the process to be simulated. The element size in the mesh should be small enough to represent all the details in the geometry and large enough to avoid unnecessary time consuming calculations in order to be cost efficient.

For non-deformable tools, mesh is only representation of the geometry, whereas for deformable bodies, the finite elements are the representation of material with a simplified behavior in small pieces. Various material behavior models are used in FEM. Rigid-plastic and elasto-plastic are the most commonly used material models in metal forming simulation. The former does not require the consideration of the linear kinematics of the finite deformation; hence, the formulation is less time consuming, more reliable, and robust. On the other hand, elasto-plastic material model should be used for residual stress analysis and net shape forming process simulations in which the elastic strains cannot be neglected. In elasto-plastic material model, the elastic behavior is taken to be linear and the plastic response is usually modeled using the Levy-Mises yield criterion (Figure 3.1).

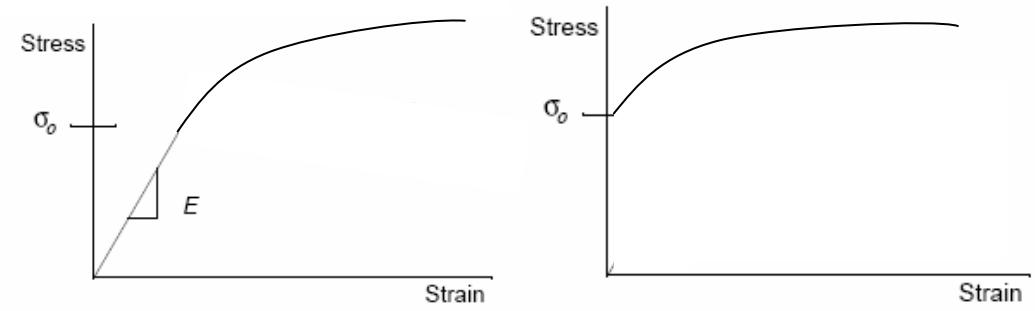


**Figure 3.1** Elasto-plastic (left) and rigid plastic (right) material behaviors

According to the requirements, element type used may also show variety in the finite element simulations. In bulk metal forming, only continuum elements are used, whereas in sheet metal forming, surface elements are preferable due to the high surface to volume ratio of the workpiece. There are four different types of elements available for the analysis of sheet metal forming processes [9]. In sheet metal forming processes for which bending occurs over a bending radius larger than roughly ten times the sheet thickness [14], membrane elements can be used, However for the deep drawing simulations, shell elements are more applicable and they are divided in to two groups which are thin and thick shell elements. Continuum elements are rarely used in sheet metal simulations, but sometimes for hydroforming and blanking simulations, they are appropriate to use. No matter surface elements or continuum elements are used, the use of triangle or tetrahedral elements in the deformable mesh should be prevented where possible. Providing the robustness and due to contact problems, it is advisable to use low order element having four nodes and using linear shape functions.

In addition, two different time integration schemes, namely implicit and explicit algorithms are used in FEM. Implicit algorithm enables a full static solution with convergence control whereas explicit algorithm is more robust and there is no check of unbalanced forces. Next section is dedicated to mathematical formulation of dynamic-explicit finite element method and comparison of two integration schemes.

## 3.2 Dynamic- Explicit Finite Element Method

The dynamic-explicit methods are based on the solution of a dynamic problem, even if it a quasi-static as in most application of metal forming. A simple one dimensional mass-spring-damper system is considered to express to bases of these methods (Figure 3.1).

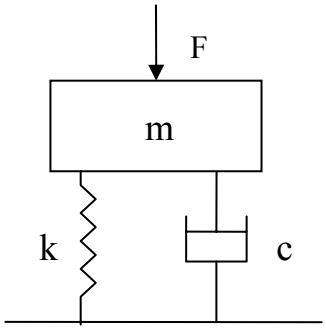


**Figure 3.1** Simple mass-spring-damper system under an external force

The equation of motion for the free-body diagram of mass is given as

$$m\ddot{u} + c\dot{u} + ku = F(t) \tag{3.3}$$

where

$m$ is the mass of the body

$c$ is the damping coefficient of the damper

$k$ is the stiffness of spring

$u$ is the displacement of mass measured from its static equilibrium position

$\dot{u}$ is the instantaneous speed of the mass at time $t$

$\ddot{u}$ is the instantaneous acceleration of the mass at time $t$

$F(t)$ is the external force as a function of $t$

Eq. (3.3) can be divided by *m* and is rewritten as:

$$\ddot{u} + 2\zeta\omega\dot{u} + \omega^2 u = f(t) \tag{3.4}$$

where

$$\begin{aligned} \omega &= \sqrt{k/m} \\ \zeta &= c/(2\sqrt{mk}) \\ f(t) &= F(t)/m \end{aligned} \tag{3.5}$$

$\omega$ is the eigen-frequency of the system and $\zeta$ is the viscous damping factor. According to the value of $\zeta$, the response of the system alternates. For $\zeta > 1$ the system is overdamped, for $\zeta < 1$ underdamped and for $\zeta = 1$ critically damped. Critically damped systems tend to reach the equilibrium position the fastest when an external force is applied. For the critically damped system ($\zeta = 1$) from Eq. (3.5) damping coefficient should be equal to

$$c = 2\omega m \tag{3.6}$$

The equation of motion given in Eq. (3.4) can be solved by applying the central difference method:

$$\begin{aligned} \ddot{u}^t &= \frac{1}{\Delta t^2}(u^{t+\Delta t} - 2u^t + u^{t-\Delta t}) \\ \dot{u}^t &= \frac{1}{2\Delta t}(u^{t+\Delta t} - u^{t-\Delta t}) \end{aligned} \tag{3.7}$$

Substituting Eq. (3.7) into Eq. (3.5) and rearranging yields:

$$\left[\frac{1}{(\Delta t)^2}m + \frac{1}{2\Delta t}c\right]u^{t+\Delta t} = F(t) - ku^t + \frac{m}{(\Delta t)^2}\left[2u^t - u^{t-\Delta t}\right] + \frac{c}{2\Delta t}u^{t-\Delta t} \tag{3.8}$$

The solution of displacement at time $t + \Delta t$ only depends on the displacement of the known states at times $t$ and $t - \Delta t$, this time discretization scheme is named as dynamic explicit integration of the equation of motion. In case of the implicit integration methods, the solution depends also on the displacements of the unknown state at time $t + \Delta t$, which is usually expressed as dependency of the stiffness term on the unknown displacements [9].

The time step should be smaller than a critical time step $\Delta t_{cr}$, which is

$$\Delta t_{cr} = \frac{T}{\pi} = \frac{2}{\omega} = 2\sqrt{\frac{m}{k}}, \tag{3.9}$$

where $T$ is the eigen-period of the system to satisfy the condition for convergence.

Moreover for the 3-D generalization of deformable body, virtual work equation can be modified by adding an inertia term to yield

$$\int_V T_{ij}\delta u_{ij} dV = \int_A t_i \delta u_i dA - \int_V \rho \ddot{u}_i \delta u_i dV, \tag{3.10}$$

where

$T_{ij}$ is the Cauchy stress tensor

$u_{ij}$ is the gradient of the displacements

$\ddot{u}_i$ is the acceleration of material

$t_i$ is the traction vector

$\delta$ is the variational operator

$\rho$ is the density

The finite element spatial discretization of this equation yields

$$[M]\ddot{u}^t = \{F^t\} - \{I^t\}, \tag{3.11}$$

where

$[M]$ is the consistent mass matrix

$\{F\}$ is the external force at time t

$\{I\}$ is the internal force at time t

An artificial damping term $[C]$ should be added to Eq. (3.11) in order to provide the stability. This yields to

$$[M]\{\ddot{u}^t\} + [C]\{\dot{u}^t\} = \{F^t\} - \{I^t\} \tag{3.12}$$

Using central difference method given in Eq. (3.7) the above equation can be rewritten as

$$\begin{aligned} &\frac{1}{(\Delta t)^2}[M] + \frac{1}{2\Delta t}[C]\{u^{t+\Delta t}\} = \{F^t\} - \{I^t\} + [M]\frac{1}{(\Delta t)^2}\left(2\{u^t\} - \{u^{t-\Delta t}\}\right) \\ &+ [C]\frac{1}{2\Delta t}\{u^{t-\Delta t}\} \end{aligned} \tag{3.13}$$

The initial conditions for nodal displacements, velocities, internal and external forces at the time $t = 0$ are given; however the nodal displacements at time $-\Delta t$ are also required at the very first step and it can be obtained from:

$$\{u^{-\Delta t}\} = \{u^0\} - \{\dot{u}^0\}\Delta t - \frac{1}{2}\{\ddot{u}^0\}(\Delta t)^2 \tag{3.14}$$

where the initial accelerations $\{\ddot{u}^0\}$ is given by

$$[M]\{\ddot{u}^0\} = \{F^0\} - \{I^0\} - [C]\{\dot{u}^0\} \tag{3.15}$$

To increase the computational efficiency the consistent mass and damping matrices are approximated by diagonal (lump) matrices: Eq. (3.13) is uncoupled on the left hand side and no factorization is necessary. Furthermore, this approximation has proven itself quite useful since on one hand the central difference method is known to shorten the vibration period whereas the use of lumped matrices increase this period, thus a balanced total effect is obtained at the end [9].

The lumped damping matrix is assumed as the linear combination of the mass and the stiffness matrix:

$$[C] = c_1[M] + c_2[K] \tag{3.16}$$

It is difficult to obtain the damping properties of the structure, so that for $c_1$ an approximation based on the critical damping condition given in Eq. (3.6) is suggested as

$$c_1 = 2\omega \quad \forall \quad \text{degree of freedom} \tag{3.17}$$

On the other hand, $c_2$ is usually taken as zero, but Schweizerhof and Hallquist [15] suggest modifying Eq. (3.13) by using an approximation instead of using Eq. (3.7).

$$\left\{\dot{u}^t\right\} \approx \left\{\dot{u}^{t-\frac{\Delta t}{2}}\right\} \tag{3.18}$$

yielding

$$\left(\frac{1}{(\Delta t)^2}[M]\right)\left\{u^{t+\Delta t}\right\} = \left\{F^t\right\} - \left\{I^t\right\} + \left(\frac{[M]}{2\Delta t} - [C]\right)\left(\frac{\left\{u^t\right\} - \left\{u^{t-\Delta t}\right\}}{\Delta t}\right) \tag{3.19}$$

The explicit algorithm integrates through time by using small time increments. The central difference operator is conditionally stable as already pointed out and the stability limit for the operator with including the damping is simplified from Eq. (3.9) to

$$\Delta t \le \frac{2}{\omega_{\max}}\left(\sqrt{1+\xi^2}-\xi^2\right), \tag{3.20}$$

where $\xi$ is the fraction of critical damping in the highest mode. Eq. (3.20) is valid for linear systems but it can be used as an estimate for nonlinear systems such as elasto-plastic metal forming problems. It is estimated that the critical time step for non-linear problems is about 50 - 80 % lower than the one computed for the linear systems [9].

In a finite element simulation the critical time step can be also approximated for each element at each step by

$$\Delta t \le \frac{L}{c_d}, \tag{3.21}$$

where $c_d$ is the elastic wave speed of material (speed of sound in that material) and $L$ is the characteristic element dimension. The elastic wave speed is obtained from

$$c_d = \sqrt{\frac{2G(1-v)}{(1-2v)\rho}} \tag{3.22}$$

Calculation of each increment in dynamic-explicit methods is very robust and less time consuming than implicit methods; however, too small time steps result in unacceptable high number of increments, which make the dynamic-explicit methods infeasible. Two numerical tricks are applied to avoid this.

The total process time is reduced by exaggerating speed of moving tool or increasing the gradient of loading curves. In order to compensate the undesired

effects of artificial inertia forces numerical damping is applied. This treatment is not suggested and an additional precaution should be taken for the analysis involving strain rate sensitive materials. In addition, increase in the density of the material leads a reduction in the total number of increments since it reduces the sound of speed in the material and hence increases the minimum allowable time step. The additional artificial inertia forces cannot be reduced by introducing numerical artificial damping but these forces may be taken over by the rigid dies since in deep drawing most of the workpiece is supported by the dies [9]. Therefore, dynamic-explicit methods can be applied to the sheet metal forming processes successfully from this point of view.

## 3.3 Comparison of Implicit and Explicit Methods

Implicit methods satisfy the static equilibrium in the unknown final configuration of a time increment and enable a full static solution with convergence control. The increment size can be very large depending on the contact condition and the CPU time increases drastically as the element number increases because of the matrix inversion operation and accurate time integration scheme. This leads to the problem such as the divergence of the solution and the singularity of the stiffness matrix.

On the other hand, the most important advantage of the dynamic-explicit method is its robustness and independency of the stiffness term on the unknown displacement. The computational speed is faster and memory requirement is less than the static-implicit methods. In addition, the region of the wrinkles is accurately determined in dynamic-explicit methods. However, the integration scheme is only valid if the mass matrix is lumped. Furthermore, the speed advantages can hold only if element computations are as few as possible. This is satisfied only by using single quadrature elements having rather poor stress and strain accuracy. It is claimed that the error introduced by a lamped mass matrix is compensated by a reduced integration scheme of the elements; however, this causes some disadvantages that

the local stresses and spring-back is not accurately calculated and there is possibility to have hourglass (zero energy) modes.

## 3.4 Conclusion

The simulation of metal forming processes has reached today a level that allows the accurate estimation of processes parameters. The commercial FE software have user-friendly graphic user interface (GUI) and comfortable pre- and post-processors, that any technician may use the software after a few days training. However, this easiness may turn to a drawback. According to Tekkaya [9], the successful application still requires;

1. The existence of a well-defined physical problem, for which a numerical analysis can provide a solution
2. The correct idealization of this physical problem (simplifications, assumptions, detection of governing physical phenomena)
3. The correct spatial discretization of the idealized problem (type of elements, topology of the element mesh, density of element mesh)
4. The setting of correct boundary conditions (friction, heat transfer, machines, dies)
5. The use of correct material laws and parameters (flow curve, anisotropy, failure)
6. The selection of correct numerical parameters (penalty factors, convergence limits, increment sizes, remeshing criterion)
7. The economical analysis (reasonable computational times, reasonable modeling times, reasonable storage requirements)
8. The correct interpretation of the numerical results

All these points require not only the forming process knowledge but also thorough inspection about the parameters and concepts underlying a finite element analysis. Therefore, the next chapter is dedicated to the determination of optimum parameters used in the numerical simulation.

# CHAPTER 4

# DETERMINATION OF OPTIMUM PARAMETERS USED IN SIMULATIONS

## 4.1 Introduction

The sheet metal forming industry requires increased reliability of any prediction of numerical simulation, thus the consistency and verification of the numerical simulation itself becomes more important. This chapter is focused on the optimization of parameters used in the finite element codes to ensure the achievement of accurate simulation results.

Numerical simulations will be carried out for a three-dimensional cylindrical cup drawing process using a dynamic-explicit commercial FE-code. Within this investigation, process and numerical parameters to be studied are the punch speed, blank holder force, friction coefficient, element size, mesh topology, time step-scaling factor, adaptive meshing, and mass scaling. These parameters, which should be applied properly, are varied thoroughly in numerous simulations and their influence of the thickness contour, equivalent stress distribution, kinetic energy vs. punch stroke and forming force vs. displacement curves are inspected. At the end of the chapter, results of simulation using suggested optimum parameters are verified with both NUMISHEET 2002 Benchmark [16] and an analytical formulation derived by Rameakers [17, 18]. In addition, high-pressure sheet metal forming simulation results are also compared with experimental results.

## 4.2 Process Geometry

Axisymmetrical deep drawing is selected to be used for the optimization study. Setup and geometry of tools used in the benchmark are given in Figure 4.1. The punch radius is 50.00 mm and die radius is 51.25 mm. The fillet radii of die and punch are 9.5 mm and 7.0 mm, respectively. During the study, two different anisotropic materials having 1 mm thickness are used as workpieces. The radii of workpieces are 90mm for aluminum blank and 105 mm for steel blank.

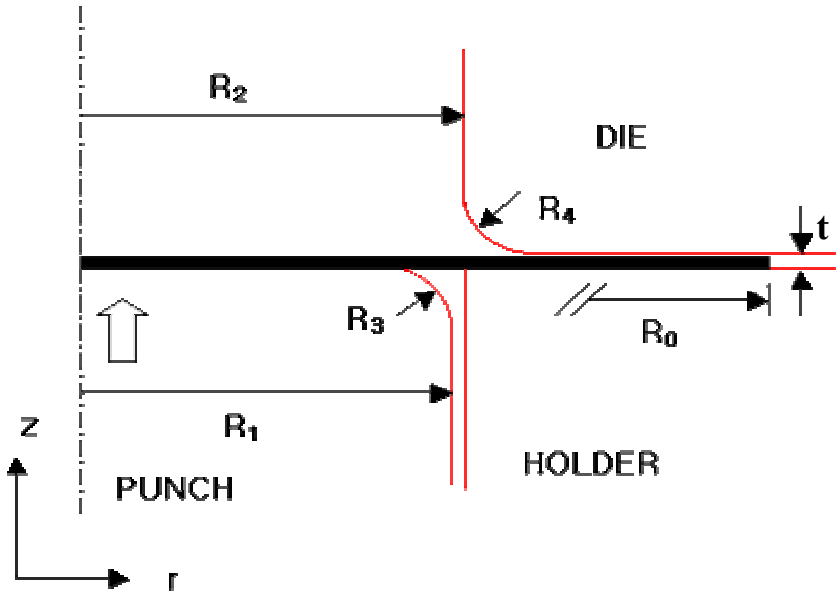


**Figure 4.1** Axisymmetrical deep drawing process [16]

## 4.3 Material Properties, Machine and Tooling Specifications

The material properties of aluminum and steel workpieces are tabulated in Table 4.1

**Table 4.1** Material properties of aluminum (6111-T4) and steel (DDQ mild steel)

| Material | E (GPa) | ρ g/cm$^3$ | ν | $\varepsilon_0$ | K (MPa) | n | R (0°) | R (45°) | R (90°) |
|---|---|---|---|---|---|---|---|---|---|
| 6111-T4 | 70.728 | 2.6 | 0.342 | 0.00256 | 538.2 | 0.2255 | 0.894 | 0.611 | 0.660 |
| DDQ Steel | 221.368 | 7.8 | 0.3 | 0.00876 | 547.3 | 0,2692 | 2.160 | 1.611 | 2.665 |

In the simulation belonging to the optimization study, punch penetrates 40 mm into the die cavity. Thus, simulations are proceeded till the required depth of 40 mm is achieved. Average friction coefficient at all contact surfaces are supplied as 0.0096 for aluminum material and 0.0426 for steel blank. Two different blank holder forces are applied for each material within the study and they are given in Table 4.2. Binder, blank holder, die and punch are assumed as rigid bodies in the simulations

**Table 4.2** Blank holder forces used for aluminum (6111-T4) and DDQ mild steel

| **6111-T4 Aluminum** | | **DDQ Mild Steel** | |
|---|---|---|---|
| Low blank holder force (LBHF) kN | 10 | Low blank holder force (LBHF) kN | 10 |
| High blank holder force (HBHF) kN | 50 | High blank holder force (HBHF) kN | 70 |

## 4.4 Process Parameters

In Figure 4.2, finite element model of cup drawing process is shown. Process parameters, such as punch velocity, blankholder force, and friction coefficient will be investigated for the given material properties and process specifications throughout the series of simulations and their effects on the results are observed.

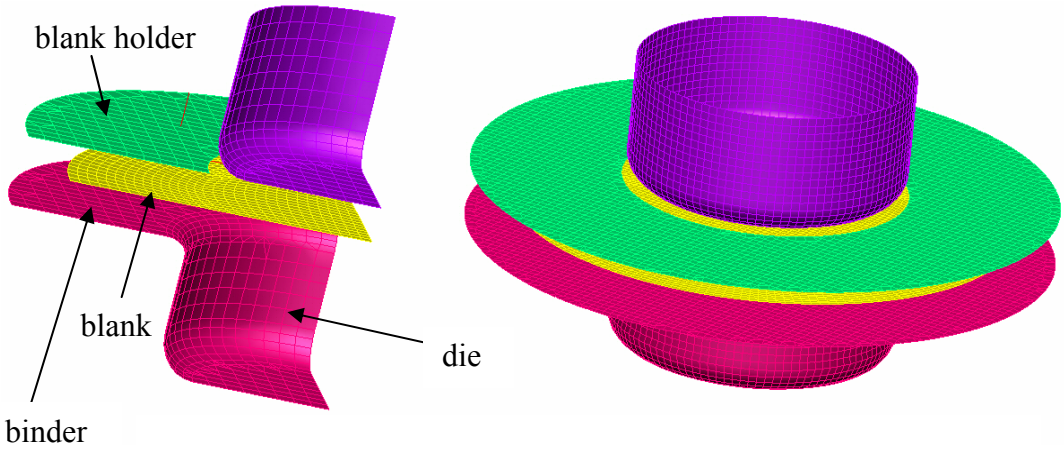


**Figure 4.2** Finite element model of axisymmetrical cup drawing

### 4.4.1 Punch Velocity

In this section, the effect of punch speed on the analysis' accuracy and CPU time will be inspected. For this purpose a series of different punch velocities are used to simulate the processes for both aluminum and steel materials.

Punch velocities are 0.02 m/s, 0.1 m/s, 0.5 m/s, 1 m/s, 2 m/s, 5 m/s, 10 m/s, 15 m/s, 20 m/s, 50 m/s, 100 m/s, 200 m/s, 500 m/s, and 1000 m/s

First simulation is done with constant punch velocity of 0.02 m/s that is a relatively low speed; however, after seven days of computation the simulation does not end up with a result. Therefore, higher punch velocities are started to be used and the first satisfactory result is obtained when the punch velocity is 0.05 m/s. A series of simulation with different punch velocities is performed and it is found that in the range of velocities between 0.05 m/s and 20 m/s, the thickness distribution results of simulations display insignificant dissimilarities whereas the computational time of simulations are drastically disparate (Figure 4.3).

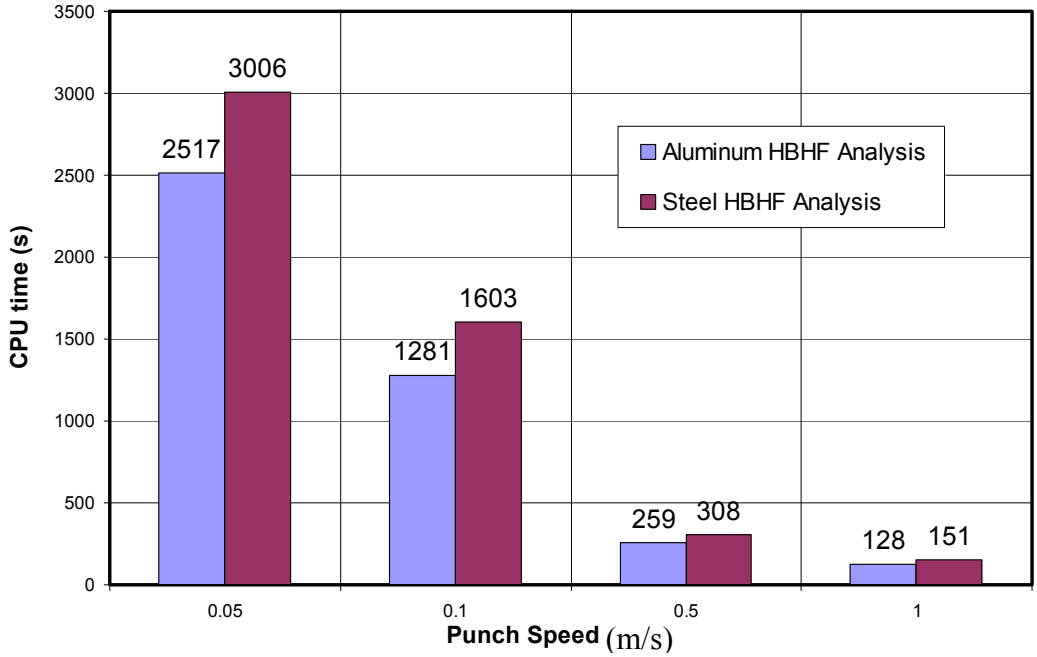


**Figure 4.3** Effect of punch speed on CPU time

Thickness contours of aluminum and steel workpieces subjected to high blankholder force (50kN) at different punch velocities are given in Figure 4.4 to Figure 4.11. The results belong to the final state of cup drawing process obtained after the punch stroke of 40 mm.

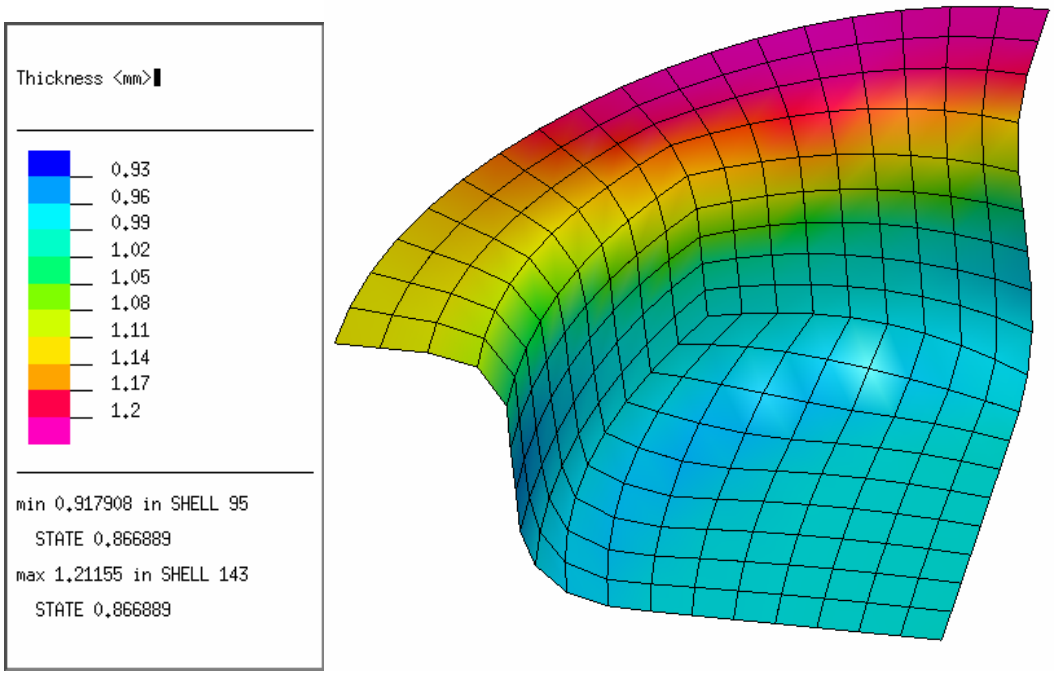


**Figure 4.4** Thickness contour for aluminum sheet material at final step of HBHF analysis with punch speed of 0.05 m/s

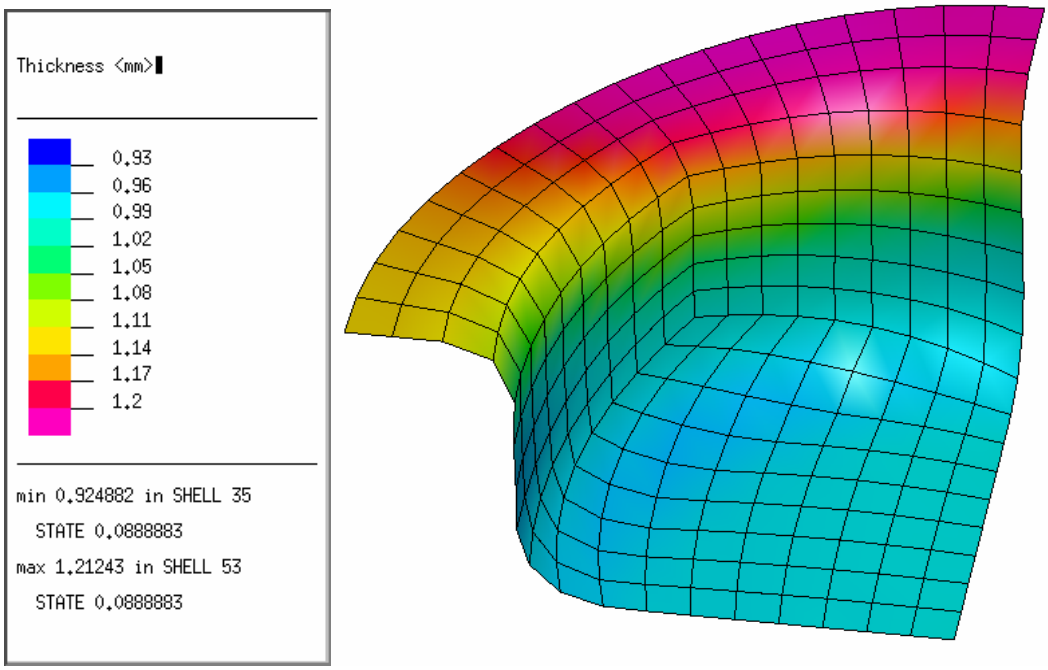


**Figure 4.5** Thickness contour for aluminum sheet material at final step of HBHF analysis with punch speed of 0.5 m/s

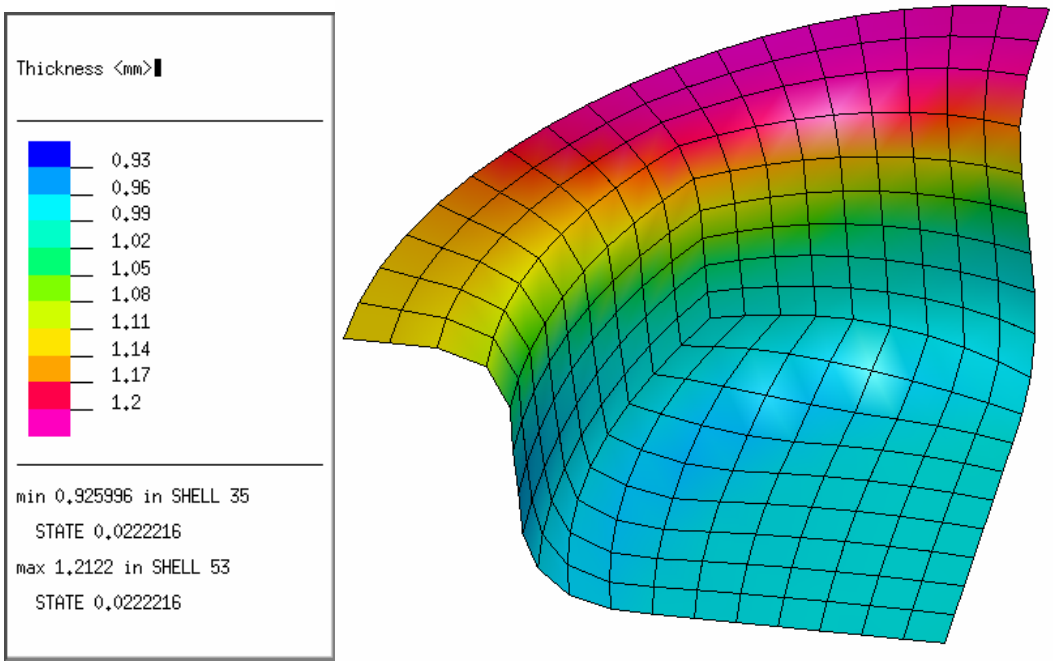


**Figure 4.6** Thickness contour for aluminum sheet material at final step of HBHF analysis with punch speed of 2 m/s

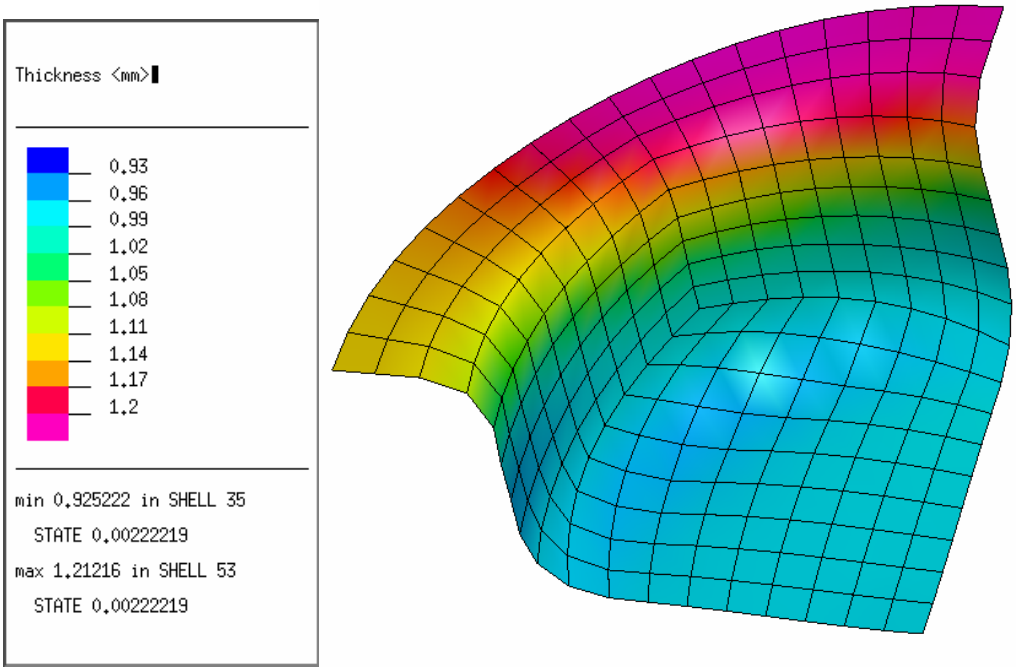


**Figure 4.7** Thickness contour for aluminum sheet material at final step of HBHF analysis with punch speed of 20 m/s

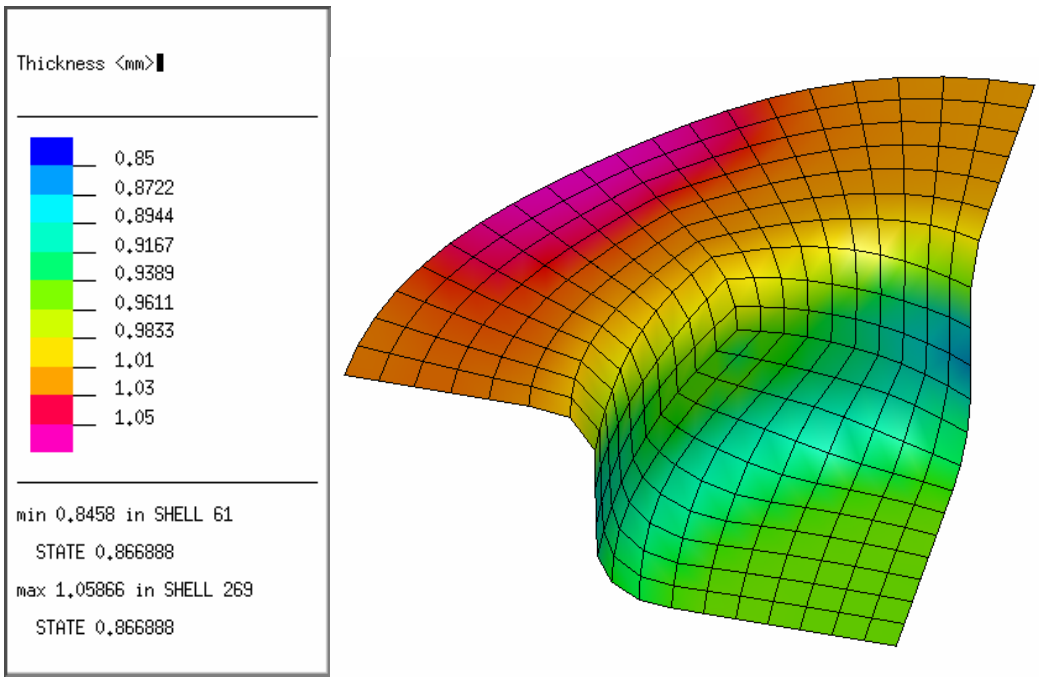


**Figure 4.8** Thickness contour for steel sheet material at final step of HBHF analysis with punch speed of 0.05 m/s

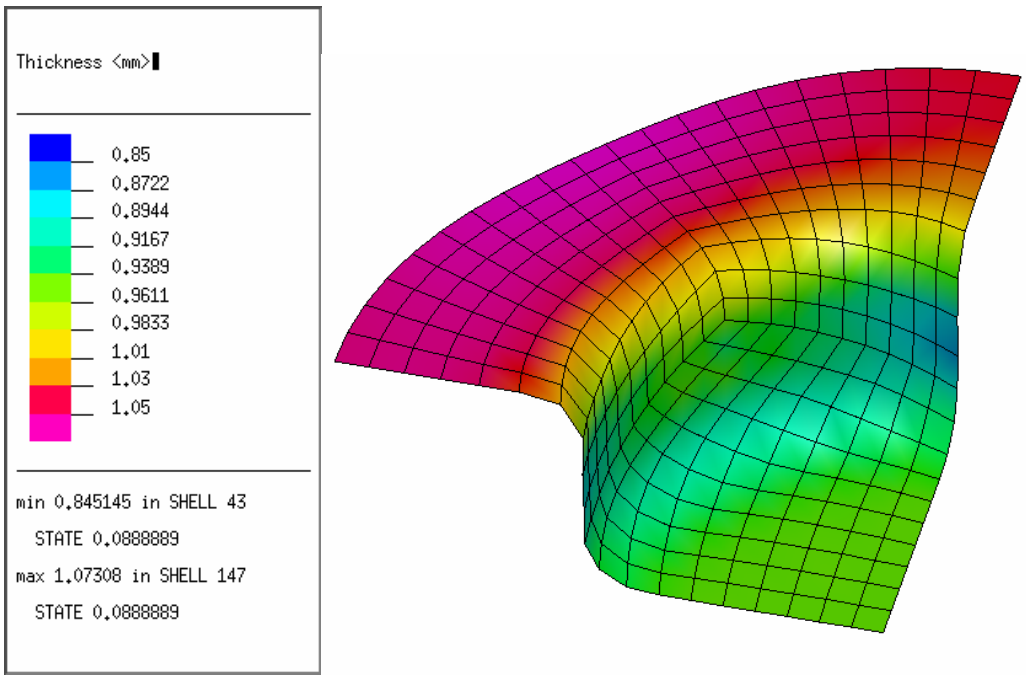


**Figure 4.9** Thickness contour for steel sheet material at final step of HBHF analysis with punch speed of 0.5 m/s

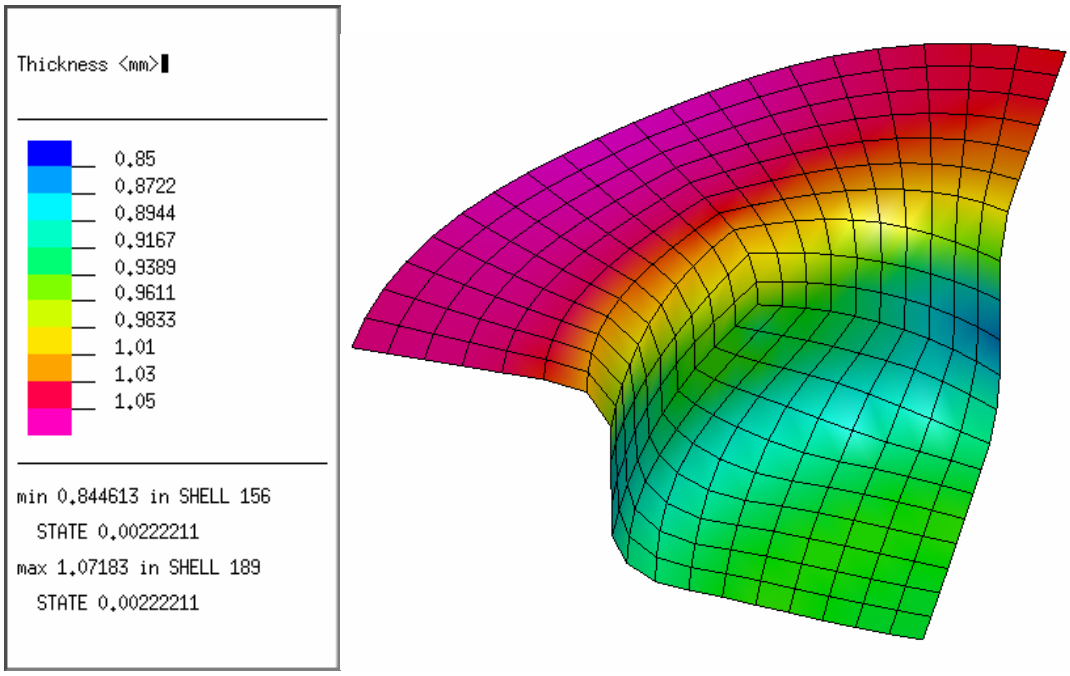


**Figure 4.10** Thickness contour at final step for aluminum HBHF analysis with punch speed of 20 m/s

As the minimum and maximum thickness values in each simulation are inspected, it could be stated that the maximum variation in magnitude of thickness values in both materials are less than 1%. The effect of varying punch velocity speed can also be observed in forming force vs. punch displacement curves. As seen in the Figure 4.11 and Figure 4.12, the results obtained by simulations in the optimum range of velocity (0.05 m/s to 20 m/s) are even more similar to each other than of the thickness contour.

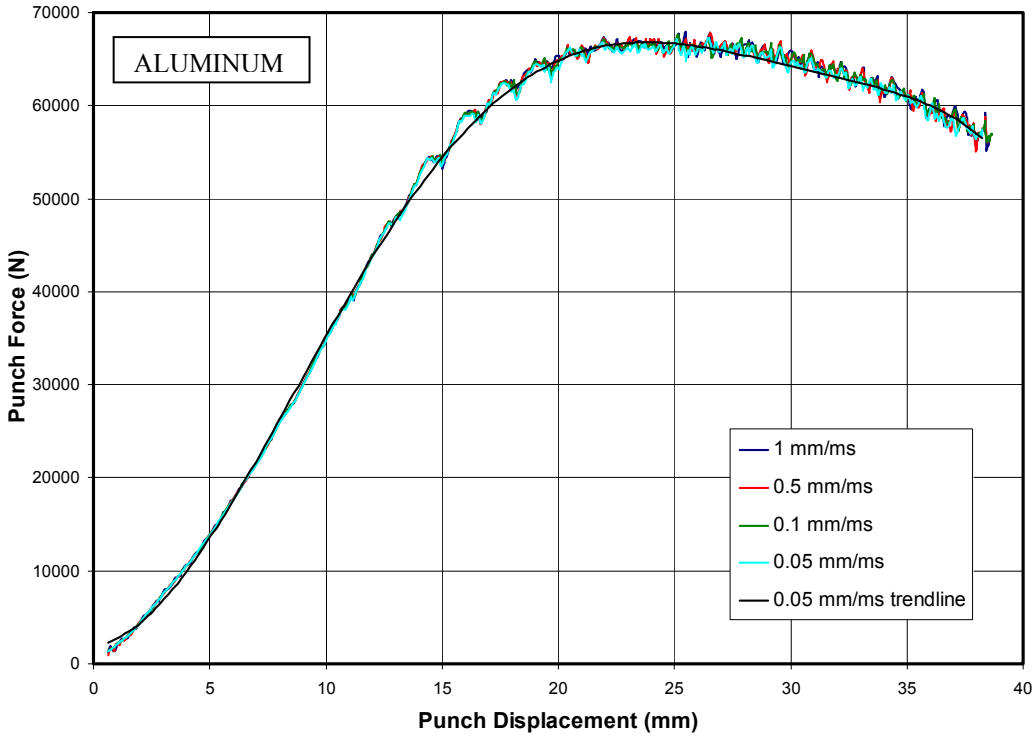


**Figure 4.11** Punch force vs. punch displacement curves of HBHF analysis of aluminum material at various punch speeds

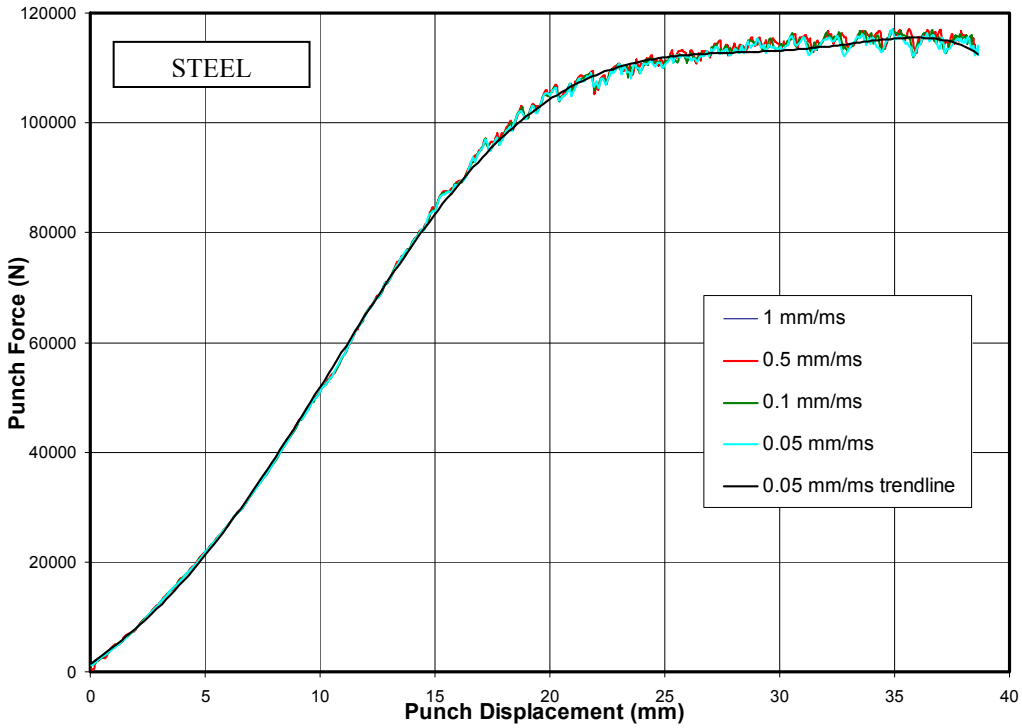


**Figure 4.12** Punch force vs. punch displacement curves of HBHF analysis of steel material at various punch speeds

On the other hand, when the punch speed reaches 50 m/s for aluminum and 20 m/s for steel workpiece (those are the upper limits of punch speed proposed for that process simulation), the presence of large vibrations cause the results to become invalid due to the dynamic effects (Figure 4.13 and 4.14).

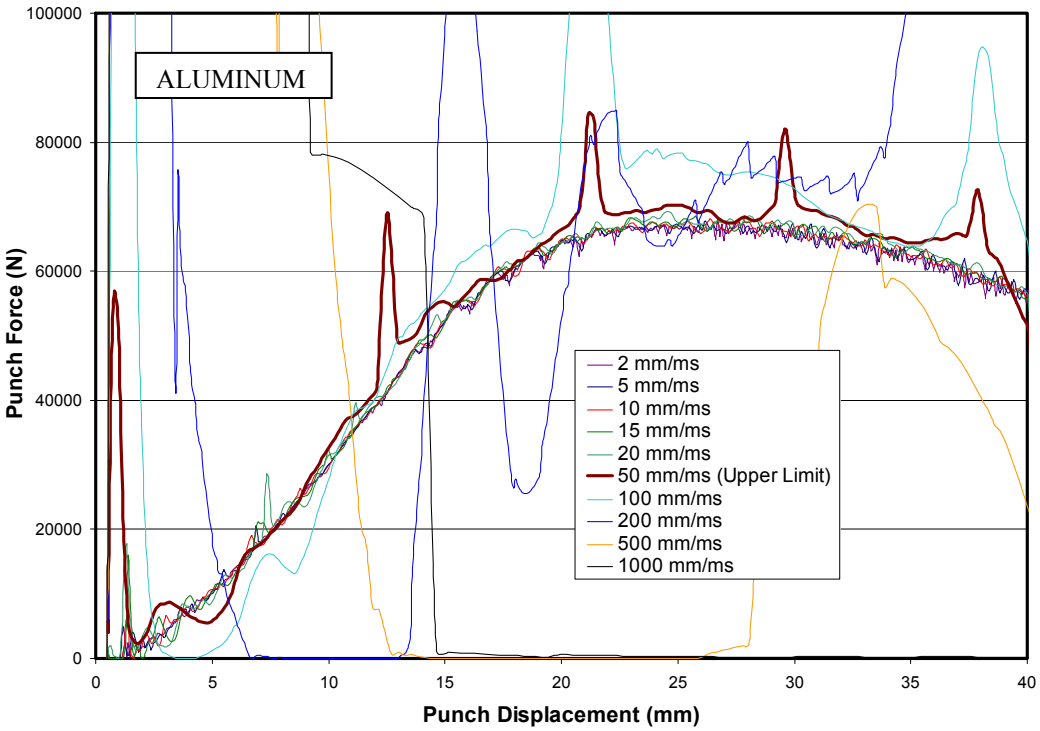


**Figure 4.13** Punch force vs. punch displacement curves of HBHF analysis of aluminum material at various punch speeds between 2 m/s and 1000 m/s

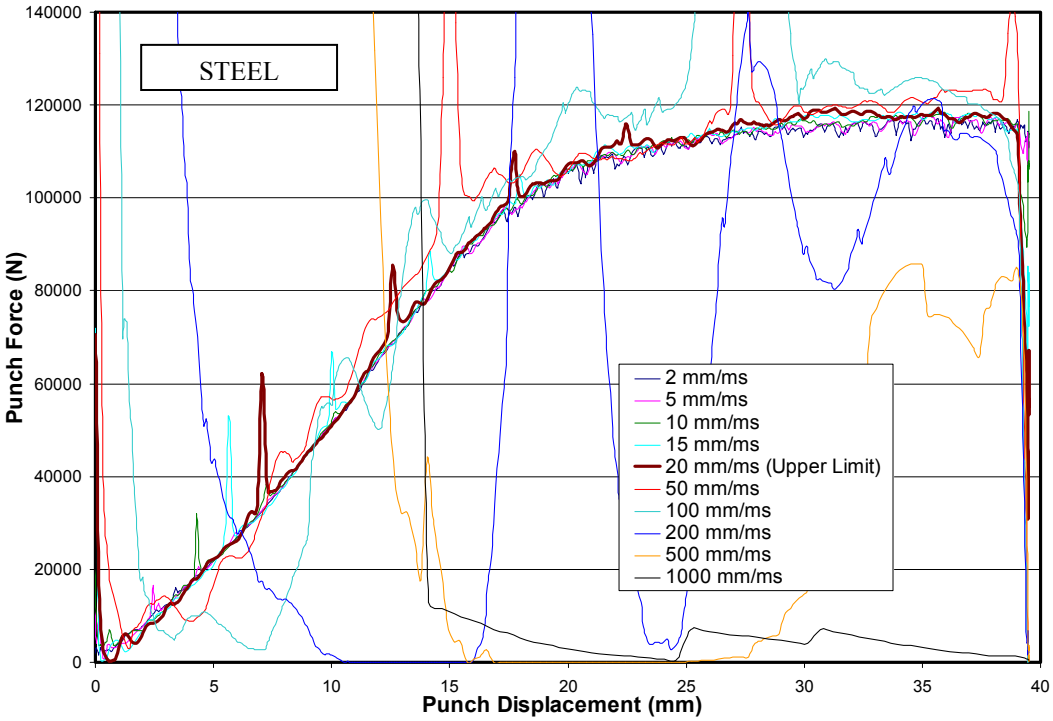


**Figure 4.14** Punch force vs. punch displacement curves of HBHF analysis of steel material at various punch speeds between 2 m/s and 1000 m/s

Dynamic-explicit codes have this problematic phenomena, therefore software using this kind of solver, generates some damping coefficients to avoid high frequency vibrations and hourglass modes. Additionally, it is advisable to assign load or velocity as continuous, differentiable curves. Although it is easier and it seems reasonable to assign a constant velocity for a moving tool, undesired dynamic effects arise due to the rapid strike of the punch to the deformable body that is sheet in this case. As the consequence of this collision, the blank starts to vibrate forcefully, and the precision of the simulation is diminished because of the exaggerated vibrations. However, in the real case, firstly, tool is stationary and then it will start to accelerate till it reaches maximum velocity, stays constant at that value for some time, after all of that it starts to decelerate and becomes immobile. Thus, assigning the velocity as a function of time (Figure 4.15), similar to the real case, reduces the vibration that occurs at the initial contact between blank and the moving tool. This makes the simulation more reliable, realistic, and accurate.

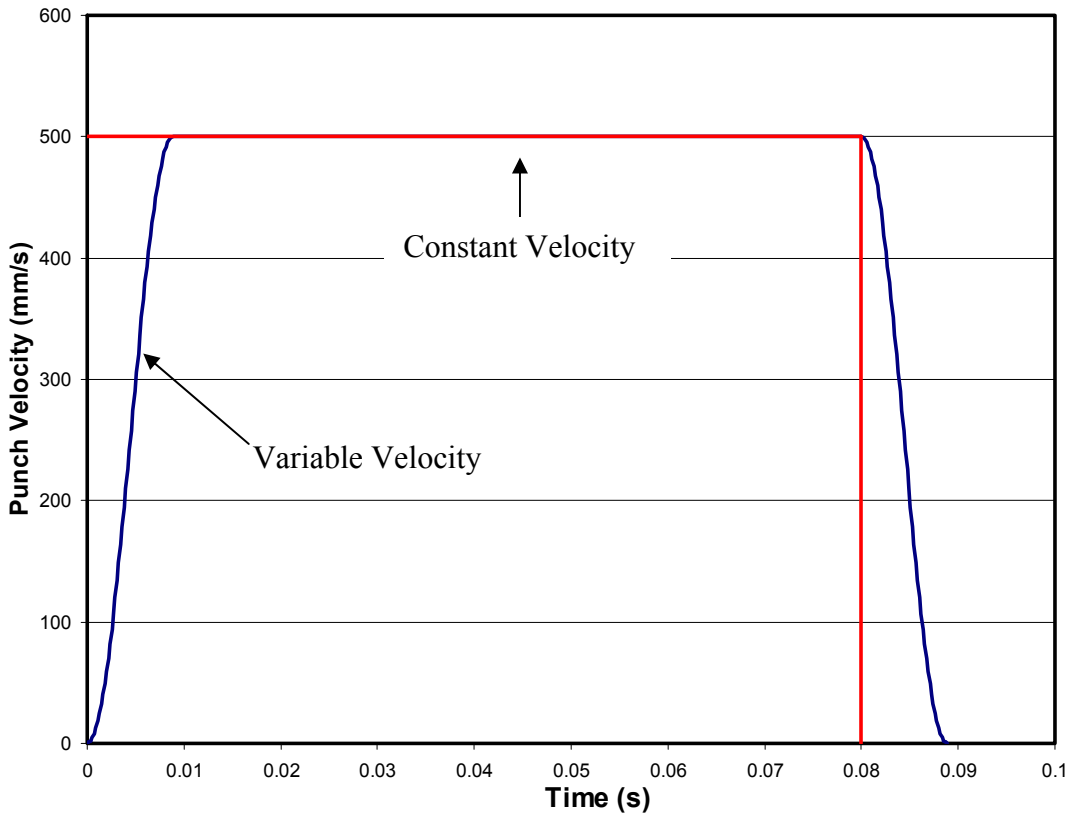


**Figure 4.15** Comparison of variable and constant punch velocities

The presence and intensity of vibrations can be clearly observed both in the kinetic energy of deformable body vs. punch stroke curve (Figure 4.16).

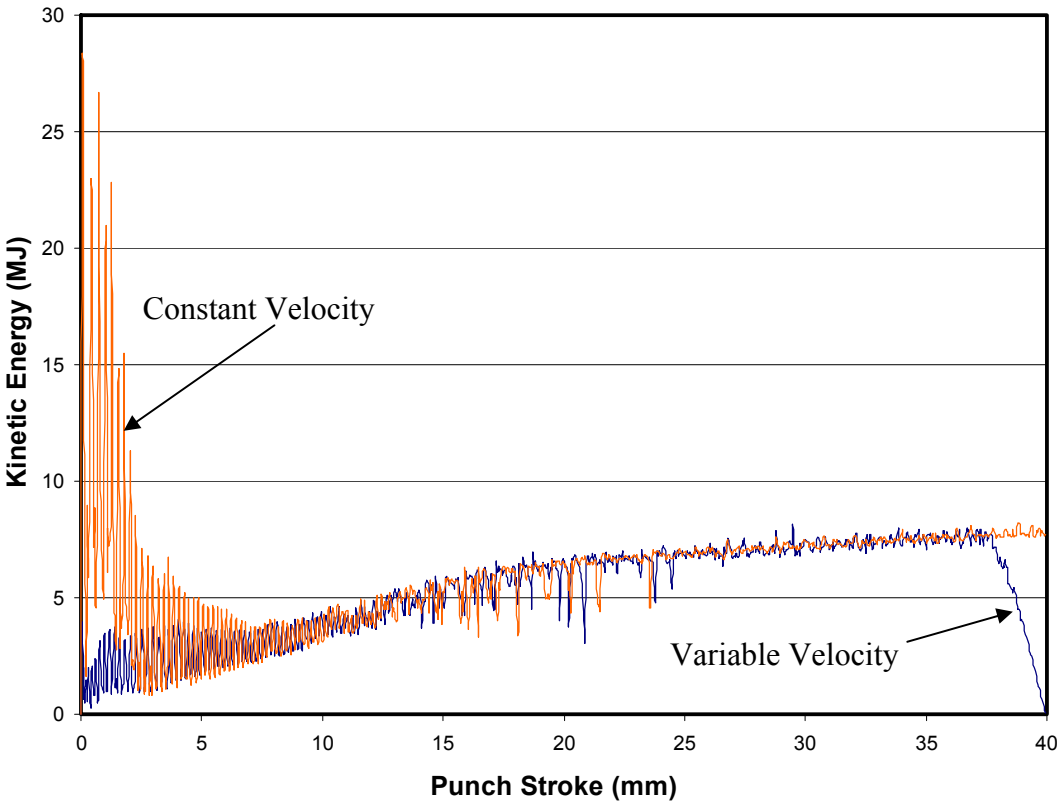


**Figure 4.16** Comparison of kinetic energy of blank vs. punch stroke curves for simulations using variable and constant punch velocities respectively

Figure 4.16 refers to results for HBHF analysis of aluminum material using maximum tool speed of 0.5 m/s. The kinetic energy of a blank sheet is theoretically calculated and it is equal to 8 MJ when the punch reaches its maximum speed of 500 m/s. As seen in the Figure 4.16 both simulation results converges to the value of 8 MJ, yet one is more oscillating.

### 4.4.2 Blank holder Force

By changing the blank holder force from 0.5 kN to the upper limit (50 kN for aluminum, 70 kN for steel) only, ten simulations were prepared for each material to observe the effect of blank holder force on the simulation results.

It revealed that severe wrinkles start to occur at blank holder forces lower than 5 kN for steel, and 2.5 kN for aluminum (Figure 4.17).

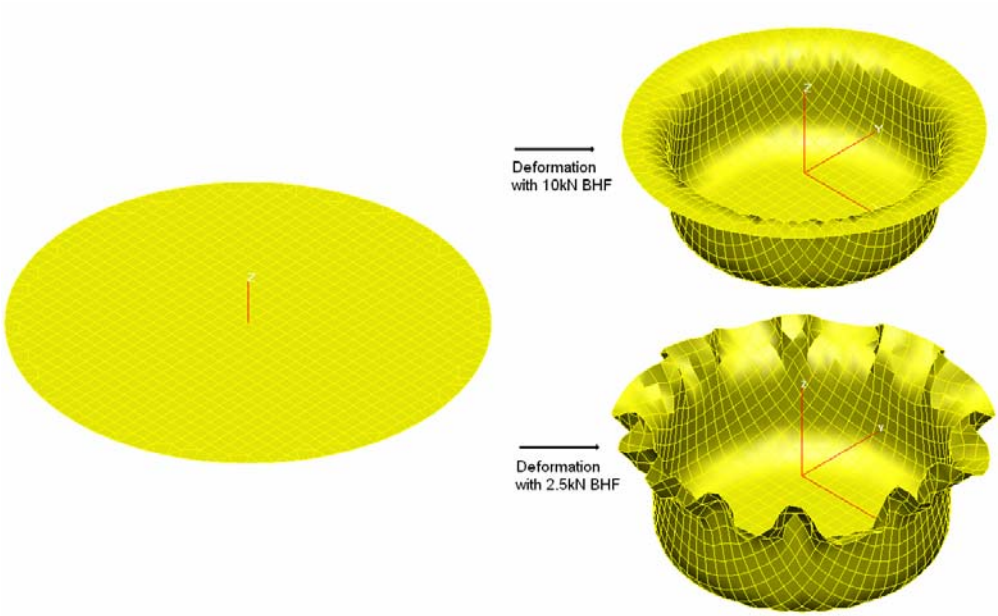


**Figure 4.17** Effect of blank holder force on wrinkling in cup drawing simulation using aluminum workpiece

Besides the visual observation of wrinkling, another method that is more objective was also used. In the cylindrical coordinate system, z-coordinate and θ-coordinate of the nodes at the rim of the flange were recorded and fluctuation on z-axis with respect to θ-axis was tabulated. However, all fluctuation observed are not solely due to the wrinkling. The source of these fluctuations can be explained with numerical errors and anisotropic material under rigid tool. Anisotropy, which can be defined as resistance to deformation in thickness direction, causes an inhomogeneous

thickness distribution on the flange. Furthermore, this inhomogeneity results in some gap between the rigid tool and the less thickened part of the flange. At this unsupported region, those local fluctuations are observed. On the other hand, the consequence of numerical error can be either the round-off error, which was the usual source of error when numerical solution procedures are used, or incompatible discretization of rigid tools and deformable body (Figure 4.18 and Figure 4.19). Normally the mesh structures of the tools are considered to be used only to represent the geometry and they are not carefully concerned. However if a poor mesh is used for a rigid body, contact problems arise and introduce unrealistic effects on the results.

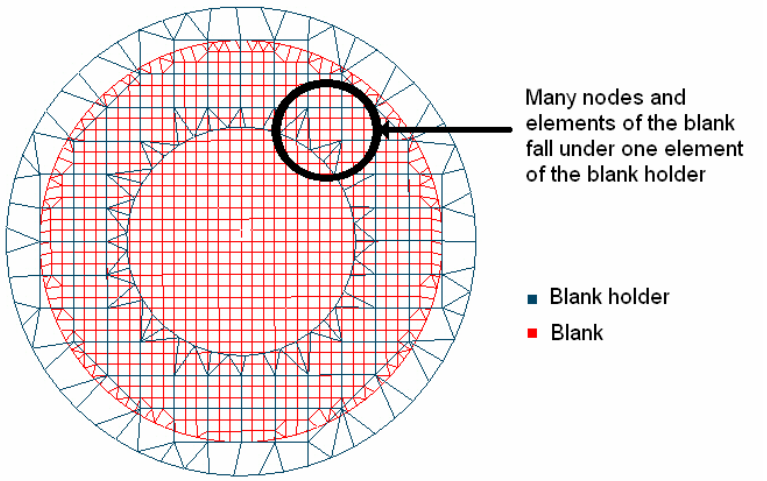


**Figure 4.18** An example to incompatible discretization of rigid tool (blank holder) and deformable body (blank)

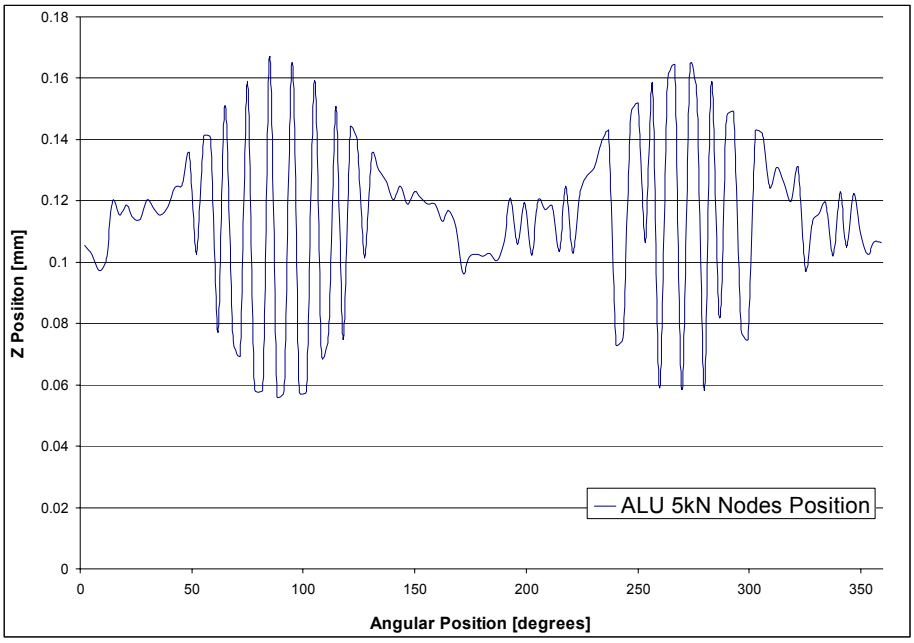


**Figure 4.19** An example to incompatible discretization of rigid tool (blank holder) and deformable body (blank)

The change in blank holder force does not bring any computational work; thus as expected, the variation of blank holder force does not affect the CPU time (Figure 4.22). On the other hand, force vs. displacement curves show that more forming force is required as the blank holder force increases (Figure 4.20 and 4.21). However, the magnitude of increase in the forming force is proportional to the friction coefficient, which will be discussed in the next section.

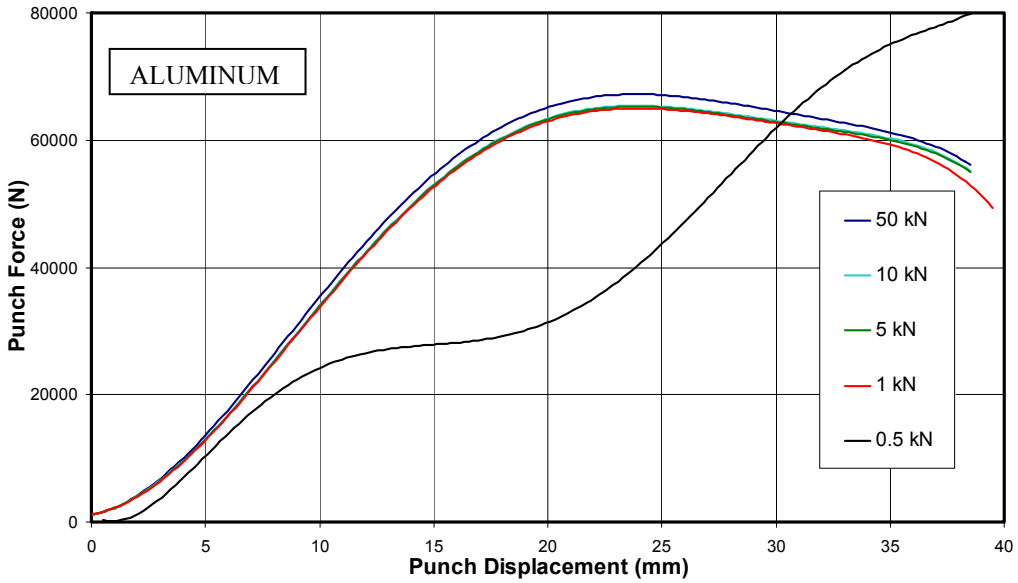


**Figure 4.20** Punch force vs. displacement trend-lines at various blank holder forces

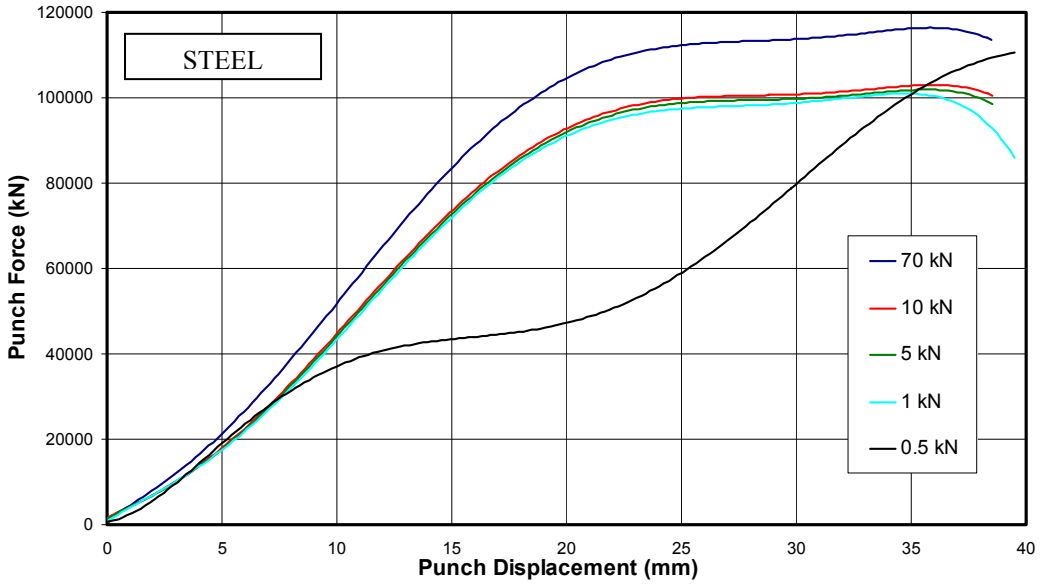


**Figure 4.21** Punch force vs. displacement trend-lines at various blank holder forces

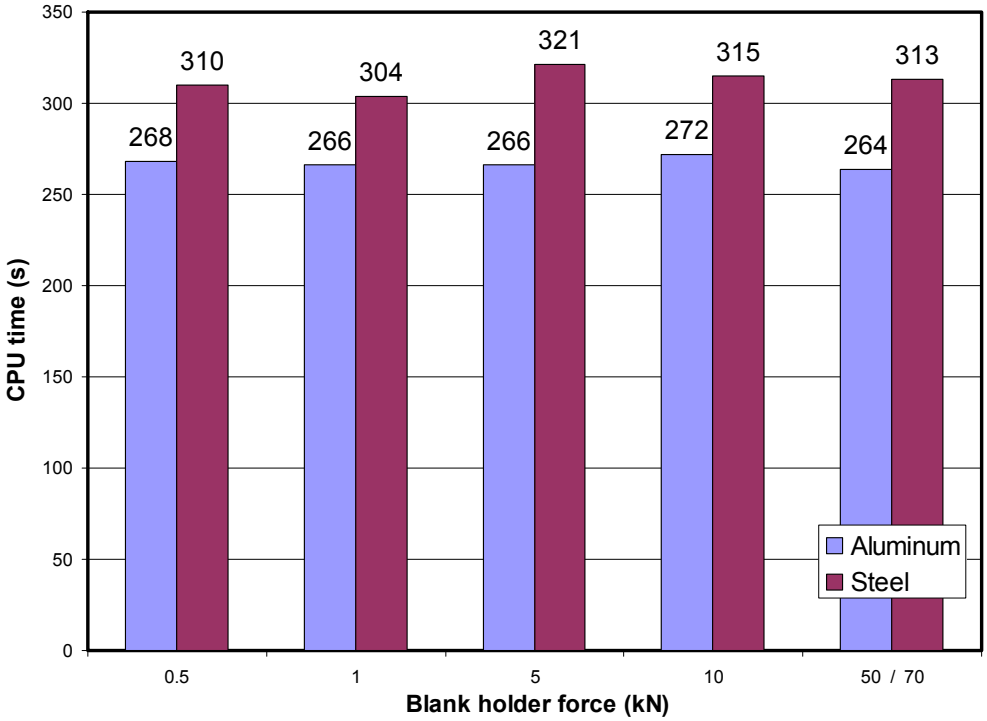


**Figure 4.22** CPU time of each simulation using various blank holder forces

### 4.4.3 Friction Coefficient

In this section, the effect of Coulomb friction upon the result of the analyses is inspected. Three simulations with three different friction coefficients and one simulation with no lubrication for each material were performed (Table 4.3). It was seen that the non-lubricated simulation ended up with the excessive stretching of the blank, thus extreme deformation of the elements. Therefore, two more simulations with finer blank mesh for the non-lubricated case were done.

Actually, punch force vs. punch stroke curves of first three simulations with low friction coefficients are very close to each other (Figure 4.23 and 4.24). On the other hand, the non–lubricated case results in a peak in the force displacement curve (at nearly 20mm of punch stroke).

**Table 4.3** Various friction coefficients and corresponding blank element sizes for process simulation of aluminum and steel workpieces

| Aluminum | | Steel | |
|---|---|---|---|
| **Friction coefficient (μ)** | **Element size** | **Friction coefficient (μ)** | **Element size** |
| 0.0087 | 5 | 0.0420 | 5 |
| 0.0096 | 5 | 0.0426 | 5 |
| 0.0105 | 5 | 0.0439 | 5 |
| 0.1348 (no lubricant) | 5 | 0.1459 (no lubricant) | 5 |
| 0.1348 (no lubricant) | 3 | 0.1459 (no lubricant) | 3 |
| 0.1348 (no lubricant) | 2 | 0.1459 (no lubricant) | 2 |

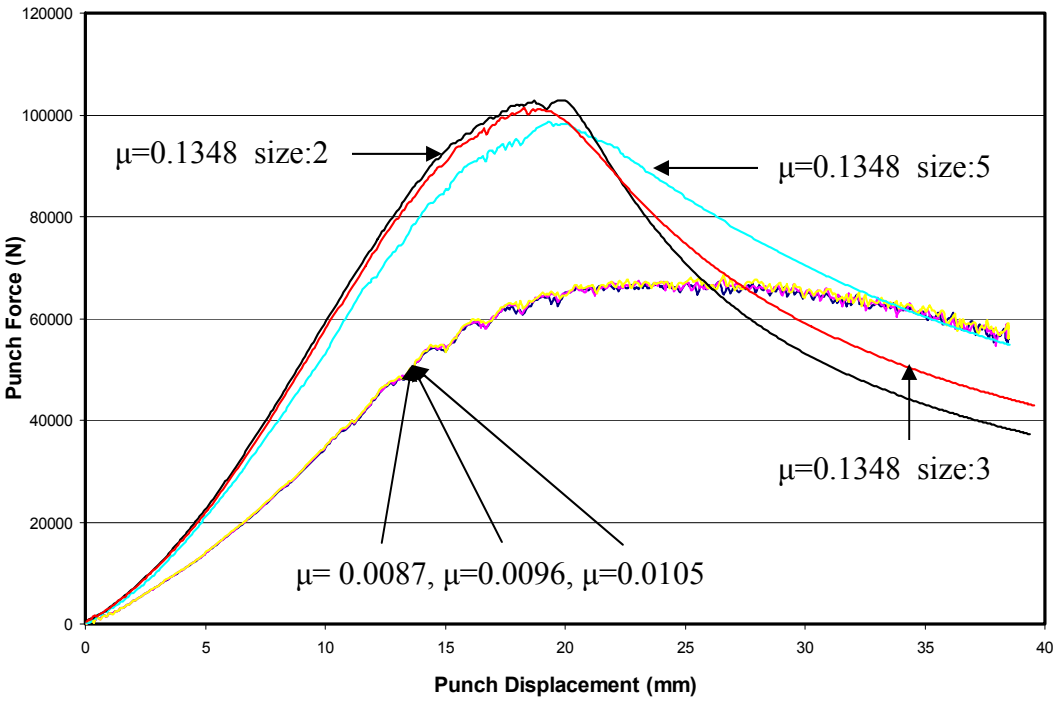


**Figure 4.23** Punch force vs. displacement curves of aluminum cup drawing simulations having various friction conditions

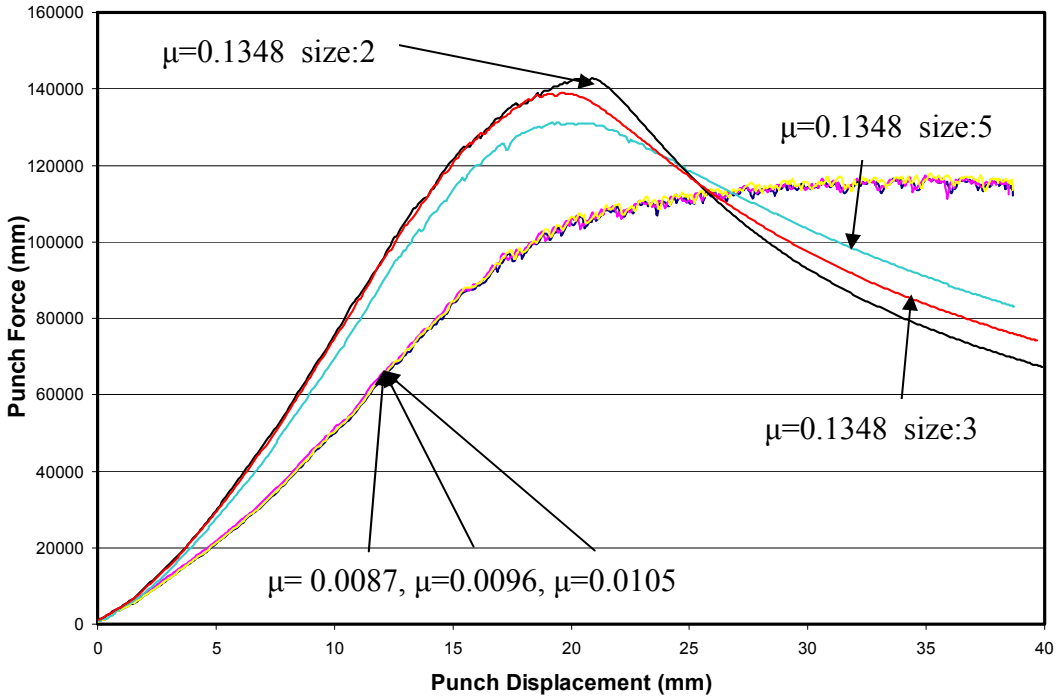


**Figure 4.24** Punch force vs. displacement curves of steel cup drawing simulations having various friction conditions

As stated above, this is due to stretching of the flange between non-lubricated blank holder and binder; however, when three simulations results are observed it is clearly seen that there are remarkable differences at the punch force vs. punch stroke curves. Stretching in the simulations having no lubrication, also cause excessive deformation of elements. These unwanted distortions in the elements decrease the accuracy and the reliability of the results. Finer mesh or remeshing (adaptive mesh) is usually a solution to distorted elements in the simulations. Remeshing will be considered later; on the contrary, the influence of finer mesh can be revealed within these simulations. The variations in results obtained from the simulations using maximum element sizes of 5 mm and 3 mm is obvious, however the ones for element sizes of 3mm and 2 mm are very similar to each other. It can be concluded that maximum element size of 3 mm is sufficient for reliable results even if there is an excessive deformation in the process due to the non-lubricated tools.

## 4.5 Numerical Parameters

Besides the process parameters, the effects of numerical parameters on the simulation results are also inspected. While keeping the other variables constant, numerical parameters, which have no physical meaning at all, have been altered systematically in a series of simulations. Element size, mesh topology, time step scaling factor, adaptive meshing, and mass scaling are the parameters in the scope.

### 4.5.1 Element Size

As explained before decreasing the deformable body element size can be preferable to obtain more precise results; however, the increase in number of elements not only results in a drastic increase in CPU time but also may cause an overstiff discretization. Hence, an intensive care should be taken for the judgment on element size. For that reason, four identical simulations with quadratic elements having four different edge lengths (7 mm, 5 mm, 3 mm, and 2 mm) were performed to determine the trade-off of the accuracy and time.

Figure 4.25 and 4.26 give the effect of different blank element sizes on the force - displacement relationship of the analyses for aluminum and steel materials:

It is clearly seen that two curves belonging to simulations with element size of 2 mm and 3 mm are almost identical or show small improvement. Use of 2 mm elements has improved the result, yet numerical simulations are feasible if and only if they are accurate enough and cost efficient. The question about the optimum element size is revealed in Figure 4.27 that the cost paid is significantly high for that amount of improvement in the results.

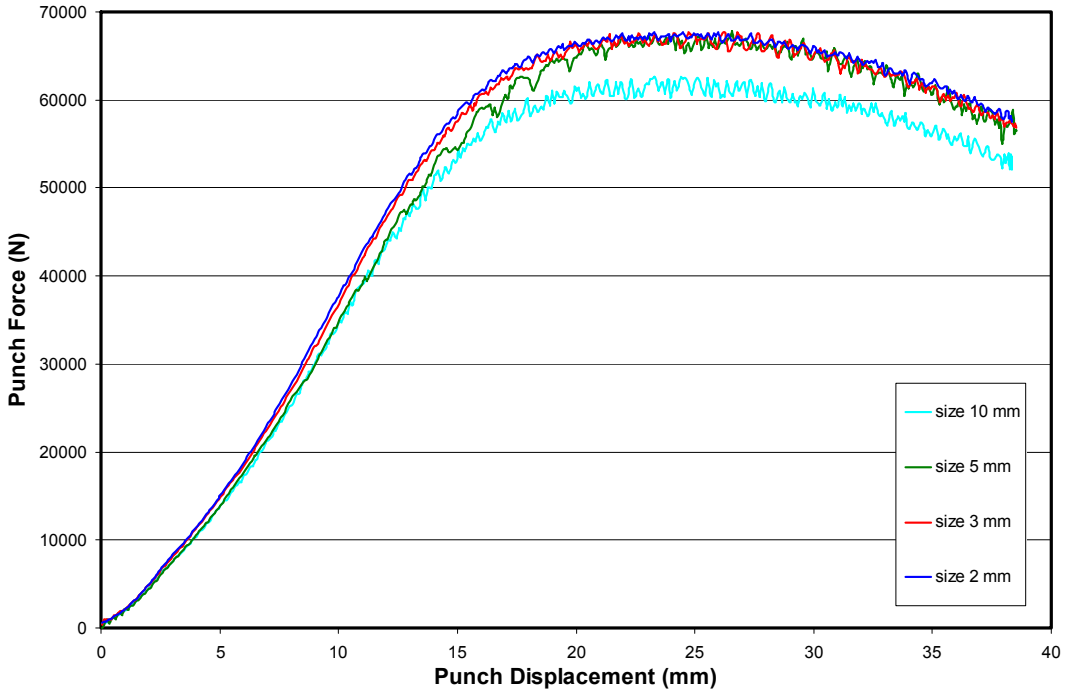


**Figure 4.25** Punch force vs. displacement curves of aluminum cup drawing simulations using element sizes 10 mm, 5 mm, 3 mm, and 2 mm respectively

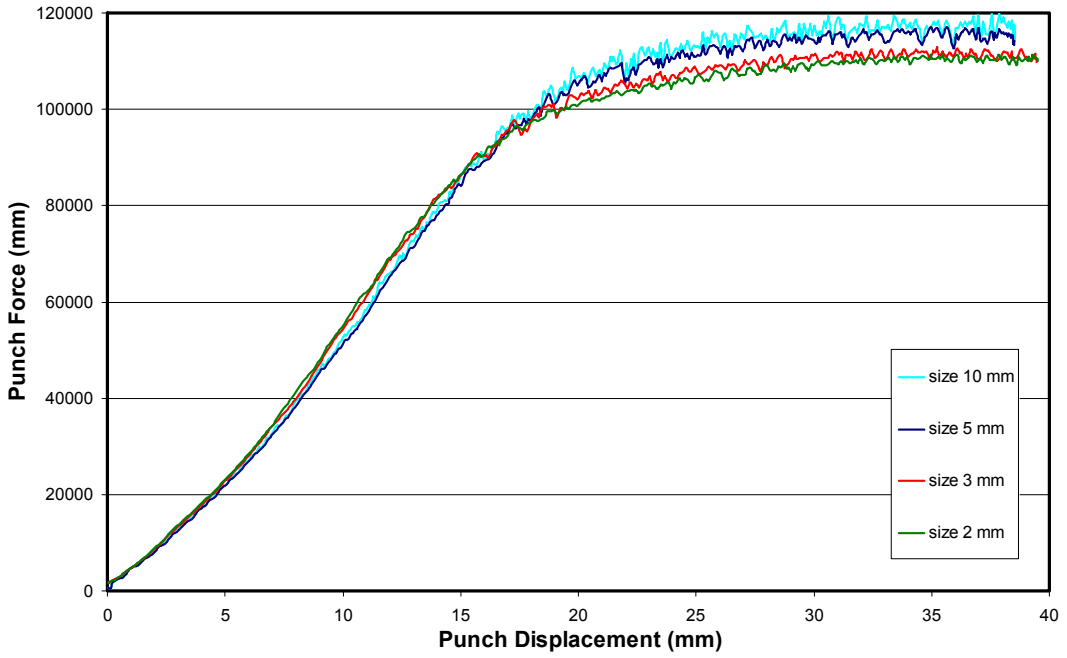


**Figure 4.26** Punch force vs. displacement curves of steel cup drawing simulations using element sizes 10 mm, 5 mm, 3 mm, and 2 mm respectively

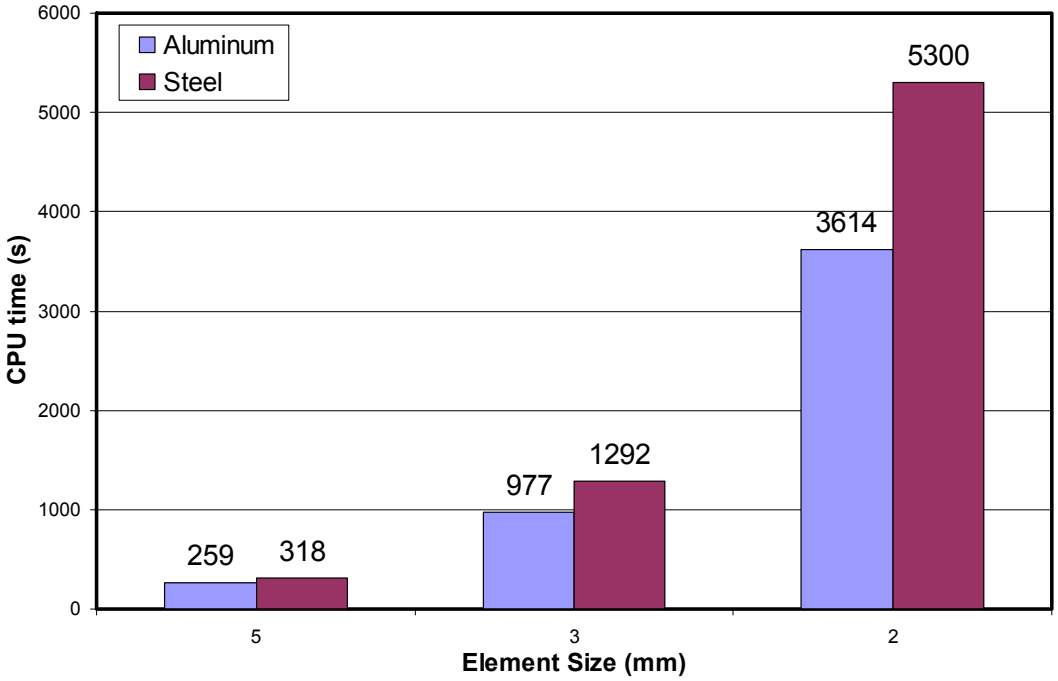


**Figure 4.27** Comparison of CPU time of each simulation using element sizes 5 mm, 3 mm, and 2 mm respectively

### 4.5.2 Mesh Topology

Beside the element size, the mesh topology is also important in finite element simulations. Mesh of each body in the simulations should be a good representation of its geometry and they should be compatible to each other. Furthermore, although the initial mesh looks uniform and smooth, it can be subjected to strong distortions and lose some computational abilities during the process. It is known that quality of the analyses depends on the quality of the elements; therefore, it is always suggested to perform some trial simulations to observe the performance of discretization.

In the following figures, the simulation results of two different mesh topologies will be compared. Figure 4.28 gives the blank mesh structures with an average element size of 2 mm:

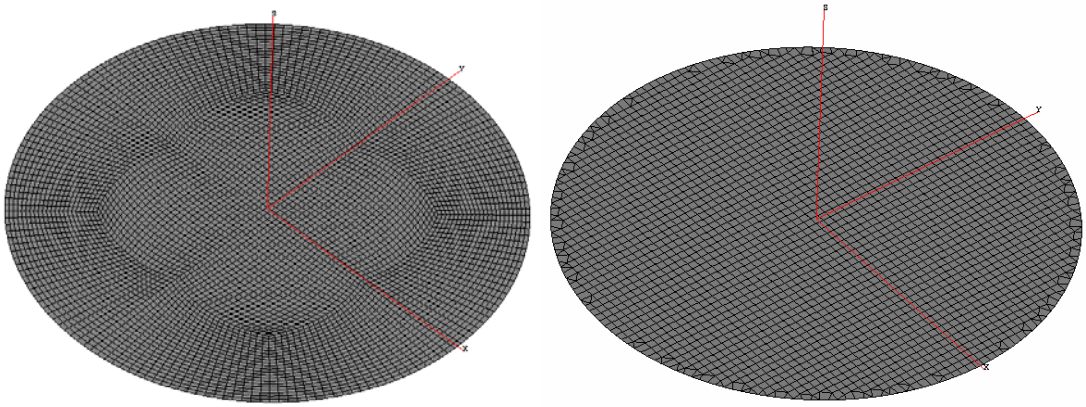

**Figure 4.28** Two different blank mesh topology (left: Structure A, right: Structure B)

If the equivalent plastic strains calculated at the mid-plane of the deformable bodies are inspected, it can be found that minimum strains are higher, maximum strains are lower for mesh structure B compared to mesh structure A in both analysis of aluminum and steel materials (Figure 4.29, 4.30, 4.31 and 4.32). Same difference can be obtained when the force - displacement curves are observed. Forming force requirements for mesh structure b are a little bit higher than for that of Structure A. According to this fact, it can be stated that although the same material properties are used in both simulations, using different mesh topologies may influence the stiffness of the deformable body. The effect of mesh topology on simulation results is obvious but it is not possible to state which topology gives results that are more reliable. Experimental verification of simulation is the best procedure to reveal the answer to this question, however a prediction which is based on the contour smoothness, can be made by looking at the equivalent plastic strain figures. Contours belonging to mesh structure A are much smoother than the mesh structure B's.

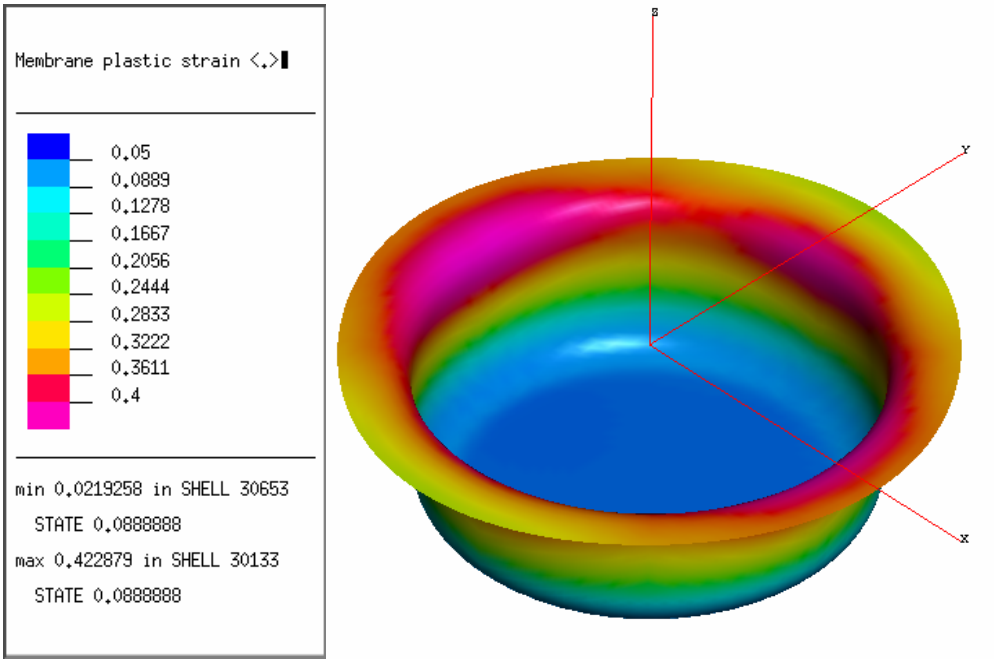


**Figure 4.29** Equivalent plastic strain contour at final step of HBHF analysis of aluminum workpiece having mesh structure A

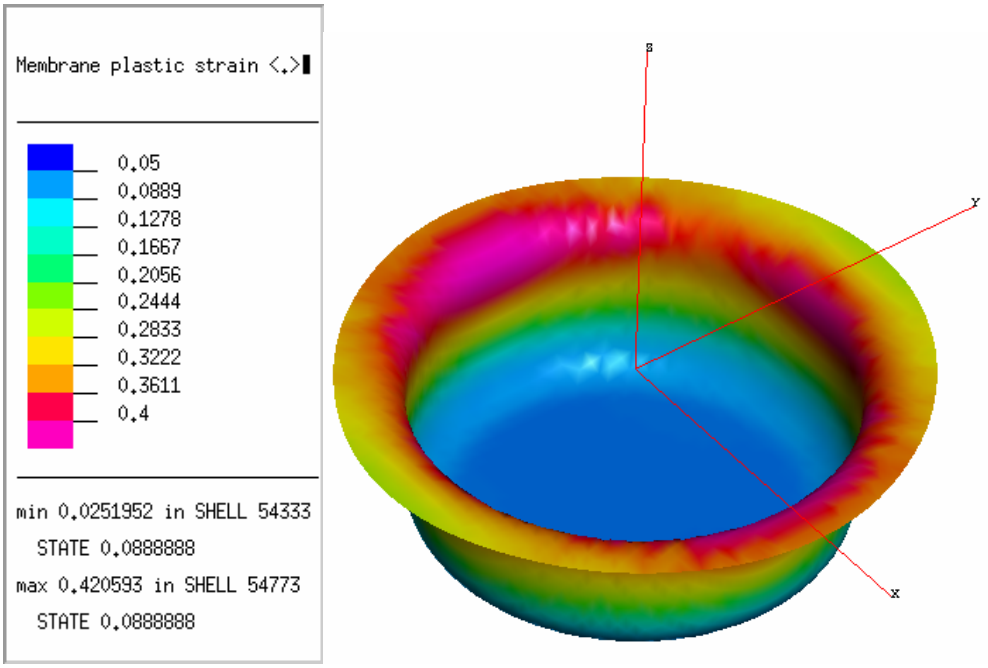


**Figure 4.30** Equivalent plastic strain contour at final step of HBHF analysis of aluminum workpiece having mesh structure B

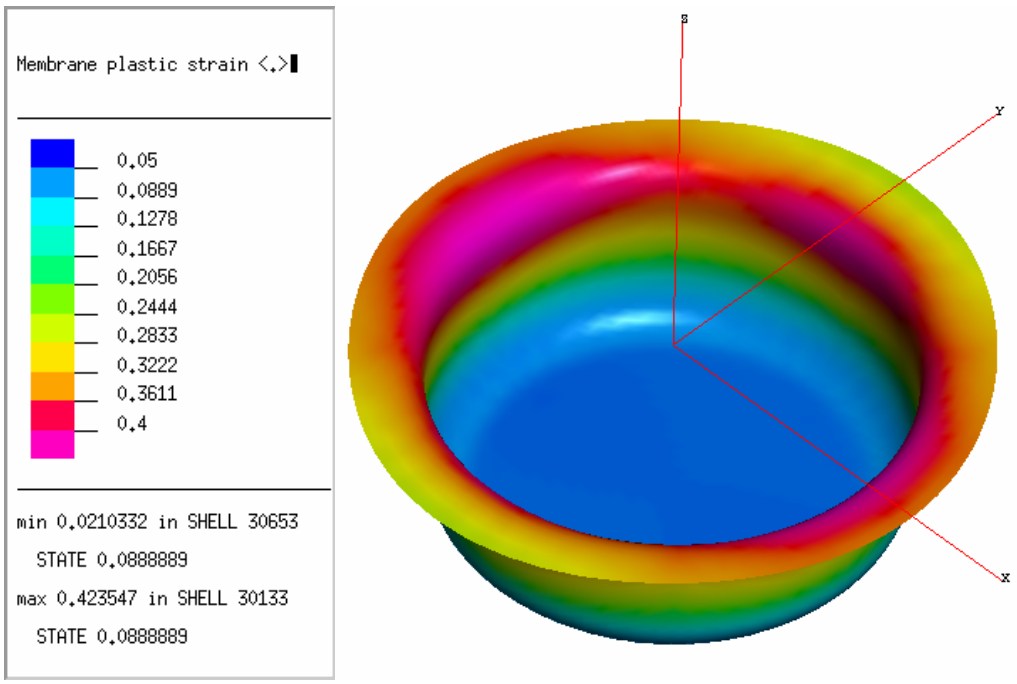


**Figure 4.31** Equivalent plastic strain contour at final step of LBHF analysis of aluminum workpiece having mesh structure A

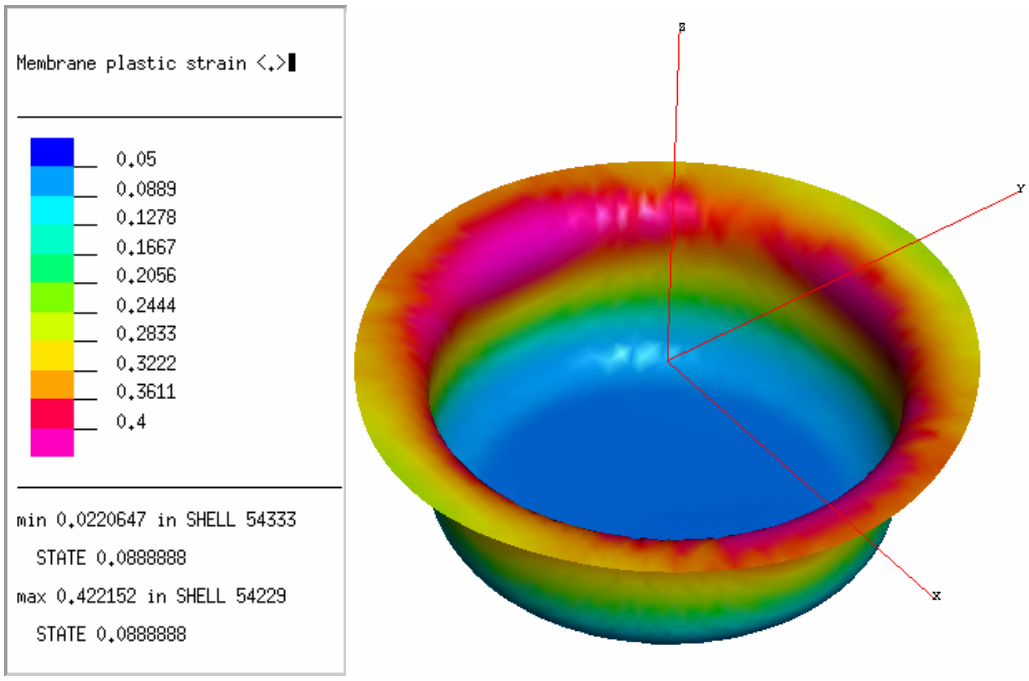


**Figure 4.32** Equivalent plastic strain contour at final step of LBHF analysis of aluminum workpiece having mesh structure B

### 4.5.3 Time Step Scaling Factor

In Dynamic - Explicit Nonlinear Finite Element Codes, the state of the simulation is not continuously calculated. Instead, total process time is divided into a large number of steps called increments and for each increment; the state of the simulation is calculated. The interval between two consecutive increments is called the time step (Figure 4.33):

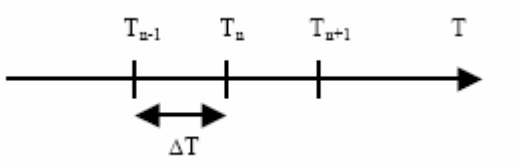


**Figure 4.33** Time step

A local time step is associated with each shell element. This element time step $\Delta T_{el}$ is assumed equal to the time taken by an elastic wave to pass through the element. Hence, it depends on the size, density, and elastic modulus of the element [14].

$$\Delta T_{el} = \frac{l}{\sqrt{\frac{E}{\rho}}} \tag{4.1}$$

where

*l* is minimum element edge length

E is elastic modulus

ρ is density

Most of the commercial FE - codes uses some stability protections in time step calculations. If elements are exposed to significantly large bendings during the simulation, Eq. (4.2) must be used for calculation of element time step especially if the mesh contains small and thick shell elements.

Besides, there are two criteria to define the characteristic length of a shell element, the *large* and *small* criteria. The former one takes the longest edge of the element as the characteristic length, the latter uses the smallest element's edge length. The large criterion is the standard criterion, whereas the small criterion is more stringent and it can assure solution stability in severe cases (availability of highly distorted mesh), however the use of the small criterion may considerably reduce the time step and so increase the CPU time [11].

$$\Delta T_{el} = \min\left( \frac{s}{\sqrt{\frac{E}{\rho}}}, \frac{s}{\sqrt{\frac{E}{\rho}}} \times \frac{s}{t} \times \sqrt{\frac{3(1-\nu)}{2}} \right) \tag{4.2}$$

where

s is the characteristic element edge length

t is the sheet thickness

$\nu$ is poisson's ratio

Furthermore, stability of the explicit method is ensured if global time step is lower than the smallest element time step. Global time step is obtained according to the following equation.

$$\Delta T_{Gl} = \zeta \times \left( \sqrt{1+\xi^2} - \xi \right) \times \min\left( \Delta T_{el} \right) \tag{4.3}$$

where

$\zeta$ is time step scaling factor

$\Delta T_{el}$ is element time step

$\xi$ is a damping ratio calculated by the solver

Default value for the time scale factor is 0.9; however, six different values are inspected to observe the influence of time scale factor on the simulation results. The results of simulations using time step scaling factors 0.5, 0.7, 0.9 and 1.0 respectively, are exactly equal to each other if forming force curves are inspected. However, CPU time increases as global time step is decreasing (Figure 4.36). On the other hand, simulations using time scale factors larger than 1 can not ensure the stability of the algorithm. They end up with invalid results (Figure 4.34 and 4.35) that show strange behaviors (Figure 4.37).

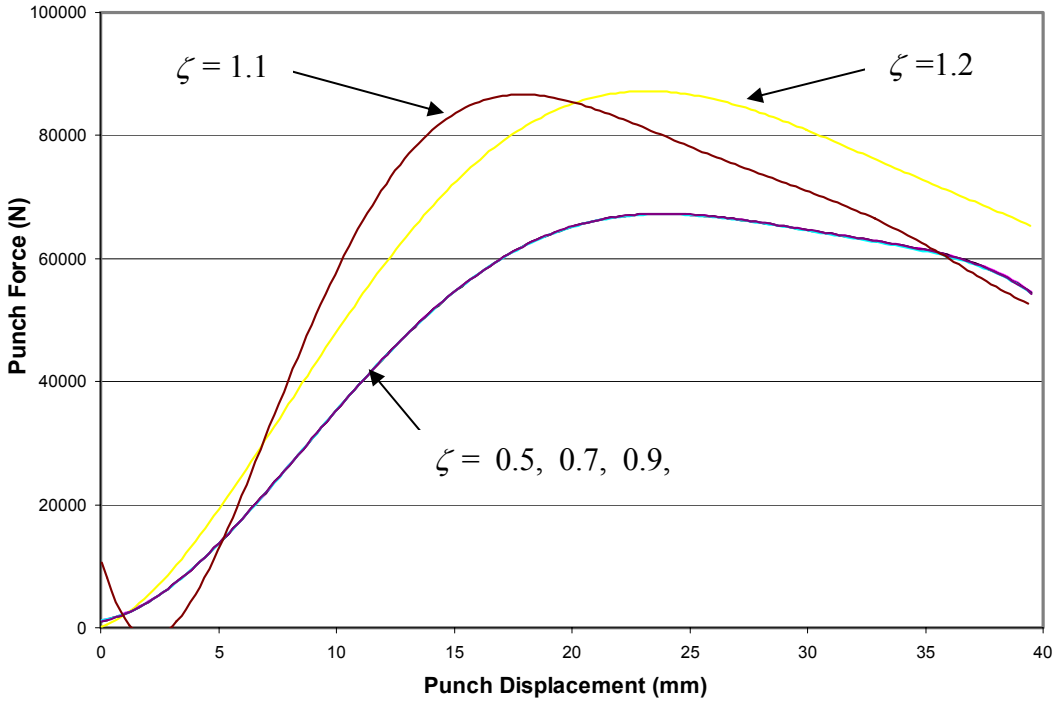


**Figure 4.34** Punch force vs. displacement curves of aluminum cup drawing simulations using time step scaling factor 0.5, 0.7, 0.9, 1.0, 1.1 and 1.2

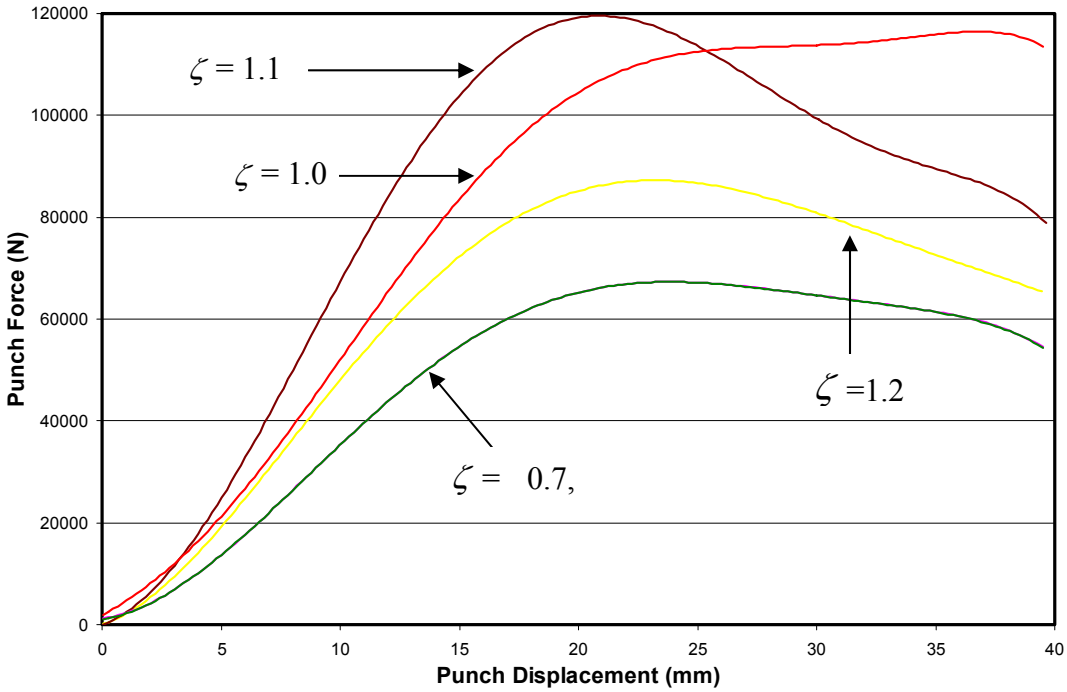


**Figure 4.35** Punch force vs. displacement curves of steel cup drawing simulations using time step scaling factor 0.5, 0.7, 0.9, 1.0, 1.1 and 1.2

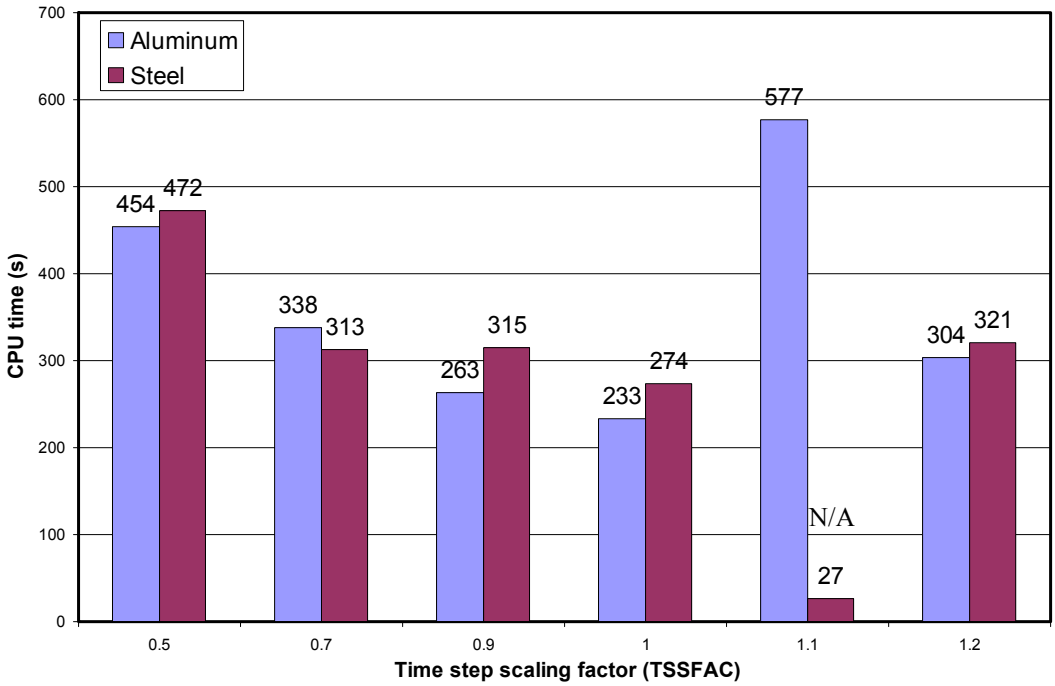


**Figure 4.36** Comparison of CPU time of each simulation using different time step scaling factors

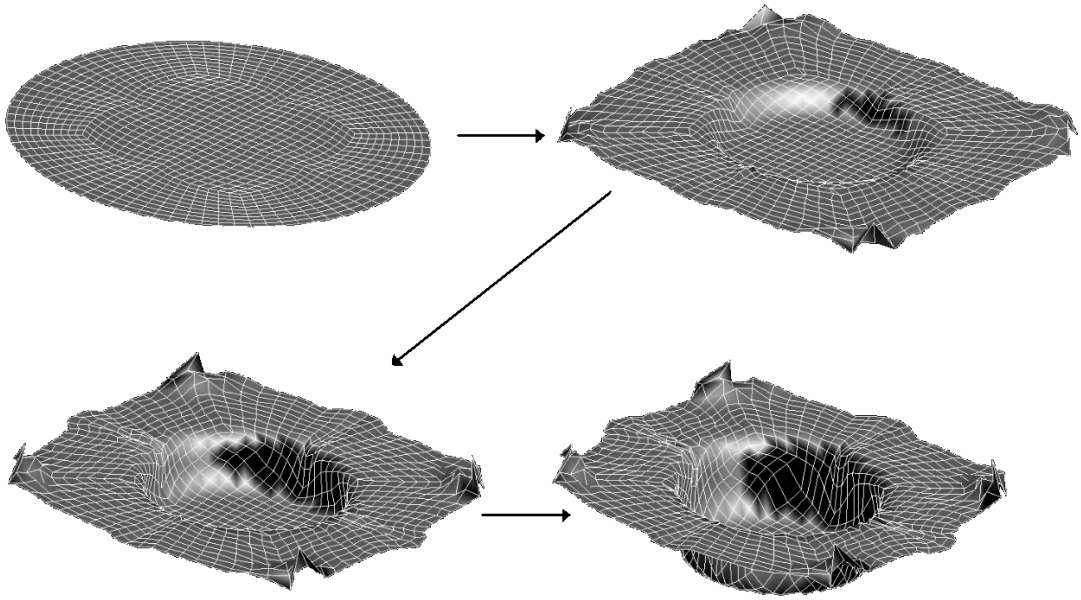

**Figure 4.37** Four different stages of a cup drawing simulation using time step scaling factor ( $\zeta$ ) equal to1.2

### 4.5.4 Adaptive Mesh

The adaptive meshing automatically refines mesh of a deformable body where and when certain conditions exist. Usually, FE codes for sheet metal forming applications use two criteria to determine whether there should be a refinement: angle criterion and geometrical criterion.

In the angle criterion (Figure 4.38), solver refines an element when the variation of the angle between its normal and that of one of its neighbor elements exceeds a certain limit angle (generally 10°). This criterion is useful for the determination of wrinkling.

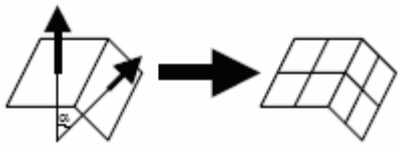


**Figure 4.38** Angle criterion

The geometrical criterion adapts the density of the mesh according to the curvature of the tool segments close to the deformable body.

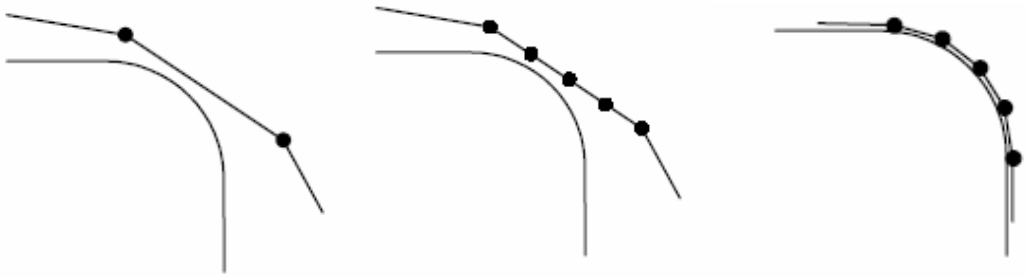

**Figure 4.39** Geometrical criterion

This criterion usually enables a more accurate calculation of the stress field. It should be activated especially when springback results are required.

The assessment of adaptive meshing is done by performing six identical simulations having different initial element sizes and refinement levels (Table 4.4). The simulations having adaptive meshing option activated, use both angle and geometrical criteria. According to these criteria, elements refine and level of refinement in the mesh are shown in Figure 4.40, 4.41 and 4.42. Refinement is done by splitting the element into four new elements that have approximately half of the initial element size.

**Table 4.4** Six successive simulations with or without adaptive meshing activated

| | Element Size (Initial) (mm) | Refinement Level | Element Size (Final) (mm) |
|---|---|---|---|
| **Simulation 1** | 5 | 2 | 2.5 |
| **Simulation 2** | 10 | 2 | 5 |
| **Simulation 3** | 5 | *no refinement* | 5 |
| **Simulation 4** | 10 | *no refinement* | 10 |
| **Simulation 5** | 10 | 3 | 2.5 |
| **Simulation 6** | 2.5 | *no refinement* | 2.5 |

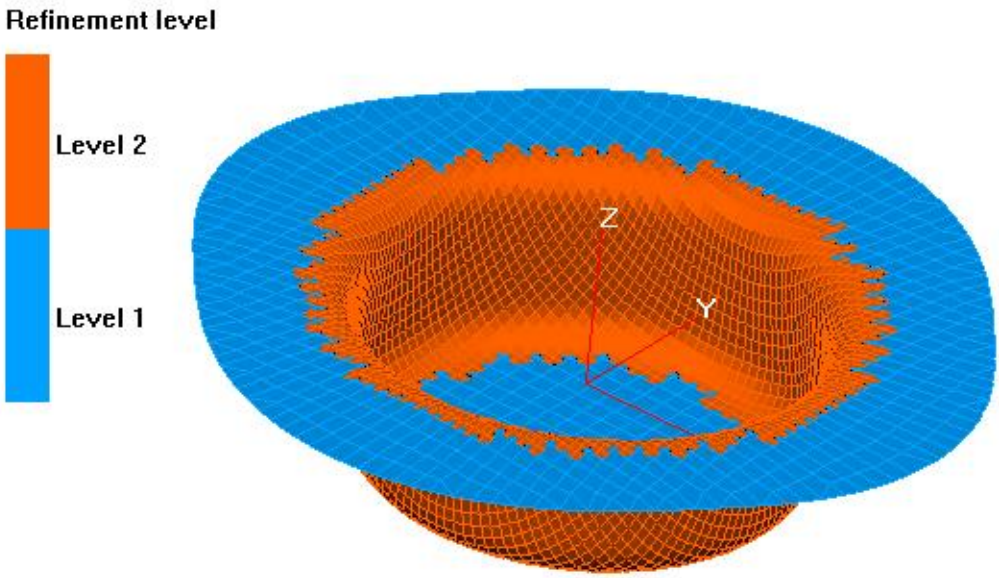


**Figure 4.40** Refinement at the final stage of Simulation 1 (max. refinement 2)

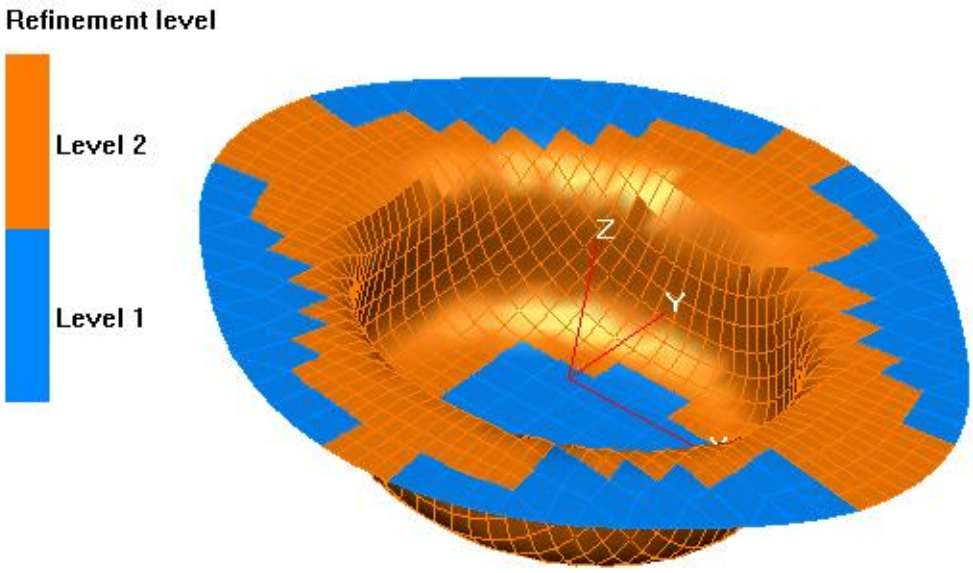


**Figure 4.41** Refinement in Simulation 2. Final element size of refined elements are approximately 5 mm

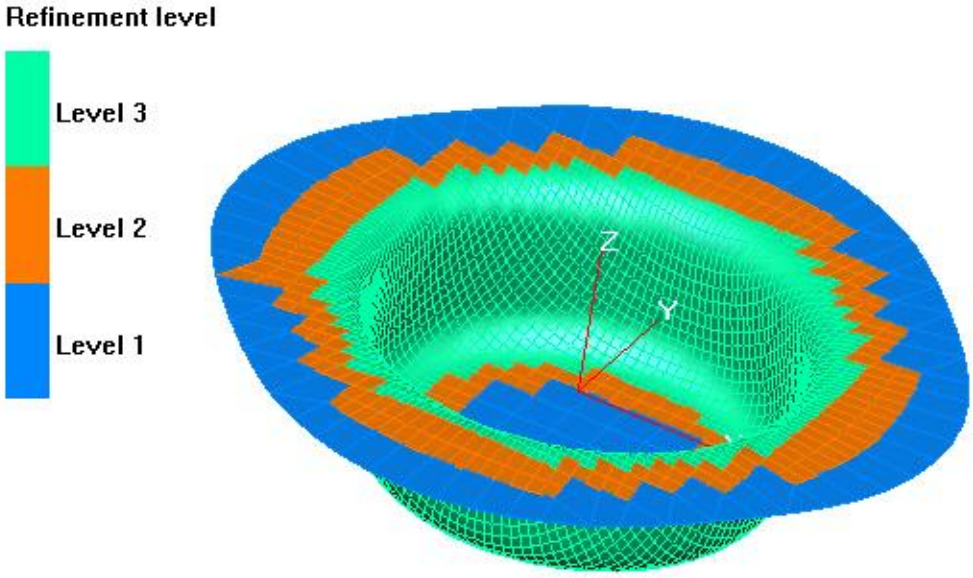


**Figure 4.42** Simulation 5 uses three refinement levels, approximate element sizes are 10 mm (level 1), 5 mm (level 2) and 2.5 mm (level 3)

As seen in the Table 4.4 and Figure 4.40, 4.41 and 4.42, adaptive meshing changes the element size and thus, reduces the time step. The effects of element size and time step on simulation results was considered in Sections 4.5.1 and 4.5.3 respectively. It was stated before that finer meshes result in solutions that are more accurate yet, CPU time drastically increases as the element size decreases. In adaptive meshing instead of doing all the simulation with fine mesh, simulation starts with coarse elements where the computations are less critical and then they are split into finer element to compensate the accuracy requirements. For that reason, adaptive meshing is an elegant way of balancing the accuracy with the cost of computation. However, the success of adaptive meshing depends on the intelligence of the refinement algorithm used by the solver.

Figures 4.43 to 4.48 show the thickness calculation of each simulation whose meshing properties are given in Table 4.5. Simulations 3, 4, and 6 have no refinement whereas simulations 1 and 2 use refinement level two and simulation 5 uses level three. At the final stage, simulations 1, 5, and 6 have approximately same minimum element size (2.5 mm).

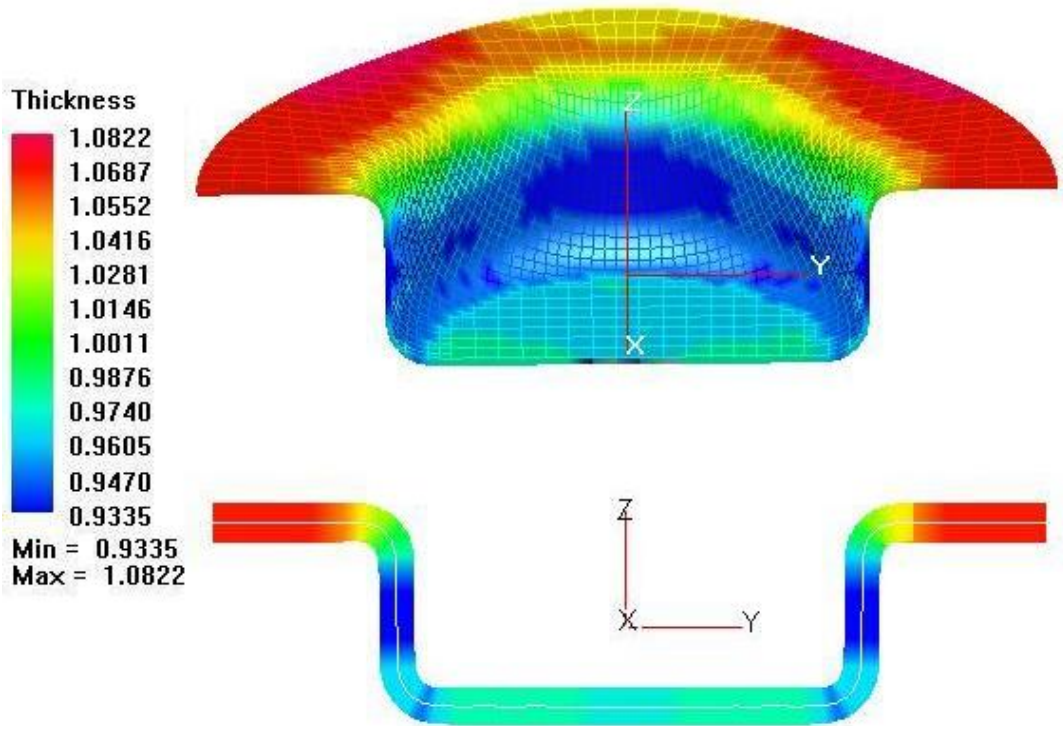


**Figure 4.43** Thickness contour of simulation 1 at 2D (X=0 plane) and 3D sections

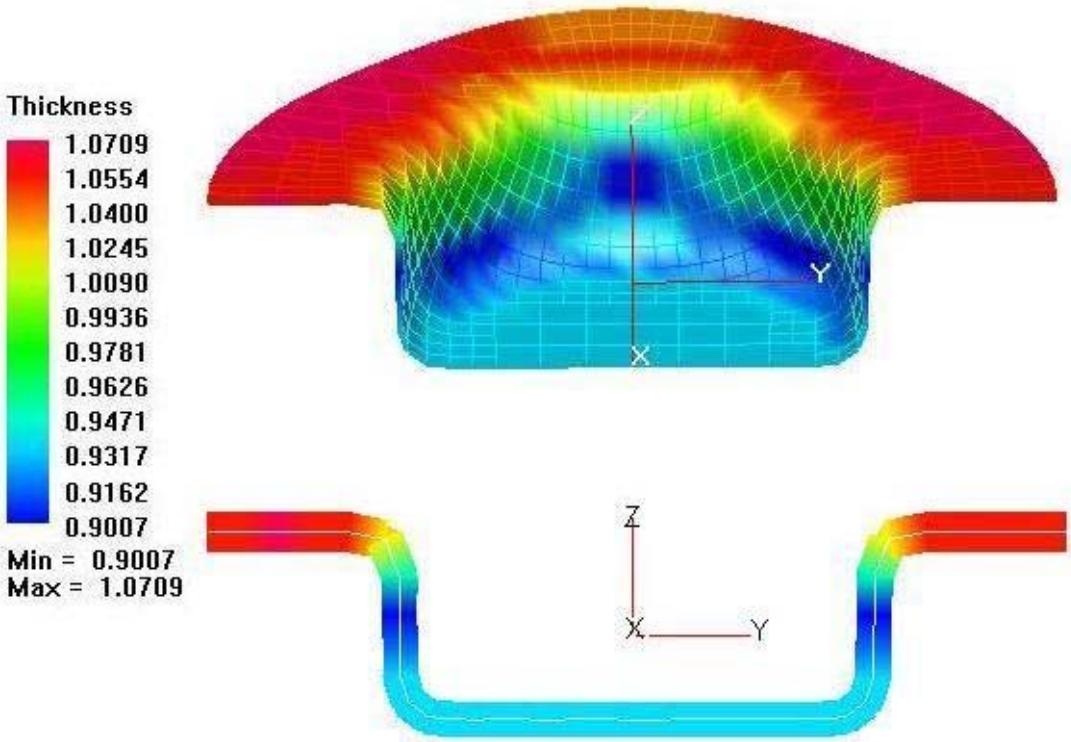


**Figure 4.44** Thickness contour of simulation 2 at 2D (X=0 plane) and 3D sections

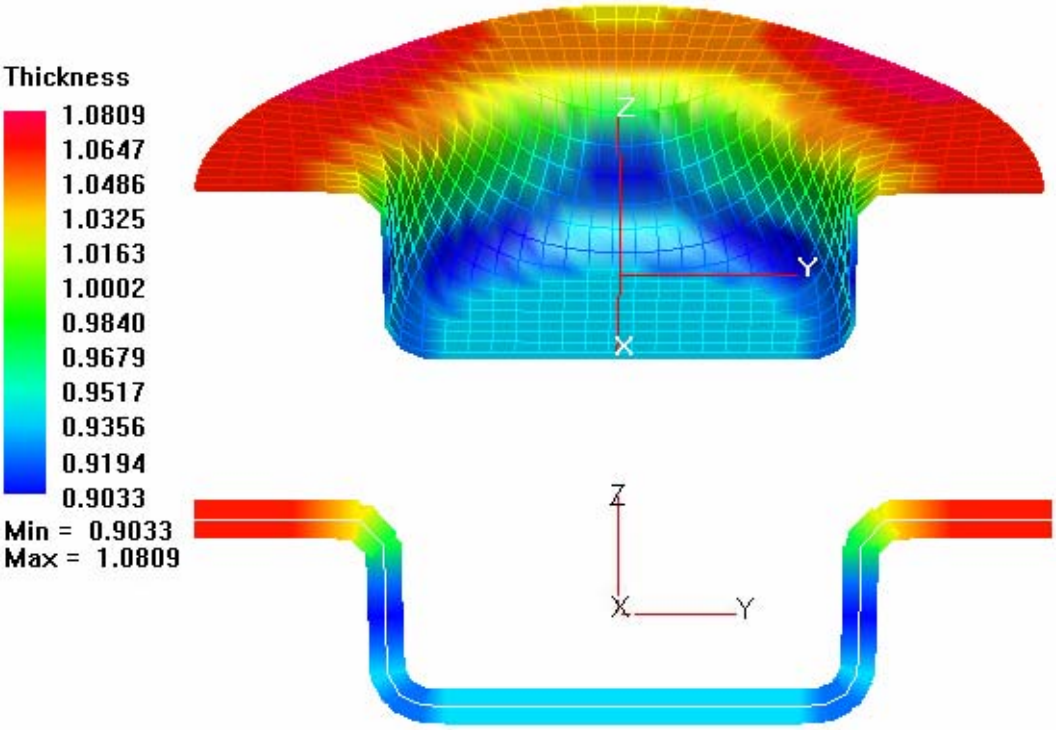


**Figure 4.45** Thickness contour of simulation 3 at 2D (X=0 plane) and 3D sections

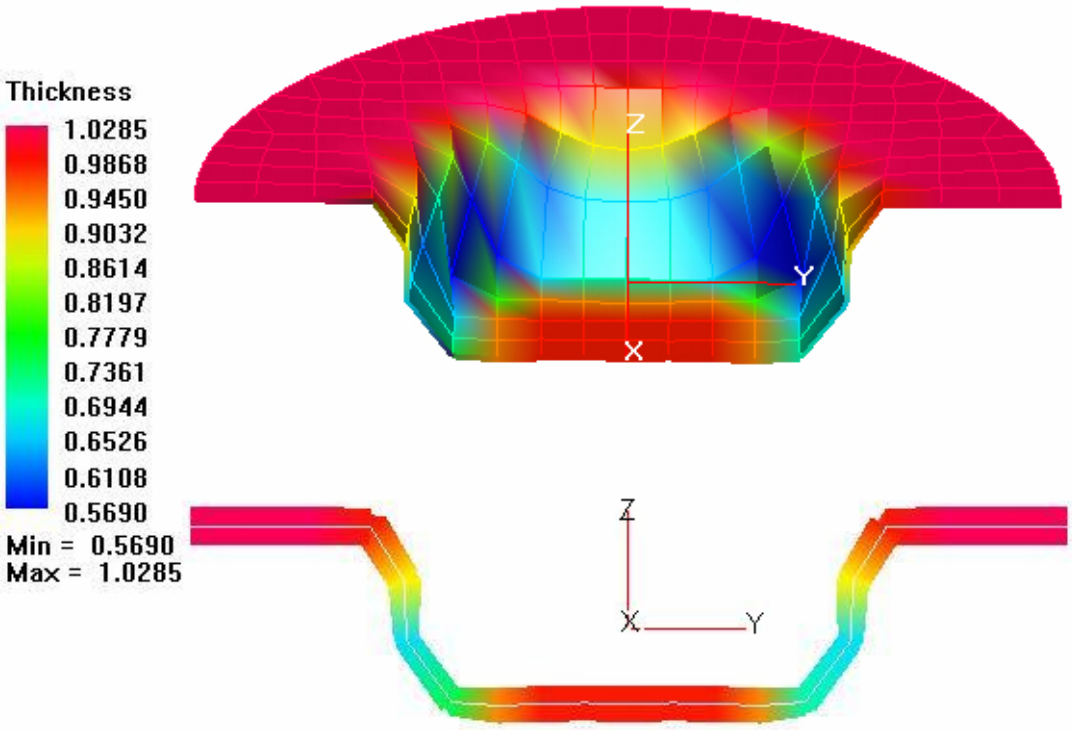


**Figure 4.46** Thickness contour of simulation 4 at 2D (X=0 plane) and 3D sections

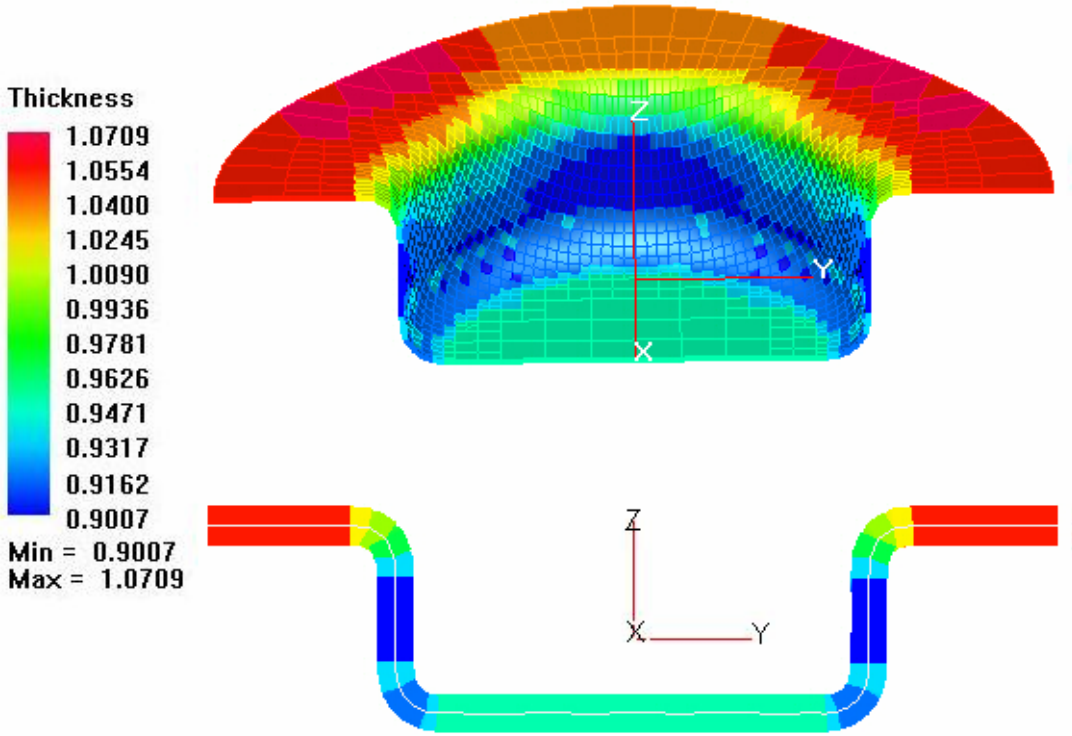


**Figure 4.47** Thickness contour of simulation 5 at 2D (X=0 plane) and 3D sections

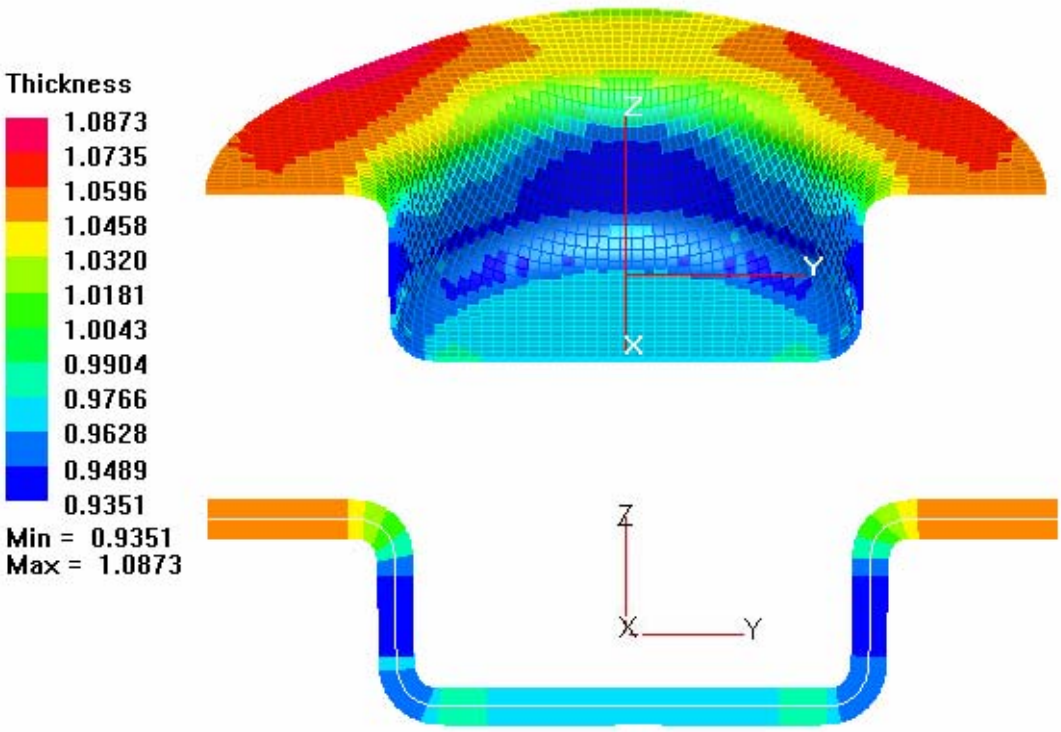


**Figure 4.48** Thickness contour of simulation 6 at 2D (X=0 plane) and 3D sections

When the thickness contours are observed, it is seen that although six simulations have different initial element sizes and refinement levels, they can be classified into three groups. Independent from the initial element sizes and level of refinement, simulation whose final element sizes are compatible to each other belong to the same group.

Simulation 4 belongs to the first group with final element size of 10mm. Its initial element size is also 10 mm and no refinement is used through the simulation. It is clearly seen in Figure 4.46 that 10 mm as an initial element size is unacceptable for this analysis and the results obtained are invalid. For that reason, other results of simulation 4 will not be considered further and they are excluded from assessment.

Simulation 2 and 3 are the members of second group having final element size of 5 mm. Although simulation 2 has initial element size of 10 mm like the simulation 4 does, the results are acceptable since the adaptive meshing is activated. During the

simulation, mesh is subdivided into smaller elements where necessary and by this way, high improvement is achieved in the calculations. Compared with the simulation 2 whose initial and final element sizes are approximately 5 mm, the result of simulation 3 are satisfying. Thickness contour curves (Figure 4.49) and punch force – displacement curves (Figure 4.50) of both simulations are compatible to each other. The only difference between two simulations is the CPU time spent. Simulation 2 predicts the same result much faster than the simulation 3 since adaptive meshing was utilized.

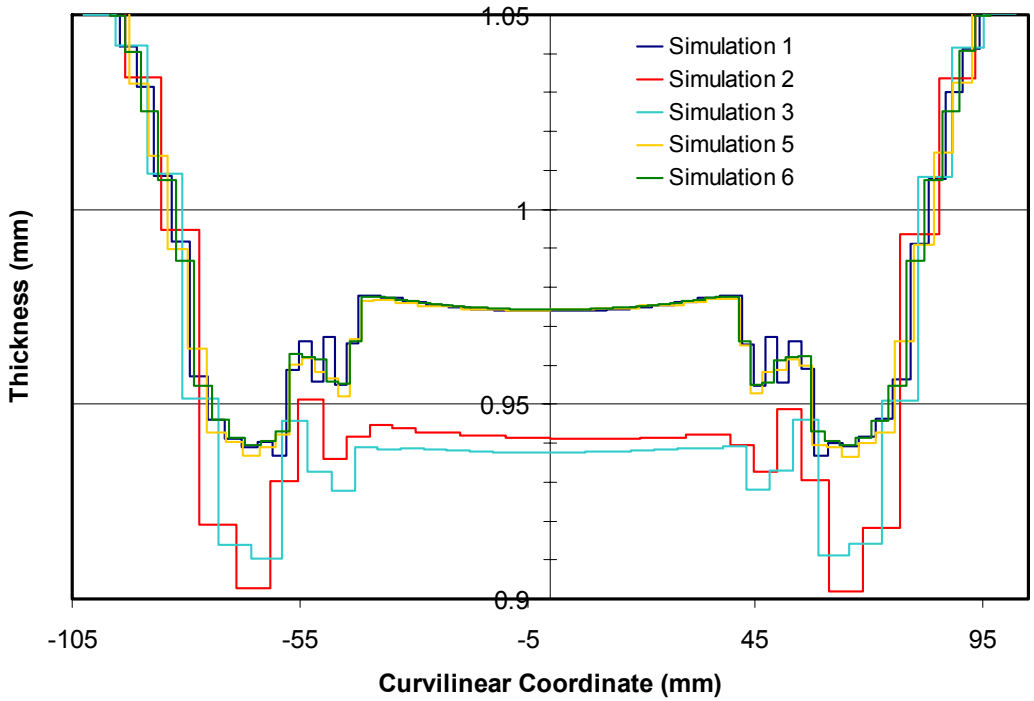


**Figure 4.49** Thickness distribution of each simulation along the curvilinear coordinate on X=0 plane

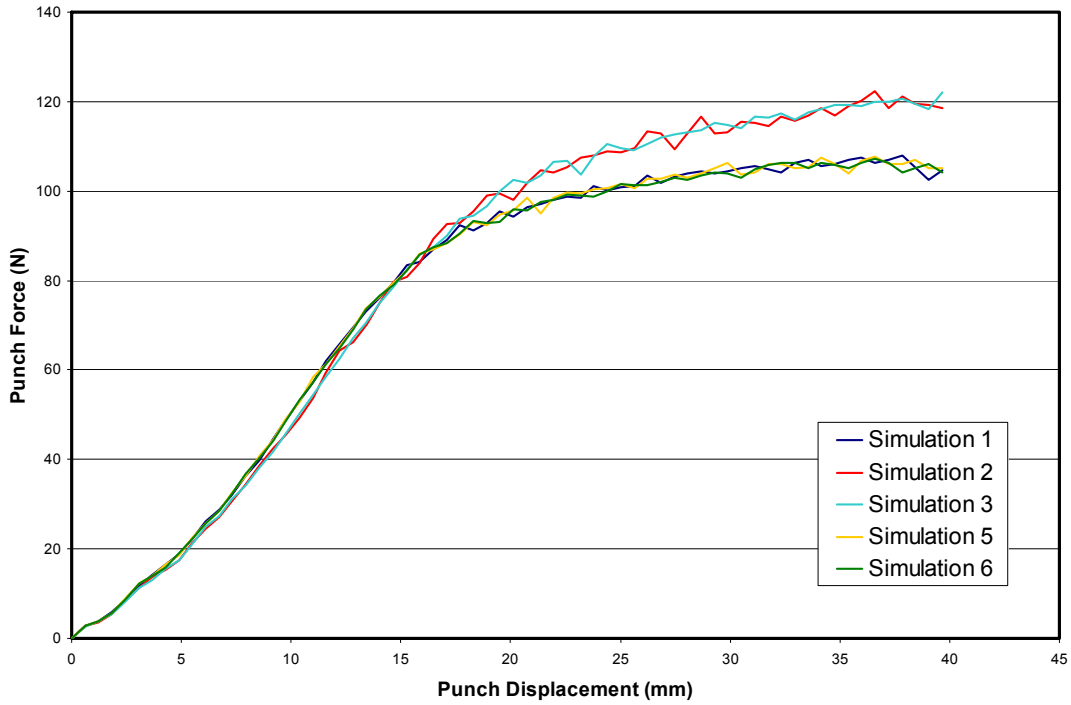


**Figure 4.50** Punch force – displacement curve of simulations

Although simulations 5, 1 and 6 have different initial element sizes of 10 mm, 5 mm and 2.5 mm respectively, having the same final element size (2.5 mm) makes them belong to the same group. As the thickness contour curves and punch force – displacement curves are inspected, another similarity is observed that the results are almost the same even though the mesh sizes and mesh density is completely different in all three simulations. Simulation 6 consists of uniform mesh whose elements size is 2.5 mm. No refinement is used and only 9% percent of change occurred in the time step as well as in the element size, according to the Eq. (4.1) through the simulation (Table 4.6). There are 20649 elements at the end of the simulation and CPU time is very high compared to the other simulations (Figure 4.48). On the other hand, in simulation 1, two dominant element sizes exist in the mesh at the end of the analysis. Refinement level 2 is used in the simulation, which means that a part of the initial mesh consisting of 5 mm elements are split into four child elements whose sizes are approximately 2.5 mm (Figure 4.43). Total element size at the end of the simulation is less than that of simulation 6 and the decrease in the time step during the simulation is about 55 % through the simulation because of

the refinement of some elements (Table 4.6). Simulation 5, which is the last analysis of group 3, consists of elements with 10 mm length at the beginning of the simulation. It is shown before in Figure 4.46 that results obtained with element size of 10 mm are obviously unacceptable and invalid, however it is observed in the Figures 4.47 that the result of simulation 5 is nearly identical with the results of simulation 6 (Figure 4.48), which uses 2.5 mm long elements in the whole simulation. This improvement is the consequence of using 3 level refinement in the simulation. 10 mm long elements are first divided into four elements with 5 mm length and then again subdivided into 2.5 mm long elements where and when certain conditions exist to satisfy the accuracy requirement and exhibit geometry details properly in the analysis (Figure 4.42). There is 81% percent of time step decrease during the simulation. This huge amount of reduction can be explained with high level of refinement (level 3). The simulation starts with relatively large time steps and then as the analysis proceeds and size of the elements decrease so that time step is reduced to avoid instability. However, when the overall performance is concerned, it is seen that the most time efficient analysis is done by simulation 5 within the third group (Figure 4.52).

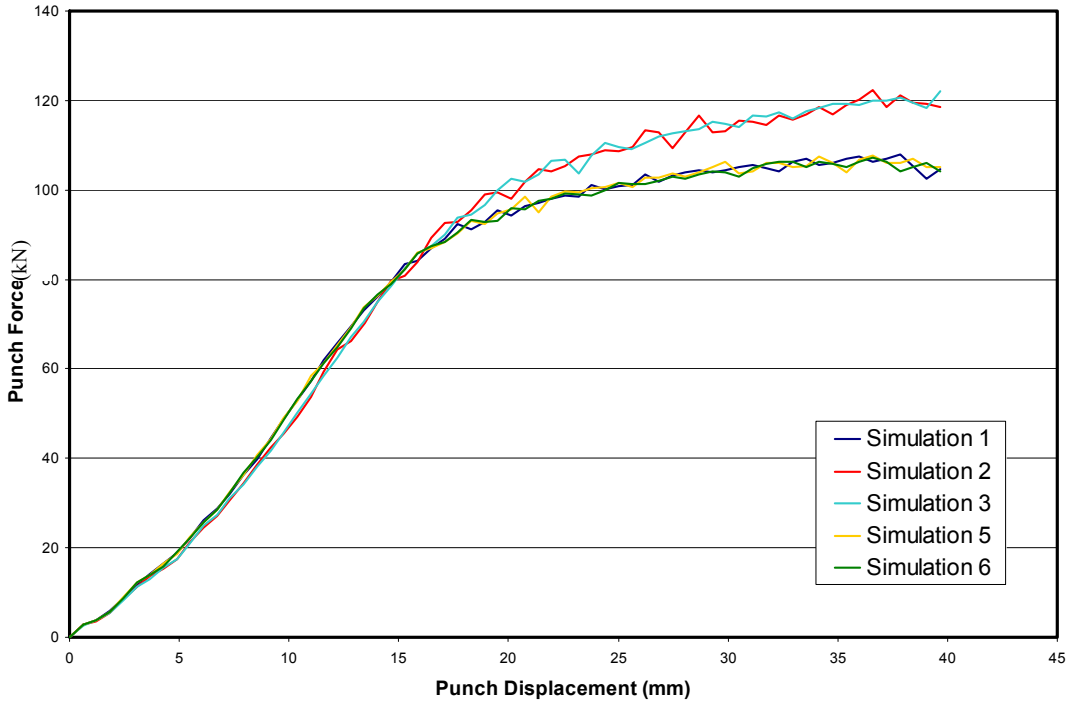


**Figure 4.51** Punch force – displacement curve of simulations

**Table 4.6** Computational times and time step changes of simulations

| | Initial Time Step (s) | Final Time Step (s) | Decrease in Time Step (%) | CPU Time (s) |
|---|---|---|---|---|
| Simulation 1 | 5.15E-04 | 2.33E-04 | 55% | 2384 |
| Simulation 2 | 1.24E-03 | 4.78E-04 | 61% | 633 |
| Simulation 3 | 5.15E-04 | 4.68E-04 | 9% | 837 |
| Simulation 5 | 1.24E-03 | 2.34E-04 | 81% | 1993 |
| Simulation 6 | 2.47E-04 | 2.25E-04 | 9% | 3761 |

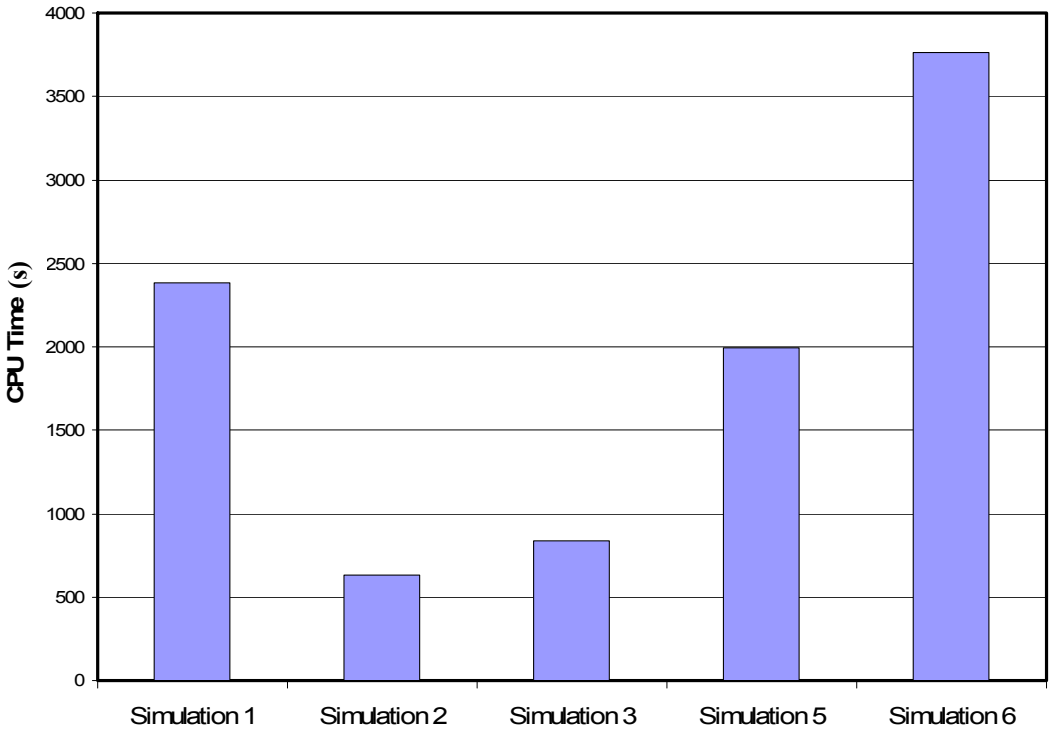


**Figure 4.52** Comparison of CPU times of simulations

All these simulations reveal that adaptive meshing is a powerful tool to establish a transition between initial and final elements having different lengths during the simulation, but it should be activated cautiously since unnecessary usage can significantly increase the CPU time.

### 4.5.5 Mass Scaling

The purpose of mass scaling is to reduce CPU time by increasing the time step. The increase of the time step leads to a reduction of the number of increments, hence to a reduction in the CPU time, since the latter is proportional to the number of increments. To do this, the mass of some elements is artificially increased, thus according to Eq. (4.2), element time step also increases to achieve the stability. However, increase in the mass of the elements increases the inertia of deformable body, and this can lead to erroneous results, therefore the mass scaling should be used cautiously.

Inspection of the effect of mass scaling on the accuracy of analysis results is done by using a series of mass scaling factors respectively in the simulations.

**Table 4.7** A series of simulations having various element sizes, refinement levels and mass scaling factors

| | **Element Size (mm)** | **Refinement Level** | **Mass Scaling** | |
|---|---|---|---|---|
| | | | **Reference Size (mm)** | **Corresponding Time Step (s)** |
| **Simulation 1** | 5 | 2 | *no mass scaling* | |
| **Simulation 2** | 5 | 2 | 1.70 | 2.84E-04 |
| **Simulation 3** | 5 | 2 | 5 | 8.34E-04 |
| **Simulation 4** | 10 | 2 | *no mass scaling* | |
| **Simulation 5** | 10 | 2 | 10 | 1.67E-03 |
| **Simulation 6** | 10 | 3 | *no mass scaling* | |
| **Simulation 7** | 10 | 3 | 2.06 | 3.43E-04 |
| **Simulation 8** | 10 | 3 | 5 | 8.34E-04 |
| **Simulation 9** | 10 | 3 | 10 | 1.67E-03 |

Within the assessment, there are three simulations having the mass scaling option disabled. In the other six simulations, various mass scaling factors are used on elements having different lengths (Table 4.7). Nine simulations can be divided into

three groups according to the meshing properties. First three simulations have the same element size and refinement level. Three different mass scaling parameters are applied to the simulation respectively within the group. All remaining simulations have 10 mm long elements at the initial step. Simulations 4 and 5 use refinement level 2 and they from the group two, whereas simulations 6, 7, 8, and 9 have level 3 refinement and they belong to group three.

The assessment of the simulations will be done within the subgroups according to the results showing the thickness distribution, forming force – displacement relation, and equivalent plastic stress variation.

Figures 4.53 to 4.61 show the 3D thickness distribution and 2D thickness section cut of each simulation taken on *X=0* plane.

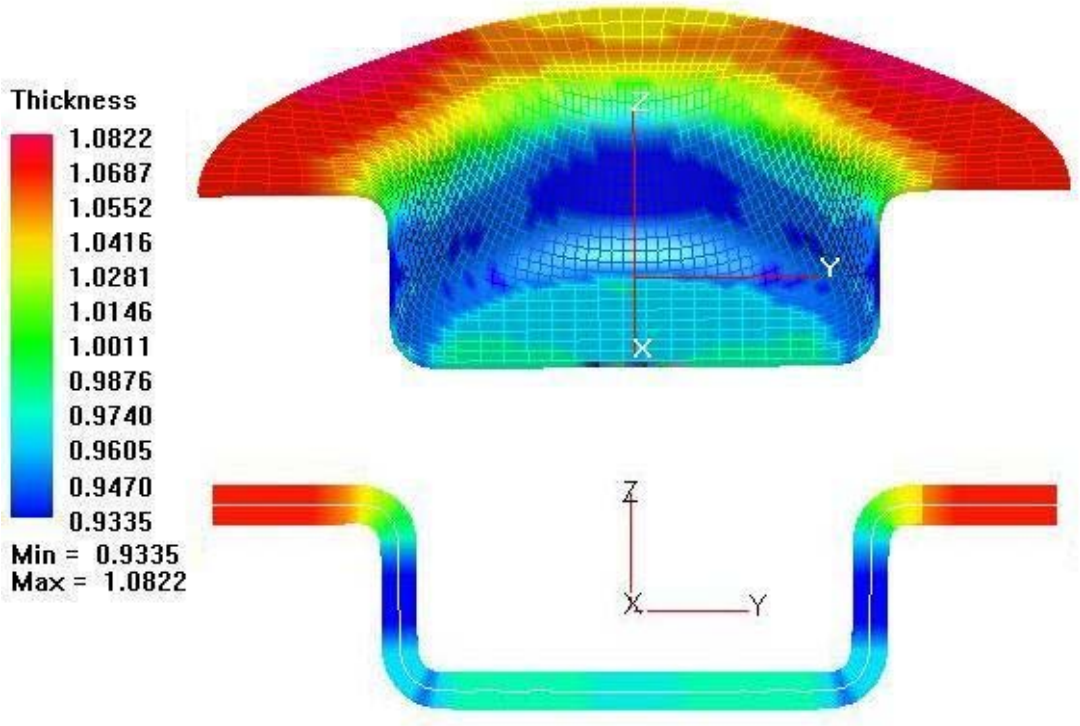


**Figure 4.53** Thickness contour of simulation 1 at 2D (X=0 plane) and 3D sections

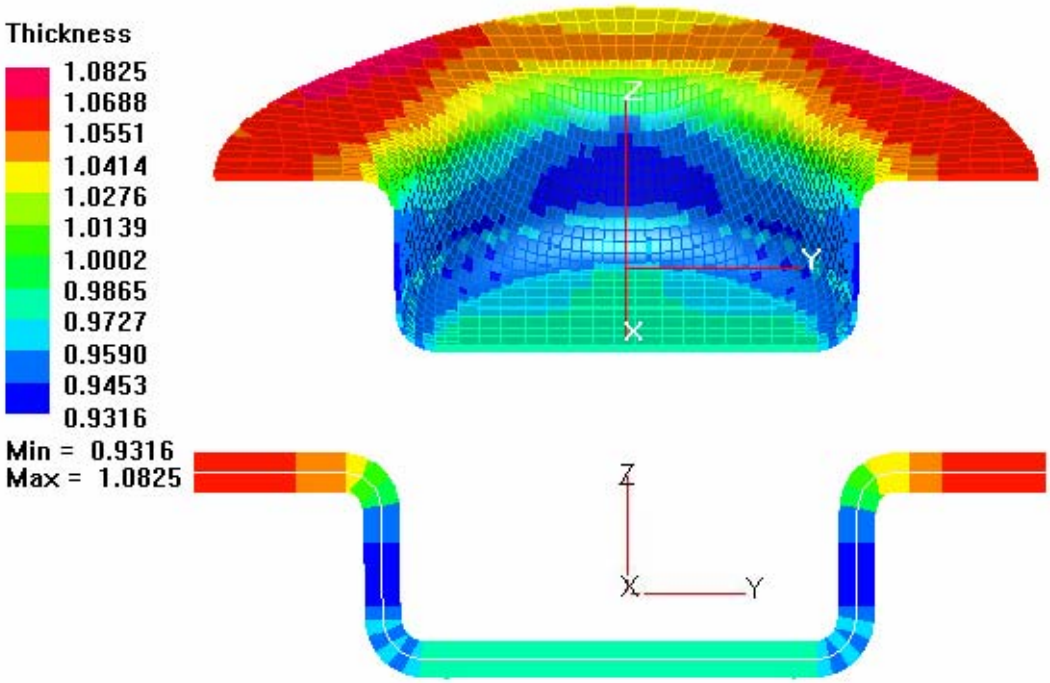


**Figure 4.54** Thickness contour of simulation 2 at 2D (X=0 plane) and 3D sections

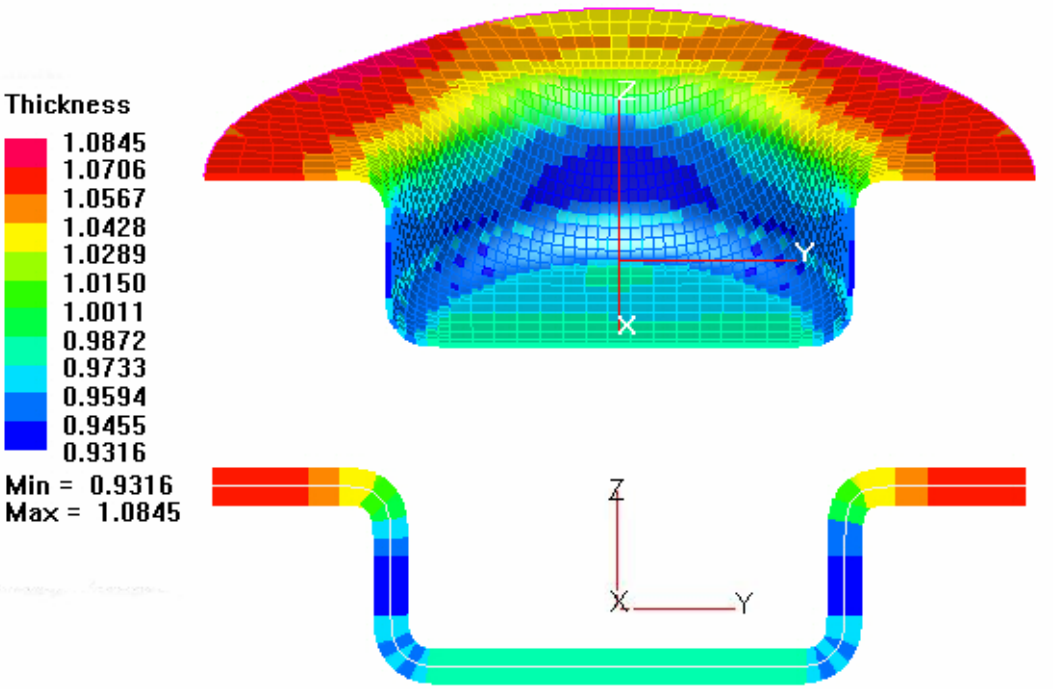


**Figure 4.55** Thickness contour of simulation 3 at 2D (X=0 plane) and 3D sections

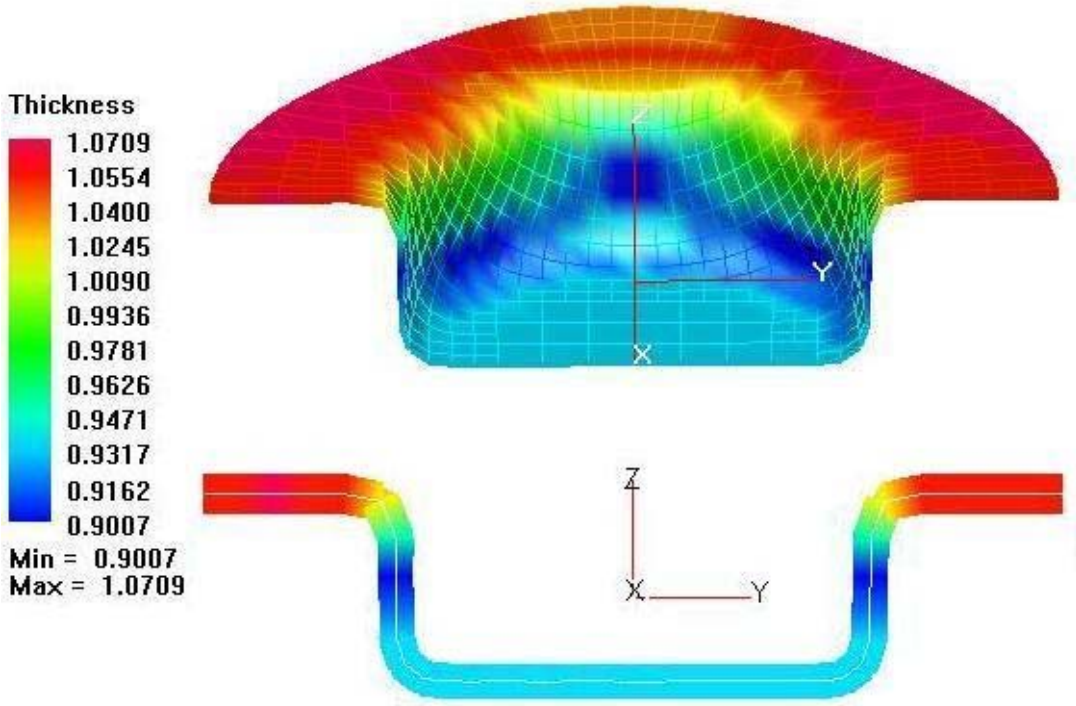


**Figure 4.56** Thickness contour of simulation 4 at 2D (X=0 plane) and 3D sections

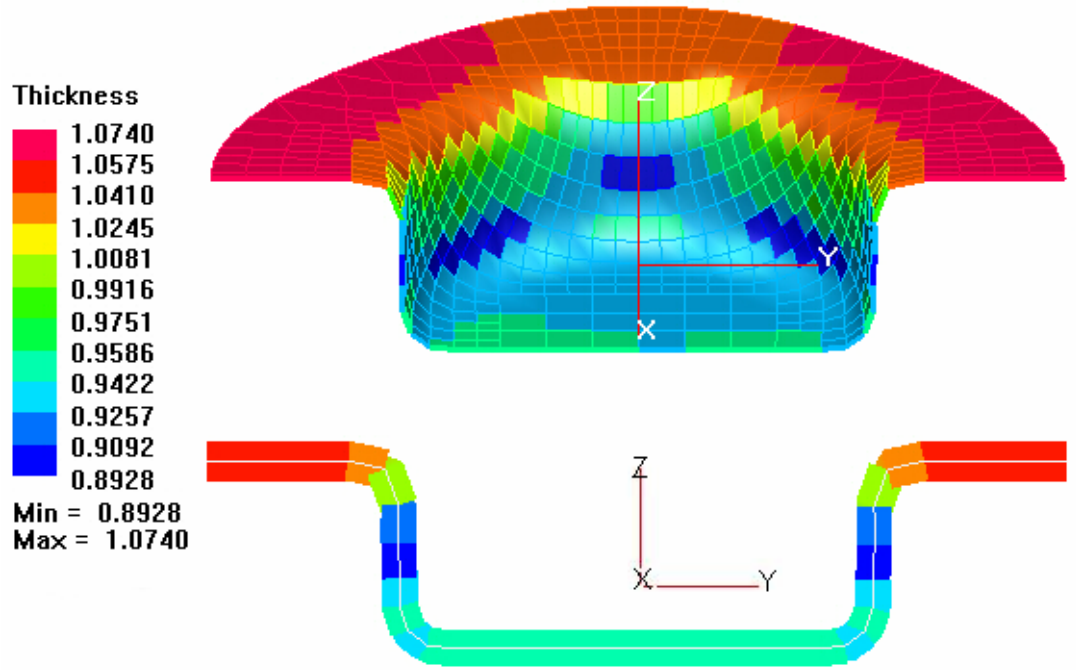


**Figure 4.57** Thickness contour of simulation 5 at 2D (X=0 plane) and 3D sections

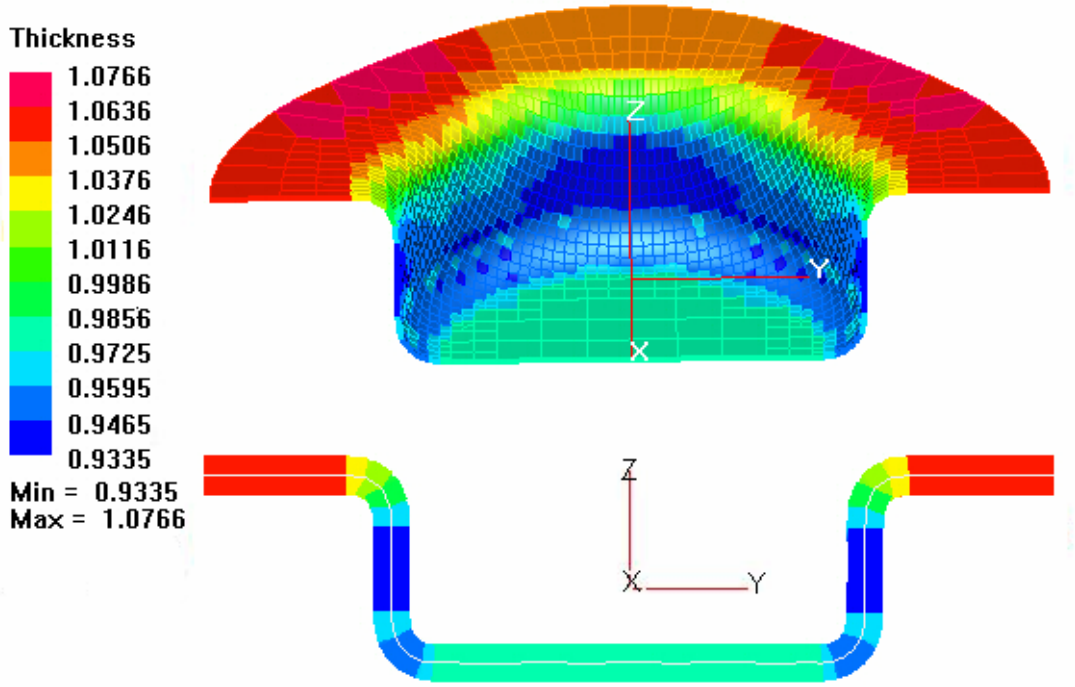


**Figure 4.58** Thickness contour of simulation 6 at 2D (X=0 plane) and 3D sections

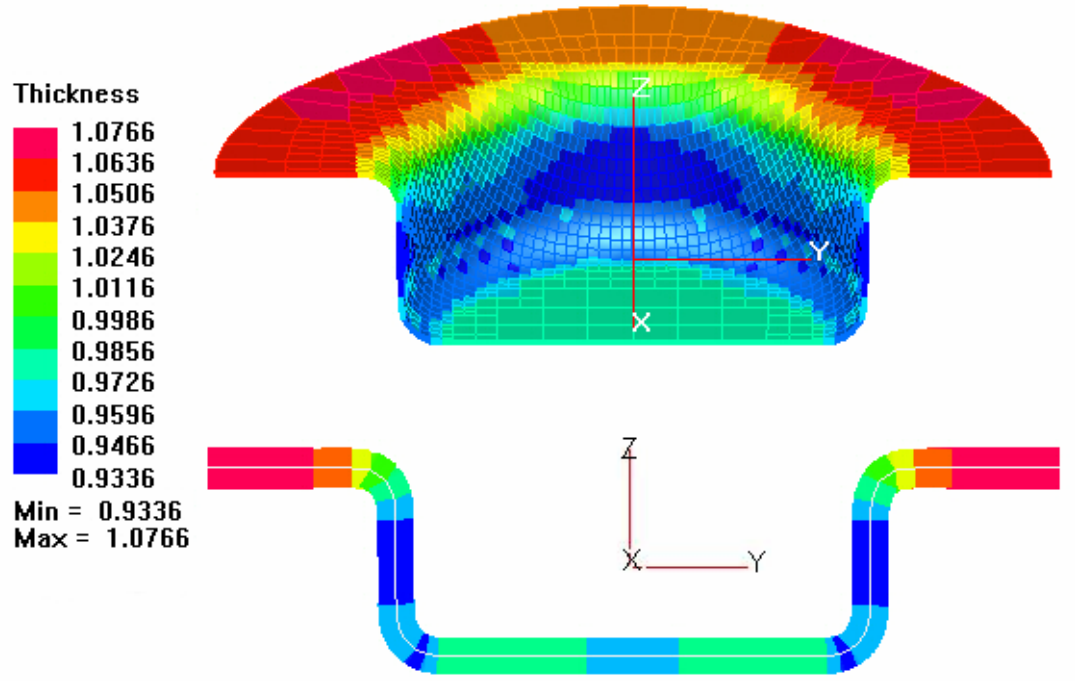


**Figure 4.59** Thickness contour of simulation 7 at 2D (X=0 plane) and 3D sections

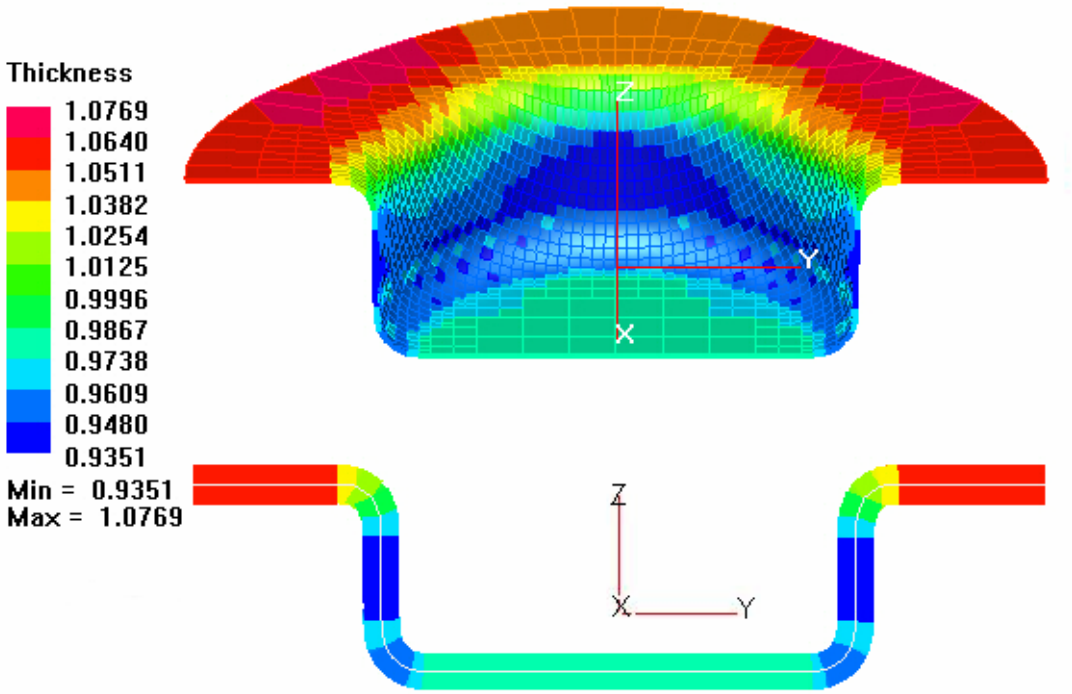


**Figure 4.60** Thickness contour of simulation 8 at 2D (X=0 plane) and 3D sections

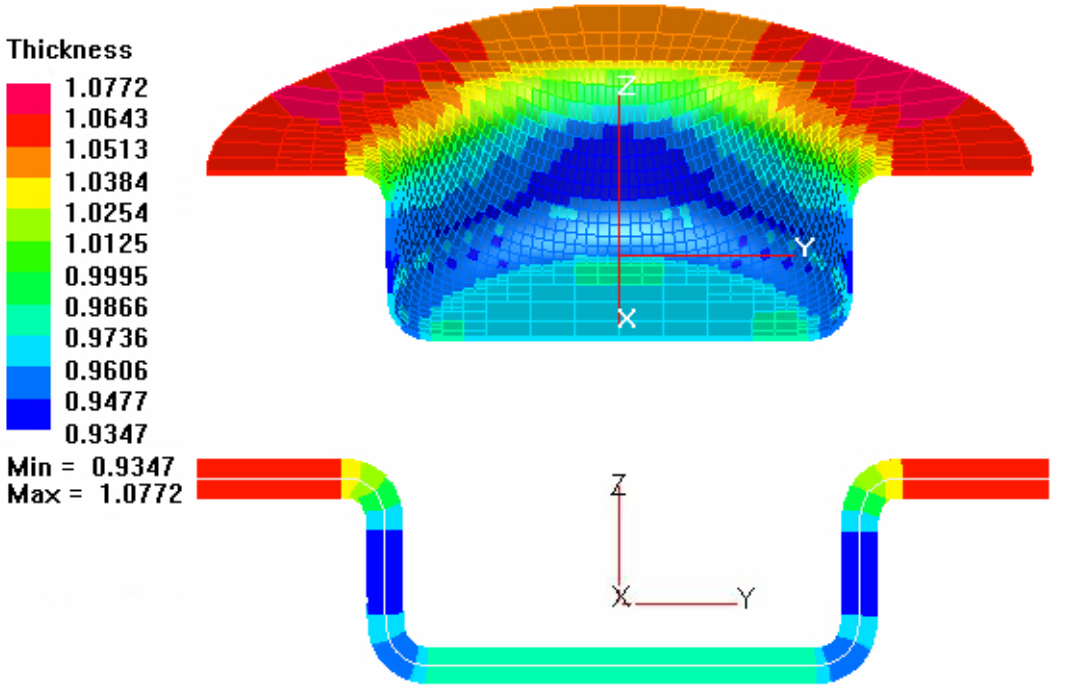


**Figure 4.61** Thickness contour of simulation 9 at 2D (X=0 plane) and 3D sections

When the thickness contours are inspected, only simulation 4 and 5 show some variation (Figure 4.62). If more precise observation is done on the thickness contour, it is seen that results of simulations 1, 2, 3 (Figure 4.63) and 6, 7, 8, 9 (Figure 4.64) are compatible with each other.

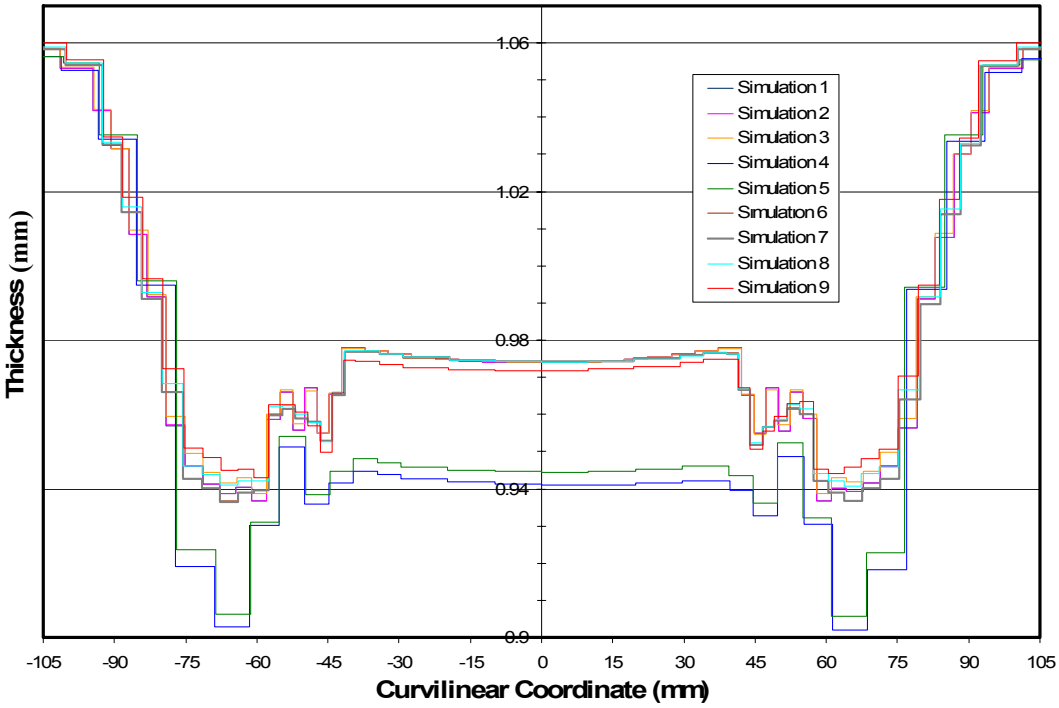


**Figure 4.62** Thickness distribution of all simulation along the curvilinear coordinate on X=0 plane

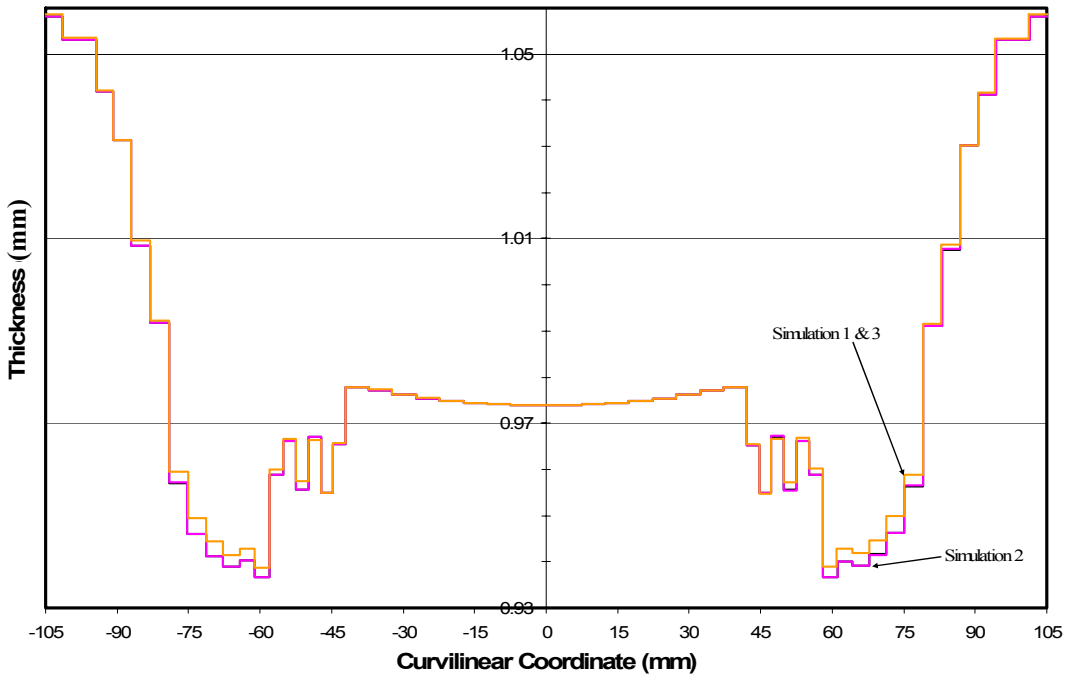


**Figure 4.63** Thickness distribution of simulations 1,2 and 3 along the curvilinear coordinate on X=0 plane

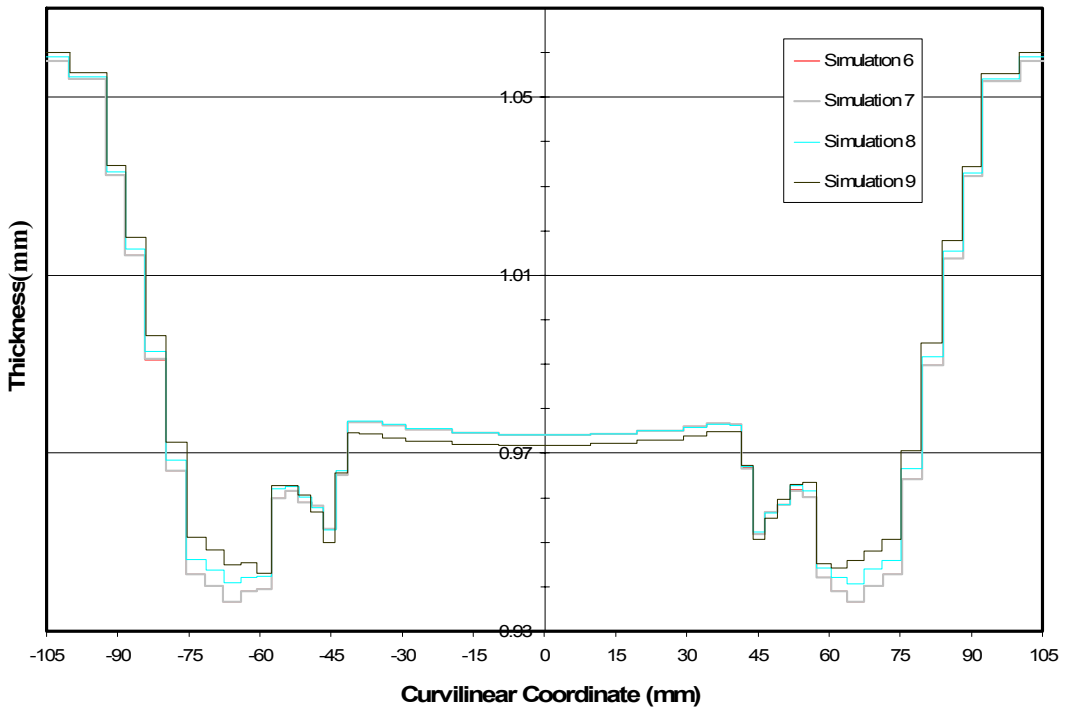


**Figure 4.64** Thickness distribution of simulations 6 ,7 ,8 and 9 along the curvilinear coordinate on X=0 plane

When the forming force (punch force) - displacement curves of all simulations are observed, two sets of curves are obviously seen (Figure 4.65). Simulations 4 and 5 whose element sizes are approximately 5 mm at the final stage, forms the upper set of curves, whereas remaining six simulations` force - displacement curves belong to the lower set of curves. In addition, it is seen that simulations 5 and 9 exhibit a sudden fall at the end of the force - displacement curves. The reason of this unexpected behavior is the large mass scaling factor used in both simulations.

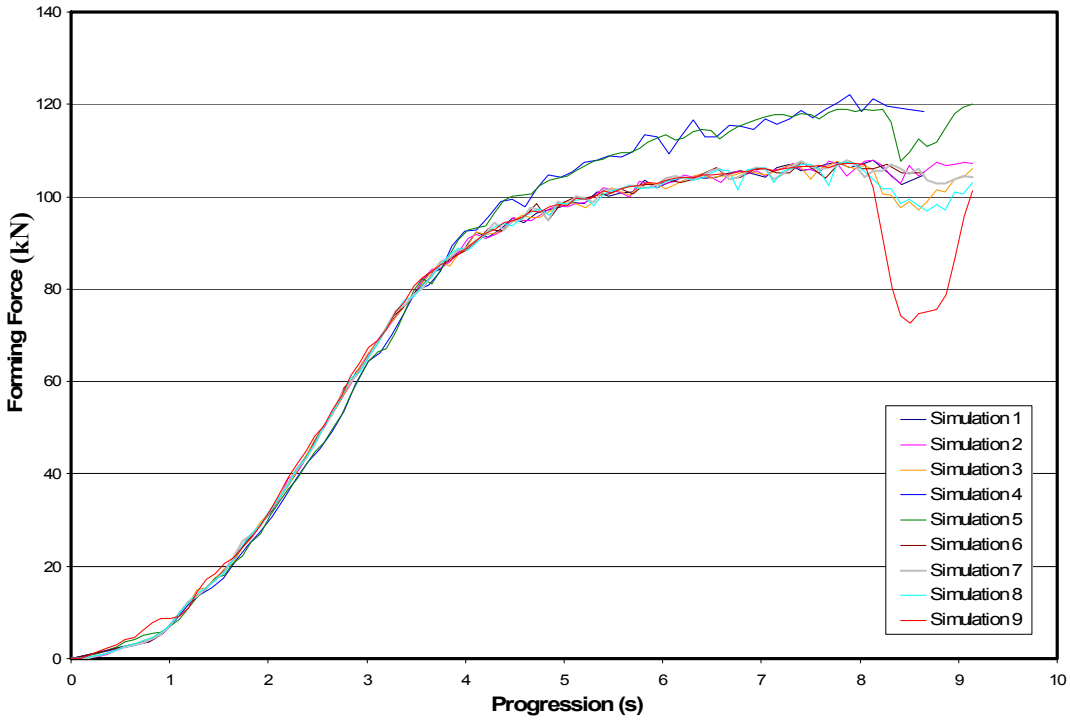


**Figure 4.65** Punch force – displacement curves of simulations

As equivalent plastic stress variations on 2D and 3D sections are observed (Figure 4.66 to 4.74), it appears that the effect of mass scaling and mass scale factors become more obvious in the stress calculations. The results show 10% variation between the upper and lower bound of set of curves. Moreover it is known that simulations 4 and 5 estimates the thickness distribution lower than the others (Figure 4.62). On the contrary, in case of stress calculation they predict higher stress values (Figure 4.75).

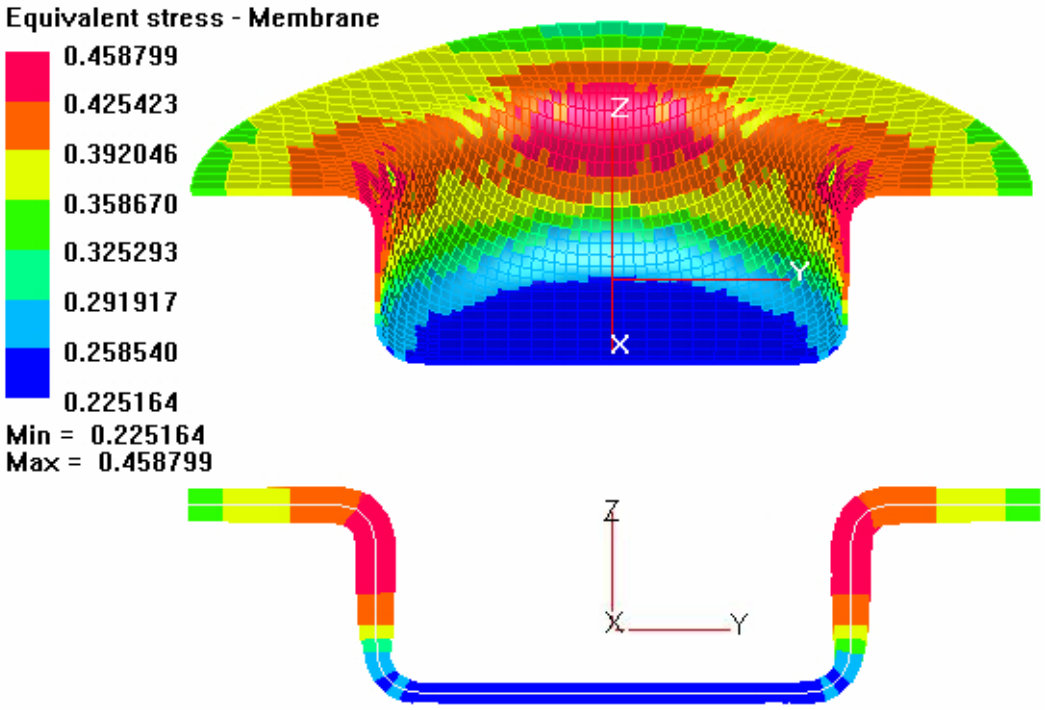


**Figure 4.66** 2D and 3D Eq. stress contours of simulation 1 on X=0 plane

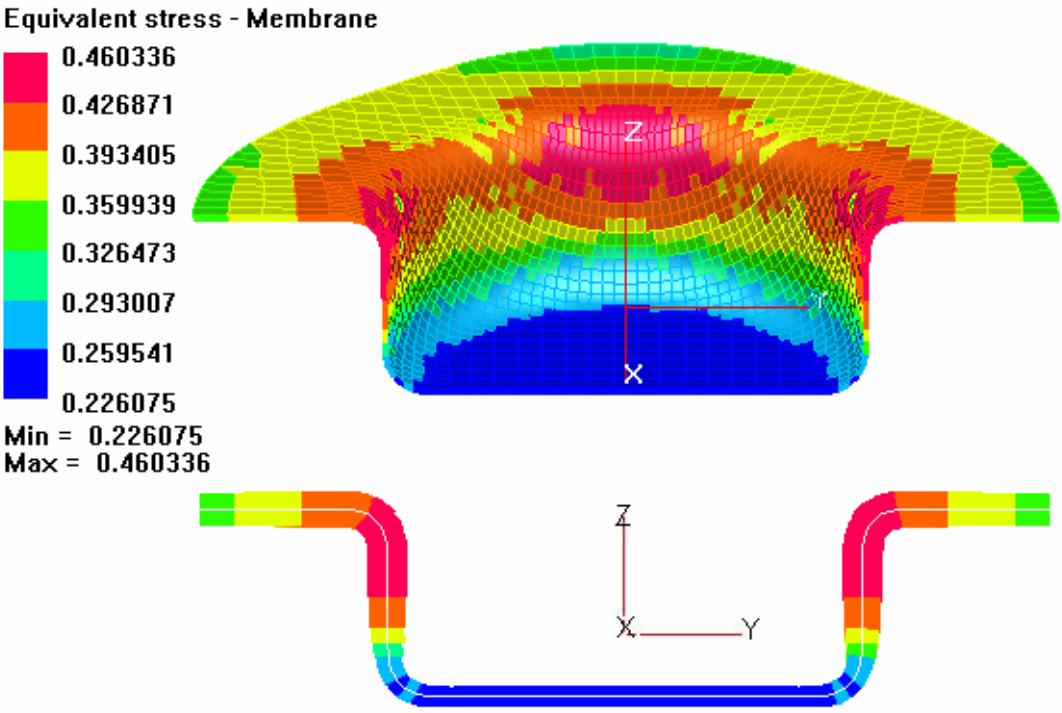


**Figure 4.67** 2D and 3D Eq. stress contours of simulation 2 on X=0 plane

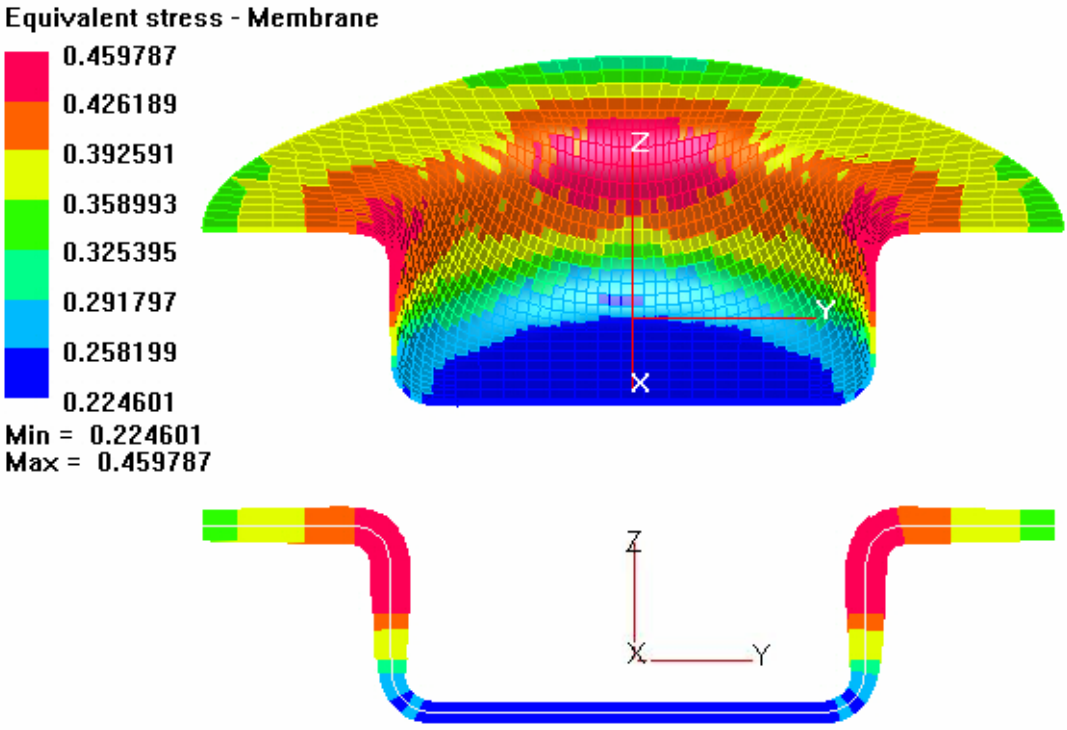


**Figure 4.68** 2D and 3D Eq. stress contours of simulation 3 on X=0 plane

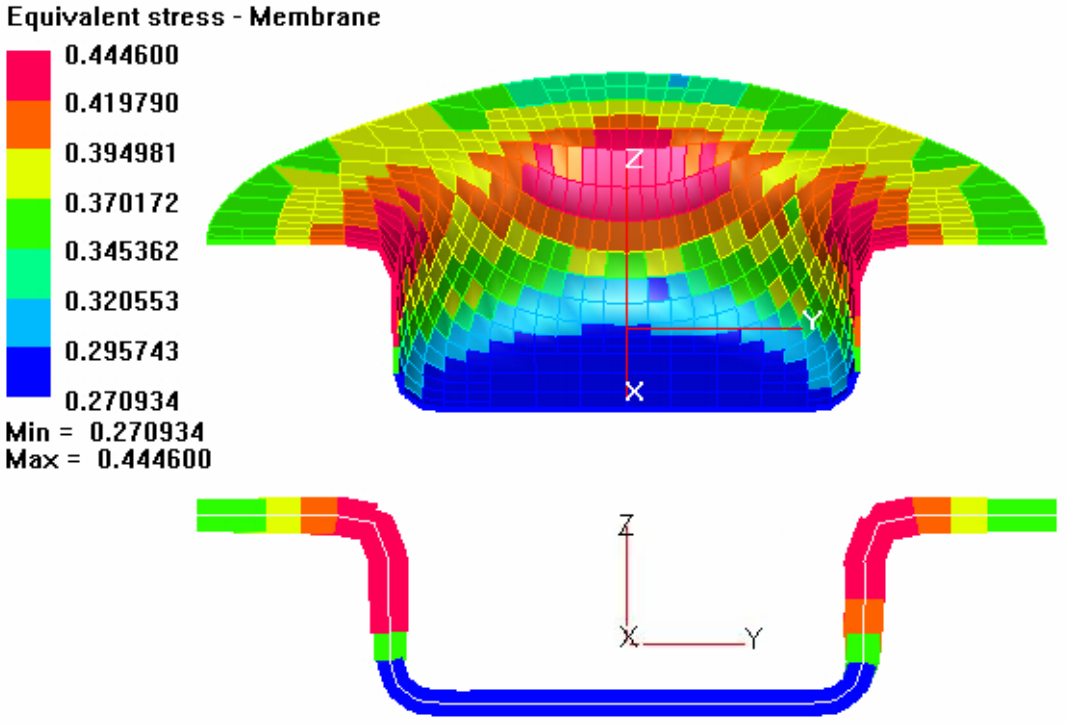


**Figure 4.69** 2D and 3D Eq. stress contours of simulation 4 on X=0 plane

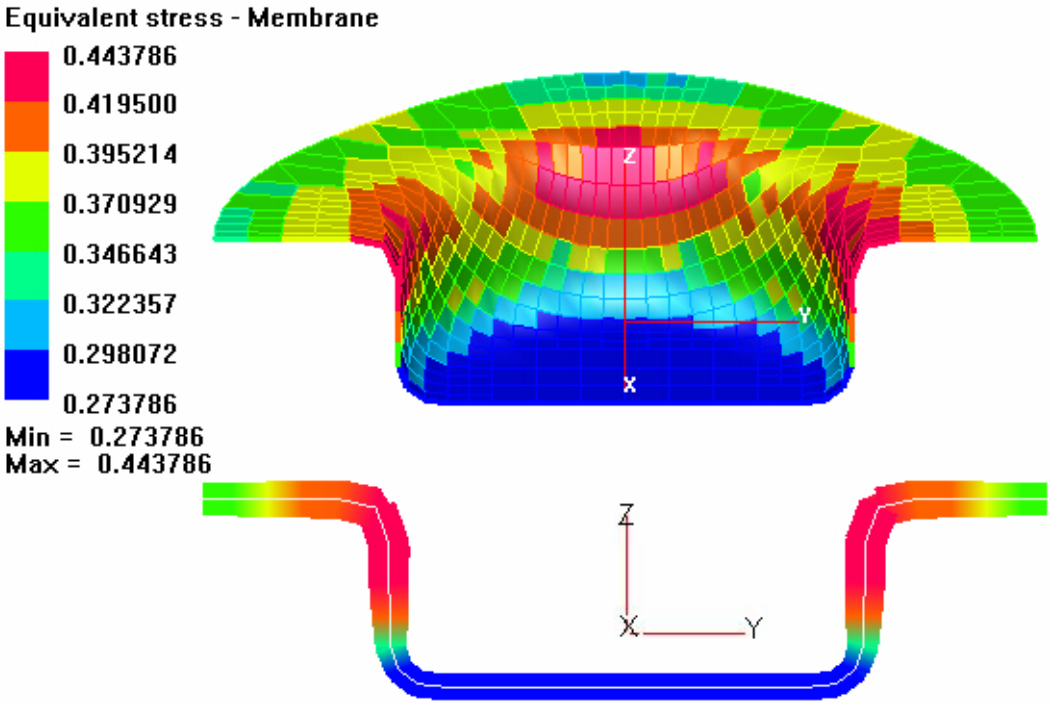


**Figure 4.70** 2D and 3D Eq. stress contours of simulation 5 on X=0 plane

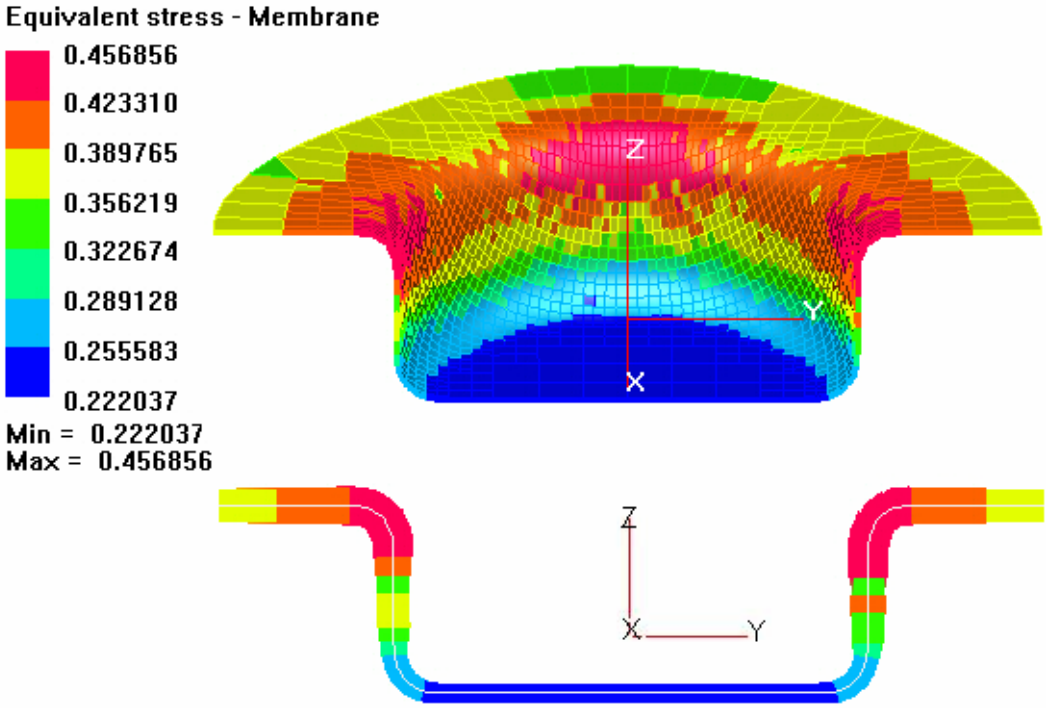


**Figure 4.71** 2D and 3D Eq. stress contours of simulation 6 on X=0 plane

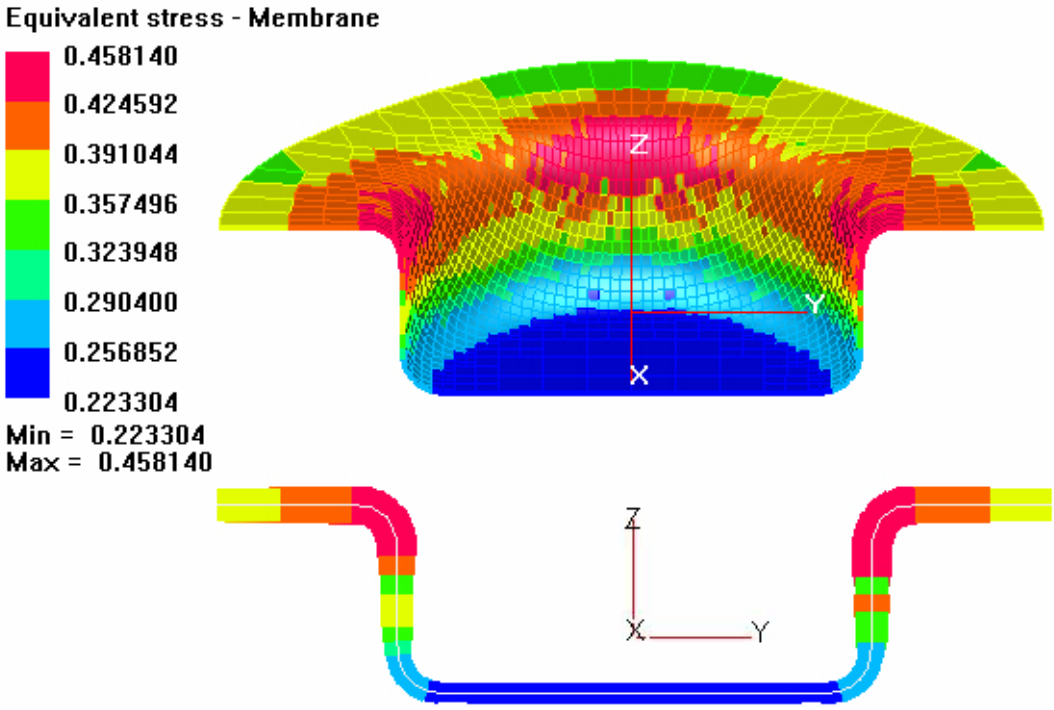


**Figure 4.72** 2D and 3D Eq. stress contours of simulation 7 on X=0 plane

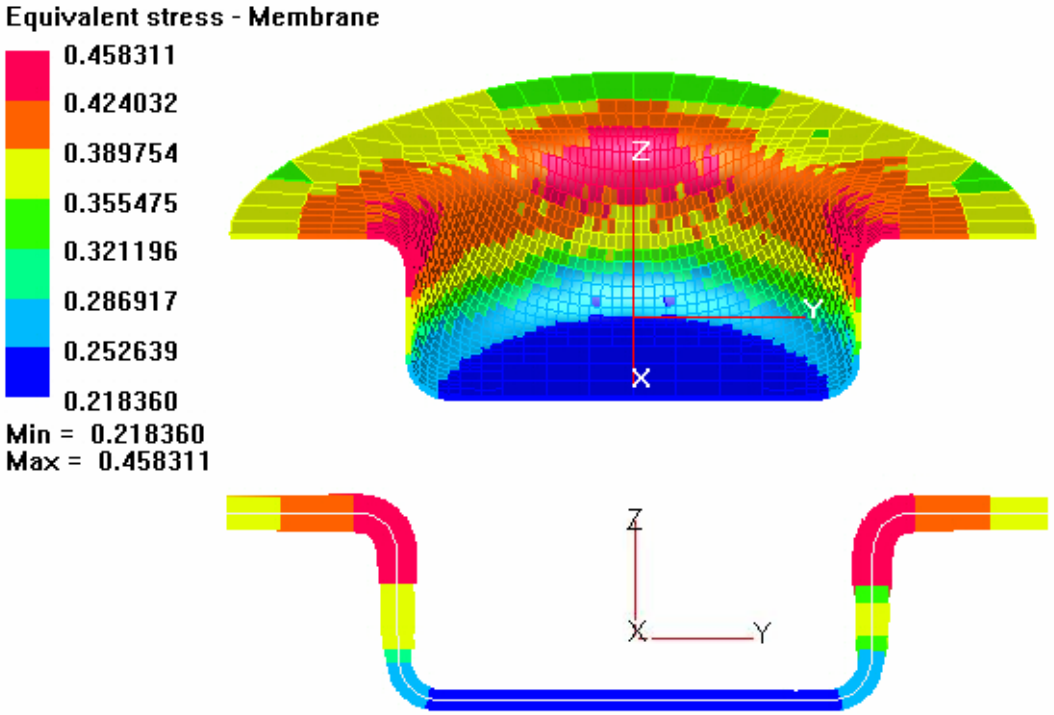


**Figure 4.73** 2D and 3D Eq. stress contours of simulation 8 on X=0 plane

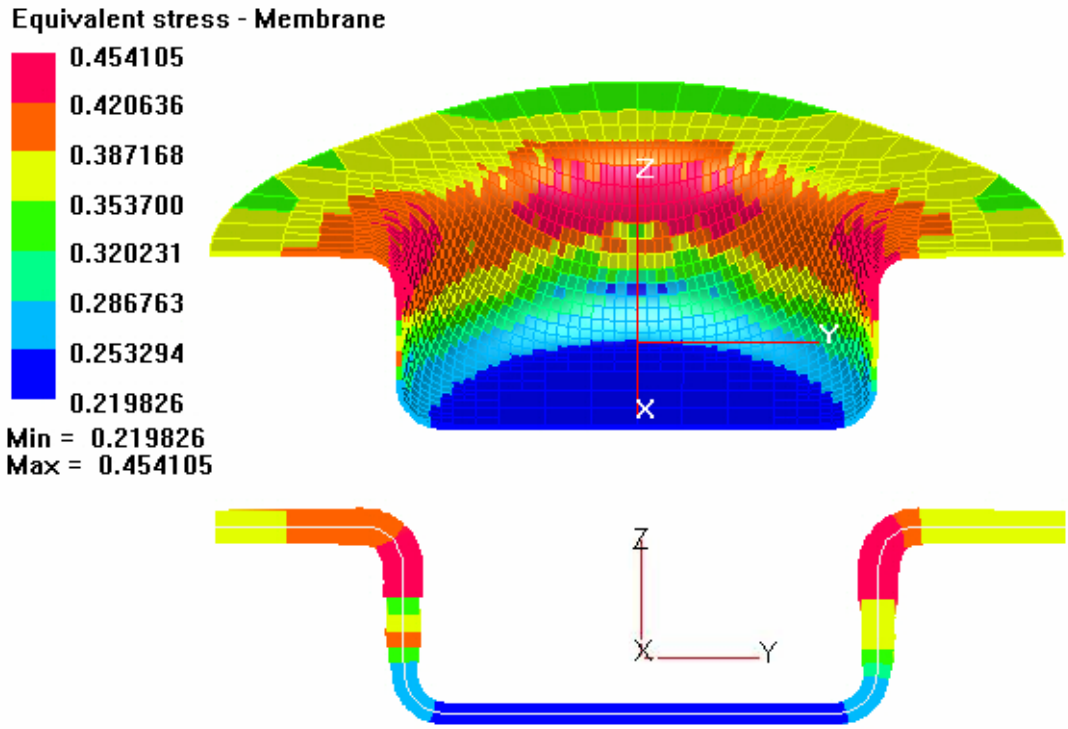


**Figure 4.74** 2D and 3D Eq. stress contours of simulation 9 on X=0 plane

If a precise observation is done on the equivalent stress variation along the bottom part of the 2D section, three more sets of curves are noticed. The results of simulations 1, 2, and 3 are similar to each other and they are the upper bound of those six curves. Furthermore, stress curve of simulation 8 is more likely to that of simulation 9 and together they form the lower bound. Equivalent stress variation curves of simulations 6 and 7 shows another correlative behavior between each other and they are in the middle of upper and lower bounds (Figure 4.76). The tendency toward forming groups in the simulation result is not by chance instead, they group together according to the similarities between the element size, refinement level and magnitude of mass scaling used (Table 4.7).

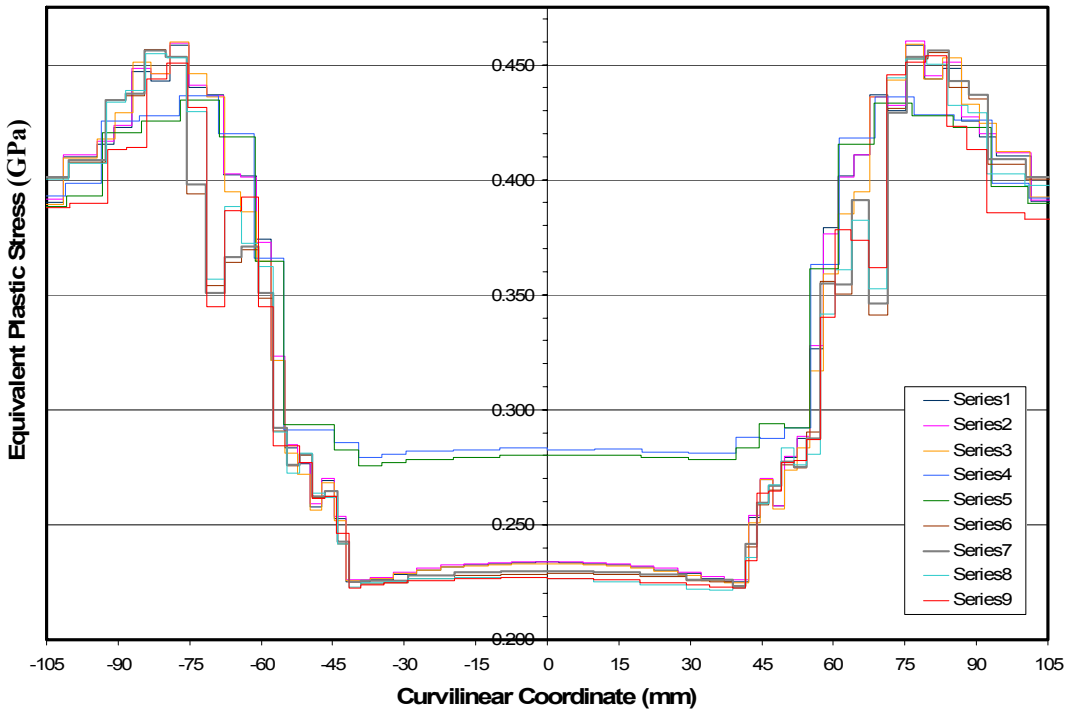


**Figure 4.75** Variation of Equivalent stress along the curvilinear coordinate on X=0 plane (All Simulations)

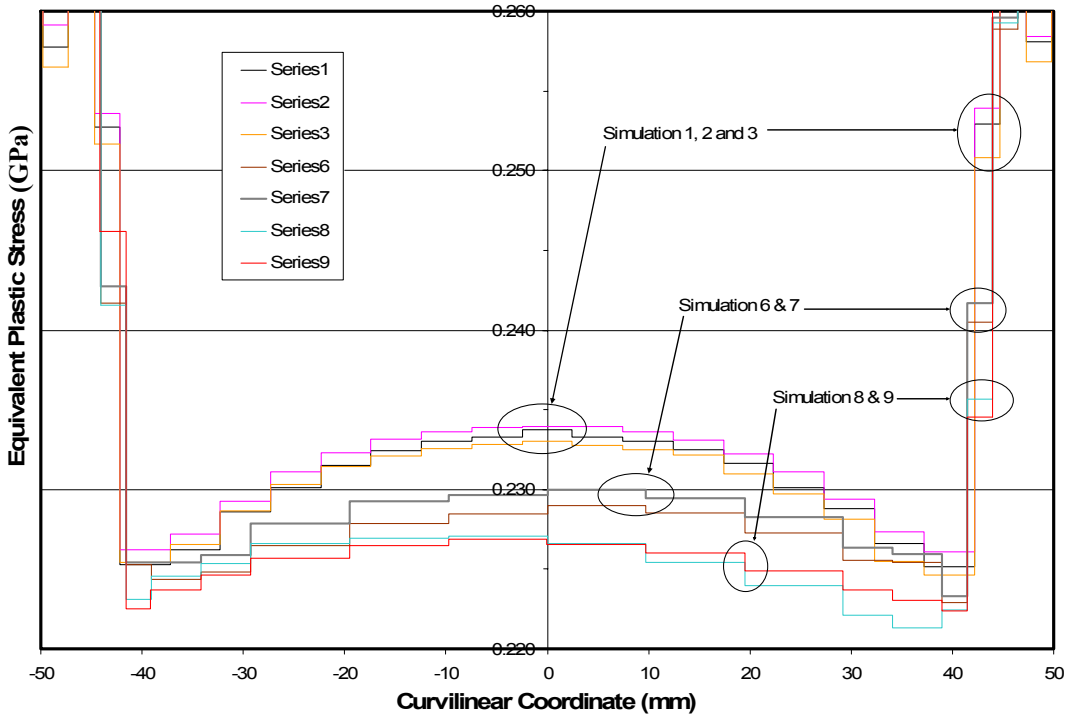


**Figure 4.76** Variation of Equivalent stress along the curvilinear coordinate on X=0 plane (Simulation 1,2,3,6,7,8 and 9) (Bottom of the cup)

In simulations 3, 5 and 9 large mass scaling factors are used. The reference element size given for the mass scaling is equal to the initial element size. Therefore, solver increases mass of some element at the beginning of the simulation to achieve the stable time step value suitable for the element size. Table 4.8 shows the number of scaled elements and the increase in the mass of the deformable body.

**Table 4.8** Amount of mass increase in the simulations

| | **Number of Elements Scaled** | **Total Mass Before Scaling (kg)** | **Total Mass After Scaling (kg)** | **Increase in Mass (%)** |
|---|---|---|---|---|
| Simulation 3 | 1389 | 0.263 | 0.341 | 29.50% |
| Simulation 5 | 352 | 0.263 | 0.357 | 35.85% |
| Simulation 9 | 352 | 0.263 | 0.357 | 35.85% |

The initial and final time steps of simulations, the decrease in time step during the analysis and CPU time of each simulation is listed in Table 4.9. It is seen that simulation 5 has the fastest CPU time while simulation 1 has the slowest. However, the assessment of simulations should be done within each subgroup according to the accuracy requirement of the process since subgroups have different accuracy levels in the prediction of stress variation or thickness distribution. Comparison of CPU time of each subgroup is given in Figure 4.77.

First, considering the sudden fall, that has no physical meaning, in the forming force - displacement curve of simulations 5 and 9, it can be suggested that large mass scaling parameter (e.g. 10 mm) that causes an increase larger than 20% in the weight of deformable body should not be used although they are the two fastest simulations in the assessment.

Mass scaling option is disabled in the simulation 4, but since the final element size is larger than the other simulation, it is still accepted as a fast computation. However, accuracy in determination of thickness distribution and forming force calculation is poor because of the insufficient mesh size.

When the first group formed by simulations 1, 2 and 3 is observed, it is seen that simulation 3 is the most favorable one. Three simulations predict identical thickness distributions; however, simulation 3 performs this prediction 40 % faster than simulation 1 (no mass scaling). If residual stresses are concerned, parameters used in simulation 2 are suggested. The CPU time reduction in simulation 2 is more than 20 percent.

**Table 4.9** Time step changes and computational times of each simulation

| | **Initial Time Step (s)** | **Final Time Step (s)** | **Decrease in Time Step (%)** | **CPU Time (s)** |
|---|---|---|---|---|
| Simulation 1 | 5.15E-04 | 2.33E-04 | 55% | 2.38E+03 |
| Simulation 2 | 5.15E-04 | 2.84E-04 | 45% | 1.90E+03 |
| Simulation 3 | 8.34E-04 | 8.31E-04 | < 1% | 1.35E+03 |
| Simulation 4 | 1.24E-03 | 4.78E-04 | 61% | 6.33E+02 |
| Simulation 5 | 1.67E-03 | 1.66E-03 | < 1% | 5.56E+02 |
| Simulation 6 | 1.24E-03 | 2.34E-04 | 81% | 1.99E+03 |
| Simulation 7 | 1.24E-03 | 3.40E-04 | 73% | 1.85E+03 |
| Simulation 8 | 1.24E-03 | 8.29E-04 | 33% | 9.46E+02 |
| Simulation 9 | 1.67E-03 | 1.66E-03 | < 1% | 5.10E+02 |

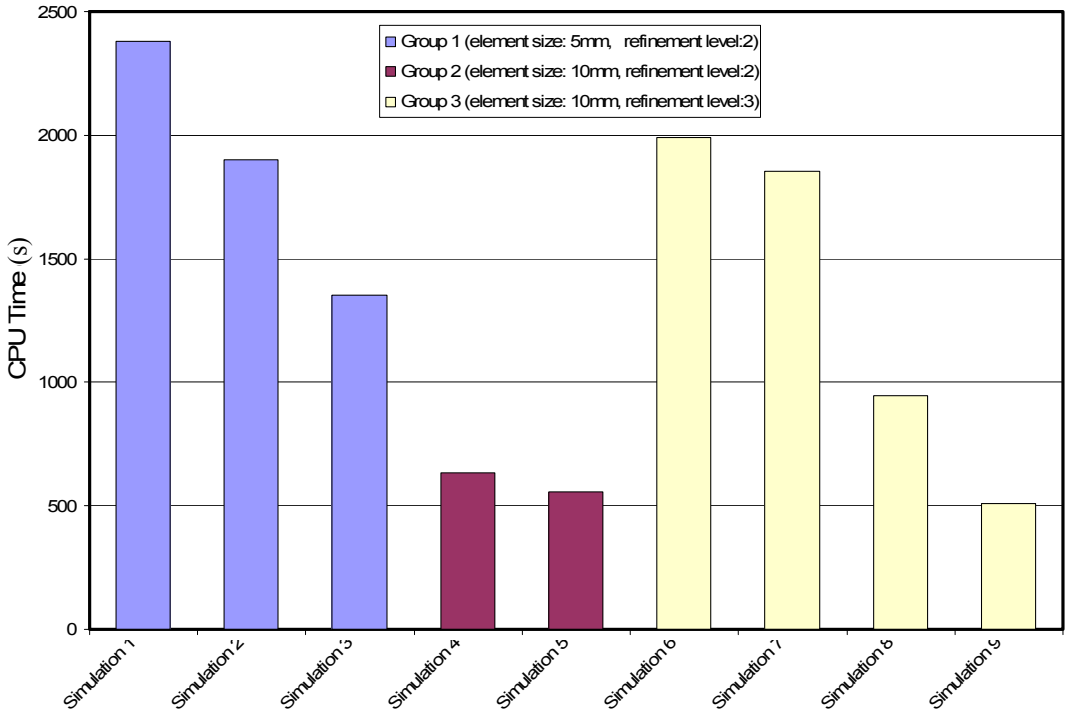


**Figure 4.77** CPU time of each simulation within 3 groups

## 4.6 Comparison with NUMISHEET 2002 Benchmarks

According to the proposed process and numerical parameters at Sections 4.4 and 4.5, a cylindrical cup drawing numerical experiment is prepared to compare the simulation results with NUMISHEET 2002 Benchmark in order to verify that those parameters are optimum and useful for dynamic-explicit finite element codes.

Setup and geometry of tools used in the benchmark are given in Figure 4.78. It is an axisymmetrical deep drawing process where the punch radius ($R_1$) is 50.00 mm and die radius ($R_2$) is 51.25 mm. The fillet radii of punch ($R_3$) and die ($R_4$) are 7.00 mm and 9.50 mm, respectively. In the same process setup, two different anisotropic materials with 1 mm thickness are used as workpieces. The radii of workpieces are 90 mm for aluminum blank and 105 mm for steel blank. Those geometrical data are used to build the meshes in the simulations.

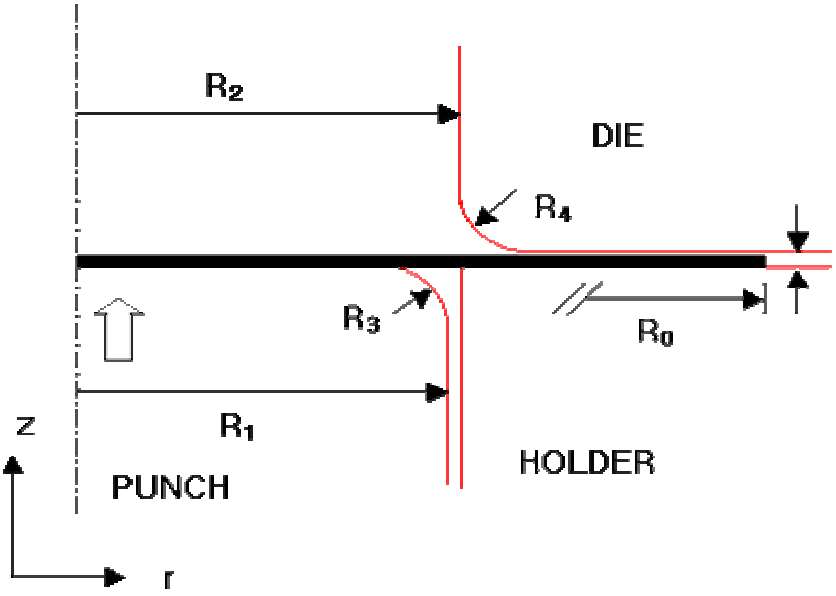


**Figure 4.78** Axisymmetrical deep drawing process

The material properties of aluminum and steel workpiece are supplied by two companies; ALCOA (USA) and POSCO (Korea). Those are tabulated in Table 4.10 and they are used for both benchmark and simulation.

**Table 4.10**Material properties of aluminum (6111-T4) and steel (DDQ mild steel)

| **Material** | **E (GPa)** | **ρ g/cm$^3$** | **ν** | **$\varepsilon_0$** | **K (MPa)** | **n** | **R (0°)** | **R (45°)** | **R (90°)** |
|---|---|---|---|---|---|---|---|---|---|
| 6111-T4 | 70.728 | 2.6 | 0.342 | 0.00256 | 538.2 | 0.2255 | 0.894 | 0.611 | 0.660 |
| DDQ Steel | 221.368 | 7.8 | 0.3 | 0.00876 | 547.3 | 0,2692 | 2.160 | 1.611 | 2.665 |

In the benchmark, it is desired that punch penetrates 40 mm into the die cavity. Thus, simulation is preceded until the required depth of 40 mm is achieved. Average friction coefficient at all contact surfaces are supplied as 0.0096 for aluminum material and 0.0426 for steel blank.

Two different blank holder forces are applied for each material in the benchmark (Table 4.11). Low blank holder force (LBHF) is applied to observe the wrinkle creation on the flange, whereas high blank holder force (HBHF) is used to determine the limits of the process.

**Table 4.11** Blank holder forces used for aluminum (6111-T4) and DDQ mild steel

| **6111-T4 Aluminum** | | **DDQ Mild Steel** | |
|---|---|---|---|
| Low blank holder force (LBHF) kN | 10 | Low blank holder force (LBHF) kN | 10 |
| High blank holder force (HBHF) kN | 50 | High blank holder force (HBHF) kN | 70 |

Twenty-three participants have supplied results to the benchmark. Seven of the participants performed experiments, whereas the rest of them participated with simulation results obtained by different finite element codes. Information about the participants can be found in Appendix A.

The comparison between simulation and benchmark is done by inspecting forming force - displacement curve, thickness variation along 0°, 45°, and 90° directions, outer radius of flange and number of wrinkles occurred on the flange. Those results are compared for both aluminum and steel blanks. Firstly, the benchmark of steel sheet material is concerned.

Figure 4.79 shows the comparison of simulation (S-HBHF) with the experiments done by different participants, for high blank holder forces respectively. The coherence between the simulation result and AE-04 can be noticed clearly. Results supplied by other participants are slightly higher that the simulation result, however this insignificant difference may exist because of the external influences. For example, Atzema (Appendix A) from Corus Research, Development and Technology has stated that grid applied to the steel blank has influenced the friction condition, thus it increased the force - displacement 5 percent.

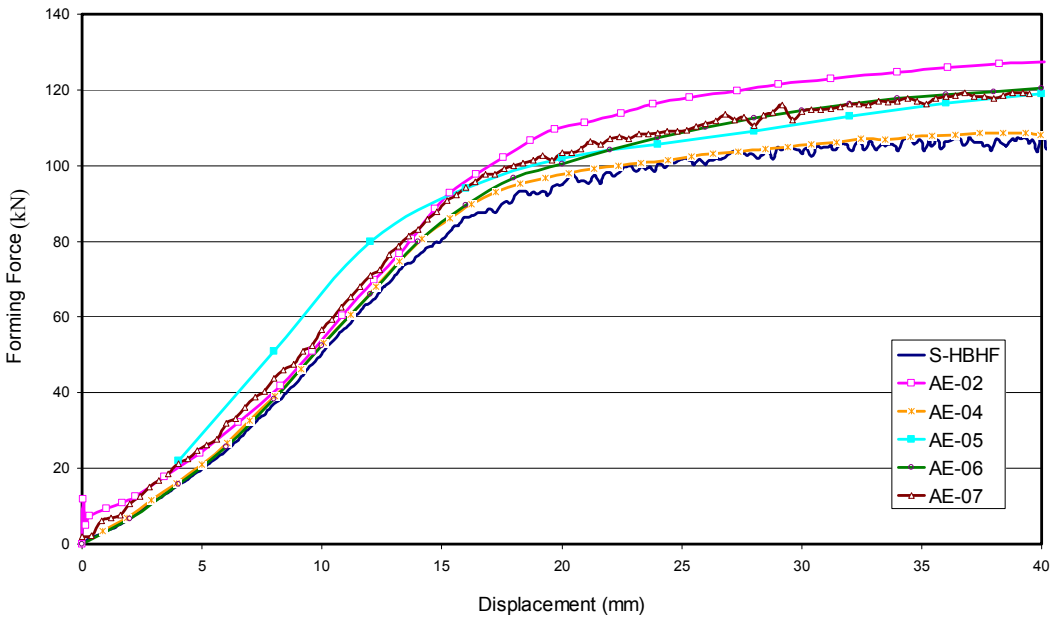


**Figure 4.79** Comparison of forming force-displacement curve of simulation with five benchmark experiments

Outer profiles of flange are compared in Figure 4.80 and 4.81 for steel blank with high blank holder force (HBHF). In Figure 4.80, the outer circumference of flange is plotted in Cartesian coordinates and in Figure 4.81; it is plotted with respect to the $r$ and $\theta$ in cylindrical coordinates.

It is shown that the simulation result only shows some variations from benchmark experiments AE-02 and AE-07 and is compatible with other three experiments. The reason of the variation can be the misalignment of the blank according to the rolling direction and eccentric placement of blank on the die. In the simulation (S-HBHF) such incorrect orientations cannot happen since the recent finite element codes have features like “auto-positioning”.

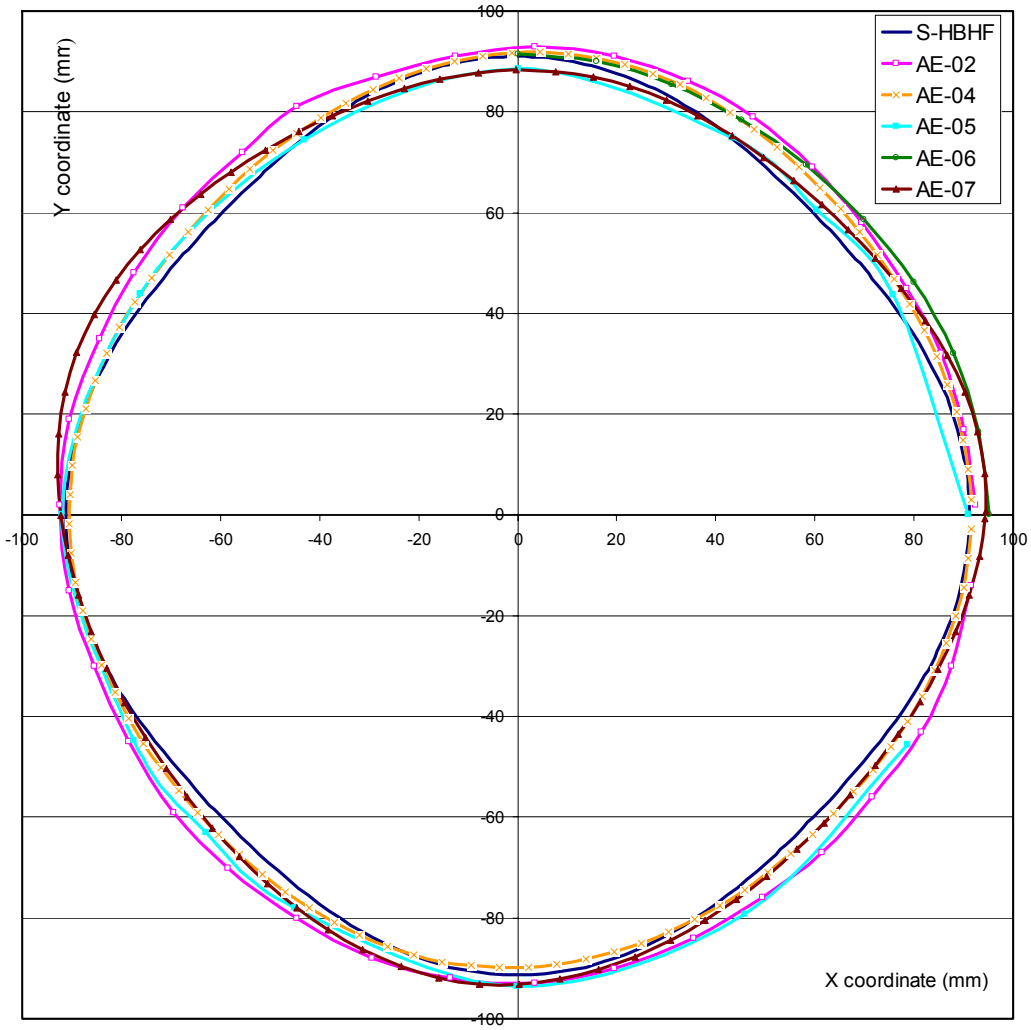


**Figure 4.80** Comparison of outer circumference of steel flanges of simulation (S-HBHF) and benchmark experiments (plotted in Cartesian coordinates)

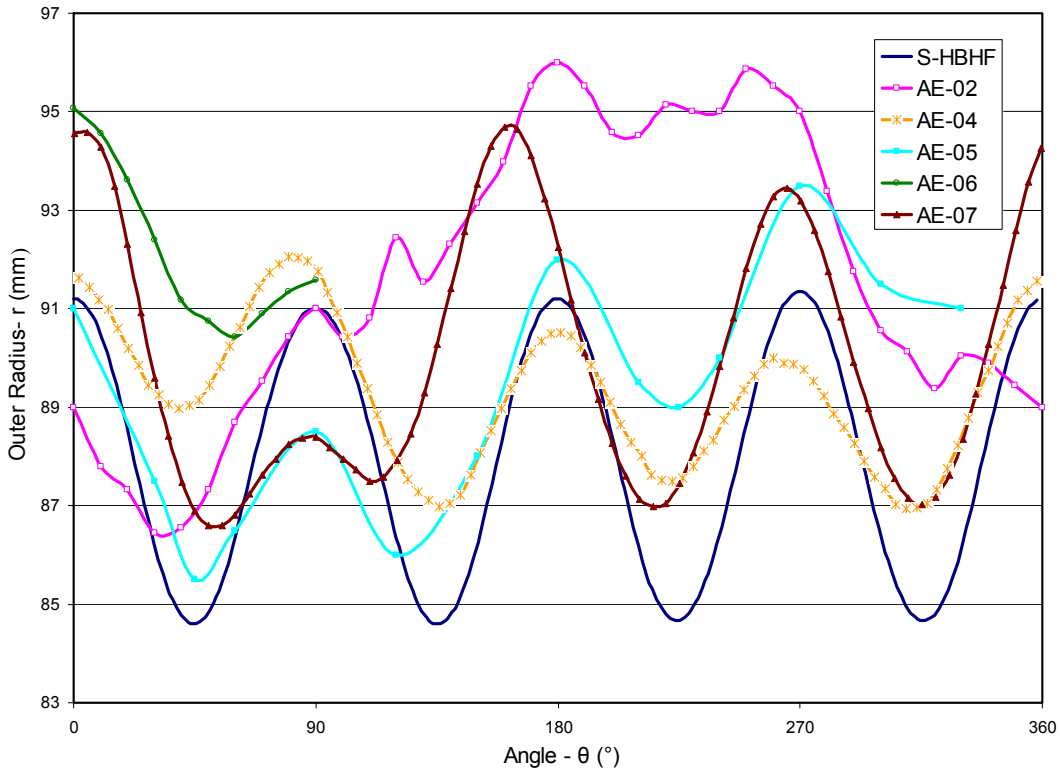


**Figure 4.81** Comparison of outer circumference of steel flanges of simulation (S-HBHF) and benchmark experiments (plotted with respect to the r and θ in Cylindrical coordinates starting from rolling direction)

Thickness variation along 0°, 45°, and 90° directions with respect to rolling direction of simulation (S-LBHF) having low blank holder force (LBHF) is respectively given and compared in Figures 4.82, 4.83, and 4.84 with the result of three benchmark experiments.

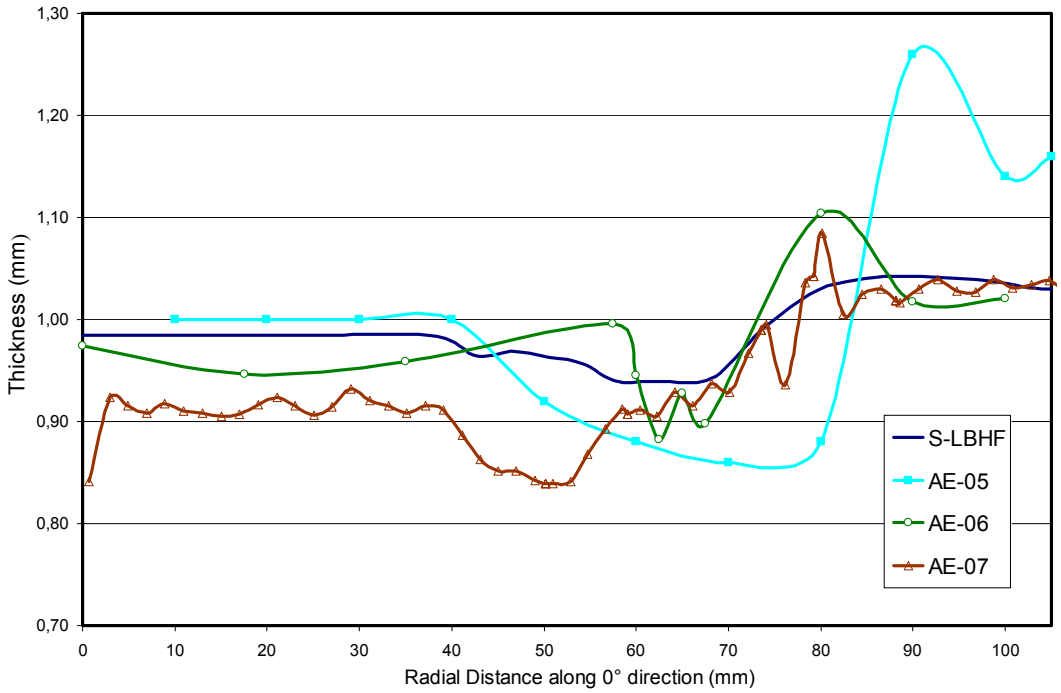


**Figure 4.82** Thickness distributions along 0° direction (rolling direction).

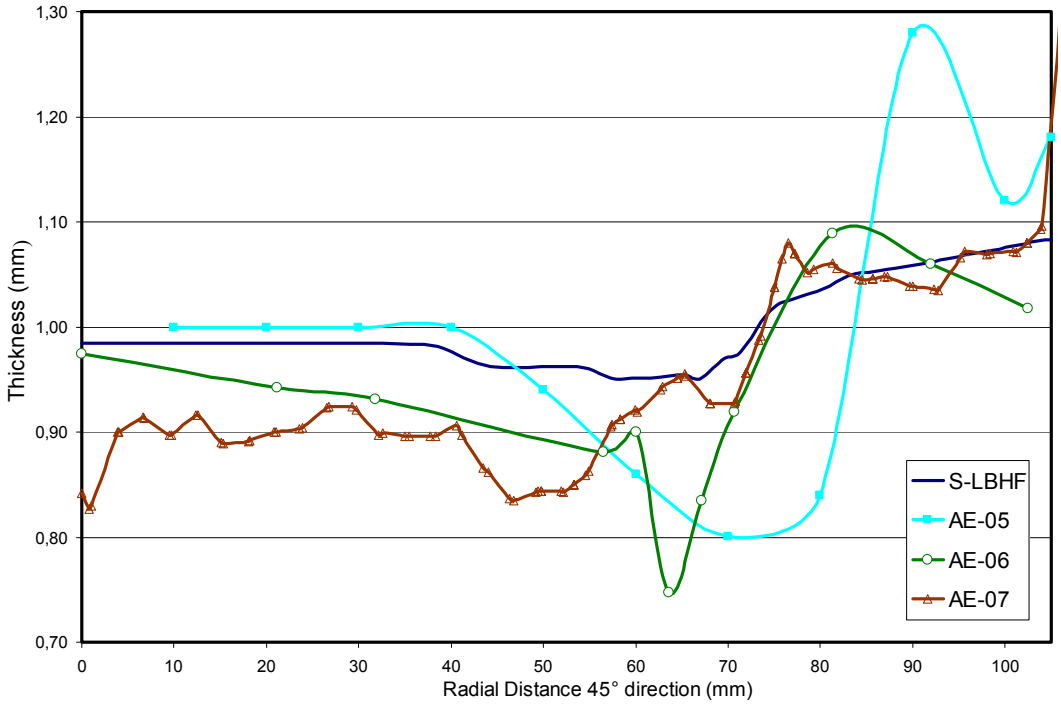


**Figure 4.83** Thickness distributions along 45° direction.

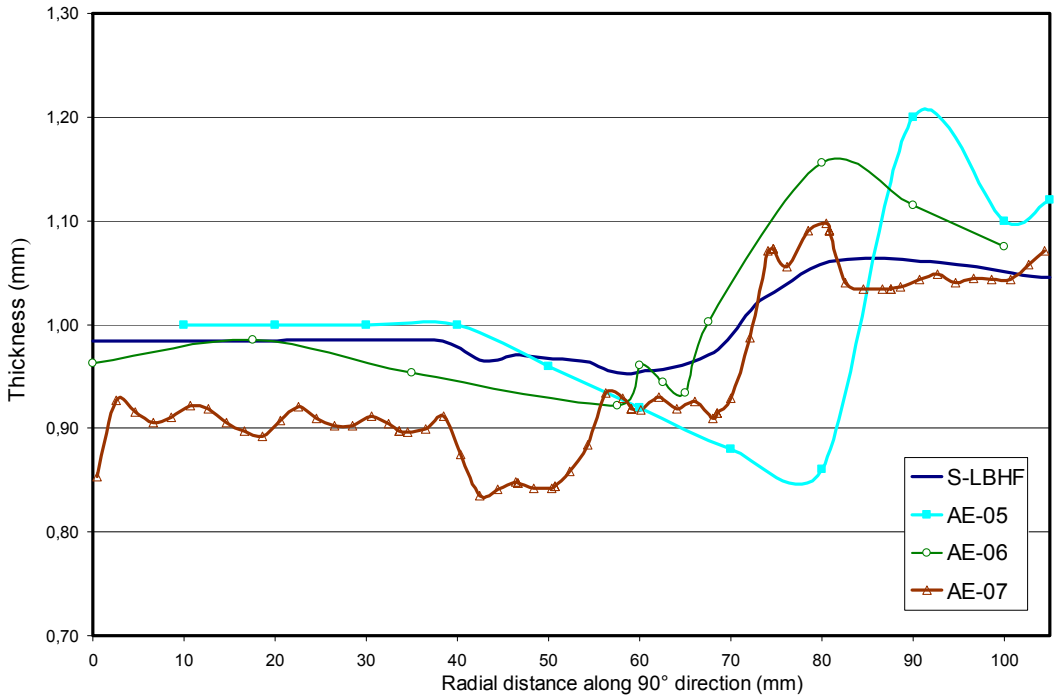


**Figure 4.84** Thickness distributions along 90° direction.

It is seen in thickness variation figures that even the result of experiments are not in agreement with each other, so it is hard to validate the simulation result by considering the thickness variation. Possible reason of wide variation in the experimental results can be related with the quality of the tools and the precision of the experiment and the measurement. If the thickness distributions along the first 40 mm of the radial distance in all directions are observed, the results of experiment AE-05 is reasonable. Blank is almost not deformed plastically at that region since the bottom of punch is a smooth horizontal plane. Thus, the thickness distribution should be almost constant between 0 and 40 mm. Result of experiment AE-07 shows some deviations in thickness along the bottom part. The cause of this behavior can be the poor quality of the punch surface, and as well as the bad condition of setup including improper lubrication. If the thickness distribution of experiment AE-06 is inspected in all directions, it is seen that the problem is more drastic. Since there is no plastic deformation at the bottom of the workpiece, the thickness variation is expected to be almost the same in all directions. Yet, a great deviation is observed in the result. Possible cause of this unexpected deviation

can be explained with non-planer geometry of the punch bottom surface and deviated stroke of punch from z-axis. Not the values but the trend of simulation (S-LBHF) result is compatible with the expected behavior. It has a constant thickness close to the initial value (1mm) along the bottom of the workpiece, it decreases along the die cavity fillet, and lateral surface and it increases and becomes more than initial thickness (1mm) along the flange.

In addition, when blank holder force is decreased from 70kN to 10 kN in the deep drawing process, wrinkles may occur on the flange. Dynamic explicit finite element codes using shell elements are capable of showing the wrinkling. In Figure 4.85 and Figure 4.86, the estimation of wrinkling zone and number of wrinkles are compared with the benchmark experiments.

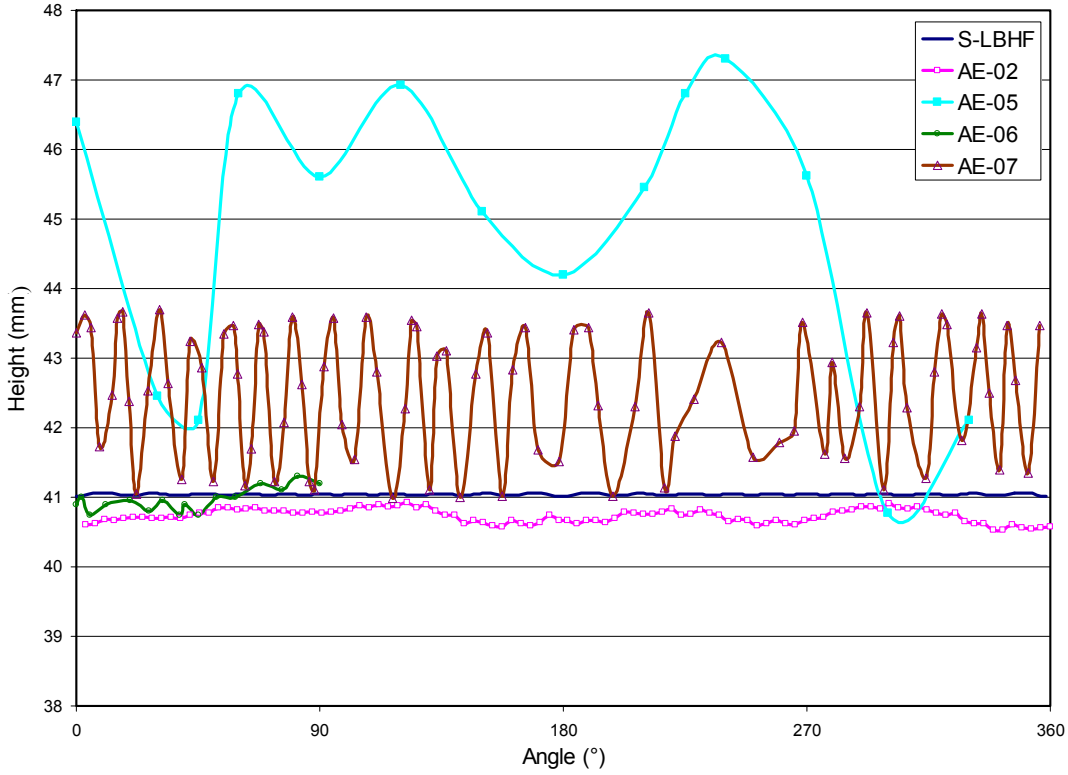


**Figure 4.85** Z (height) vs. θ (angle) cylindrical coordinates of flange outer profile of simulation (S-LBHF) and benchmark experiments.

Height of outer profile of the flange at the final step is measured by taking the lower surface of the bottom of the workpiece as reference (z=0). Punch stoke is given as

40 mm, so that the height distribution (z coordinate) of the flange circumference is expected to show deviation around 41 mm (Punch stroke + initial sheet thickness). The results of experiments AE-02, AE-06, AE-07 and simulation (S-LBHF) satisfy this condition.

Results of experiment AE-05 are not reliable since very low number of data point is used for the measurement. In addition, in Figure 4.85, no wrinkle is observed for the experiment AE-05 however, in Figure 4.86, it is stated that there are 22 wrinkles counted on the flange.

When the rest of the results are observed, wrinkles are clearly noticed but the range and amplitude of the wrinkles show variations. The reason of difference in the range can be explained with the incorrect referencing in the measurement and excessive or inadequate stroke of punch. The reason of changes in amplitude of wrinkles can be related with the possible differences in the applied blank holder force. Experimental setup may be insufficient to transfer the desired force (10kN) exactly onto the flange.

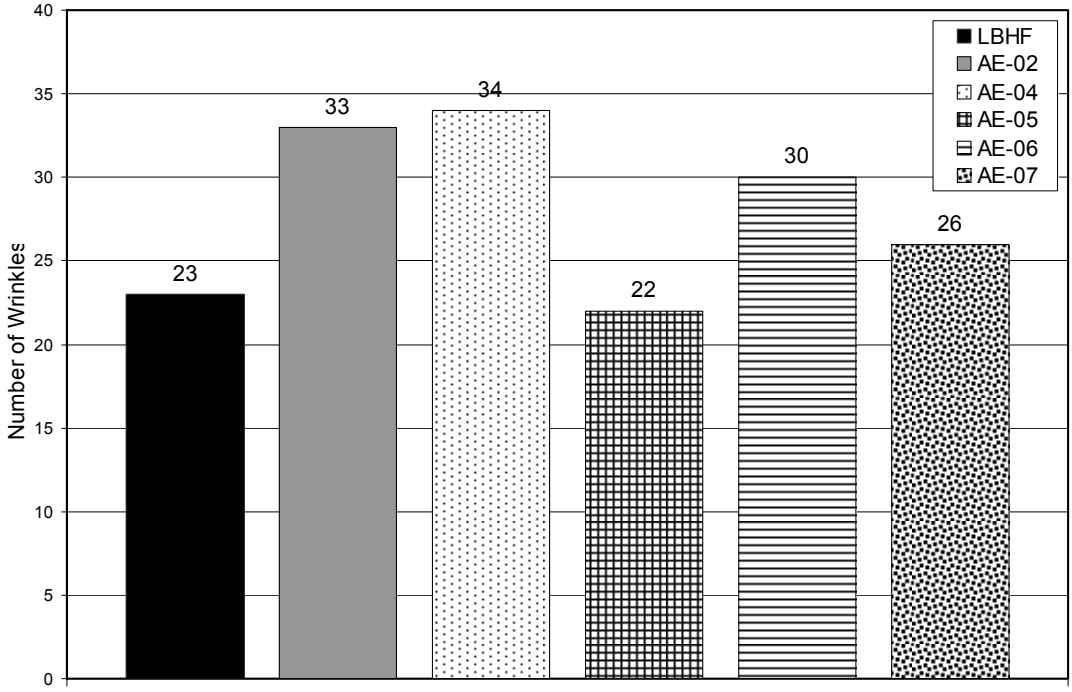


**Figure 4.86** Number of wrinkles on the flange of S-LBHF and benchmarks

Almost all simulation results of steel material are verified with benchmark experiments. The compliance between the results is not only determined by the general behavior but also satisfied numerically. Besides the cylindrical cup drawing of steel blank, aluminum material is also concerned.

Figure 4.87 shows the force - displacement curves and compares the simulation (A-HBHF) with deep drawing experiment of aluminum. As the curves are inspected, it is seen that there is 25 percent to 45 percent variation between the results. Yet the experiments themselves differ from each other about 20 percent. To reveal the reason of poor estimation and large variation between the results, further studies are performed.

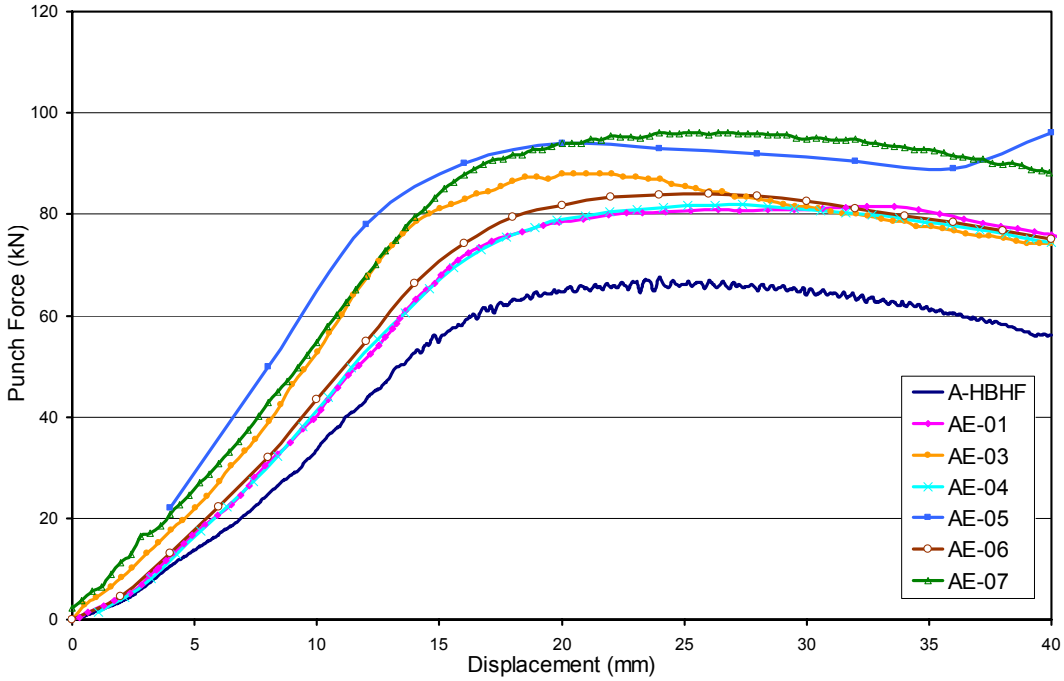


**Figure 4.87** Comparison of forming force-displacement curve of simulation (A-HBHF) with six benchmark experiments

First, simulation (A-HBHF) results are compared with 14 benchmark simulations. Figures 4.88, 4.89 and 4.90 show the comparison between the forming force - displacement curves of simulation (A-HBHF) and benchmark simulations.

Dynamic-Explicit, Static-Explicit and Implicit finite element codes are used by the participants in the benchmark. AS2, AS3, AS7, AS13, AS14, and AS16 estimate lower than the simulation result (A-HBHF) whereas results of AS1, AS8, and AS15 are higher estimations. AS5, AS6, AS10, and AS12 have exactly the same result with the simulation (A-HBHF). It is also know that AS6 and AS12 used the same commercial finite element code with the simulation (A-HBHF). Unlikely, the result of AS11 meets with lower bound of benchmark experiment results (Figure 4.89). When the information about AS11 is inspected (Appendix A), it is noticed that implicit finite element code is used. However, AS8, AS9, AS15, and AS16 also employed implicit codes but they underestimated the experimental results. The other differing property of the AS11 is the material law utilized in the analysis.

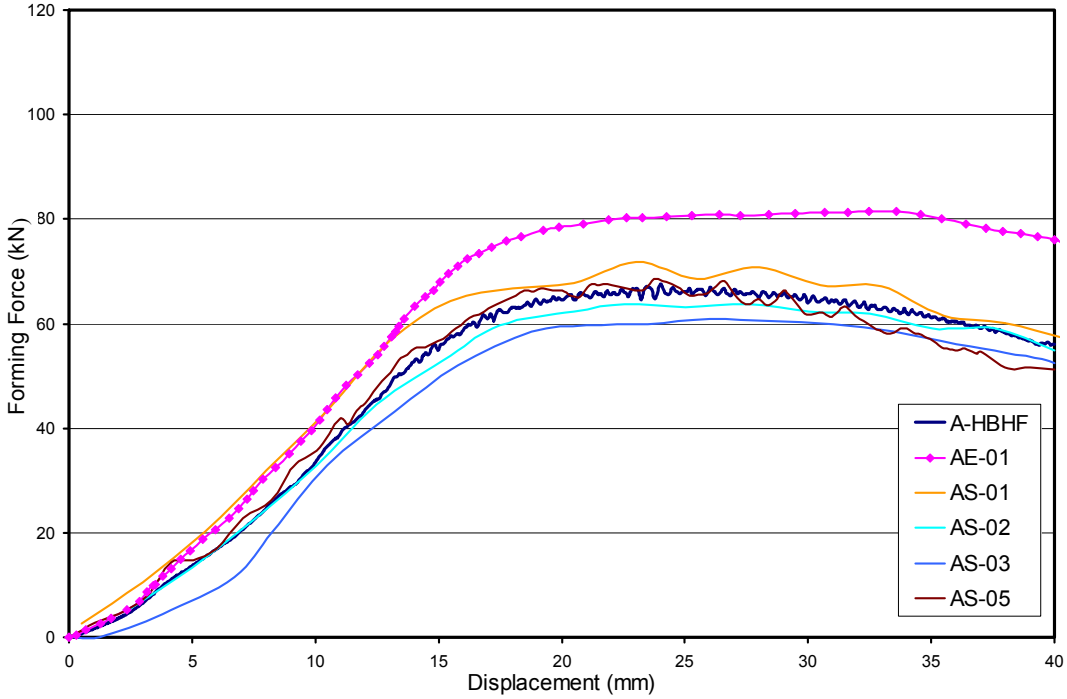


**Figure 4.88** Comparison of forming force-displacement curve of simulation (A-HBHF) with benchmark simulations (1)

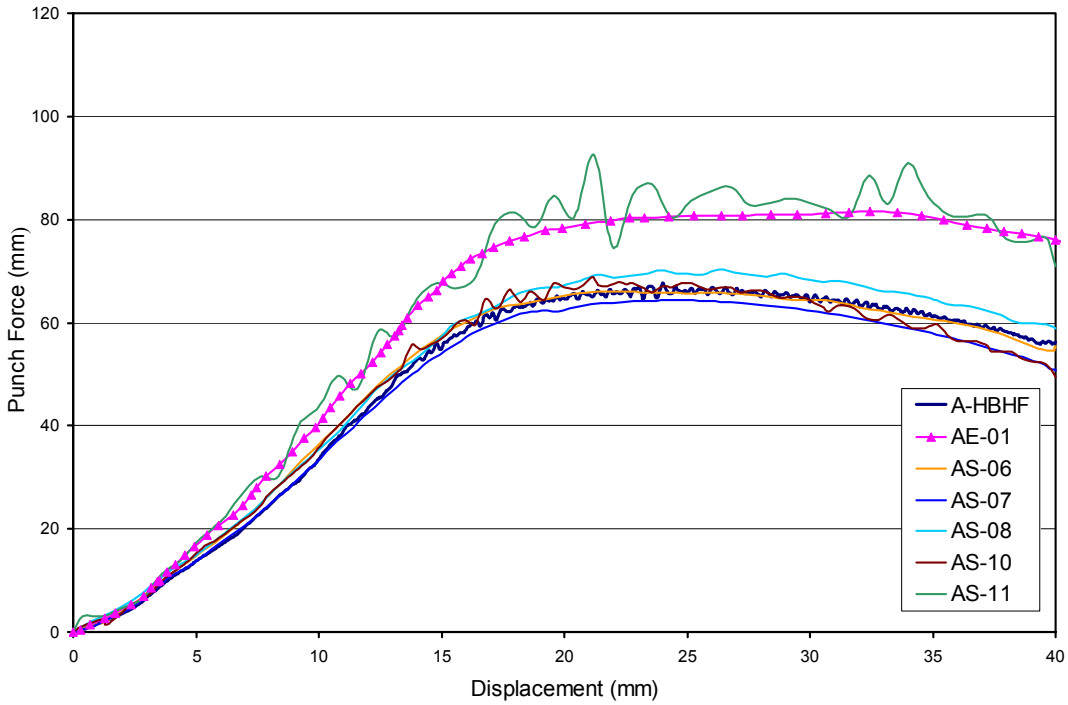


**Figure 4.89** Comparison of forming force-displacement curve of simulation (A-HBHF) with benchmark simulations (2)

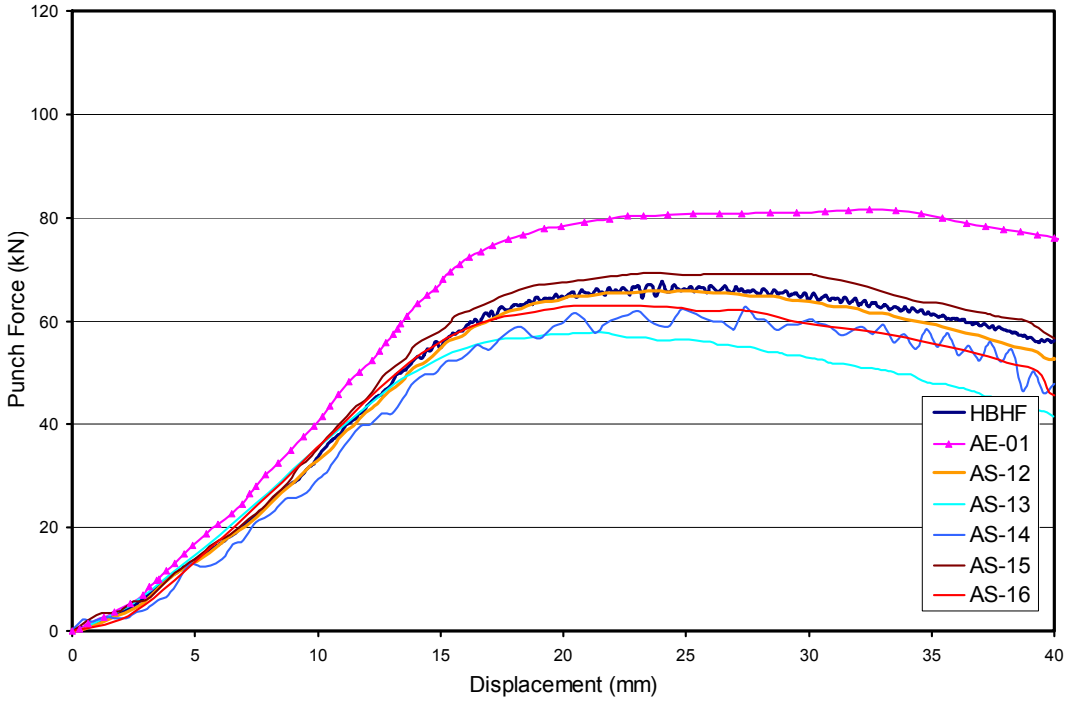


**Figure 4.90** Comparison of forming force-displacement curve of simulation (A-HBHF) with benchmark simulations (3)

According to the planar anisotropy data supplied by the NUMISHEET for the aluminum workpiece, Orthotropic Hill 1948 Isotropic Hardening material law is used in the simulation (HBHF Sim) as well as in all benchmark experiments except AS11. However, Banabic [9] states that Hill 1948 yield criterion should be only used for obtaining simple approximations of the anisotropic behavior of sheet metals and it would be better to avoid its use especially for aluminum alloys. Hill 1990, Barlat and Karafillis-Boyce yield criteria can be used to obtain more accurate models for the plastic behavior of anisotropic sheet metals, including the aluminum alloys. Nevertheless, those criteria need excessive experiments and material data that are not provided by the NUMISHEET, thus Hill 48 yield criterion is used as material law in the simulations. This reveals why aluminum alloy deep drawing simulation predicts poor results. Therefore, no more results are compared with the benchmark; instead, additional study on the yield criteria is done.

For anisotropic materials, the present state-of-the art is somewhat confusing since various yield criteria are proposed up to now and they are still being used. In practice, the choice of a yield criterion depends on the experimental constraints. Table 4.12 lists the experimental data required for the formulation of various yield criteria [9]. Except for Hill 1948, these yield criteria necessitate the experimental determination of the equibiaxial yield stress $\sigma_b$, which requires additional work and special testing device. Therefore commercial finite element codes frequently use the Hill 1948 yield criterion. Banabic states that Hill 1948 yield criteria can represent neither the "anomalous" behavior observed by Woodthrope and Pearce [19] where $r < 1$ *and* $\sigma_b > \sigma_u$ nor the "second order anomalous" behavior where

$$\frac{r_0}{r_{90}} > 1 \ \textit{and} \ \frac{\sigma_0}{\sigma_{90}} < 1 \tag{4.1}$$

**Table 4.12** Required experimental data for the formulation of yield criteria

| **Author, Year** | $\sigma_0$ | $\sigma_{45}$ | $\sigma_{90}$ | $\sigma_b$ | $\tau$ | $r_0$ | $r_{45}$ | $r_{90}$ |
|---|---|---|---|---|---|---|---|---|
| Hill 1948 | x | | | | | x | | x |
| Hill 1990 | x | x | x | x | x | | x | |
| Chu 1995 | x | | | x | | x | x | x |
| Barlat et al. 1996 | x | x | x | x | | x | x | x |
| Lin, Ding 1996 | x | | x | x | | x | x | x |

## 4.7 Comparison with Analytical Formulations

Simulations compared with NUMISHEET 2002 Benchmarks [16], are also compared with analytical formulation proposed by Ramaekers [17, 18]. Hence, a computer program that uses the formulations derived by Ramaekers (given in Appendix B) is written to calculate the forming force for cylindrical cup drawing process.

According to Ramaekers, forming force in axisymmetrical deep drawing is the summation of four components:

$$F_D = F_{Dfl} + F_{Frfl} + F_{D\rho} + F_{Fr\rho} \tag{4.4}$$

where

$F_{Dfl}$ is the deformation force of the flange

$F_{Frfl}$ is the friction force between flange and tool

$F_{D\rho}$ is bending - rebending force at the die fillet

$F_{Fr\rho}$ is the friction force at the die fillet

Also critical forming force that is the upper limit of the forming forces regarding the admissible thinning in sheet is approximated by Kals [18] as;

$$F_C = \frac{\left(\frac{R+1}{\sqrt{2R+1}}\right)^{n+1} \cdot n^n}{\left[\frac{s_0}{\rho_P} + \frac{s_0}{r_p} + \mathrm{e}^{n-\frac{\sqrt{2R+1}}{R+1}\varepsilon_0}\right]} \tag{4.5}$$

where

$R$ is the mean anisotropy factor

$n$ is Krupkowsky material law coefficient

$s_0$ is initial sheet thickness

$r_\rho$ is the punch radius

$\rho_p$ is punch fillet radius

$\varepsilon_0$ is the strain history of material

Computer program is run for the calculation of the forming force of cylindrical cup drawing process of DDQ steel sheet whose material and process data is given in Table 4.13.

**Table 4.13** Material properties and process parameters used in the analytical formulation for aluminum workpiece

| **Material Properties** | | **Process Data** | | | |
|---|---|---|---|---|---|
| C (MPa) | 547.763 | Punch radius (mm) | 50 | $\mu_{fl}$ | 0.0426 |
| $\varepsilon_0$ | 0.008755 | Die radius (mm) | 51.25 | $\mu_{\rho}$ | 0.12 |
| n | 0.26921 | Punch fillet (mm) | 7 | $P_{bhl}$ | 2.564 |
| $R_0$ | 2.16 | Die fillet (mm) | 9.5 | | |
| $R_{45}$ | 1.611 | Blank radius (mm) | 105 | | |
| $R_{90}$ | 2.665 | Blank thickness (mm) | 1 | | |

The results of the program is given in Figure 4.91 including critical forming force, four force component curves, forming force curve with respect to instantaneous drawing ratio $\beta(i)$, which is

$$\beta(i) = \frac{r_u(i)}{r_i} \tag{4.6}$$

where

$r_u(i)$ is the radius of the rim of the sheet at increment $i$

$r_i$ is the mean radius of punch ($r_p$) and die ($r_d$)

All the force values are dimensionless which means that

$$F^* = \frac{F}{2\pi r_i s_0 C} \tag{4.7}$$

where

$F$ is true force value

$r_i$ is the mean radius of punch ($r_p$) and die ($r_d$)

$s_0$ is the initial sheet thickness

$C$ is the hardening coefficient

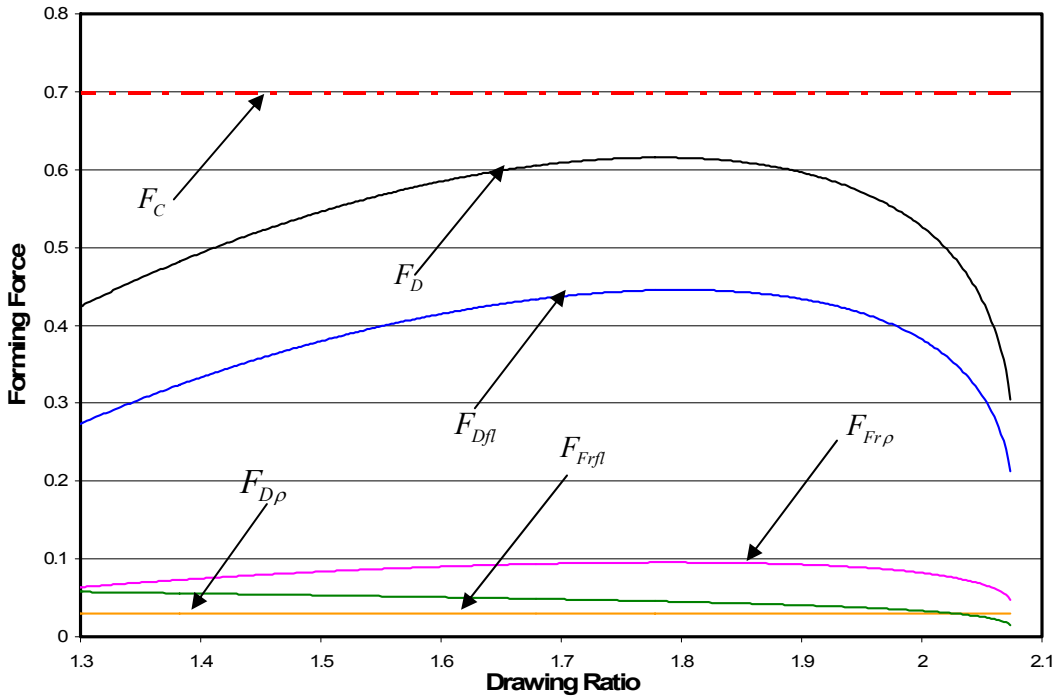


**Figure 4.91** Friction force on the flange ($F_{Frfl}$), friction force at the die fillet ($F_{Fr\rho}$), bending-rebending force at the die fillet ($F_{D\rho}$), flange deformation force ($F_{Dfl}$), critical force ($F_C$) and total forming force ($F_D$)

Same material properties and process data are also used in the simulation and punch force - displacement curve is obtained at the end of the analysis. Figure 4.92 shows initial, final, and intermediate stages of simulation and its thickness distribution. In the axisymmetrical deep drawing simulation, punch force can be taken as equal to

the forming force and it is drawn with respect to the instantaneous drawing ratio $\beta(i)$ that is defined with Eq. (4.6).

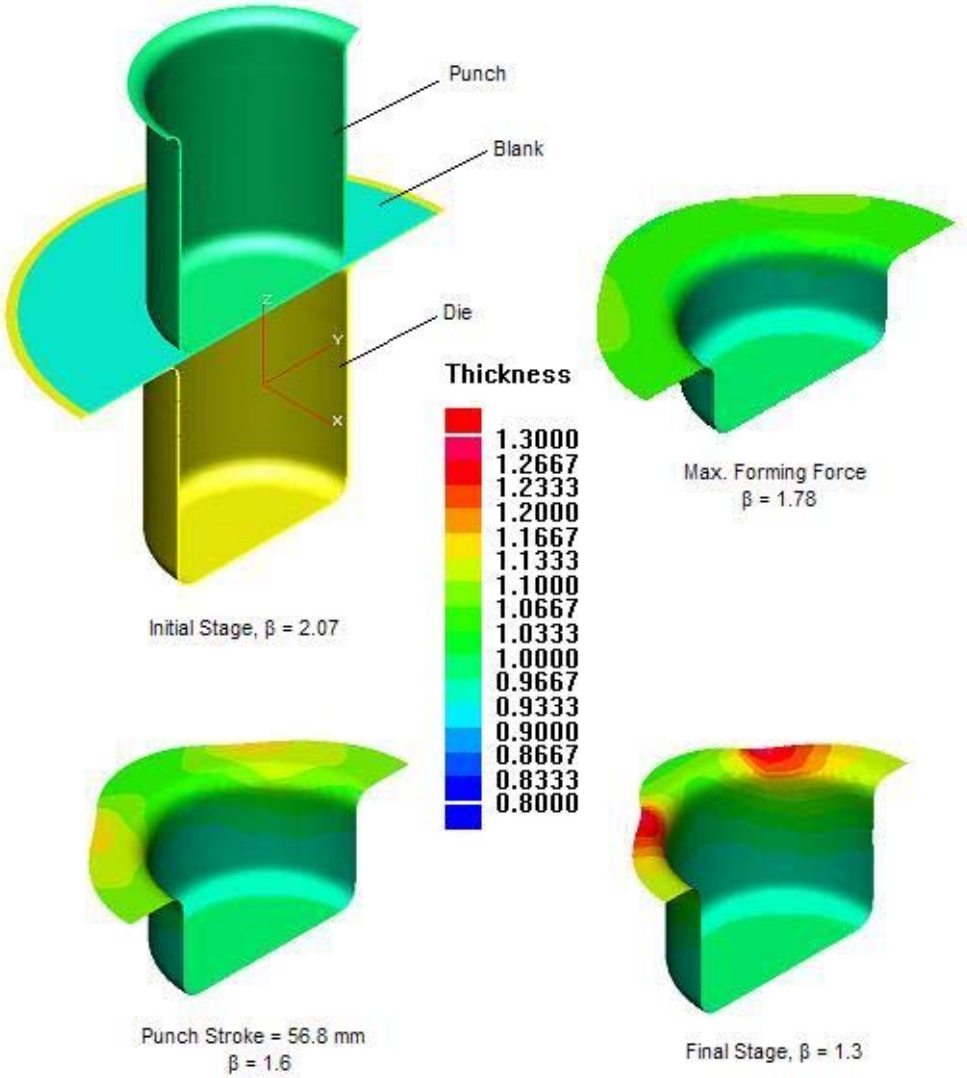


**Figure 4.92** Initial, intermediate and final stages of axisymmetrical deep drawing simulation and the thickness distribution

Figure 4.93 shows that forming force curves of analytical formulation and numerical experiment are very similar to each other almost at all regions except the initial and final increments. The source of the dissimilarity at the beginning of the process is related with the formulation of the analytical approach. It assumes that

forming force has a non-zero value at the very first increment of the process whereas in the simulation the calculation starts when the punch is stationary and has no contact with the blank, thus the forming force is zero. Besides, the simulation result is higher than the analytical formulation at the late increments of the process where the thickened flange is drawn into the die cavity. During the flange drawn-in, ironing may occur. Simulation can calculate the ironing force that increases the overall forming force but analytical formulation suggested by Ramaekers [17] is not able to consider the ironing; therefore it estimates lower forming force.

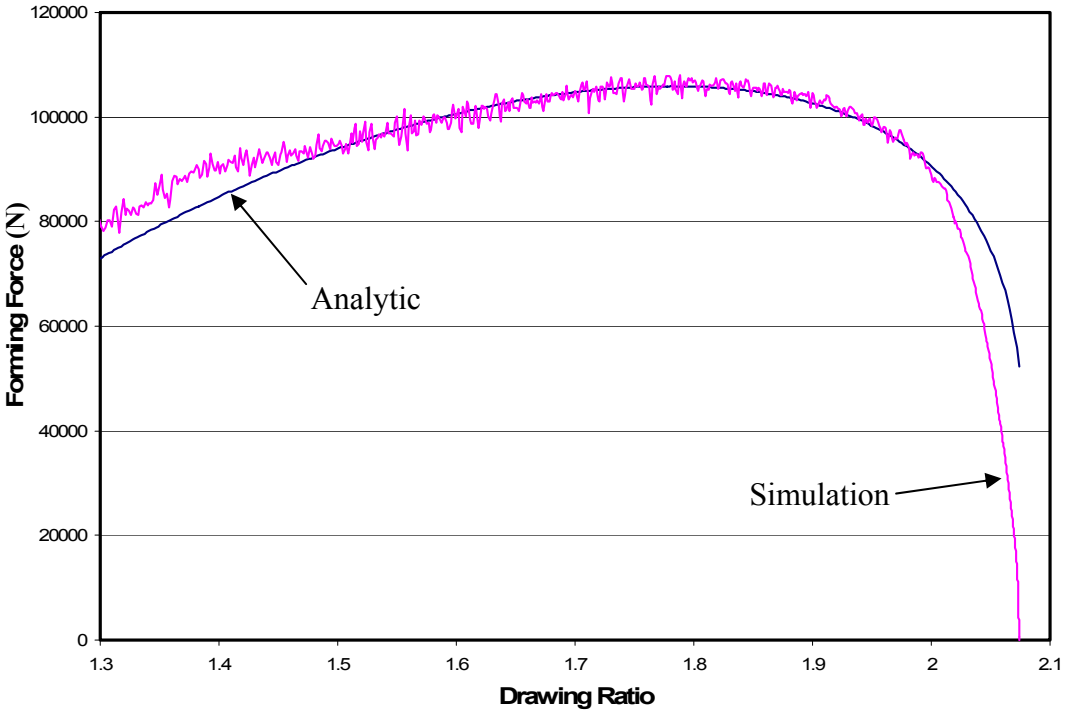


**Figure 4.93** Comparison of forming force vs. instantaneous drawing ratio of simulation and analytical formulation

Same comparison is also done for the aluminum workpiece whose radius is 90 mm All the other material properties and process parameters used in the calculation program and simulation are given in Table 4.14.

**Table 4.14** Material properties and process parameters used in the analytical formuation for aluminum workpiece

| Material Properties | | Process Data | | | |
|---|---|---|---|---|---|
| C (MPa) | 538.2 | Punch radius (mm) | 50 | $\mu_{fl}$ | 0.0096 |
| $\varepsilon_0$ | 0.00256 | Die radius (mm) | 51.25 | $\mu_p$ | 0.12 |
| n | 0.2255 | Punch fillet (mm) | 7 | $P_{bhl}$ | 1.831 |
| $R_0$ | 0.894 | Die fillet (mm) | 9.5 | | |
| $R_{45}$ | 0.611 | Blank radius (mm) | 90 | | |
| $R_{90}$ | 0.660 | Blank thickness (mm) | 1 | | |

Simulation of axisymmetrical aluminum deep drawing is performed by using identical data provided and forming force variation in the domain of drawing ratio ´between $\beta_{max}$=1.78 and $\beta_{final}$=1.3 is obtained and plotted with respect to the instantenous drawing ratio in Figure 4.94.

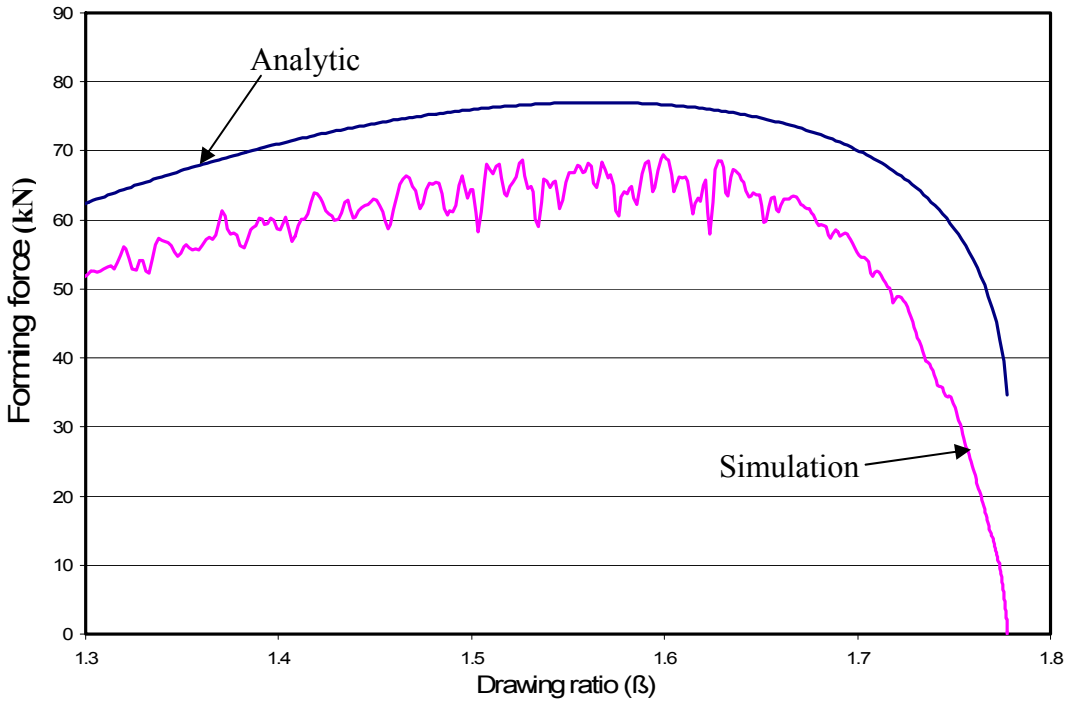


**Figure 4.94** Comparison of forming force vs. instantaneous drawing ratio of simulation and analytical formulation

Simulation presents the general behavior of the forming force curve but underestimates the value of it. This phenomenon is mentioned in Section 4.6 where the simulation is compared with experiments. Simulation using Hill 1948 yield criterion to define the plastic behavior of aluminum workpiece underestimates the contact forces and principal stresses. Comparison with analytical result also verifies the reason of poor estimations and the consequence of the usage of improper yield criteria that is explained in Section 4.6.

Additional consequences are obtained if blank holder force is increased from 50 kN to 70 kN for the same aluminum workpiece whose diameter is 105 and keeping the other variables and parameters unchanged. Figure 4.95 shows the total forming force and critical force calculated by the analytical formulation. It is seen that total forming force exceeds the critical force when the drawing ratio is equal to 1.89. This can be interpreted as excessive thinning occurs at the bottom fillet of the workpiece and process fails when the corresponding drawing ratio is achieved. The process is simulated with identical conditions. Thickness distribution at the time when the instantaneous drawing ratio is equal to 1.89 is obtained and given in Figure 4.96. As mentioned before analytical formulation shows failure since critical force is exceeded, however, as shown in the simulation result (Figure 4.96), workpiece is in the safe zone and there is admissible thinning at the bottom. This reveals another consequence of using improper yield criterion that while the force and stresses are underestimated in the simulation, thickness distribution is overestimated and results are insensitive to possible failure modes.

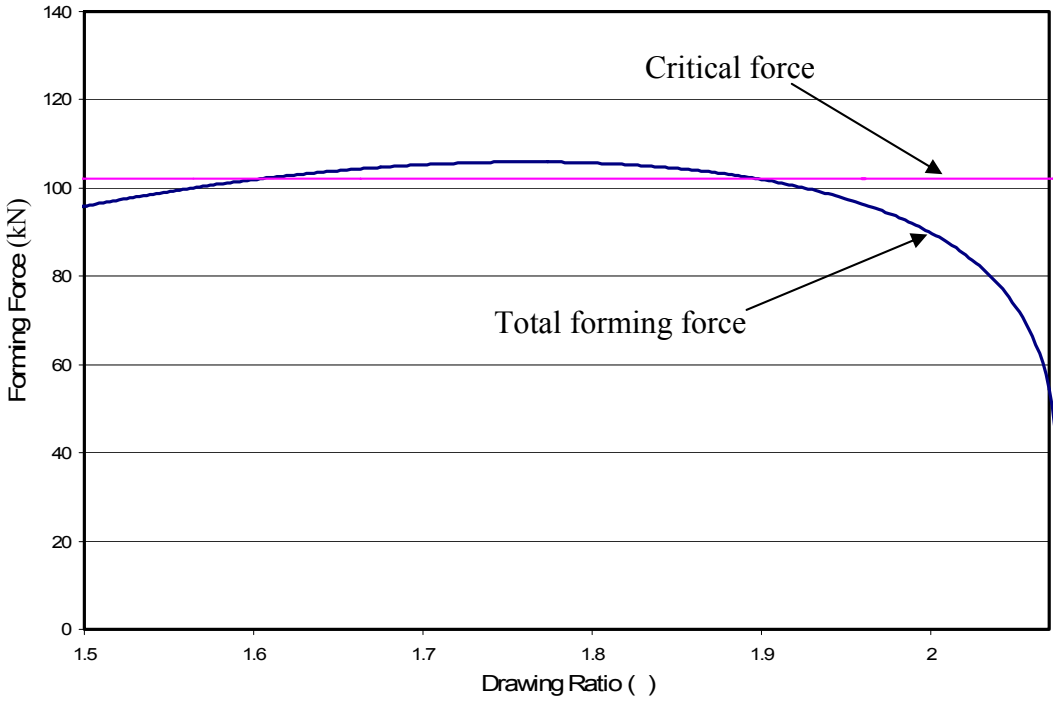


**Figure 4.95** Analytical calculation of total forming force and critical force for the deep drawing of aluminum blank

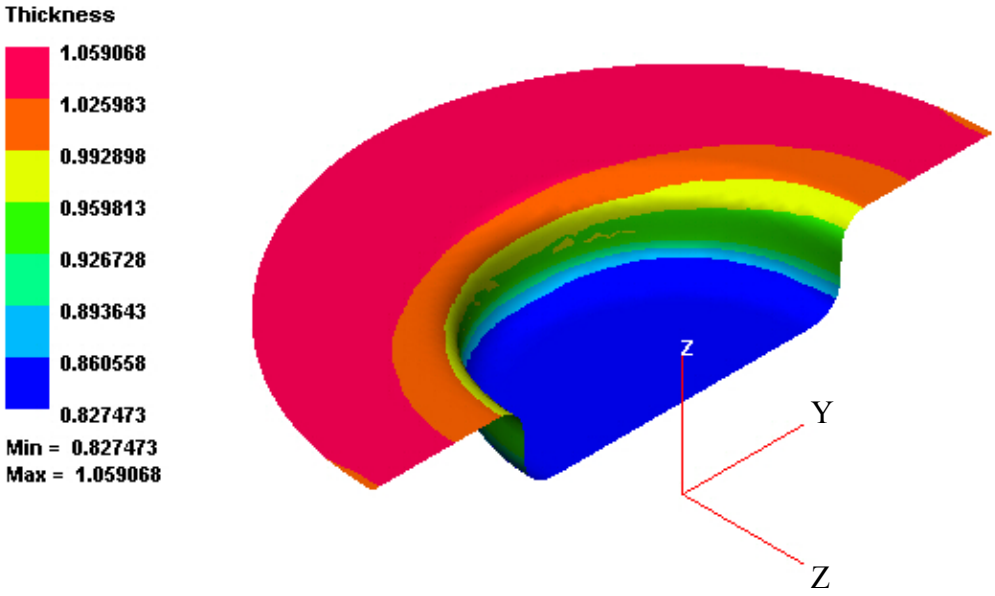


**Figure 4.96** Thickness distribution of aluminum blank at the instantaneous drawing ratio of 1.89

## 4.8 Verification of Simulation with High Pressure Metal Forming Experiment

During the last ten years, high-pressure sheet metal forming (HBU) has been developed as an alternative to the conventional deep drawing for the production of complex geometry details. In this section, the simulation of the process will be compared with the experimental result and by this way, the validation of simulation will be done as well.

Experiments were performed at the Institute of Forming Technology and Lightweight Construction (IUL), University of Dortmund, Germany with 100 MN hydroform press (Figure 4.97) including a sophisticated tool system (Figure 4.98).

Special features of this machine are the horizontally aligned frame consisting of a cast core reinforced by tensioning wires, short stroke locking cylinder, a special fluid media supply, and a tool change system that allows the part handling outside of the press frame. The fluid media supply is particularly optimized for sheet hydroforming. A filling cylinder generates a large volume flow of 30 MPa supplemented by a pressure intensifier which generates low volume flows by pressures up to 200 MPa.

The main characteristic of active fluid medium-based processes is the substitution of rigid tool components (i.e. punch or die) by a fluid. Instead of a punch, a pressurized fluid medium is used in HBU to force the sheet material taking the shape of the die. Figure 4.99 shows HBU tool system with characteristic components:

- Supply plate which closes the cavity by a sealing
- Die
- Multi-point blank holder system for material flow control in the flange area

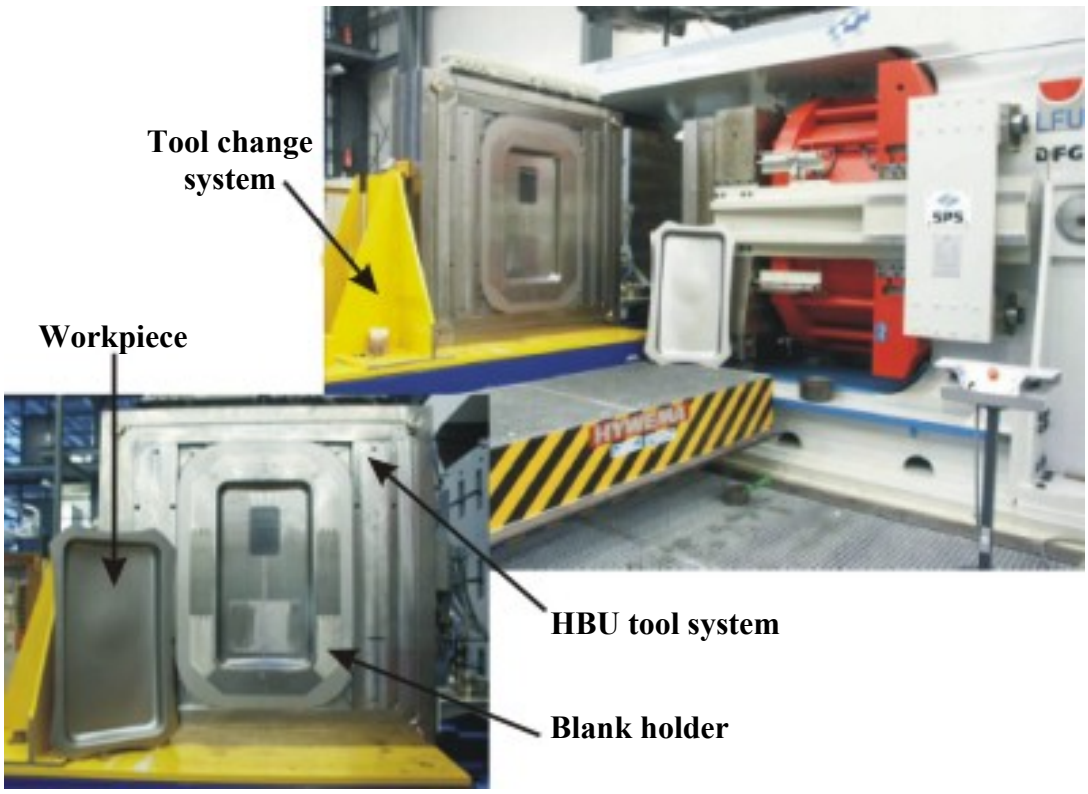


**Figure 4.97** 100MN Hydroform Press

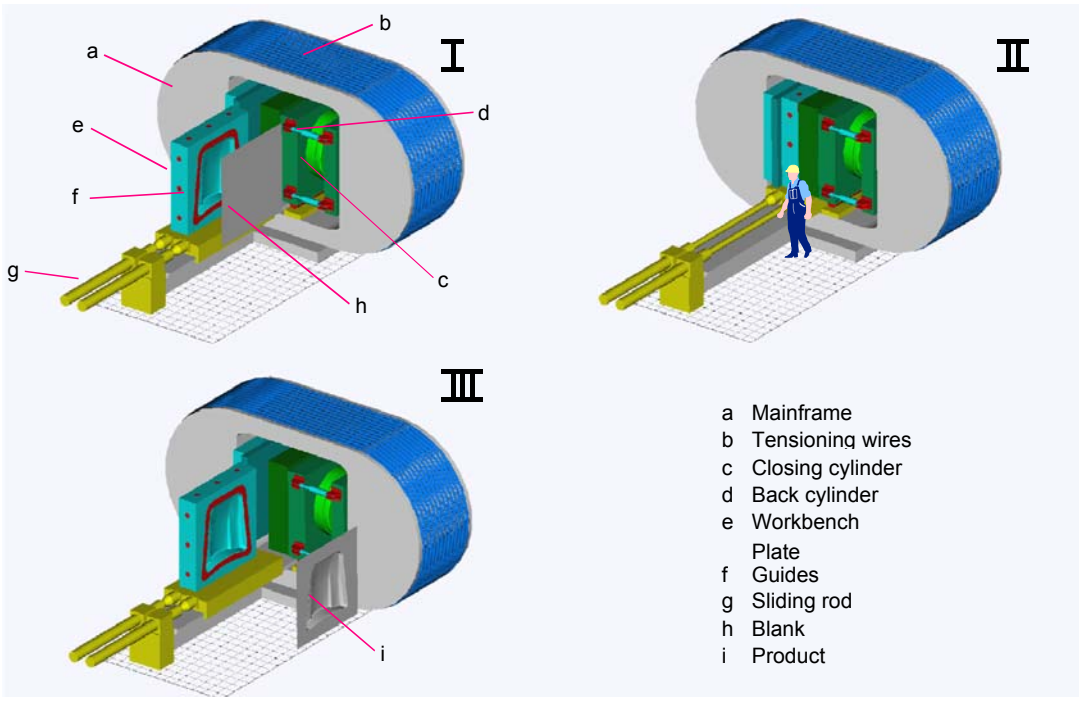


**Figure 4.98** Hydroform press and sophisticated tool system

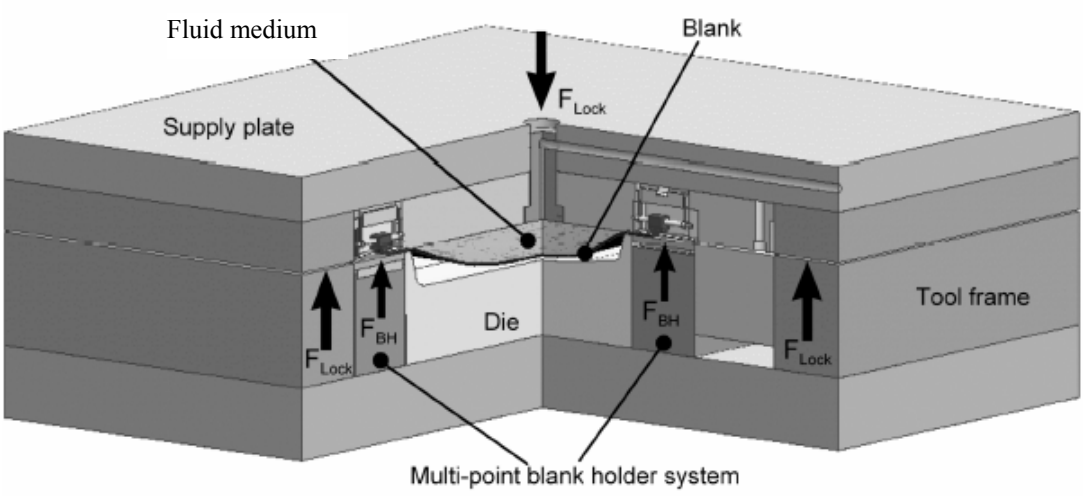


**Figure 4.99** HBU tool system with characteristic components

After applying the necessary locking force, the process is initiated by a pump or a pressure intensifier, which generate the required volume flow. Following a free formstage, the final shape is reached by the contact of the sheet with the die during a form-based stage and by calibration.

A multi point blank holder system, consisting of 10 membrane short stroke cylinders, can effectively control the local and temporal distribution of the surface pressure, and consequently the material flow in the flange area. Segmented blank holder plates transmit the blank holder force on the sheet metal flange. Each membrane short stroke cylinder is controlled by a separate proportional valve.

Figure 4.100 shows the finite element model of multi point blank holder, binder, blank, and die having complex geometry (forming element). HBU tools are simplified as idealized, rigid body. Multi point blank holder pressure, area and corresponding forces are given in Table 4.15. The blank is defined as deformable body and undeformed blank dimensions are given in Table 4.16. The material behavior of the blank is described by the flow condition of Hill (1948) and modeled by Belytscho-Tsay quad shell elements having 5 integration points. Material data and piecewise hardening curve are also listed in Table 4.16.

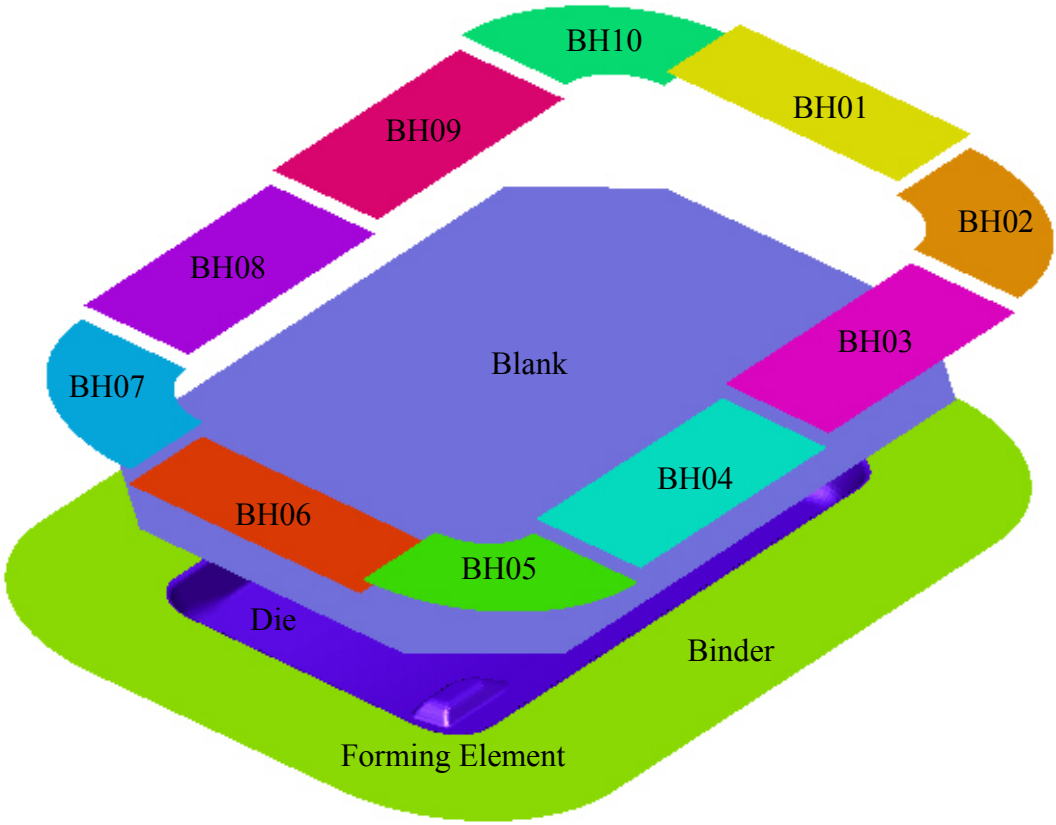


**Figure 4.100** Finite element model of high pressure sheet metal forming

**Table 4.15** Pressure, area and corresponding force of multi point blank holder

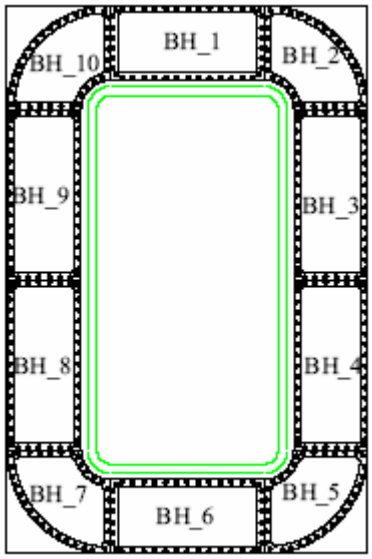


| Segment | Pressure (MPa) | Area ($mm^2$) | Force (N) |
|---|---|---|---|
| BH_1 | 4.5 | 53320 | 239940 |
| BH_2 | 1.5 | 39660 | 59490 |
| BH_3 | 4.5 | 61031 | 274640 |
| BH_4 | 4.5 | 61031 | 274640 |
| BH_5 | 1.5 | 39660 | 59490 |
| BH_6 | 4.5 | 53320 | 239940 |
| BH_7 | 1.5 | 39660 | 59490 |
| BH_8 | 4.5 | 61031 | 274640 |
| BH_9 | 4.5 | 61031 | 274640 |
| BH_10 | 1.5 | 39660 | 59490 |

**Table 4.16** Dimensions and material properties of DC 04 low carbon steel workpiece whose thickness is 1mm and rolling direction is (1,0,0)

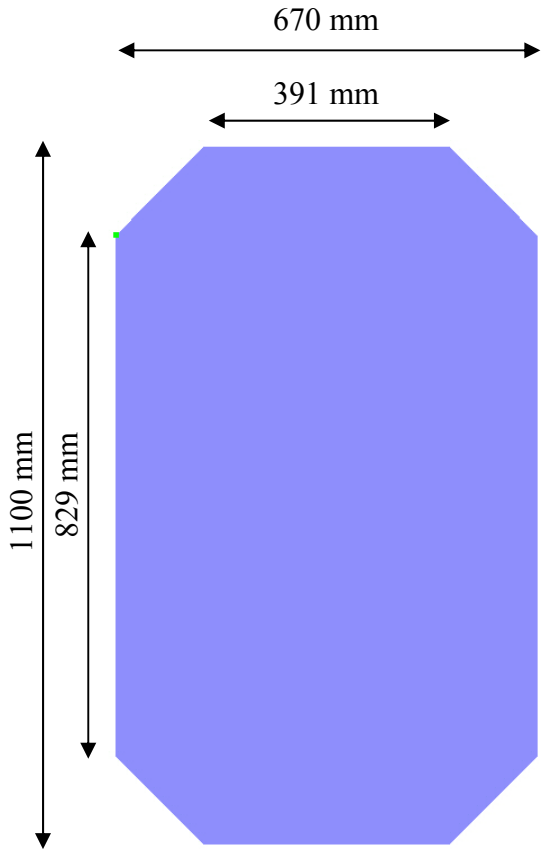


| **Material: DC04 low carbon steel** | | | |
|---|---|---|---|
| $R_0$ | 1.494 | E (GPa) | 206 |
| $R_{45}$ | 1.612 | ν | 0.33 |
| $R_{90}$ | 2.07 | ρ(kg/m$^3$) | 7800 |
| **Piecewise linear hardening curve** | | | |
| **Strain** | | **Stress (MPa)** | |
| 0 | | 134 | |
| 0.05 | | 238 | |
| 0.1 | | 287 | |
| 0.15 | | 319 | |
| 0.3 | | 377 | |
| 0.4 | | 401 | |
| 0.5 | | 421 | |
| 0.6 | | 437 | |
| 0.7 | | 451 | |
| 0.8 | | 463 | |

Coulomb friction law and friction coefficient of 0.03 between contact surfaces are used. In addition, adaptive meshing and mass scaling numerical tools are properly used where necessary.

Figure 4.101 shows the thickness contour result obtained by simulation. The thinning zones are four corners of the workpiece and sharp edges of the forming elements. The minimum sheet thickness is observed on the bottom corner of the forming element, which exposed to about 25% thinning.

The charts in the Figure 4.102 and Figure 4.103 validates the simulation results by comparing them with the experimental thickness distributions measured by micrometer along the horizontal (Cut 1) and vertical (Cut 2) section cuts.

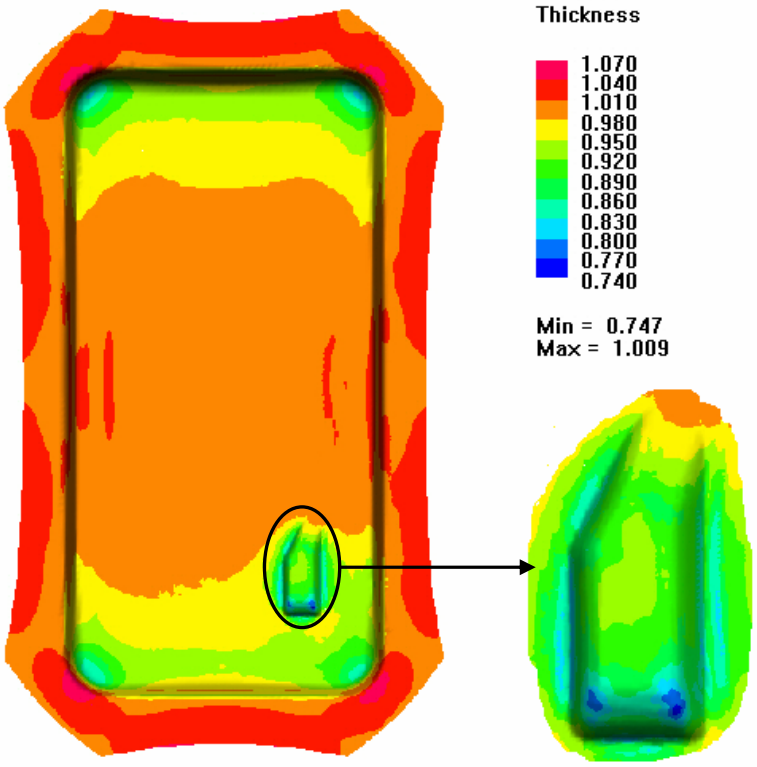


**Figure 4.101** Thickness contour of whole blank and the detail of forming element

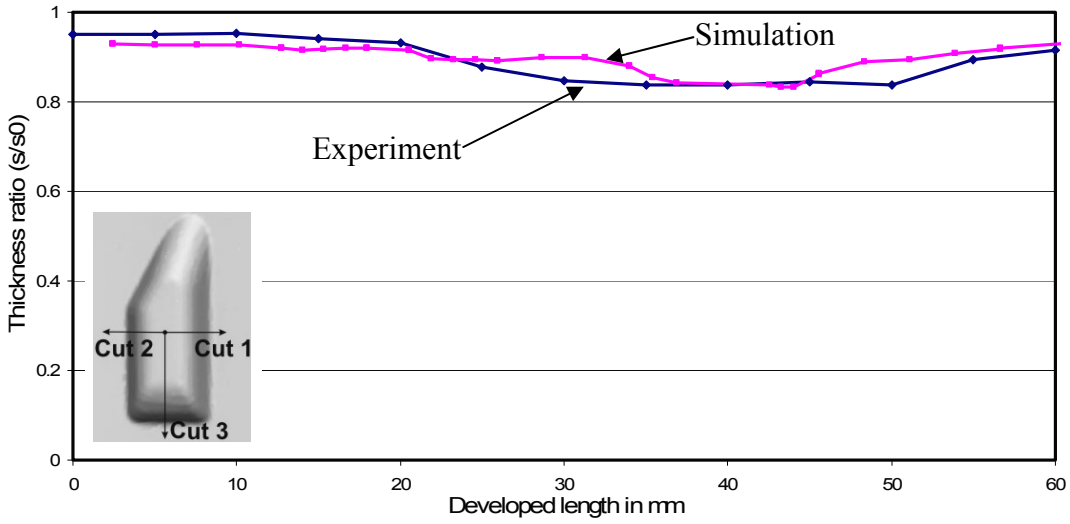


**Figure 4.102** Comparison of simulation and experiment (Cut 1)

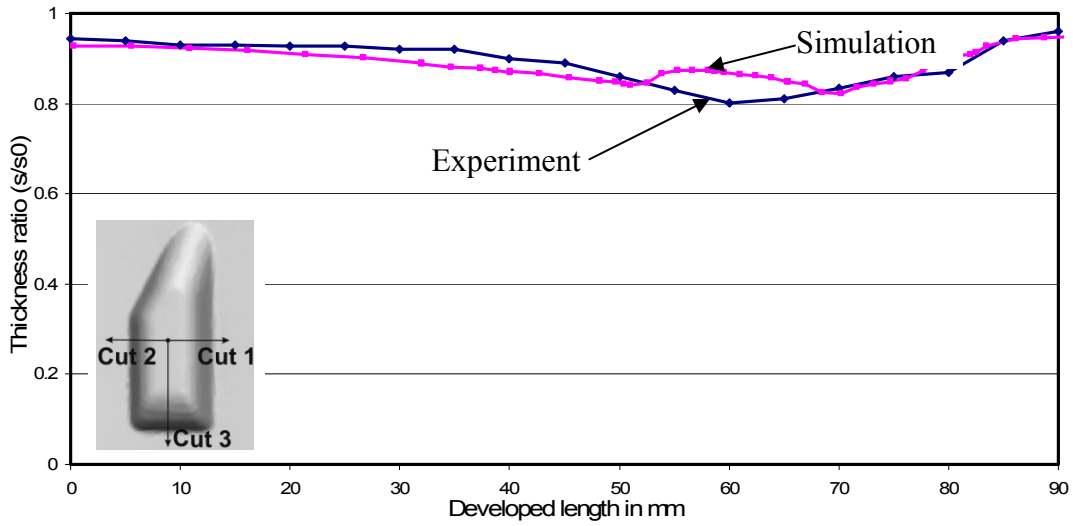


**Figure 4.103** Comparison of simulation and experiment (Cut 3)

Recent studies show that the orientation of blank relative to the die cavity has influence on the forming limit of sheet materials [20]. To test the capability of the finite element simulation, different variations of blank orientation are simulated. Table 4.17 lists six different orientations that are both simulated and experimentally drawn. Blank 1 is positioned centrically, Blank 2 - Blank 5 are shifted about 10 mm along the symmetric axes, and Blank 6 has a superposition of vertical and horizontal shift about 10 mm. Comparisons of horizontal and vertical section cuts along the forming elements between the differently oriented blanks are shown in Figure 4.102. Minimum sheet thicknesses in the area of forming element of each simulation with different blank orientations are illustrated in Figure 4.103. The simulation results are coherent with experimental findings. Blank 2 and blank 6, which are shifted in left direction, feature the least thinning along the right sidewall of the forming element.

This part of the study shows that explicit finite element code is eligible enough to simulate the fluid medium assisted sheet metal forming process reliably, if optimum parameters determined in the early sections of chapter 4 are used properly.

**Table 4.17** Variation of blank orientation relative to the initial position

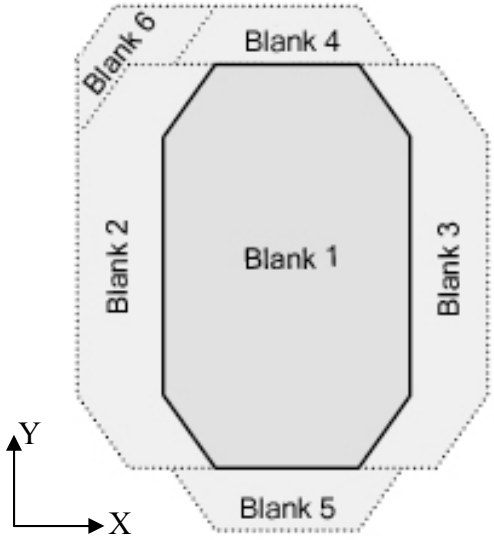


| | Shifting towards | |
|---|---|---|
| | **X direction** | **Y direction** |
| **Blank 1** | 0 | 0 |
| **Blank 2** | -10 | 0 |
| **Blank 3** | 10 | 0 |
| **Blank 4** | 0 | 10 |
| **Blank 5** | 0 | -10 |
| **Blank 6** | -10 | 10 |

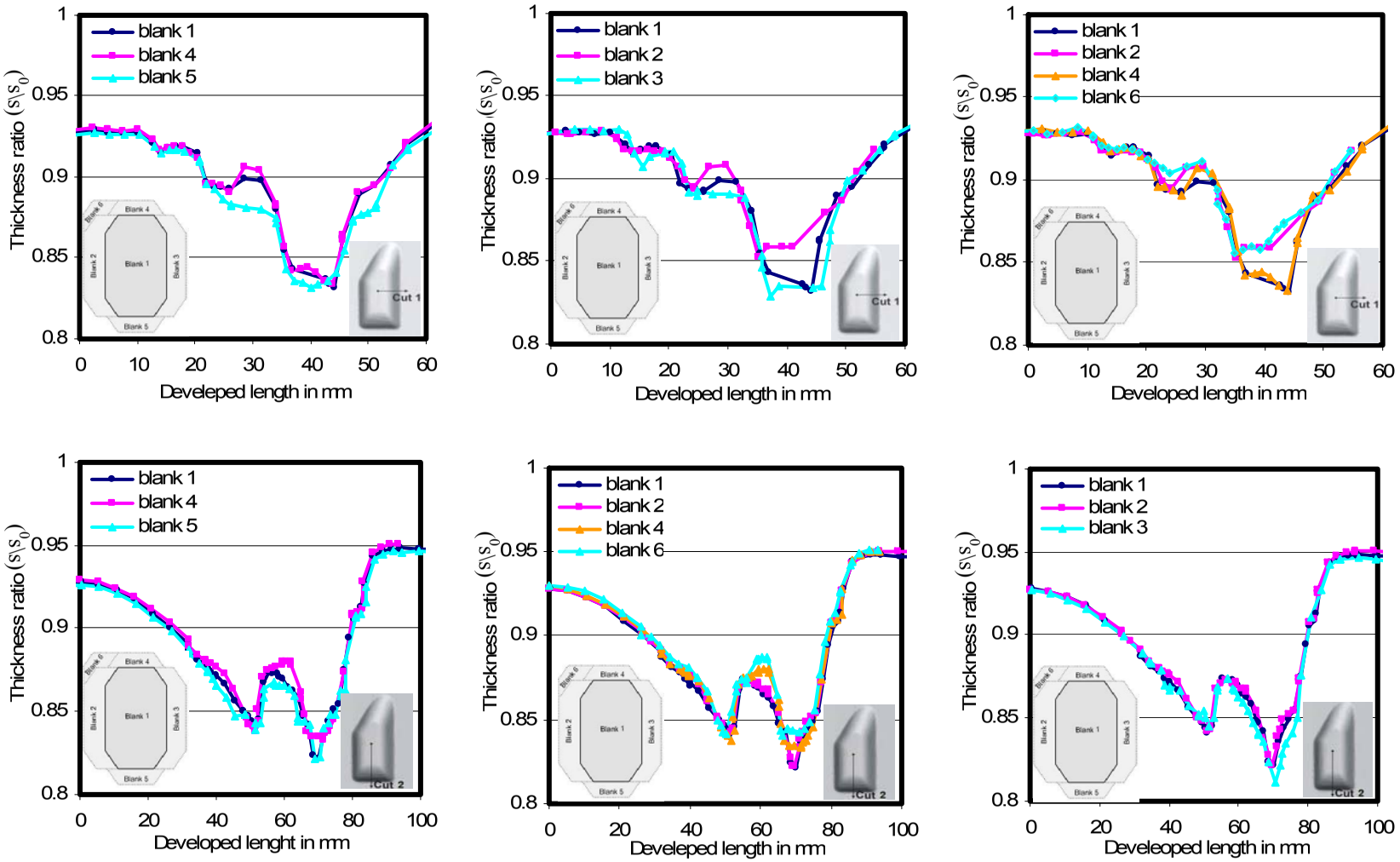


**Figure 4.104** Comparison of the thickness variation of differently oriented blanks

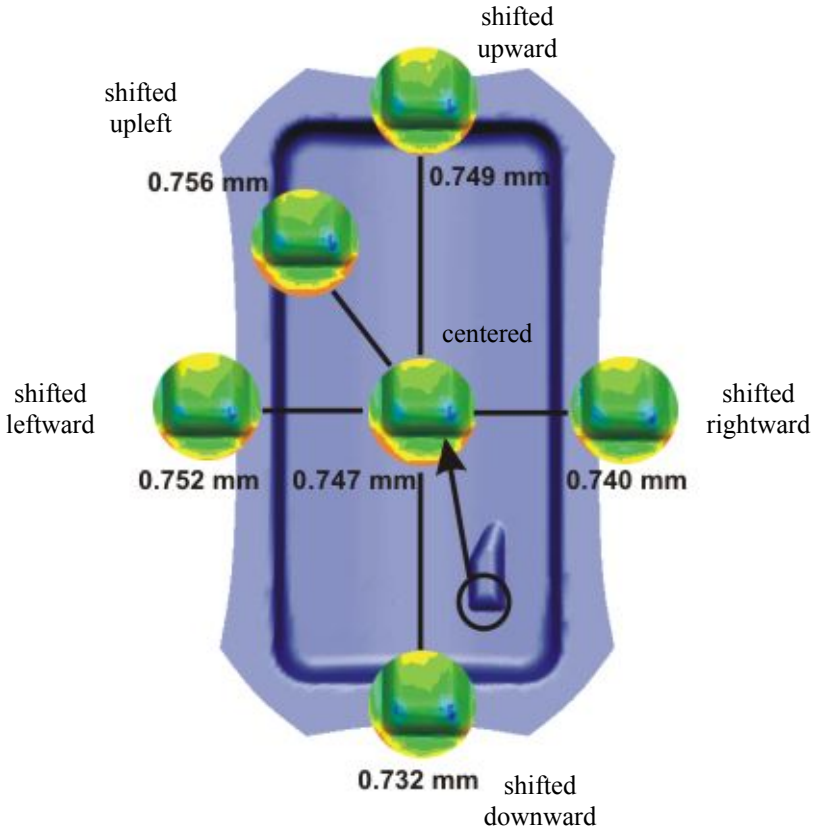


**Figure 4.105** Minimum sheet thickness in the area of the forming element for different oriented blanks

# CHAPTER 5

# ASSESSMENT OF SHEET METAL FORMING PROCESSES

## 5.1 Introduction

In this chapter, assessment of three sheet metal forming processes, conventional deep drawing (DD), hydro-mechanical deep drawing (aquadrawing), and high-pressure metal forming (HBU) will be done by performing systematic numerical experiments. Validation of numerical experiments and optimization of parameters were already done in Chapter 4 and theory of FE code used in the numerical experiment was studied in Chapter 3. Furthermore, the competing three sheet metal forming processes were described in Chapter 2.

As the material, stainless steel St14 is used within the assessment study and elasto-plastic material model with orthotropic Hill 48 isotropic hardening law is used in the simulations to model the workpiece having 1 mm thickness. Hardening and FLD (forming limit Diagram) curves are defined by data points and together with the orthotropic anisotropy coefficients; they are taken from the element library of the FE software. Those are also given in Appendix D, listed in Tables D.1 and D.2.

Belytschko-Tsay shell elements with 5 integration points using Gauss integration rule along the thickness direction are used in the simulations. Average element size of deformable body mesh is between 3 to 5 mm and adaptive mesh with refinement level 2 is used in the all simulations of assessment study. In addition, also mass scaling option is utilized and one-fourth of initial average element size is used as the corresponding reference element size for mass scaling.

Die, punch, binder, and blank holder are modeled with shell elements as rigid body. Coulomb friction model is used between the contact bodies and friction coefficient is set to 0.05 on all surfaces.

## 5.2 Geometry Spectrum

Analysis is based on various cross-section geometries of deep drawn parts. 6 different cross-sections are used in the geometry spectrum (Figure 5.1). The spectrum starts with circular cross-section and continues with ellipses whose major / minor diameters ratios are 1.5 and 2 respectively. Fourth cross-section in the geometry spectrum is rectangle whose characteristic dimensions (long and short edge lengths) ratio is the same as the previous cross section (150 mm / 75 mm = 2). Fifth and sixth geometries are square cross-sections whose edge dimensions are equal to the diameter of circular cross section while they have 25 mm and 37.5 mm corner fillet radii respectively.

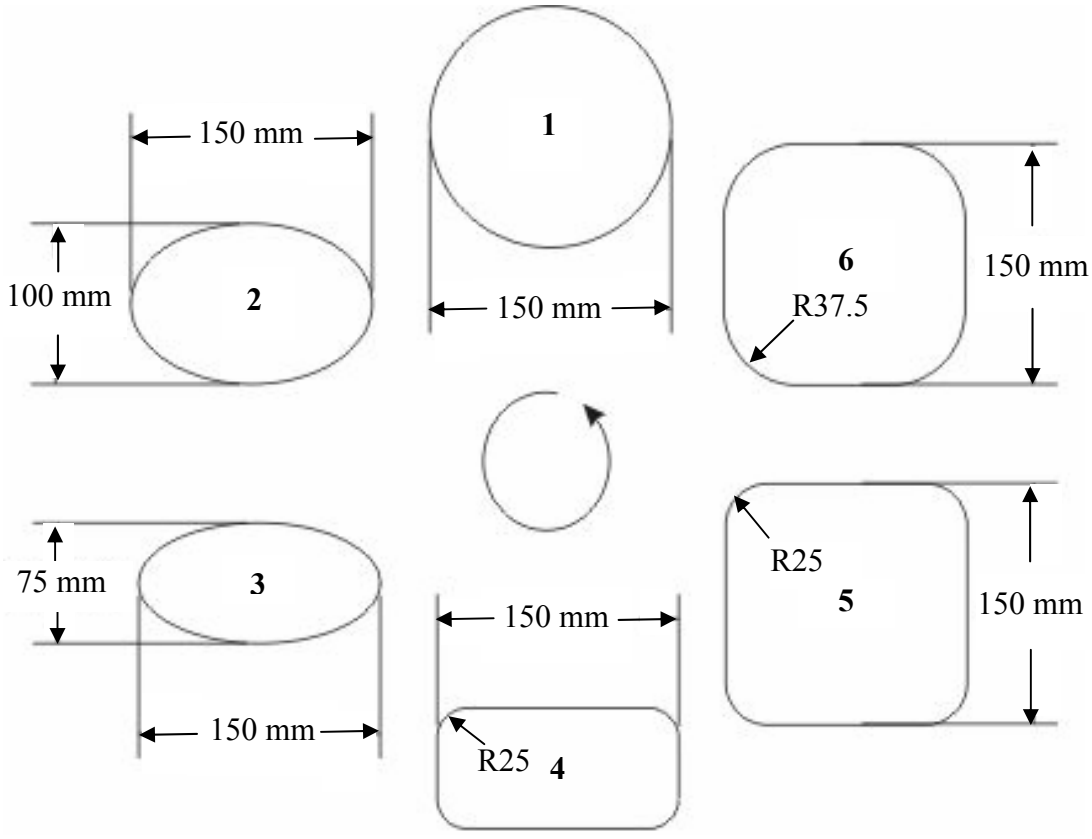


**Figure 5.1** Geometry spectrum

All the dies used in the assessment study are cylindrical or prismatic cups. Each die normally has 15 mm die inlet fillet and die cavity fillet. In some of the critical cross-sections, also cavity fillet parameter is varied to observe the effect of the dimension of fillet on the formability of sheet metal.

Furthermore, the depth of the cylindrical die varies within each cross-section according to the three reference equivalent drawing ratios ($\beta_{eq}$=1.75, 2.00, and 2.25) which is defined by

$$\beta_{eq} = \frac{A_0}{A_i} \tag{5.1}$$

where

$A_0$ is the area of undeformed blank

$A_i$ is mean area of punch and die cavity cross-sections

The depth of each die is calculated using volume constancy by

$$h_i = \frac{A_i - A_0 - A_f}{C_0} \tag{5.2}$$

where

$h_i$ is the depth of die

$C_0$ is mean circumference of punch and die

While calculating the depth of the die, it is considered that instead of fully drawing the material into the die cavity, leaving some amount of blank on the binder is aimed due to the non-uniform draw-in of material at different directions (anisotropy effect) as well as the possibility of extreme wrinkles.

Since each process may have its own process setup and process parameters, it is aimed to find out the most suitable variables such as undeformed blank dimension, blank holder force, punch velocity and fluid pressure for each process working on

each tool geometry. Therefore, those parameters may be different within the group of simulations. Only the tool geometry and lubrication conditions are kept constant throughout the whole geometry spectrum during the assessment of the processes. Undeformed blank area is also calculated by Eq. (1) with respect to the corresponding equivalent drawing ratio. This provides three different blank dimensions for each cross-section of the geometry spectrum to be simulated. It is known that the dimension and geometry of the undeformed blank highly influences the formability of the sheet metals [21, 22].

Therefore, further investigation was done on the blank geometry optimization to avoid the underestimation of formability of sheet metal having a specific surface area under specific conditions. It was found that for circular and elliptic cross-section, circular and elliptic blank geometries should be used respectively. For the rectangular and square cross-sections, rectangular and square blank geometries having corners trimmed should be preferred for realistic results and fair comparison of the processes. The detailed information about the blank geometries used for each cross section should be found in relevant sections and all calculations are given in Appendix E.

The evaluation criteria followed during the assessment study, are based on the comparisons of thickness distributions on various section cuts, forming radii of workpieces.

## 5.3 Geometry I: Circular Cross-section

The first cross-section of the geometry spectrum is a circle whose dimensions are given in Figure 5.2. Three different depths of die cavity are present whose dimensions are dependent to the equivalent drawing ratio. Tool reference dimensions given in Table 5.1, are used for building punch and die meshes in the assessment simulations. These are ±0.6 mm offset from the tool reference and the

clearance between the die and punch is 1.2 mm, which is 20% more than the initial blank thickness.

Optimum blank geometry for circular cross-section is a circle. Undeformed blank dimensions for each variant of circular cross-section are given in Table 5.1. While calculating the depth of the die, instead of fully drawing the material into the die cavity, it is aimed to leave 20 mm flange on the binder because of the non-uniform draw-in of material at different directions (anisotropy effect). All calculations about the blank dimensions and depth of dies are given in Appendix E.1.

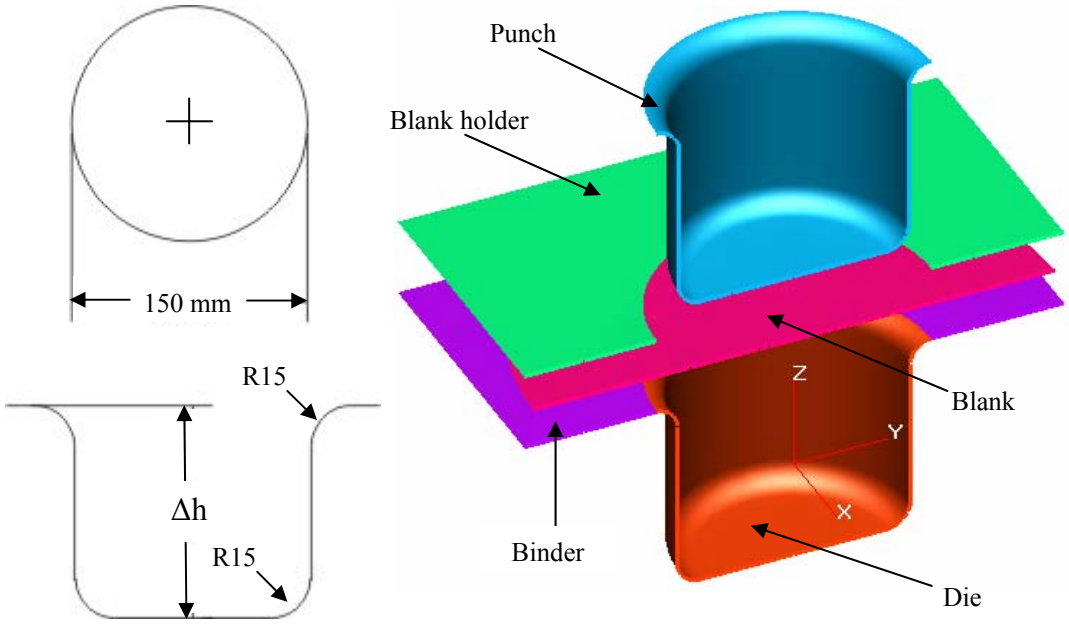


**Figure 5.2** Circular cross-section of geometry spectrum and tool geometry

Figure 5.2 shows the tool setup of conventional deep drawing process (DD). Binder, die, blank holder, and punch are shown explicitly. At each variant, only depth of the die and height of the punch are varied according to the corresponding equivalent drawing ratio. These variations in the dimensions are tabulated in Table 5.1.

**Table 5.1** Circular cross-section tool reference and blank dimensions

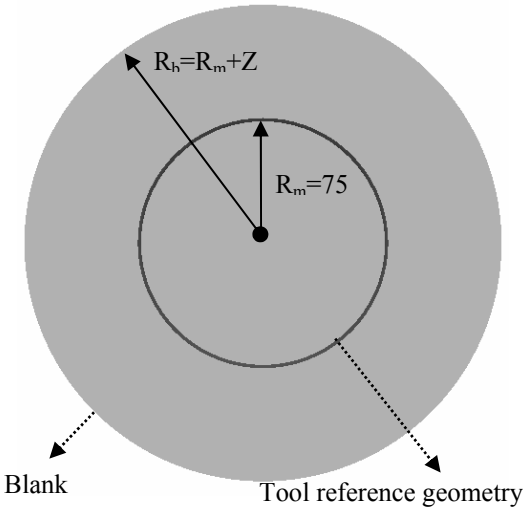


| Tool Reference Dimensions | |
|---|---|
| Mean Radius ($R_m$) | 75 mm |
| Mean Area ($A_m$) | 17671.5 mm |
| Mean Circumference ($C_m$) | 471.2 mm |

| Blank Dimensions and Δh values | | | | | |
|---|---|---|---|---|---|
| Variant | $\beta_{eq}$ | $A_b$ (mm²) | Z (mm) | $R_b$ (mm) | Δh (mm) |
| 1 | 1.75 | 54119 | 56.25 | 131.25 | 54.68 |
| 2 | 2.00 | 70686 | 75.00 | 150.00 | 89.83 |
| 3 | 2.25 | 89462 | 93.75 | 168.75 | 129.68 |

For conventional deep drawing (DD), three variants are separately simulated and successful results are obtained for each of them. Since the results are very close to each other and there is no serious comment to state individually, only the results obtained from the most severe case (variant 3) are shown and discussed.

Figure 5.3 shows the thickness contour of workpiece drawn into circular cross-section, 129.68 mm depth die (variant 3) with conventional deep drawing process. Average thinning between 5% and 10% is dominant on the bottom and lateral surfaces, which are quite satisfactory for the process.

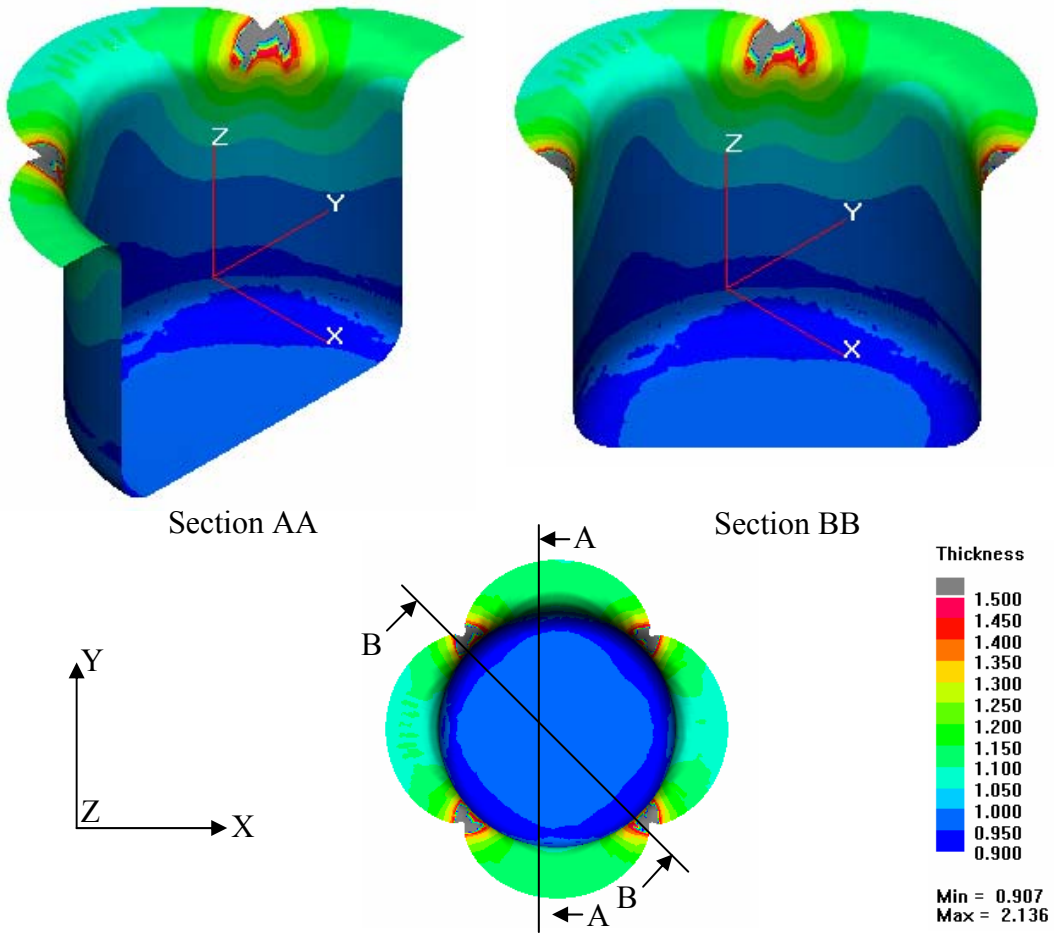


**Figure 5.3** Thickness contour of workpiece manufactured with conventional deep drawing - variant 3

The part of the blank, which contacts with the die upper fillet is not supported by a blank holder at any time. Furthermore, due to non-uniform drawn-in of material at each direction, at the directions where the material resists less to deform in thickness (45° away from the rolling direction where the R value is less), excessive thickening and folding occurs when the material is drawn up to the upper die fillet (shown in Figure 5.3 with gray color). However, it is not a failure of the process since the material at the flange is usually scrapped and trimmed off. Thus, conventional deep drawing successfully accomplishes variant 3 of circular cross-section.

Figure 5.4 represents the tool setup of hydro-mechanical deep drawing (aquadrawing). In this process, die cavity is filled with fluid medium. As the punch

penetrates, fluid medium forces the blank to take the form of the die. Fluid medium exerts counter pressure acting on the lower surface of blank. It not only provides the material to take the form of the tool system but also eliminates the negative friction effects on the die and binder surfaces. Fluid medium in the die cavity avoids the workpiece contacting with the die surface and in addition, some of the fluid can flow out between the blank and binder. This terminates the friction on the flange, which increases the maximum admissible drawing ratio.

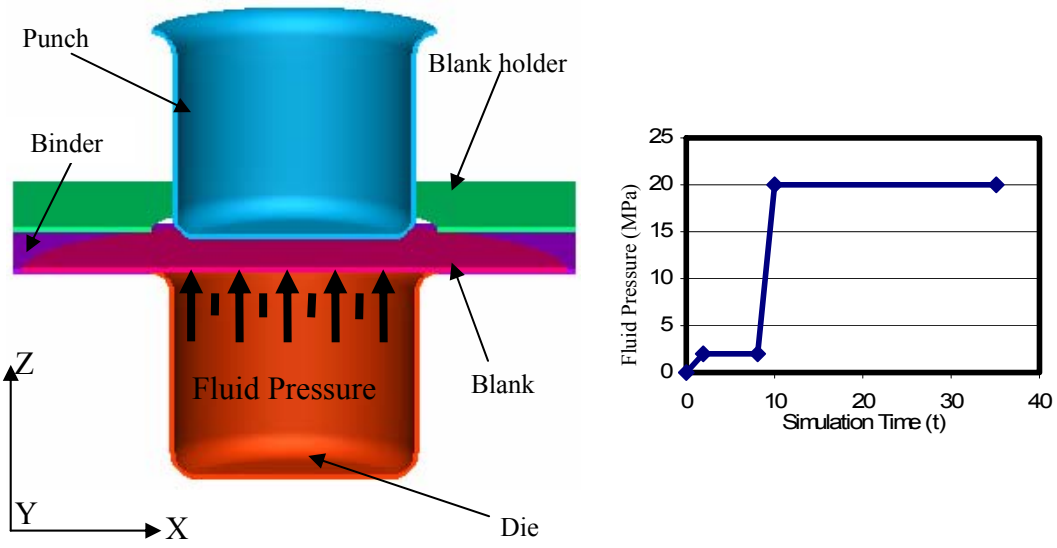


**Figure 5.4** Hydro-mechanical deep drawing (aquadrawing) process setup and counter pressure exerted by fluid on to the workpiece

Friction has not always a negative effect on the formability of the sheet metals. Most common failure mode of sheet metal forming processes is the tearing either at the bottom fillet or on the wall of the workpiece. Friction forces on the surface of the punch lead to flange material flowing into the die cavity instead of stretching the already drawn-in material. In hydro-mechanical deep drawing process, fluid medium exerts high pressure up to 20 MPa on to the lower surface of blank and make it to stick on the punch surface, thus increases the friction forces. Figure 5.5 compares the thickness contour of workpieces, manufactured with hydro-mechanical deep drawing (aquadrawing) and conventional deep drawing process. It

is seen that the amount of average thinning of hydro-mechanically drawn work piece is almost 50% less than that of conventionally drawn part. Additionally maximum thinning in the conventionally drawn workpiece occurs at the bottom fillet; however, the thickness distribution at the bottom fillet of hydro-mechanically drawn workpiece is the same as the thickness distribution at the wall of the workpiece.

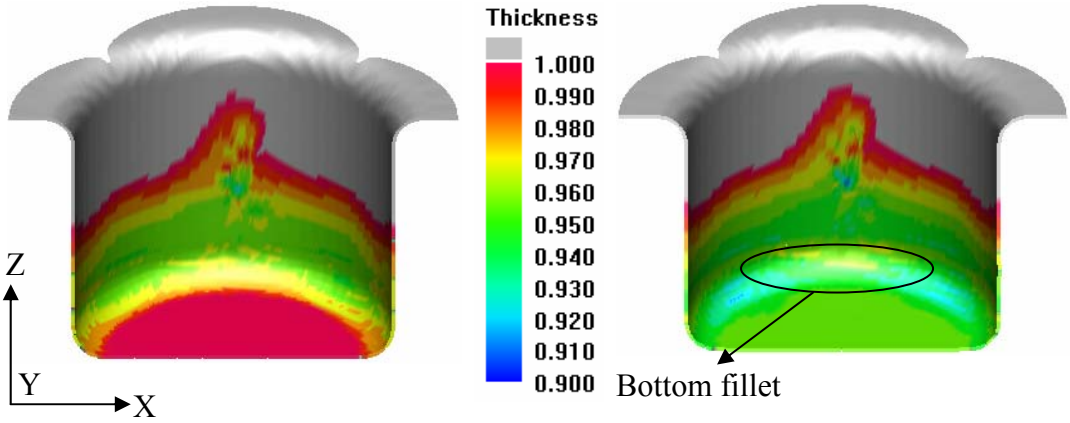


**Figure 5.5** Comparison of workpieces manufactured by hydro-mechanical deep drawing process (aquadrawing) and conventional deep drawing process (DD)

Thickness distributions of the products of two process along the section AA (z=0 plane, shown in Figure 5.3) with respect to the curvilinear coordinate are given in Figure 5.6. Both products satisfy allowable thinning which is about 30%, very easily. However, especially at the die bottom, hydro-mechanically drawn workpiece exposes less thinning. This concludes that products having higher drawing ratios can be produced much more easily with hydro-mechanical deep drawing.

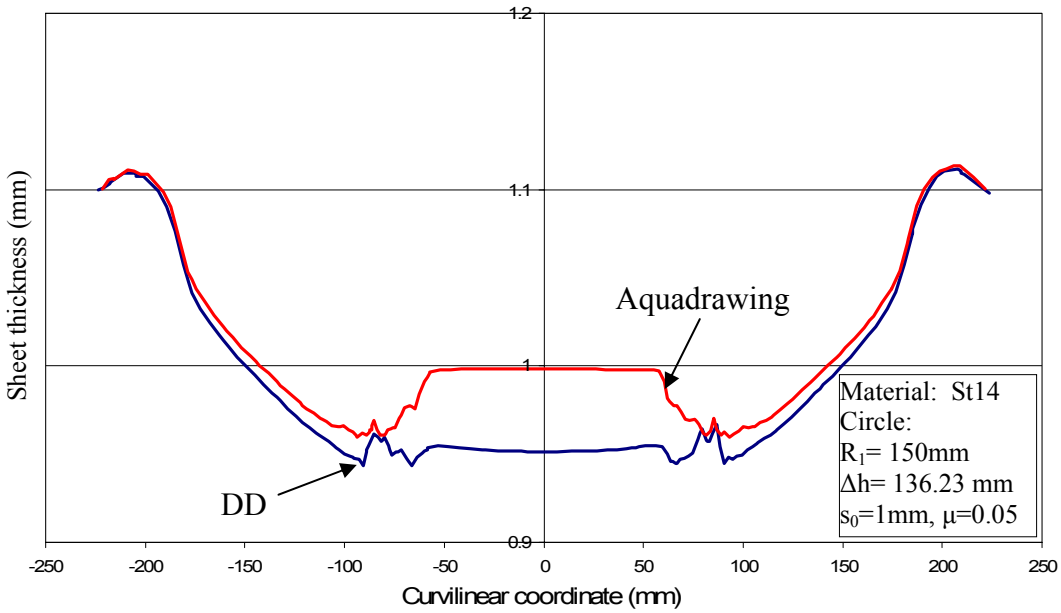


**Figure 5.6** Thickness distribution with respect to the curvilinear coordinate along the section AA of workpieces manufactured by conventional deep drawing (DD) and hydro-mechanical deep drawing (aquadrawing)

Third process in the assessment study is high-pressure sheet metal forming (HBU). It is discussed separately because of the modification in the tool setup. Punch is replaced with fluid medium that exerts forming pressure on to the upper surface of the blank (Figure 5.7). The path and history of blank deformation is also significantly different from the other two competing processes. Process starts with low pressure to bulge the blank towards the die cavity and it continues until the blank hits the die bottom. After that, higher fluid pressure (up to 40 MPa) is required for the calibration of blank to fill the small curvatures belonging to the die geometry.

All variants of circular cross-section for high-pressure sheet metal forming (HBU) are represented to identify the formability limits of the process. Figures 5.7, 5.8 and 5.9 show the initial and final stages of HBU process for variants 1, 2 and 3 respectively. Since deformation starts with the bulging of the blank at the high pressure sheet metal forming (HBU), maximum thinning occurs at the center of the

unsupported region of the blank at the early stages. In Figure 5.7, it is shown that variant 1 can be produced with maximum 10 percent thinning.

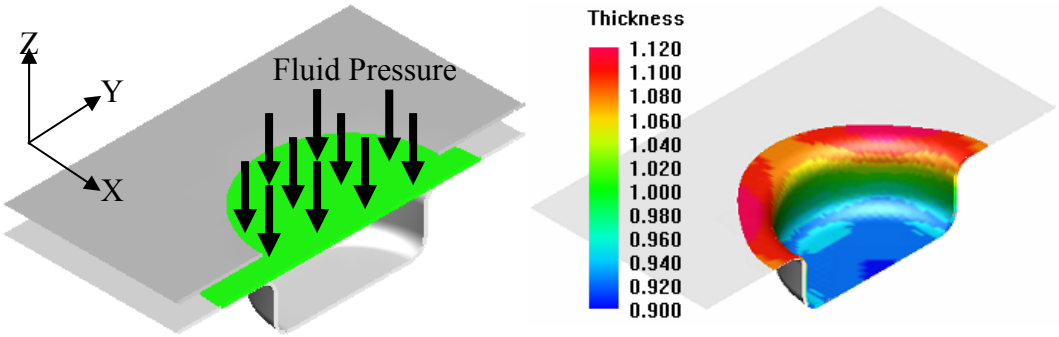


**Figure 5.7** High pressure sheet metal forming process, variant 1

Variant 2 whose depth (Δh) is 89.23 mm is simulated with high pressure sheet metal forming (HBU) and final thickness contour is shown in Figure 5.8. Maximum thinning in the workpiece is about 16 % and it is at the bottom of the workpiece. Curvatures at the die bottom (die cavity fillets) are perfectly filled with material and the workpiece takes the exact shape of the tool. According to that, die cavity fillet is not dominant in the forming limitations of circular cross-section cylindrical workpieces with high pressure sheet metal forming. Figure 5.9, which represents the variant 3, reveals that depth of the die and initial blank size are the key issues to be considered in the forming of circular cross-section workpieces with high pressure metal forming.

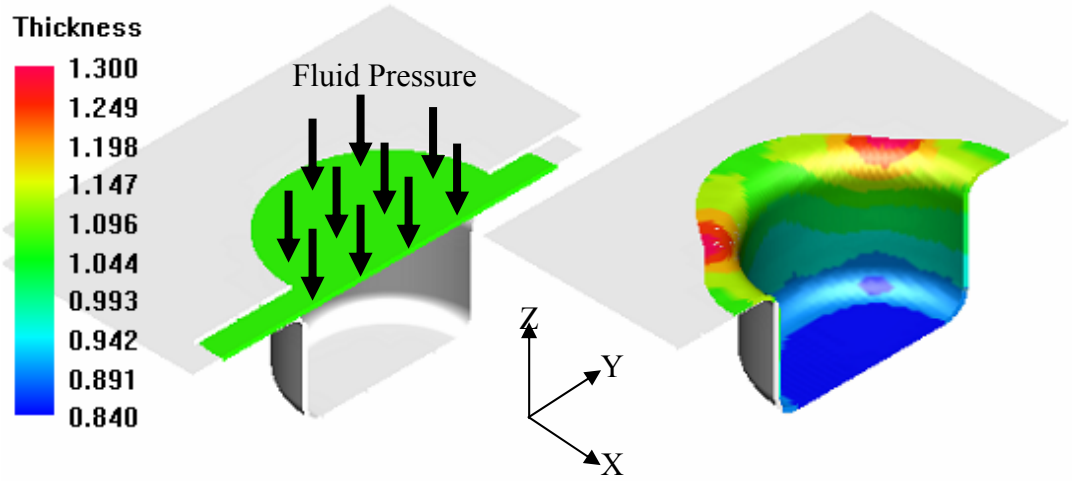


**Figure 5.8** High pressure sheet metal forming process, variant 2

In variant 2, the depth of the die is 89.23 mm and maximum thinning is about 16 %, however in variant 3, blank is exposed to 40 % thinning at the depth of 80 mm. Hence, HBU process can not progress futhermore and simulation stops due to instability which means that high pressure sheet metal forming fails at variant 3 of circular cross-section in the geometry spectrum.

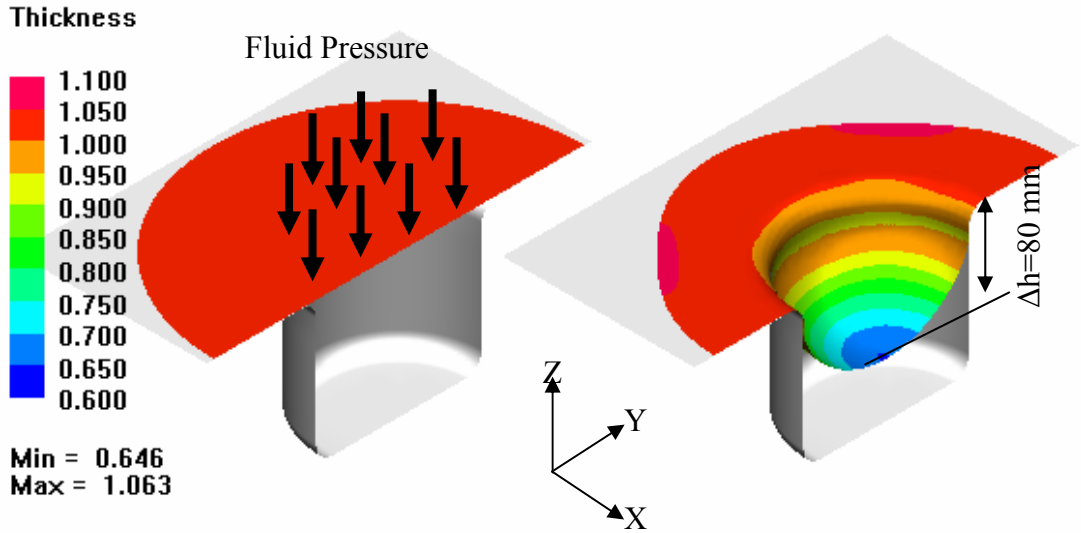


**Figure 5.9** High pressure sheet metal forming process, variant 3

## 5.4 Geometry II: Elliptic (I) Cross-section

The second cross-section of the geometry spectrum is ellipse whose major / minor diameter ratio is equal to 1.5 and dimensions are given in Figure 5.10. Three different depths of die cavity are present that change according to three reference equivalent drawing ratio. Tool reference dimensions given in Table 5.2 are used to build the punch and die meshes that are used in the assessment simulations. Those are ±0.6 mm offset from the tool reference and the clearance between the die and punch is 1.2 mm, which is 20% more than the initial blank thickness.

Optimum blank geometry for elliptic cross-section is an ellipse. Undeformed blank dimensions for each variant of circular cross-section and corresponding die depths are listed in Table 5.2 and relevant calculations are given in Appendix E.2. While calculating the depth of the die, instead of fully drawing the material into the die cavity, it is aimed to leave 20 mm flange on to the binder because of anisotropy and die upper fillet.

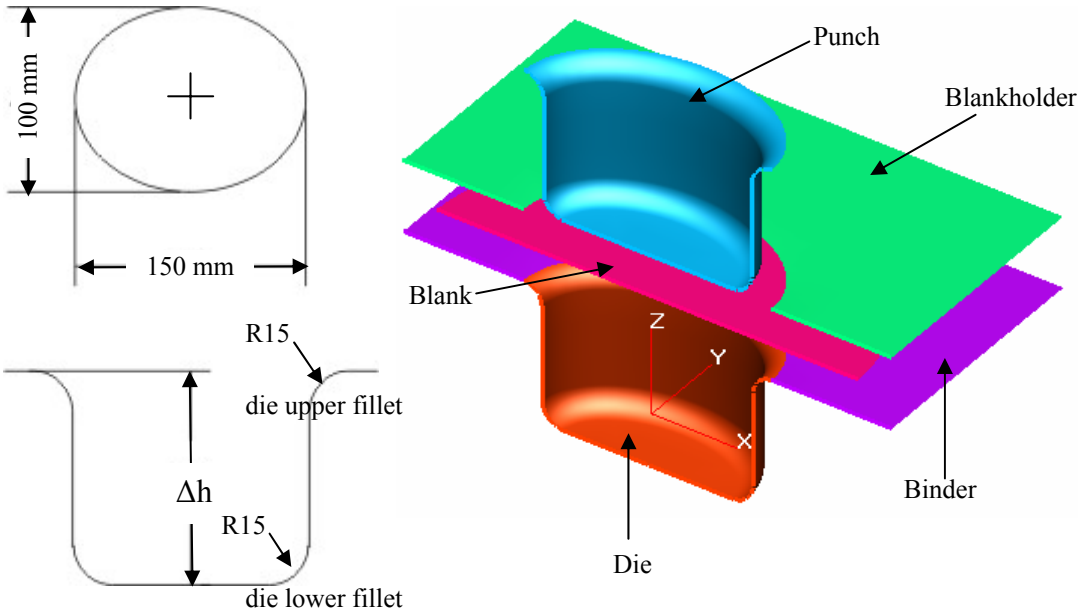


**Figure 5.10** Elliptic (I) cross-section of geometry spectrum and tool geometry

Figure 5.2 shows the tool setup of conventional deep drawing process (DD). Binder, die, blank holder and punch are shown explicitly. At each variant, only depth of the die and height of the punch varied according to the corresponding equivalent drawing ratio. Those variations in the dimensions are tabulated in Table 5.2.

**Table 5.2** Elliptic cross-section tool reference and blank dimensions

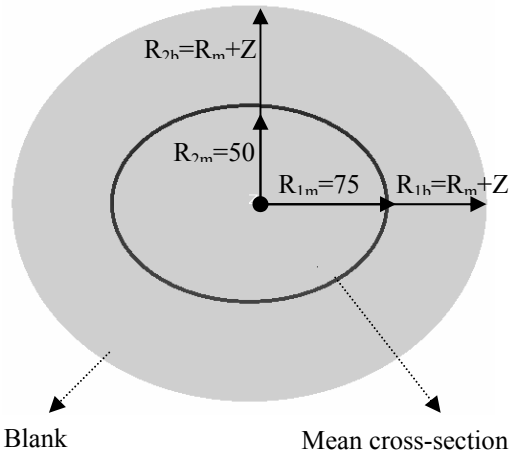


| Tool Reference Dimensions | |
|---|---|
| Mean Radii ($R_{1m}$ , $R_{2m}$) | 75 mm, 50 mm |
| Mean Area ($A_m$) | 11781 mm |
| Mean Circumference ($C_m$) | 400.5 mm |

| Blank Dimensions | | | | | | |
|---|---|---|---|---|---|---|
| Var. | $\beta_{eq}$ | $A_b$ (mm²) | Z (mm) | $R_{1b}$ (mm) | $R_{2b}$ (mm) | Δh (mm) |
| 1 | 1.75 | 36079 | 45.39 | 120.39 | 95.39 | 37.92 |
| 2 | 2.00 | 47124 | 60.61 | 135.61 | 110.61 | 65.50 |
| 3 | 2.25 | 59641 | 75.85 | 150.85 | 125.85 | 96.76 |

For conventional deep drawing (DD), three variants are separately simulated and successful results are obtained for each of them. Since the results are very close to each other and there is nothing important to comment individually, only the results obtained from the most severe case (variant 3) are shown and discussed.

Figure 5.11 shows the thickness contour of workpiece drawn into the elliptic (I) cross-section, whose die's depth is 129.68 mm (variant 3) with conventional deep drawing. Average thinning is between 5% and 15% over the workpiece surface but especially lateral surfaces perpendicular to the x-axis are more critical (maximum thinning = 15%). However, thinning distribution is admissible, results are satisfactory, and conventional deep drawing process is successful.

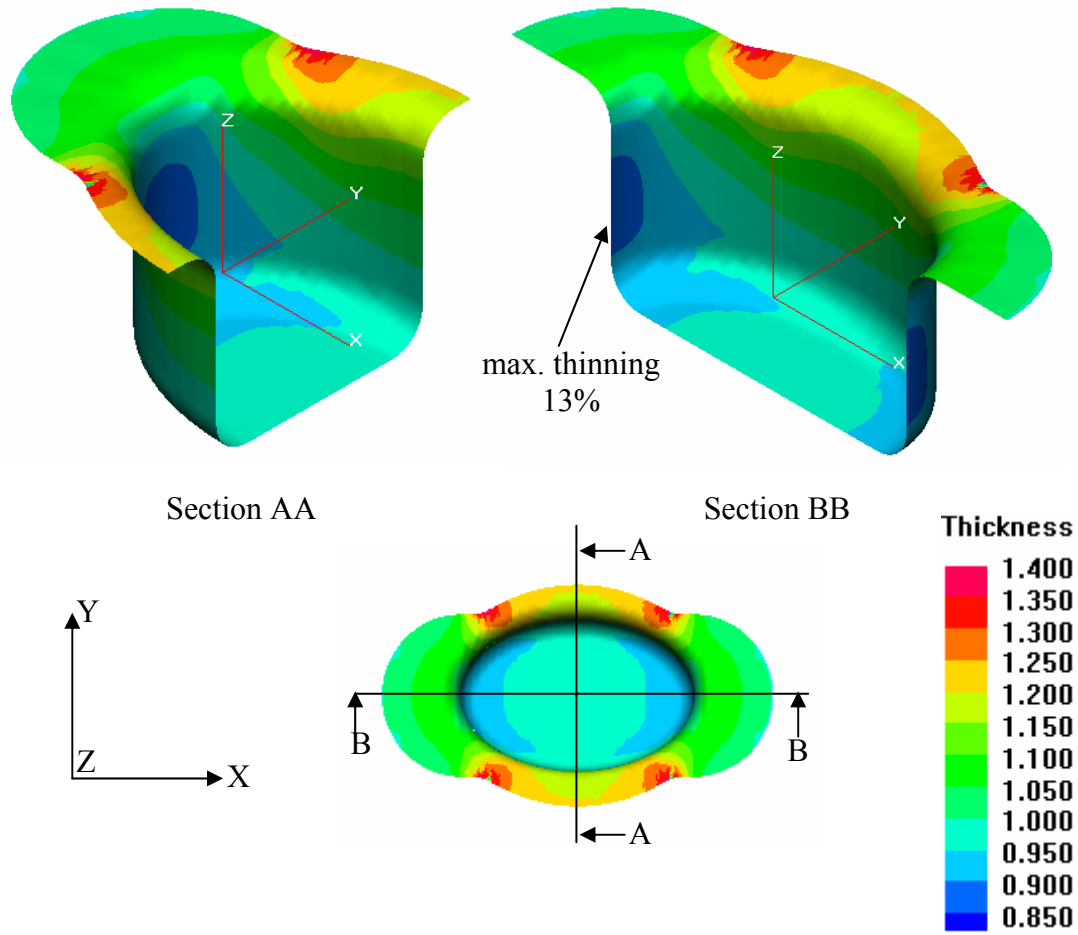


**Figure 5.11** Thickness contour of workpiece manufactured with conventional deep drawing

Figure 5.12 represents the tool setup of hydro-mechanical deep drawing (aquadrawing). In this process, die cavity is filled with fluid medium and as the punch penetrates and blank is forced to take the form of the die. Fluid medium exerts counter pressure acting on the lower surface of blank. Friction forces on the die and binder surface are eliminated and they are almost zero in the hydro-mechanical deep drawing. Furthermore counter forces exerted on to the blank lower surface generates excessive friction force between the punch and blank; however it has a positive influence on the drawability of the blank.

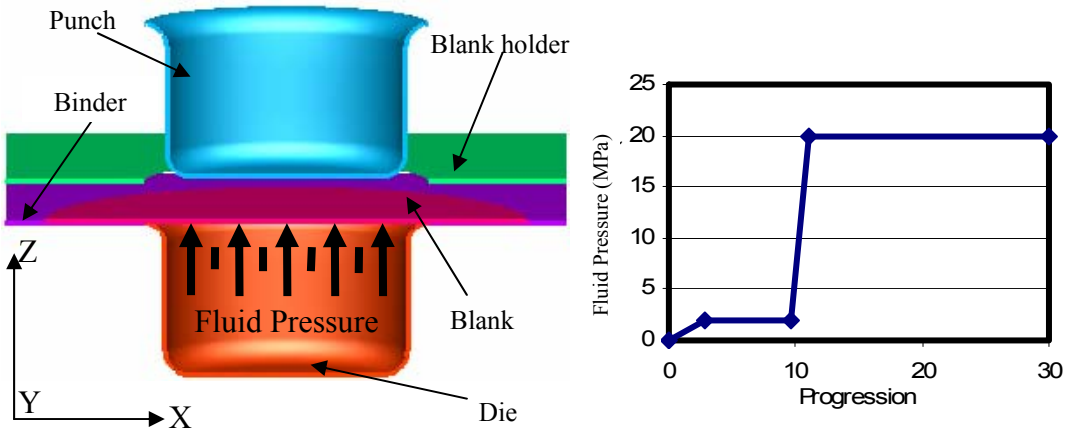


**Figure 5.12** Hydro-mechanical deep drawing (aquadrawing) setup and counter pressure exerted by fluid on to the workpiece

Figure 5.13 compares the thickness contour of workpieces, manufactured with hydro-mechanical deep drawing (aquadrawing) and conventional deep drawing (DD). Excessive thinning is observed on the lateral surfaces perpendicular to the x-axis of the conventionally drawn workpiece. In the hydro-mechanical deep drawing, workpiece is deformed less at that lateral surface.

The improvement is achieved by reducing the friction between the binder and blank. Fluid can flow out between the blank and binder, thus it terminates the friction effect on the flange.

In addition, average thickness of blank at the bottom of the workpiece is 5% higher with hydro-mechanical deep drawing than conventional deep drawing. Despite those differences, it can be stated that both processes are satisfactory in the production of workpiece with elliptic (I) cross-section.

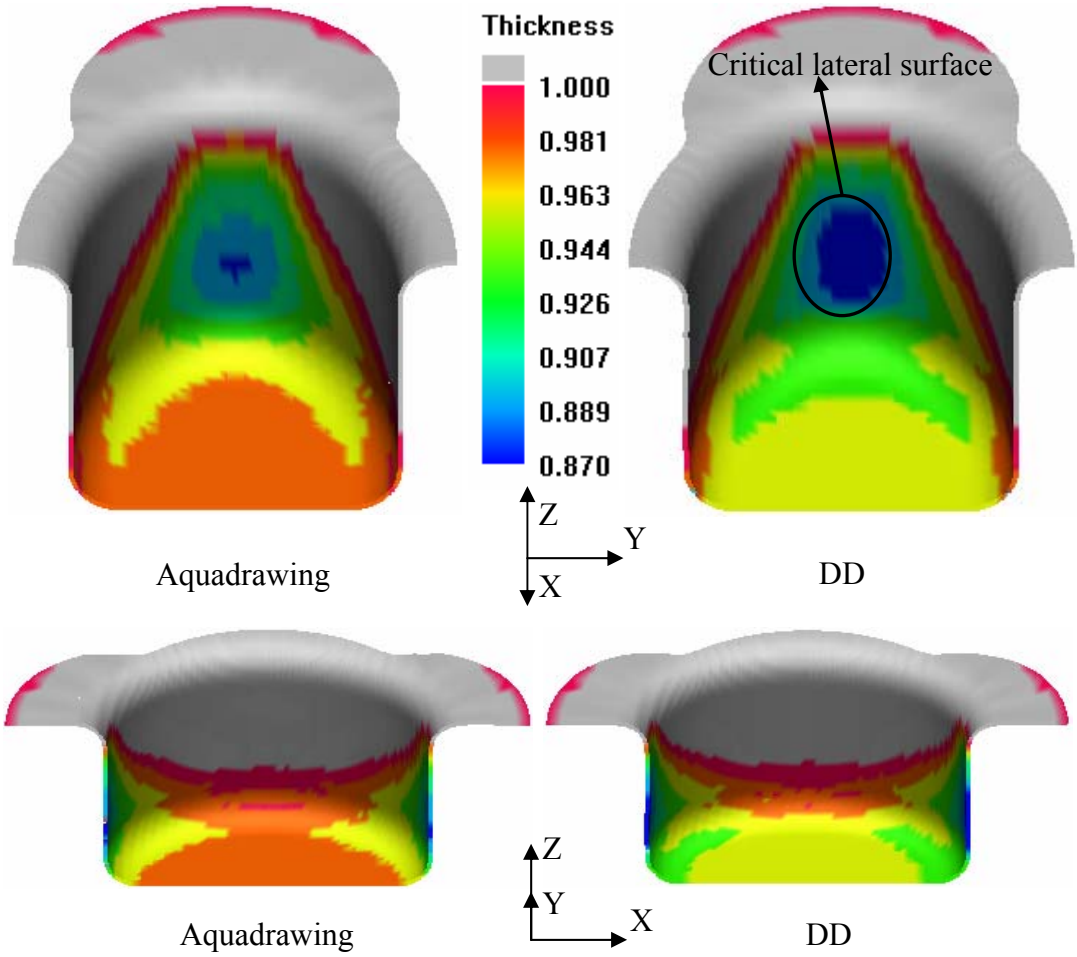


**Figure 5.13** Comparison of workpieces manufactured by hydro-mechanical deep drawing process (aquadrawing) and conventional deep drawing process (DD)

Third process in the assessment study is high-pressure sheet metal forming (HBU) in which the punch is replaced with fluid medium that exerts forming pressure on to the upper surface of blank. First two variants of the workpiece with elliptic (I) cross-section are satisfactorily produced by this process. Figure 5.7 shows the basic states of high pressure sheet metal forming (HBU) working on the variant 3 of elliptic (I) cross-section of geometry spectrum.

Process starts with low pressure to bulge the blank towards the die cavity (State 2, Figure 5.7). As the blank hits to the bottom surface, pressure is slowly increased until the blank fills the curvature and takes the form of the tool (State 3 and State 4, Figure 5.7). After the calibration, the thickness of the workpiece is decreased to

75% of the initial thickness around the die cavity curvatures, especially on the curved surfaces normal to the x-axis. This is the minimum thickness on the workpiece but it is still in the admissible range (30%), so that the process is freely assumed successful.

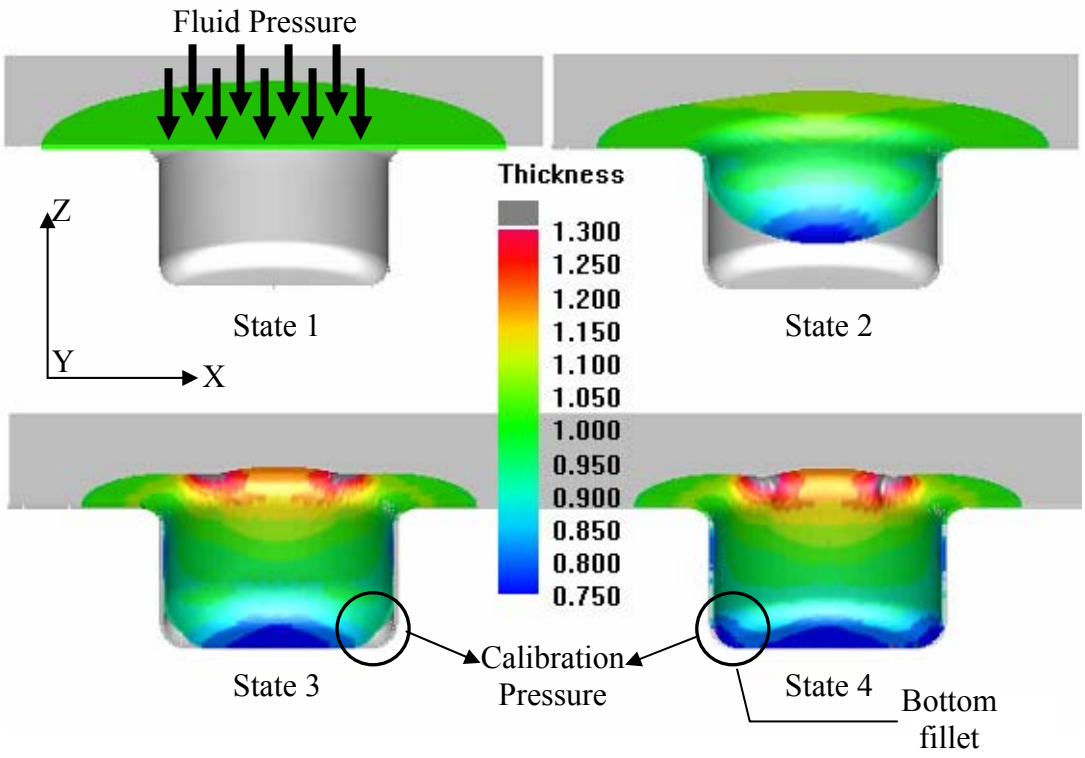


**Figure 5.14** High pressure sheet metal forming process, variant 3

Figure 5.15 summarizes the simulation results of three sheet metal forming processes for the assessment study. In the chart, blank thickness along the curvilinear coordinate of section AA and section BB of workpieces produced by each process is shown. All of the processes are successful in the production of the elliptic (I) cross-section cylindrical workpiece having 96.76 mm depth ($\beta_{eq}$=2.25), however it can be concluded that blank exposes less thinning with hydro-mechanical sheet metal forming process (aquadrawing) whereas, it deforms most with high pressure sheet metal forming (HBU).

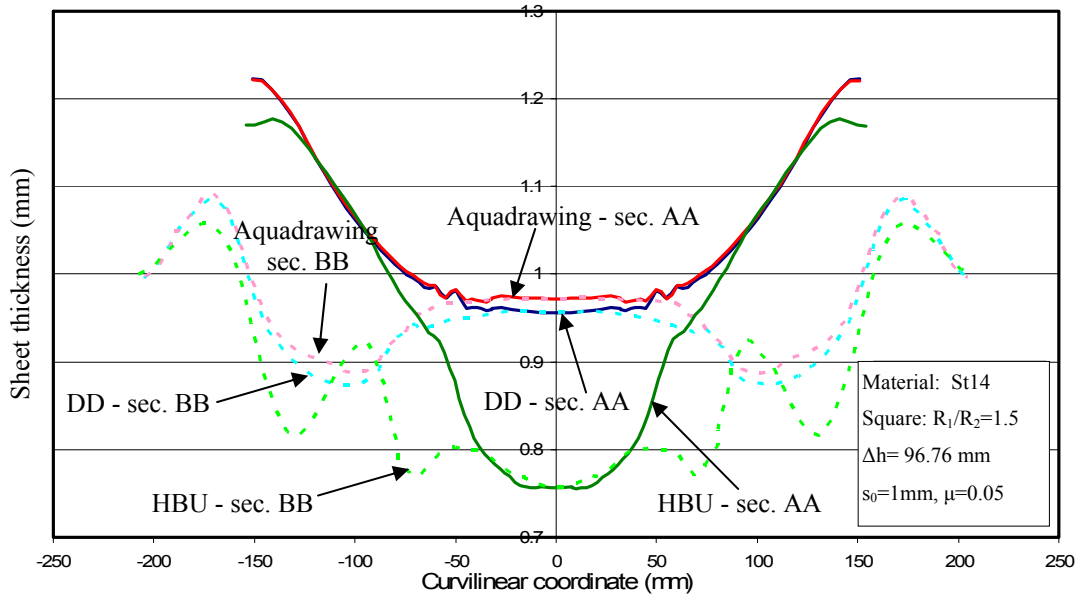


**Figure 5.15** Thickness of blank with respect to the curvilinear coordinate along the section AA and section BB of elliptic (I) workpieces manufactured by conventional deep drawing (DD), hydro-mechanical deep drawing (aquadrawing), and high pressure sheet metal forming (HBU)

Figure 5.16 represents the Forming limit diagrams (FLD) of three workpieces produced by three processes. The legend of the Figure 5.16 indicates the rupture risk of workpieces produced by each process. Rupture risk is the measure of the y distance of each element to the forming limit curve (FLC). If the point is below the FLC, the distance is multiplied by -1, which means that the higher the value of the element, the higher the risk of rupture, depending on the reference FLC.

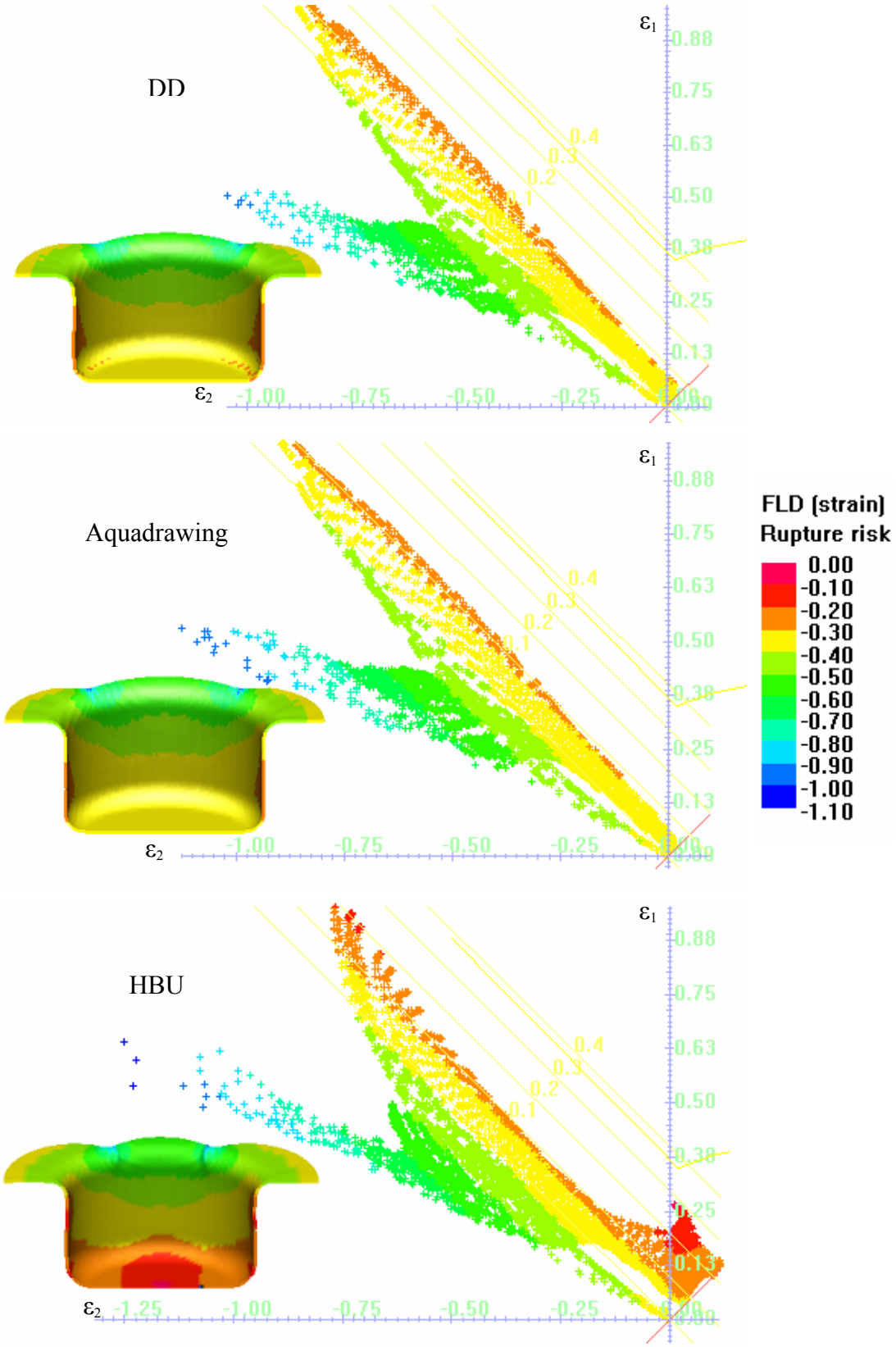


**Figure 5.16** Forming limit diagram (FLD) showing rupture risk of elliptic cross-section, variant 3 cylindrical workpieces produced by each process

## 5.5 Geometry II: Elliptic (II) Cross-section

The third cross-section of the geometry spectrum is also an ellipse but its major / minor diameter ratio is equal to 2.0. Detailed dimensions of tool system are given in Figure 5.17. There different workpieces with three different depths according to the reference equivalent drawing ratios are present. Tool reference dimensions given in Table 5.3 are used to build the punch and die meshes in the assessment simulations. Those are ±0.6 mm offset from the tool reference; thus, the clearance between the die and punch is 1.2 mm, which is 20% more than the initial blank thickness.

Optimum blank geometry for elliptic cross-section is an ellipse [21]. Undeformed blank dimensions for each variant of circular cross-section are listed in Table 5.3 and the relevant calculations are given in Appendix E.2. It should be noted that while calculating the depth of die and initial blank dimension, it is aimed to leave 20 mm flange at the final stage of each process due to upper fillet of the die and the non-uniform draw-in of material at different direction (anisotropy effect).

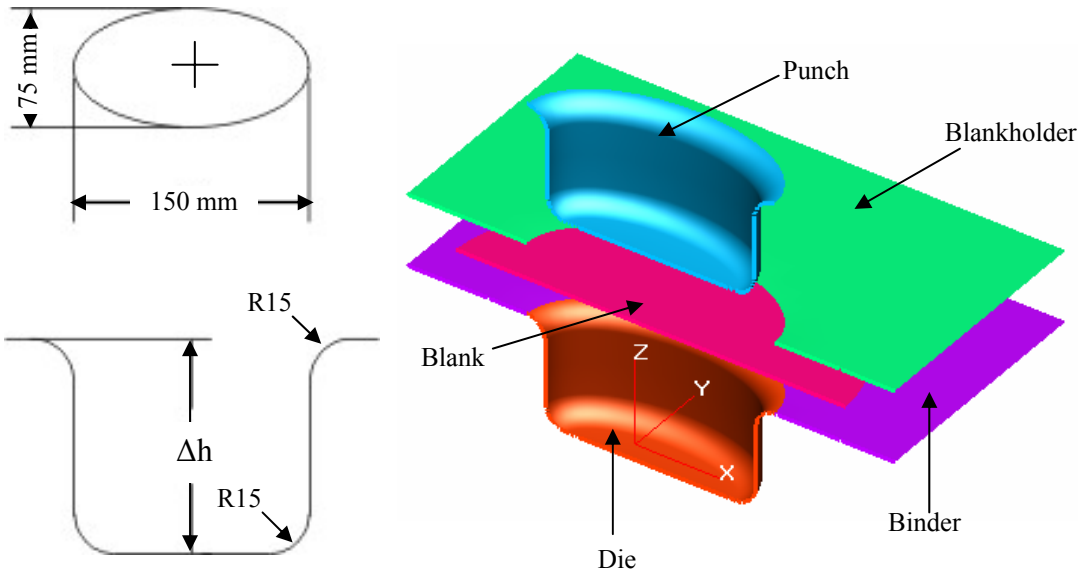


**Figure 5.17** Elliptic (II) cross-section of geometry spectrum and tool geometry

Figure 5.2 shows the tool setup of conventional deep drawing process (DD). Binder, die, blank holder, and punch are shown explicitly. At each variant, only depth of the die and height of the punch varied according to the corresponding equivalent drawing ratio. Those variations in the dimensions are tabulated in Table 5.1.

**Table 5.3** Elliptic cross-section tool reference and blank dimensions

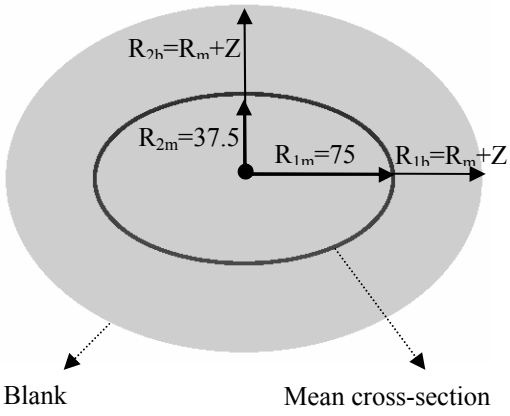


| Tool Reference Dimensions | |
|---|---|
| Mean Radii ($R_{1m}$ , $R_{2m}$) | 75 mm, 37.5 mm |
| Mean Area ($A_m$) | 8835.7 $mm^2$ |
| Mean Circumference ($C_m$) | 372.6 mm |

| Blank Dimensions | | | | | | |
|---|---|---|---|---|---|---|
| Var. | $\beta_{eq}$ | $A_b$ ($mm^2$) | Z (mm) | $R_{1b}$ (mm) | $R_{2b}$ (mm) | $\Delta h$ (mm) |
| 1 | 1.75 | 27059 | 38.43 | 113.43 | 75.93 | 26.57 |
| 2 | 2.00 | 35343 | 51.46 | 126.46 | 88.96 | 48.80 |
| 3 | 2.25 | 44731 | 64.54 | 139.54 | 102.04 | 74.00 |

Three variants, for which the successful results are obtained, are separately simulated for the conventional deep drawing process (DD). However, only the results relevant with variant 3 are worthwhile to discuss for assessment study.

Figure 5.18 represents the thickness contour of blank, drawn into a die having elliptic (II) cross-section, and 129.68 mm depth (variant 3) by using conventional deep drawing process. Maximum thinning is about 15% and it is observed over the bottom fillet and lateral surfaces along the x-axis. The change in the ratio of major / minor diameters influences the drawability of the sheet material negatively, although the corresponding depth of die (74 mm) for elliptic (II) cross-section, variant 3 ($\beta_{eq}$=2.25) is smaller than that of (96.76 mm) elliptic (I) cross- section.

However, the workpiece is still in the admissible thinning zone and process is succesful for the elliptic (II) cross-section of geometry spectrum.

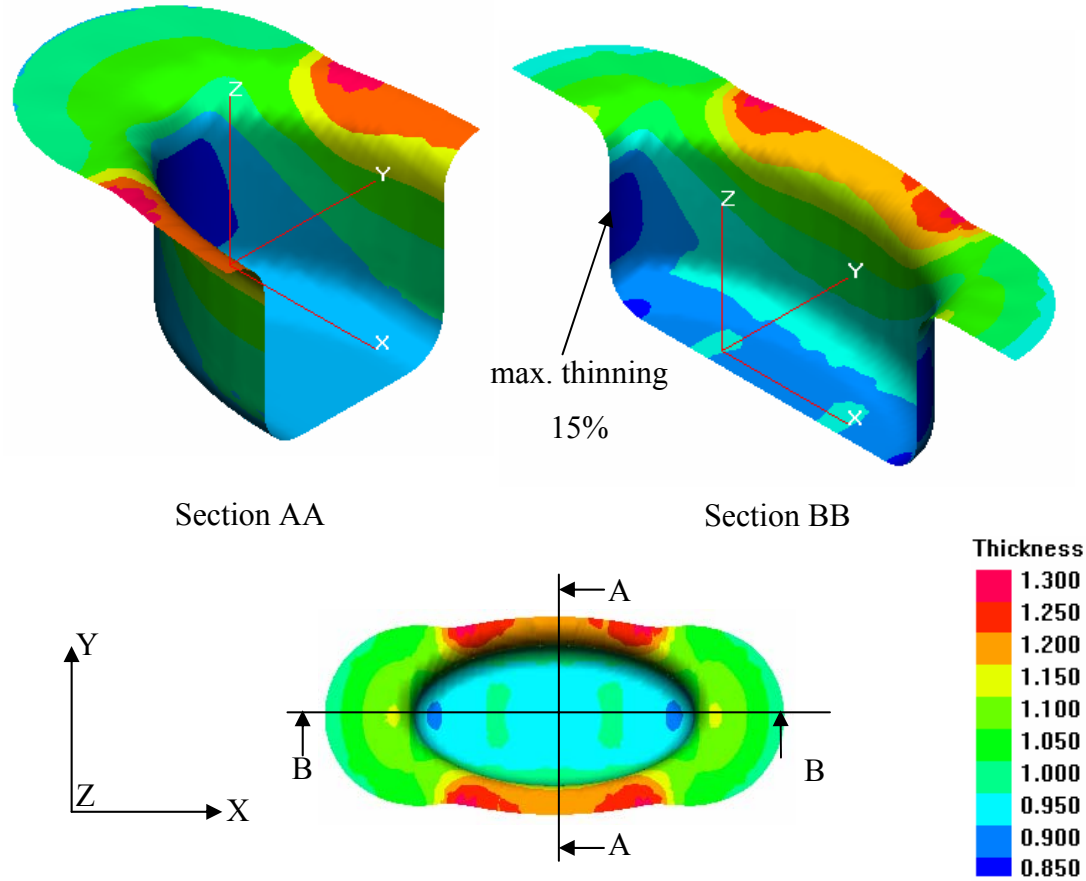


**Figure 5.18** Thickness contour of elliptic (II) cross-section, variant 3 cylindrical workpiece manufactured with conventional deep drawing process

Figure 5.19 represents the tool setup of hydro-mechanical deep drawing (aquadrawing). Counter pressure, which is generated by the fluid medium filling the die cavity, acts on the lower surface of the blank. The value of fluid pressure exerted during the process, is also given in Figure 5.19. In the early stage of the process, 2 MPa is exerted on to the lower surface of the blank until the punch penetrates into the die cavity about half way. After that, the pressure is increased up to 20 MPa and kept constant until the end of the process.

It should be also noted that friction forces decrease since the fluid medium make the blank to lose the contact with die surface and binder. Furthermore, exerting counter pressure and pushing the blank on to the punch surface generates positive effect on the drawability of the sheet metal.

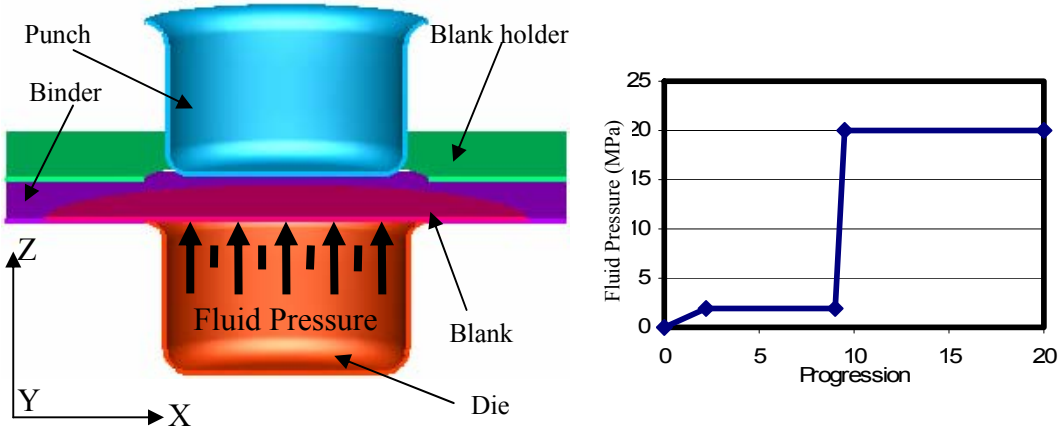


**Figure 5.19** Hydro-mechanical deep drawing (aquadrawing) process setup and counter pressure exerted by fluid on to the workpiece

Figure 5.20 compares the thickness contour of workpieces, manufactured with hydro-mechanical deep drawing (aquadrawing) and conventional deep drawing. In the conventional deep drawing (DD) simulations belonging to the elliptic (II) cross-section, excessive thinning is not only observed at the lateral curved surfaces normal to the x-axis (as it occurs in simulation of elliptic (I) cross-section), but also at some part of die cavity fillet. The additional thinning comes from the major / minor diameter ratios of second elliptic cross-section of the inspected geometry spectrum. However, this has not a severe influence on the workpieces produced by hydro-mechanical deep drawing process. The counter pressure avoids the workpiece getting thinner at the die cavity fillet of the narrow cross-section of the cylindrical die since the friction is not only reduced on the die surface and binder but also increased on the surface of punch. The improvement on the thickness of the workpiece is clearly visualized by the chart given in Figure 5.21.

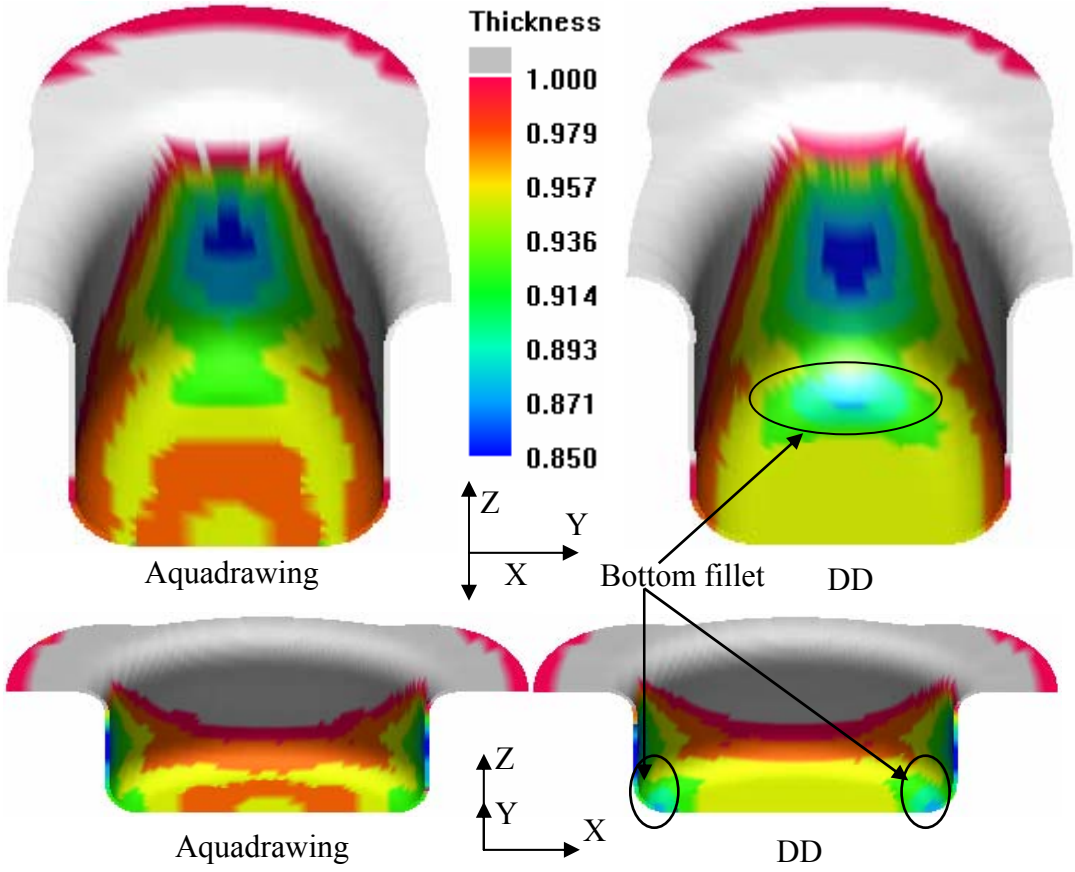


**Figure 5.20** Comparison of workpieces manufactured by hydro-mechanical deep drawing process (aquadrawing) and conventional deep drawing process (DD)

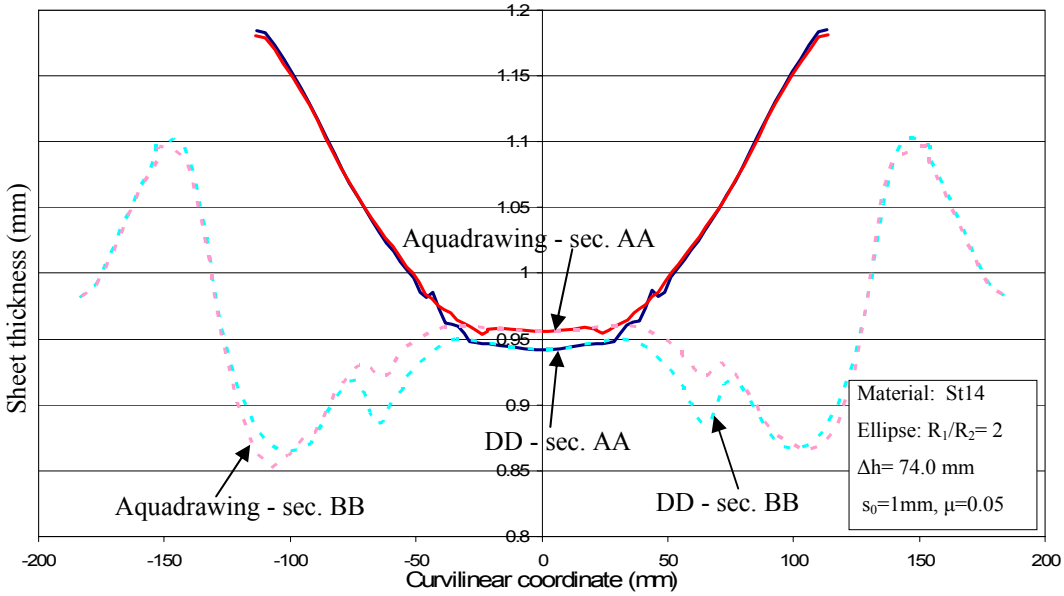


**Figure 5.21** Blank with respect to the curvilinear coordinate along the section AA and section BB of workpieces manufactured by DD and Aquadrawing

Despite these dissimilarities between the two processes, they are successful enough in the drawing of elliptic (II) cross-section when the admissible thinning range of the material (< 30%) is considered.

High-pressure sheet metal forming (HBU) is studied next for the elliptic (II) cross-section. In the circular cross-section, HBU process fails at variant 3 because of the die's depth which is rather deep for the bulging of the sheet material. However, in the elliptic (II) cross-section, a different challenge is present for the high pressure sheet metal forming process. Elliptic (II) cross-section has narrow corners and small curvatures due to its major / minor diameter ratio ($R_{1m}/R_{2m}$=2) and small die fillet radius (15 mm). Therefore, for this cross-section, small curved geometries on the die are the dominant factor in the formability of sheet material with high pressure sheet metal forming process (HBU).

Figure 5.22 shows the final stage of high-pressure sheet metal forming simulation of variant 1. Although the depth of the die is just 26.57 mm, the workpiece is produced with the maximum thinning of 30% that is on the critical limit of the material. In HBU, center of the flat bottom surface of workpiece is expected to deform highly, however since the depth is small, this is not the case. The reason of excessive thinning on the workpiece is the consequence of the narrow corners and small curvatures on the tool geometry. Small curvature on the die necessitates high calibration pressure. Thus, fluid pressure is increased during the forming phase. Moreover, high pressure avoids material flow and the required material filling the curvature, is supplied by the thinning of the blank itself. This behavior is also observed in variant 2. In Figure 5.23, it is seen that most of the bottom surface of the workpiece is deformed only 5% in thickness, whereas workpiece fails on the die cavity fillet at narrow corners.

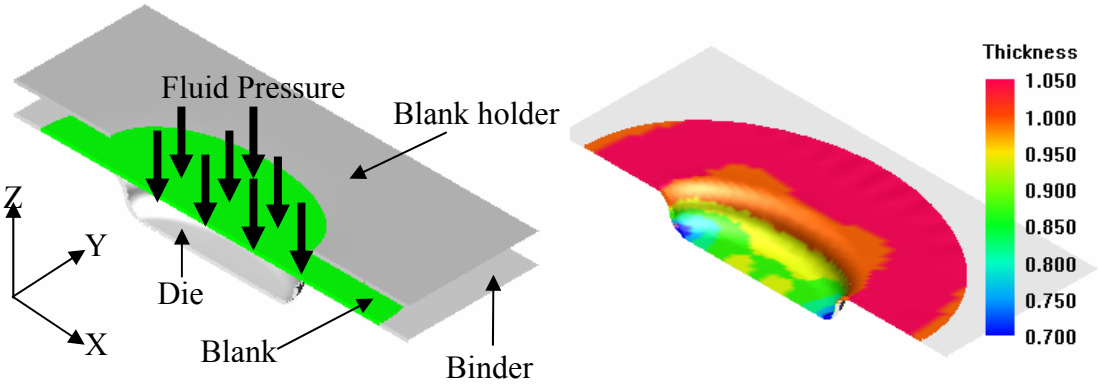


**Figure 5.22** High pressure sheet metal forming simulation of elliptic (II) cross-section, variant 1, cylindrical workpiece

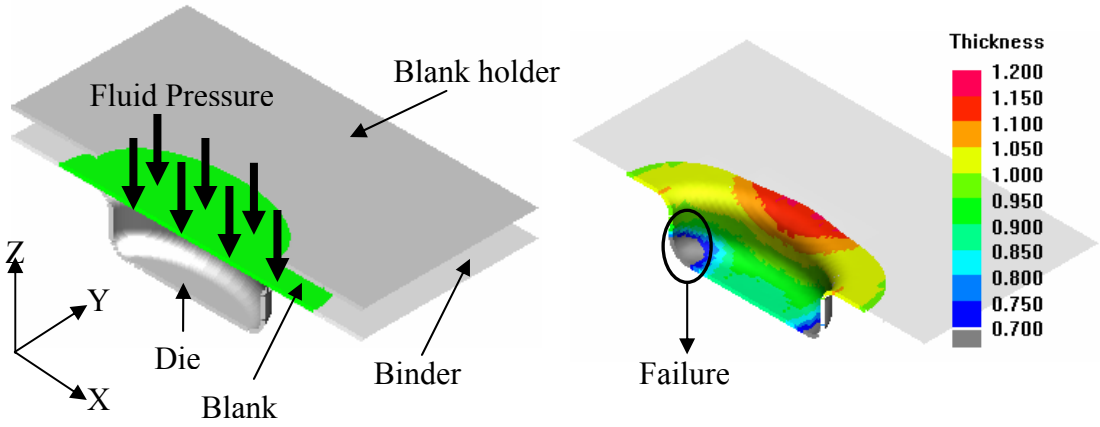


**Figure 5.23** High pressure sheet metal forming process, for elliptic (II) cross-section, variant 2

The results of variant 3 given in Figure 5.24, shows that the process is unacceptable for the production of given geometry. However, the reason of investigating the variant 3 of elliptic (II) cross-section is performing an additional study about the effect of die cavity fillet on the formability of sheet materials drawn into die with narrow cross-section.

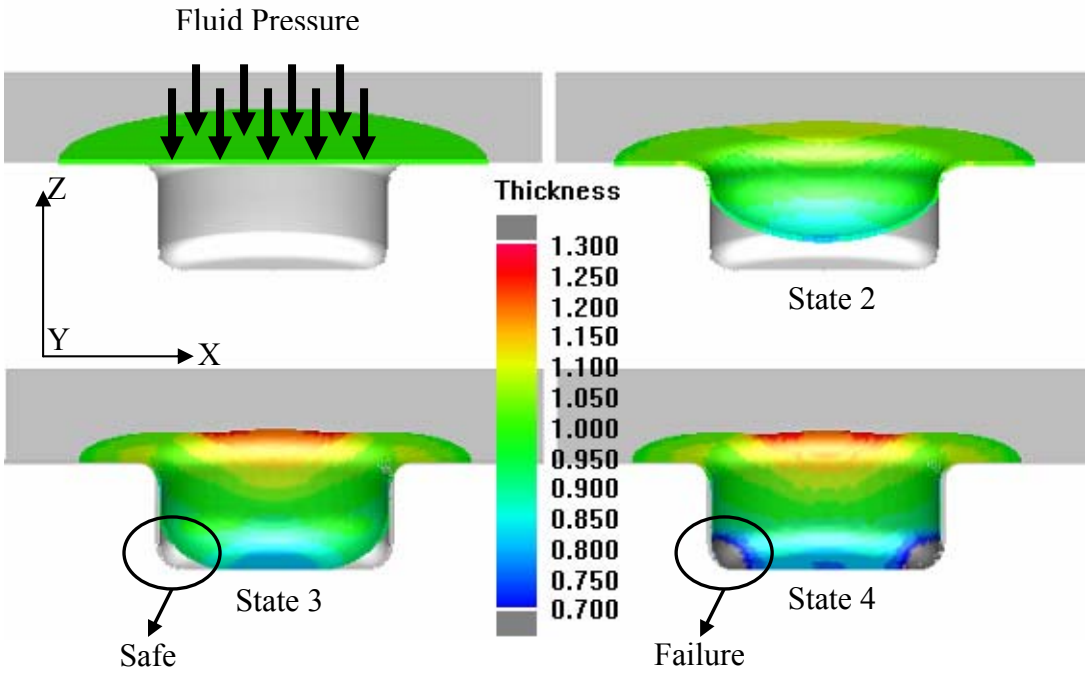


**Figure 5.24** High pressure sheet metal forming process, for elliptic (II) cross-section, variant 3

State 3 and State 4 of Figure 5.24 visualize the influence of fillet radius on the thinning of sheet material. The smaller the fillet radius, the more is the risk of failure. Additional simulations are done by varying the cavity fillet radius of the die t variant 3. Figure 5.25 shows the relation between the fillet radius of die and the thinning percentage of workpiece. By doubling the fillet radius, thinning percentage is also halved. As stated before, curvature dimensions on the die is more dominant than the depth of die in narrow cross-section cylindrical dies. This chart summarizes the characteristic of high pressure sheet metal forming process working on narrow cross section dies such as elliptic (II) cross-section of geometry spectrum.

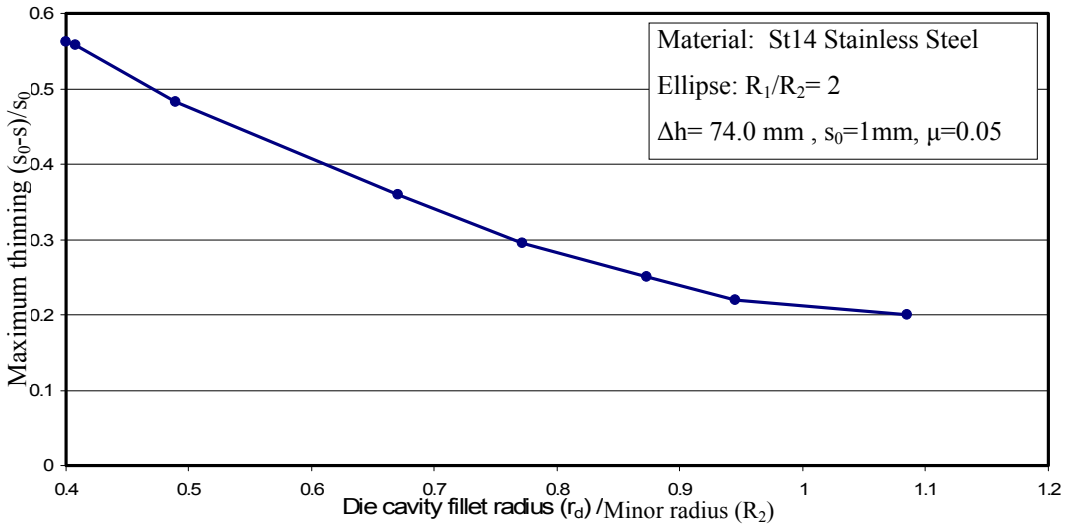


**Figure 5.25** Effect of die cavity fillet on the formability of elliptic workpiece ($\beta_{eq}$=2.25) produced by HBU

Figure 5.26 represents the Forming limit diagrams (FLD) of three workpieces (variant 3) produced by three processes. The legend of the Figure 5.26 indicates the rupture risk that is the y distance of each element from the forming limit curve (FLC). If the point is below the FLC, the distance is multiplied by -1, which means that the higher the value of the element, the higher the risk of rupture, depending on the reference FLC.

First quadrant of FLD diagram is biaxial strain region. Only the workpiece produced with HBU has elements at this quadrant. In FLD diagrams, it is seen that conventionally and hydro-mechanically drawn workpieces (variant 3) are inside the forming window. However for the workpiece (variant 3) produced by HBU, elements corresponding to the cavity fillet at the narrow corner of the die cross section are in the rupture zone. Gray colored elements exceed the yellow colored forming limit curve (FLC) and also some of the elements on the first quadrant which are in the biaxial stain region, pass the 0.3 (30 %) constant thinning line.

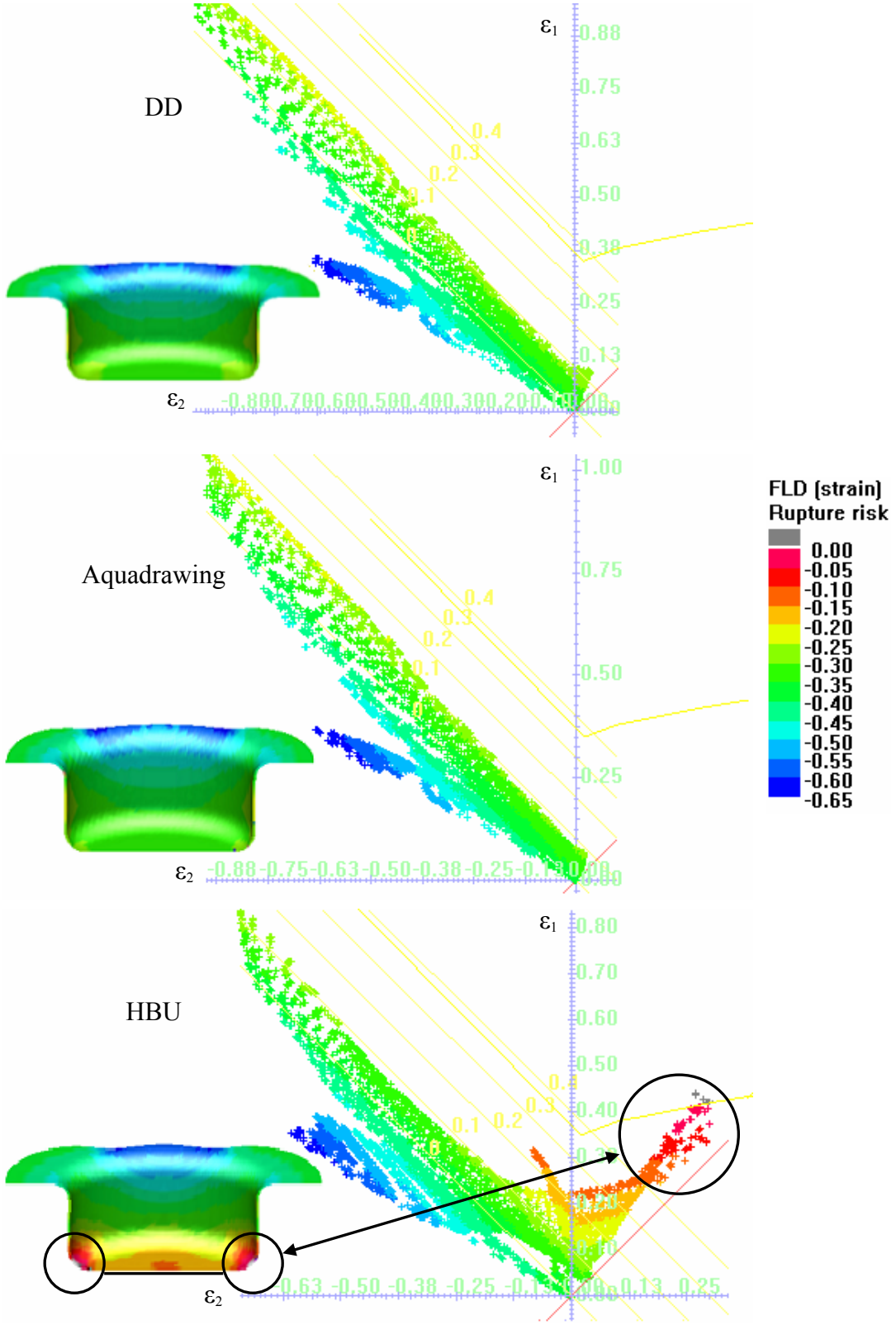


**Figure 5.26** Forming limit diagram (FLD) showing rupture risk of elliptic (II) cross-section, variant 3 cylindrical workpieces produced by each process

## 5.6 Geometry IV: Rectangular Cross-section

The fourth cross-section of the geometry spectrum is a rectangle whose aspect ratio is equal to the major / minor diameter ratio of elliptic (II) cross-section. Moreover, the corner fillet is 25 mm and three different depths of workpiece are calculated by using Eq. (5.1) and Eq. (5.2). Those parameters are given explicitly in Table 5.4 and they are used to build the punch and die meshes for the simulations used for analysis. Die and punch meshes are ±0.6 mm offset from the tool reference and the clearance is 1.2 mm which is 20% more than the initial blank thickness.

Optimum blank geometry for rectangular cross-section is not a simple geometry. Intensive study should be performed to obtain a satisfactory solution. However, it is known that trimmed quad blank is the optimum blank geometry for the quadrangle cross-sections [22, 23]. However, amount of trimming is the concerning point for the determination of optimum geometry. Numerous simulations are done to determine the satisfying dimensions and the acquirements are given in Table 5.4 for each variant of rectangular cross-section.

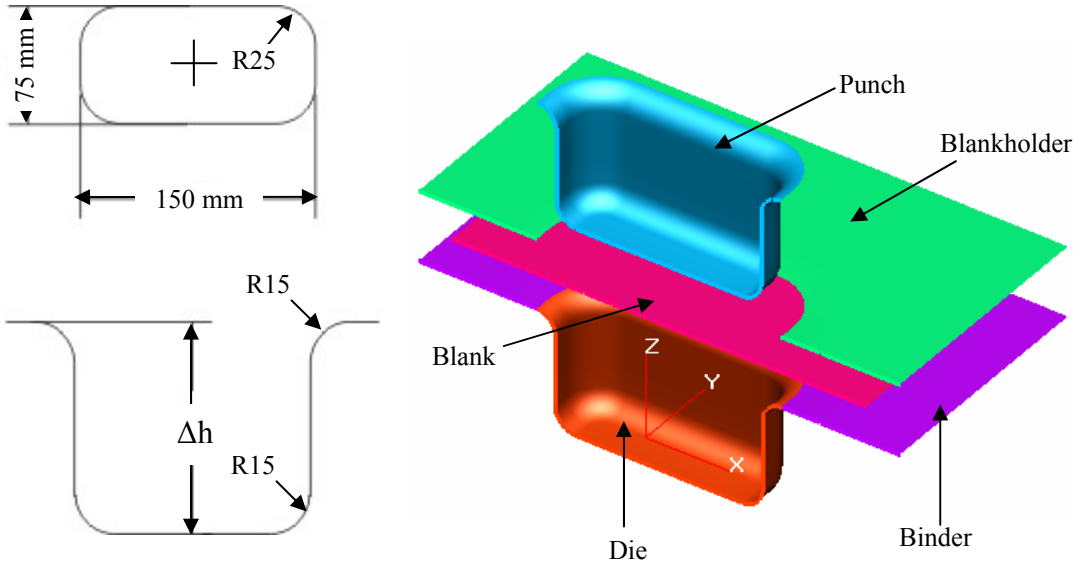


**Figure 5.27** Rectangular cross-section of geometry spectrum and tool geometry

Moreover, it should be reminded that while calculating the depth of the die, it is aimed to leave 20 mm flange on the binder because of the non-uniform draw-in of material at different directions (anisotropy effect), instead of fully drawing the material into the die cavity. All calculations about the blank dimensions and depths of dies are given in Appendix E.4.

**Table 5.4** Rectangular cross-section tool reference and blank dimensions

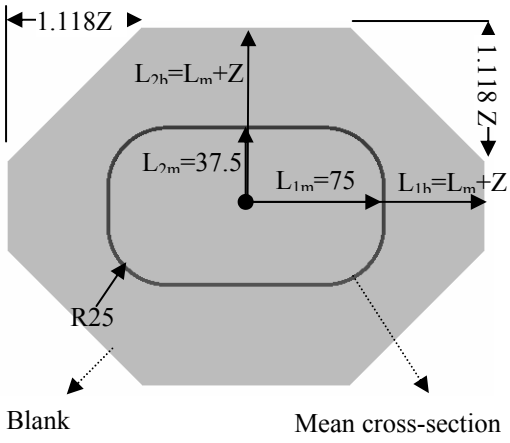


| Tool Reference Dimensions | |
|---|---|
| Mean Edge lengths ($L_{1m}$, $L_{2m}$) | 75mm,37.5mm |
| Mean Area ($A_m$) | 10713.5 $mm^2$ |
| Mean Circumference ($C_m$) | 407.1 mm |

**Blank Dimensions**

| Var. | $\beta_{eq}$ | $A_b$ ($mm^2$) | Z (mm) | $R_{1b}$, (mm) | $R_{2b}$ (mm) | Δh (mm) |
|---|---|---|---|---|---|---|
| 1 | 1.75 | 32810 | 42.02 | 117.02 | 79.52 | 28.89 |
| 2 | 2.00 | 42854 | 58.73 | 133.73 | 171.23 | 53.56 |
| 3 | 2.25 | 54328 | 76.18 | 151.18 | 113.68 | 81.53 |

Figure 5.27 shows the tool setup of conventional deep drawing. The depths of die and the area of undeformed blanks are the parameters varied in the simulations for each variant. Those variations are listed in Table 5.4.

Three variants, for which the successful results are obtained, are separately simulated for the conventional deep drawing process (DD). All the variants are successfully accomplished. Therefore, only the results relevant with variant 3 are discussed.

Figure 5.28 shows the thickness contour of workpiece drawn into die with rectangular cross-section, whose depth is 81.53 mm (variant 3). Average thinning is between 5% and 15% over the workpiece surface but especially smaller lateral surfaces are more critical (maximum thinning = 20%). However, overall thinning

distribution is admissible, and conventional deep drawing process is successful for the production of rectangular prismatic workpiece.

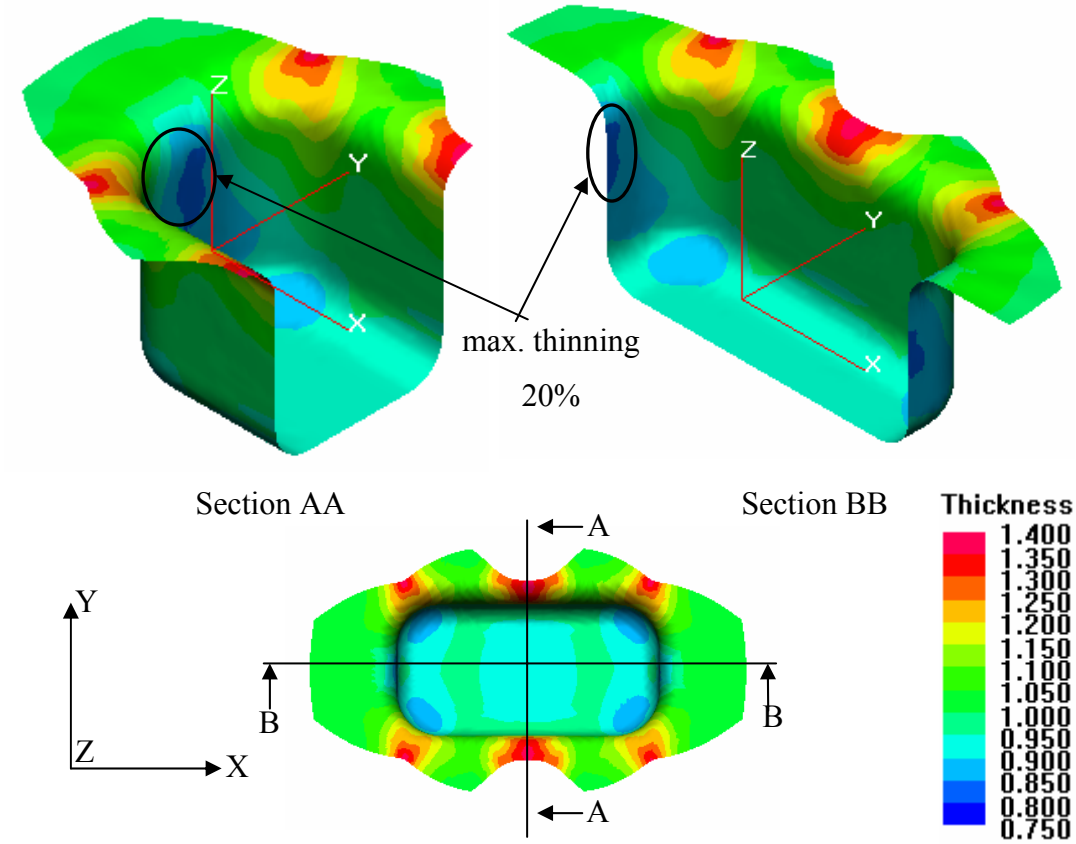


**Figure 5.28** Thickness contour of rectangular workpiece manufactured by conventional deep drawing process

Figure 5.29 represents the tool setup of hydro-mechanical deep drawing (aquadrawing) process. Different than the conventional deep drawing process (DD), in this process die cavity is filled with fluid medium that exerts counter pressure to the lower surface of the blank. The amount of pressure can vary with time. The chart in Figure 5.29 shows the counter pressure applied to the blank during the process. This pressure has positive effect on the formability of the sheet material since it helps the blank to stick on to the punch and to lose contact with die surface and binder

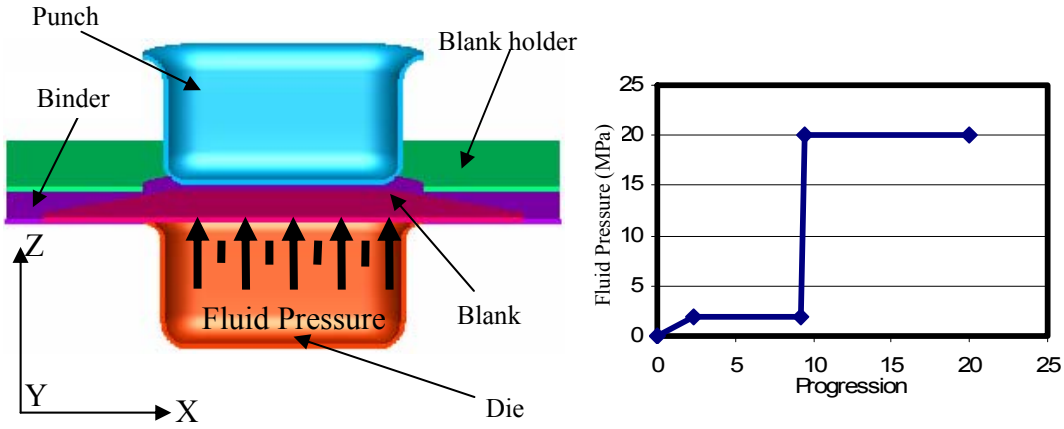


**Figure 5.29** Hydro-mechanical deep drawing (aquadrawing) process setup and counter pressure exerted by fluid on to the workpiece

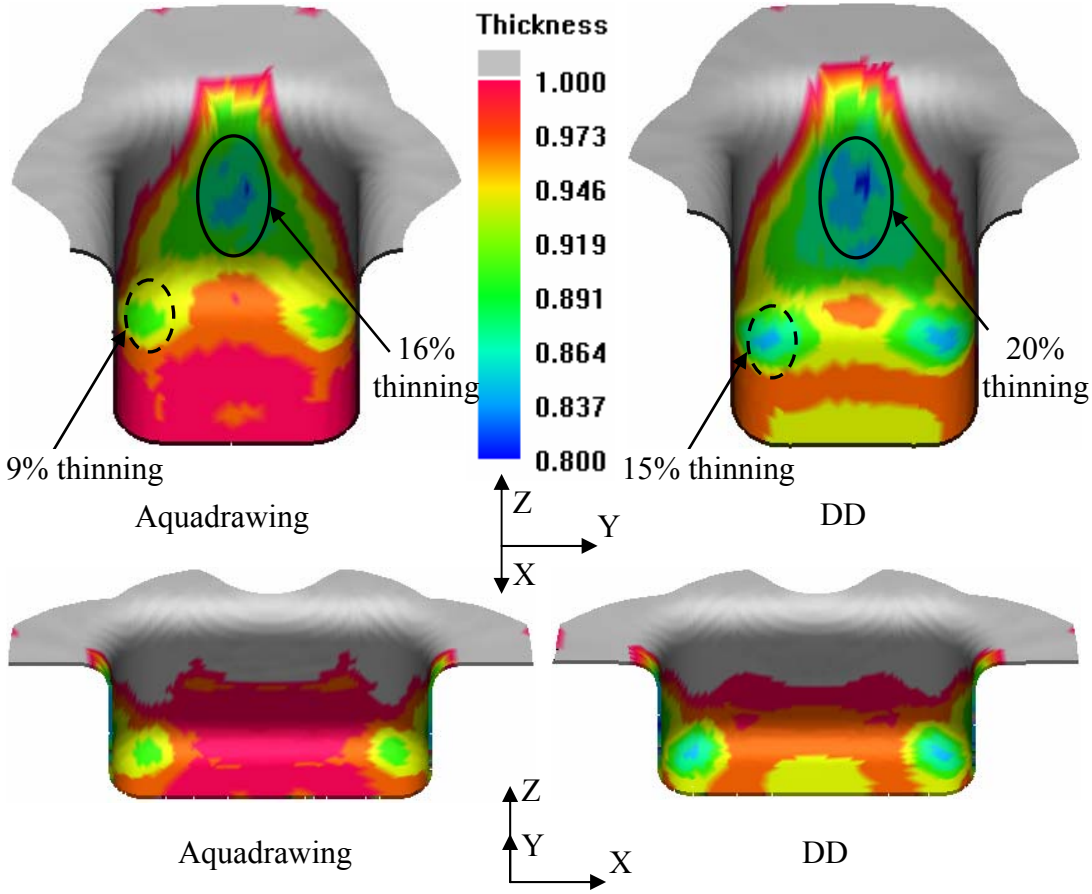


**Figure 5.30** Comparison of workpieces manufactured by hydro-mechanical deep drawing process (aquadrawing) and conventional deep drawing process (DD)

Figures 5.30, 5.31 and 5.32 compare the thickness distribution of two workpieces produced by two competing sheet metal forming processes. Figure 5.30 shows that the performance of hydro-mechanical deep drawing process in thickness distribution is about 4% to 6% better than that of the conventional deep drawing process.

Figure 5.31 shows the thickness values along the curvilinear coordinate of section AA. Hydro-mechanically drawn workpiece exhibits constant thinning (2%) along 150 mm on the middle of the section AA, whereas conventionally drawn workpiece deformed up to 5% in thickness.

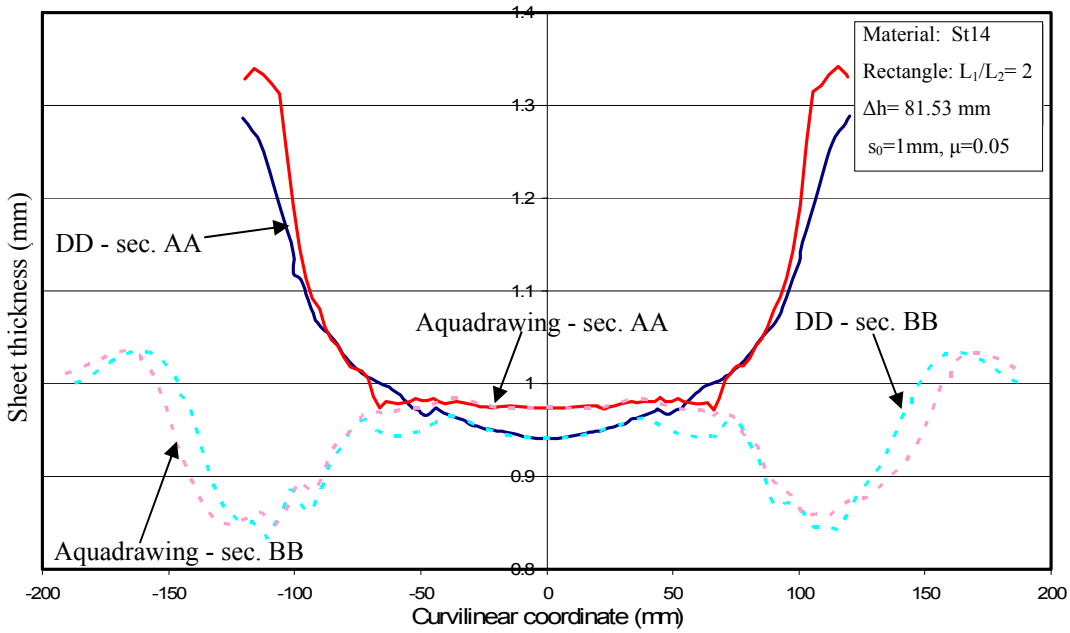


**Figure 5.31** Thickness of blank with respect to the curvilinear coordinate along the section AA and section BB of workpieces manufactured by conventional deep drawing (DD), and hydro-mechanical deep drawing (aquadrawing)

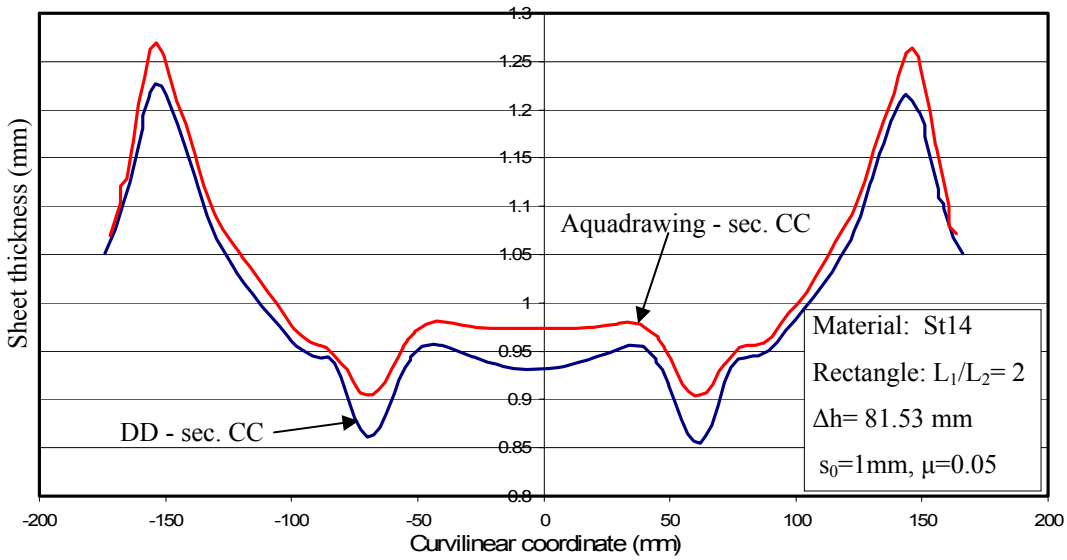


**Figure 5.32** Thickness of blank with respect to the curvilinear coordinate along the section CC of workpieces manufactured by conventional deep drawing (DD), and hydro-mechanical deep drawing (aquadrawing)

Comparison can be done more obviously with the chart given in Figure 5.32. The thickness variation curve of mechanically drawn workpiece is completely offset of the conventionally drawn workpiece along the curvilinear coordinate of section CC.

Last process in the assessment study is high-pressure sheet metal forming process (HBU). Figure 5.33 shows the final stage of high pressure sheet metal forming simulation of variant 1. Although the deep of the die is 28.89, the workpiece is exposed to 22% thinning. Maximum thinning occurs at the bottom corner zone. The reason of extreme thinning is the same as the one in elliptic (II) cross section. Small curvatures on the die surface are the dominant factor in the formability of sheet material with HBU.

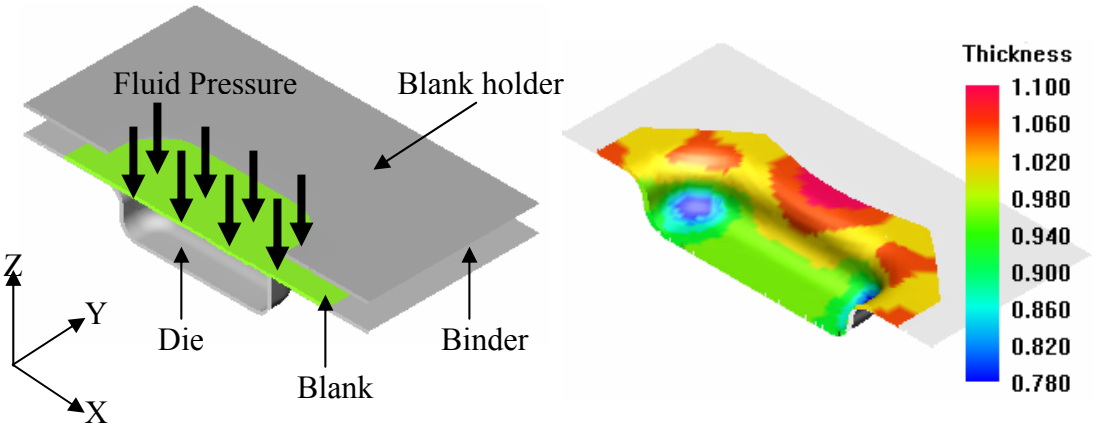


**Figure 5.33** High pressure sheet metal forming simulation of rectangular cross-section, variant 1, prismatic workpiece

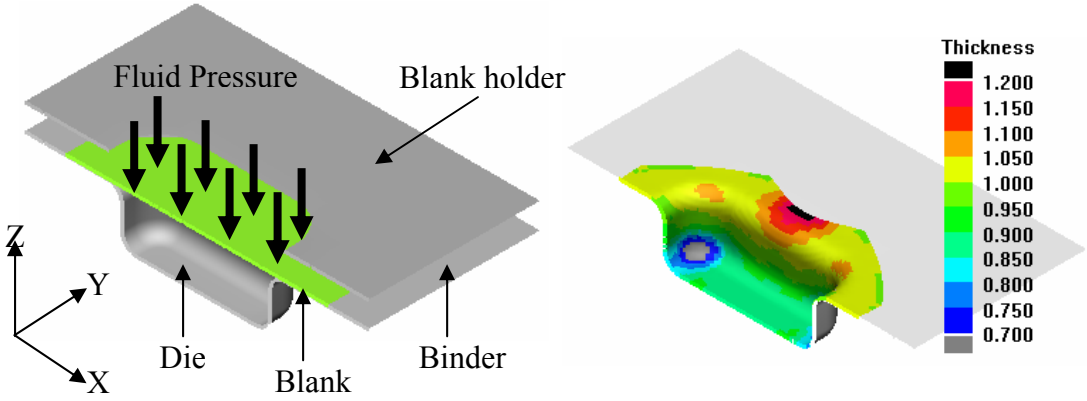


**Figure 5.34** High pressure sheet metal forming simulation of rectangular cross-section, variant 2, prismatic workpiece

In variant 2, the drawing ratio is equal to 2 and the depth is increased to 53.56 mm. The result of relevant simulation showing the thickness contour of workpiece is given in Figure 5.34. The gray colored elements indicate the region whose thinning is above the admissible limit.

Figure 5.35 shows the process stages of the third variant of rectangular cross-section. As it happens for the variant 2, the process is unacceptable for the production of the geometry. Since the calibration of small curvature is the reason of failure. Additional simulations are performed to determine the effect of die cavity

fillet on the formability of sheet material, while keeping the cross-section is the same. The result is given in Figure 5.36.

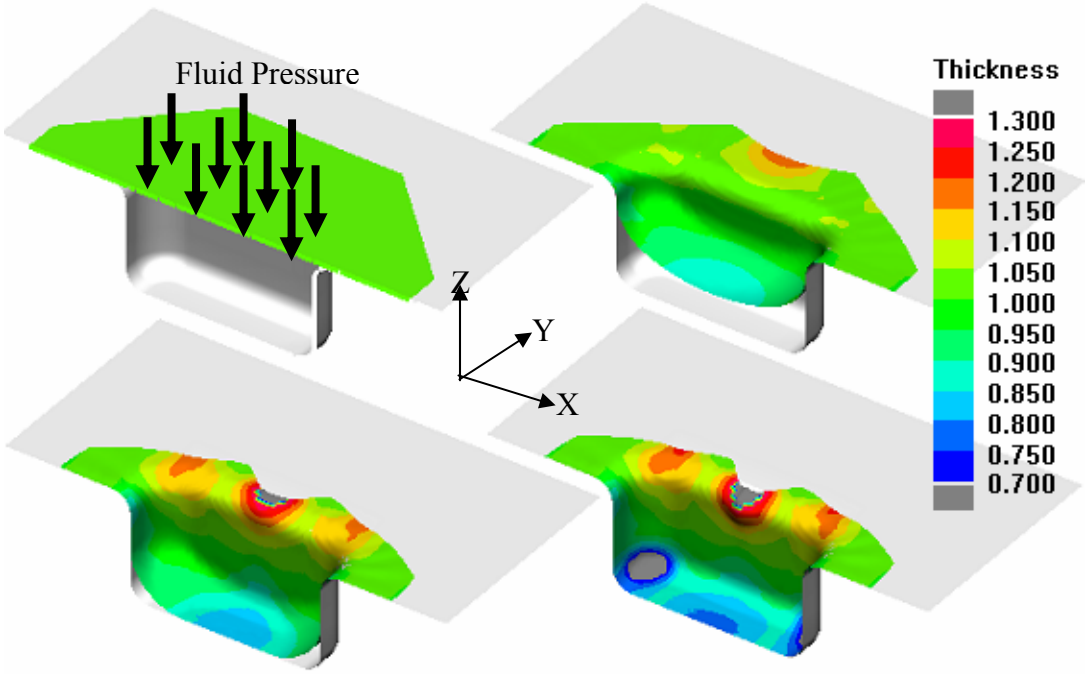


**Figure 5.35** High pressure sheet metal forming simulation of rectangular cross-section (II), variant 3, cylindrical workpiece

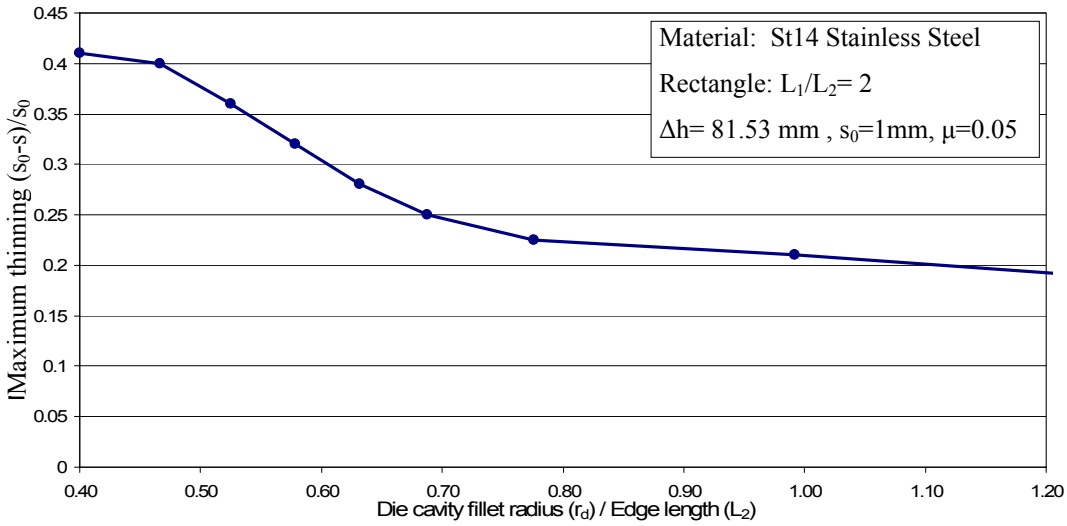


**Figure 5.36** Effect of die cavity fillet on the formability of rectangular workpiece ($\beta_{eq}$=2.25) produced by HBU

## 5.7 Geometry II: Square (I) Cross-section

The fifth cross-section of the geometry spectrum is a square whose edge length is equal to the diameter of the first cross-section (circular) of geometry spectrum. The depths of the dies for each variant are calculated by considering corresponding equivalent drawing ratios and using Eq. (5.2) and Eq. (5.1). Moreover, the reference tool dimensions are used to build the punch and die meshes to be used in the simulations of process evaluations. Those meshes are ±0.6 mm offset from the tool reference and the clearance between the die and punch is 1.2 mm, which is 20% more than the initial blank thickness.

Optimum undeformed blank geometry for square (I) cross-section is more complex than the other cross-sections. For the dies having quadrangle cross-sections, trimmed quad blank is the optimum undeformed blank [22, 23]. Additional simulations are performed to find out the optimum trimming parameters and results are given in Table 5.5 for each variant of square cross-section.

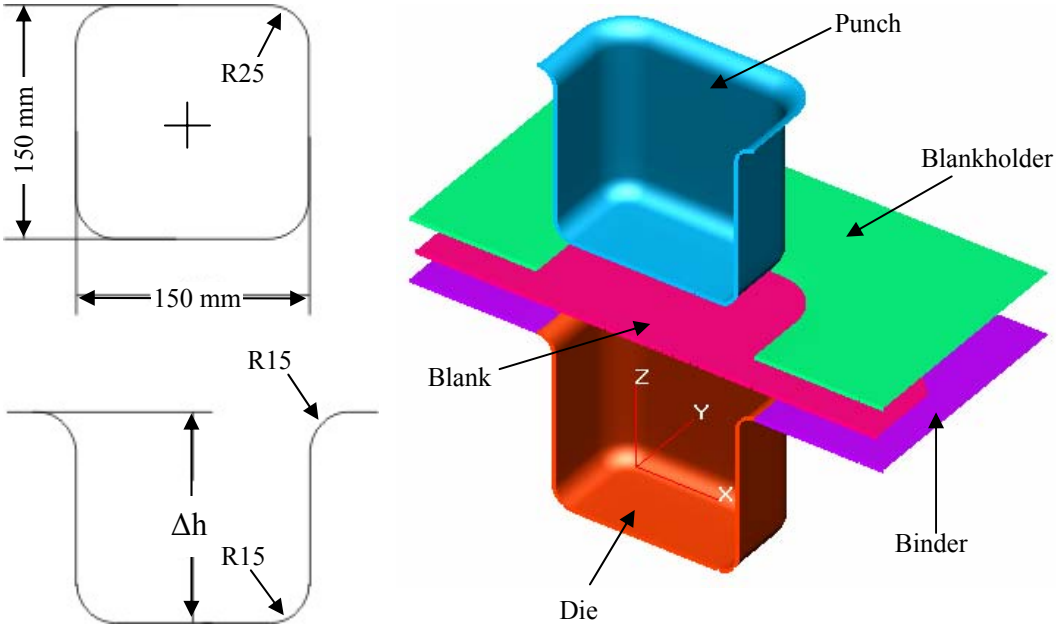


**Figure 5.37** Square (I) cross-section of geometry spectrum and tool geometry

The depth of the die is calculated by leaving 20 mm flange on the binder not only to consider the anisotropy effect but also to compensate the unsupported part of blank above the die inlet fillet. All calculations about the blank dimensions and depths of dies are given in Appendix E.5.

Figure 5.37 shows the tool setup of conventional deep drawing process (DD). In the simulation of each variant, only depth of the die and the area of undeformed blank varied according to the equivalent drawing ratio. Those parameters, for each variant are also given in Table 5.5.

**Table 5.5** Tool reference and blank dimensions of square (I) cross-section

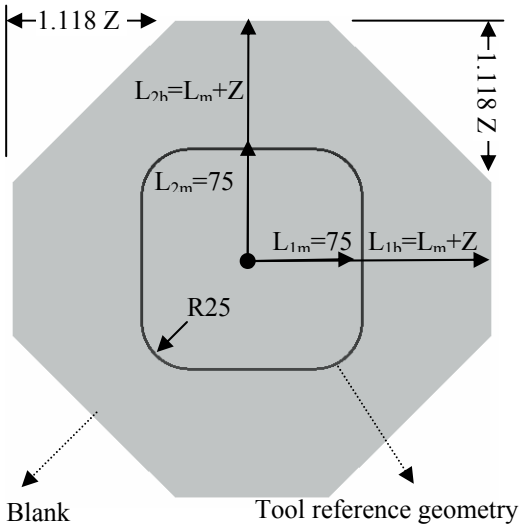


| Tool Reference Dimensions | |
|---|---|
| Mean Edge lengths ($L_{1m}$ , $L_{1m}$) | 75 mm, 75 mm |
| Mean Area ($A_m$) | 21963.5 mm |
| Mean Circumference ($C_m$) | 557 mm |

| Blank Dimensions | | | | | | |
|---|---|---|---|---|---|---|
| Var. | $\beta_{eq}$ | $A_b$ (mm²) | Z (mm) | $R_{1b}$ (mm) | $R_{2b}$ (mm) | Δh (mm) |
| 1 | 1.75 | 67263 | 64.28 | 139.28 | 139.28 | 57.38 |
| 2 | 2.00 | 87854 | 89.08 | 164.08 | 164.08 | 94.34 |
| 3 | 2.25 | 111190 | 114.84 | 189.84 | 189.84 | 136.23 |

For conventional deep drawing process (DD), three variants are separately simulated and successful results are obtained for all of them. In Figure 5.38, thickness contours of the most severe case (variant 3) are shown. The depth of the mentioned workpiece is the highest of all geometries in the spectrum yet the percentage of thinning (16%) observed at this cross-section is not the highest of geometry spectrum produced by conventional deep drawing process (DD). The most critical regions of the workpiece are four bottom corners. However, that amount of thinning is still in the admissible range (< 30%) for ST14 sheet material.

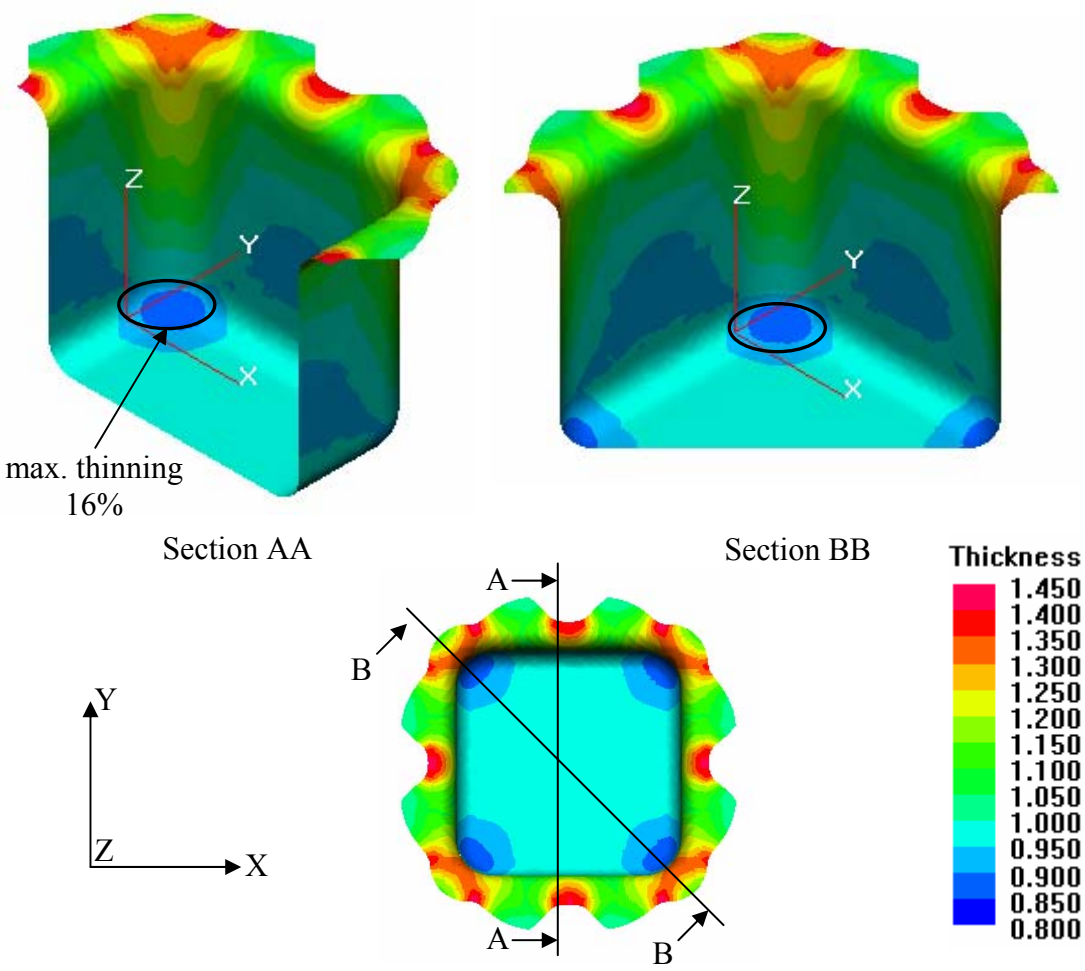


**Figure 5.38** Thickness contour of workpiece manufactured with conventional deep drawing process

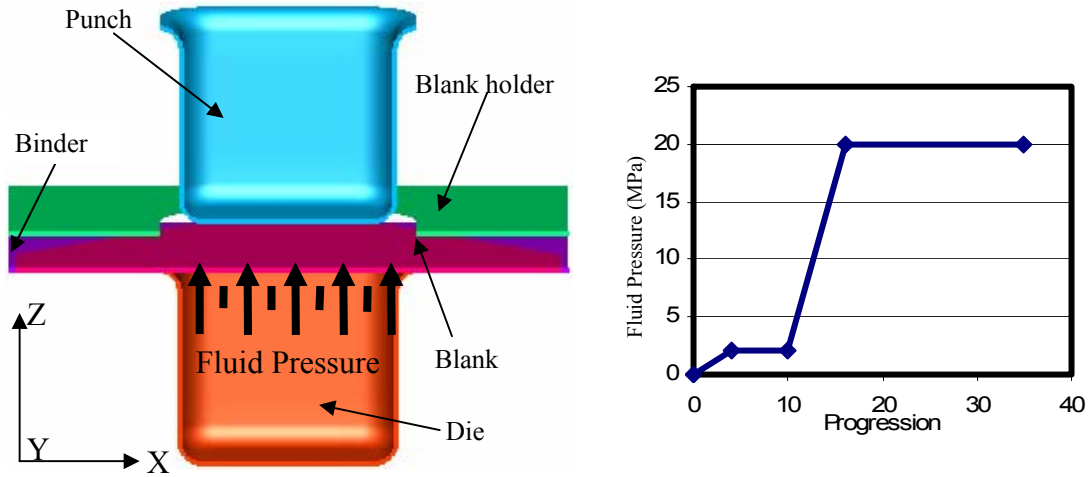


**Figure 5.39** Hydro-mechanical deep drawing (aquadrawing) process setup and counter pressure exerted by fluid on to the workpiece

Second competing process for the square (I) cross section is hydro-mechanical deep drawing process (aquadrawing) whose tool setup is given in Figure 5.39. In this process, die cavity is filled with fluid medium. As the punch penetrates into the die cavity, fluid pressure exerts counter pressure to the blank, which is simultaneously forced to take the form of the tool. This process has advantages to conventional deep drawing process [6, 8]. Friction forces on the die and binder surfaces are eliminated and they are almost zero in the hydro-mechanical deep drawing process. Furthermore, counter force exerted on to the blank lower surface generates excessive friction force between the punch and blank; however, all of these increase the drawability of the sheet material by avoiding early necking and tearing.

Figure 5.40 compares the thickness contour of workpieces, manufactured with hydro-mechanical deep drawing (aquadrawing) process and conventional deep drawing process. Excessive thinning is observed on the four bottom corners of the conventionally drawn workpiece. In the hydro-mechanical deep drawing process, workpiece is deformed less at that regions and overall thinning of workpiece is less than 8%. This improvement is achieved by reducing the friction between the binder and blank and tolerating the friction forces on the die surface.

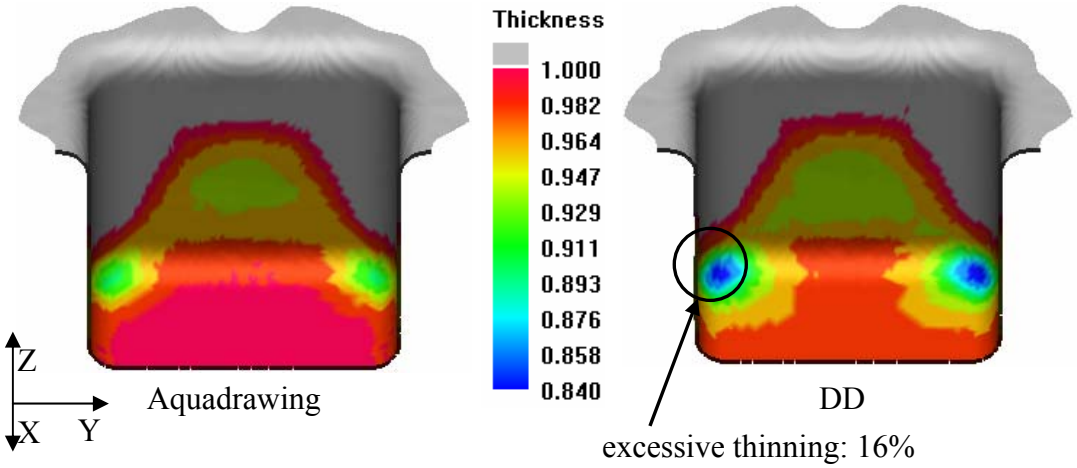


**Figure 5.40** Comparison of workpieces manufactured by hydro-mechanical deep drawing process (aquadrawing) and conventional deep drawing process (DD)

In Figure 5.41, thinning on the bottom corner of workpieces for each process can be compared more clearly, when the thickness variation curves of section CC are observed. It can be stated that maximum thinning on the workpiece is halved by using hydro-mechanical deep drawing compared to conventional deep drawing process. As it happened in the previous (rectangular) cross-section, maximum thinning is again observed on section CC that includes the bottom corners.

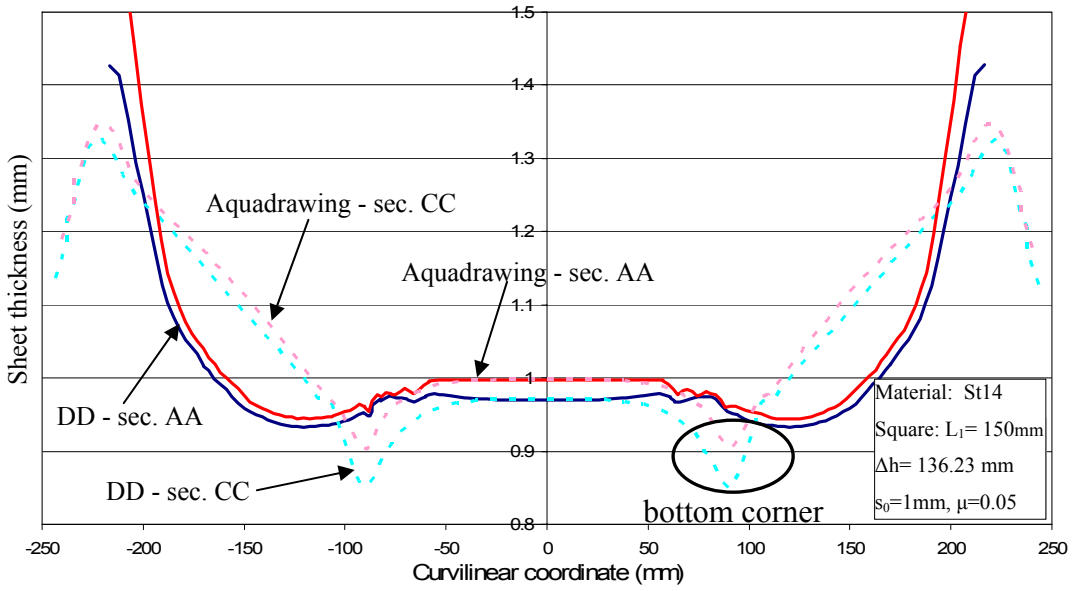


**Figure 5.41** Thickness of blank with respect to the curvilinear coordinate along the section AA and section CC of workpieces manufactured by conventional deep drawing (DD), and hydro-mechanical deep drawing (aquadrawing)

All variants of square (I) cross-section for high pressure sheet metal forming (HBU) are simulated to identify the formability characteristic the process for the chosen cross-section. Figures 5.42, 5.43 and 5.44 represent the initial and final stages of HBU process for variants 1, 2 and 3 respectively. It is claimed in the first two processes that small corner radius of square (I) cross-section has negative influence on the formability and it restricts the material flow, thus unexpected amount of thinning is observed on the workpieces. This behavior shows itself even at the first variant of square (I) cross-section when it is produced with high pressure sheet metal forming process. Grey colored elements are observed around the bottom

corners at the thickness contour of first two variants (Figures 5.42 and 5.43). Therefore, workpieces fail during the calibration phase. However, in the third variant, the main source of failure is different. Calibration starts after the blank hits to die bottom. Since the corresponding depth is relatively high (136.23 mm), the calibration phase cannot start as immediate as it happens at the previous two variants. Yet the simulation process interrupts due to the tearing at the middle of the bottom surface that is caused by the bulging of sheet material into relatively deeper die cavity.

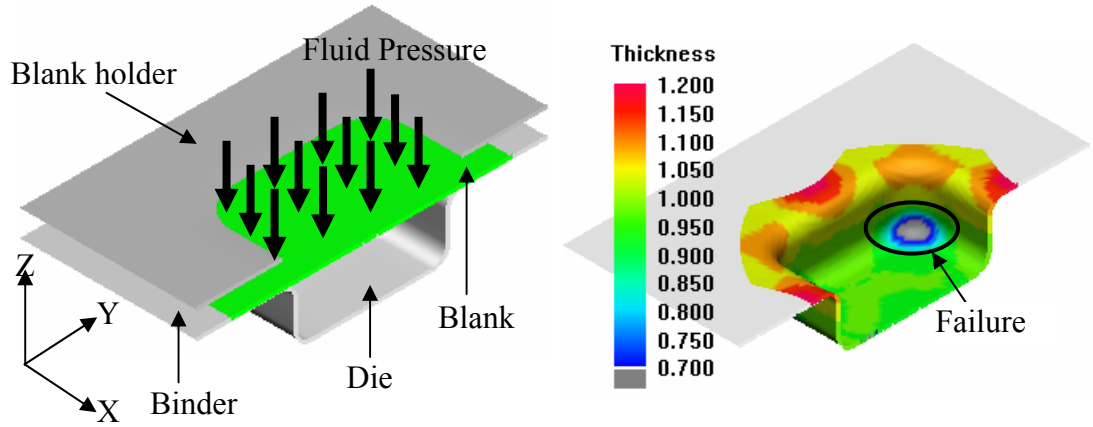


**Figure 5.42** High pressure sheet metal forming simulation of square (I) cross-section, variant 1, prismatic workpiece

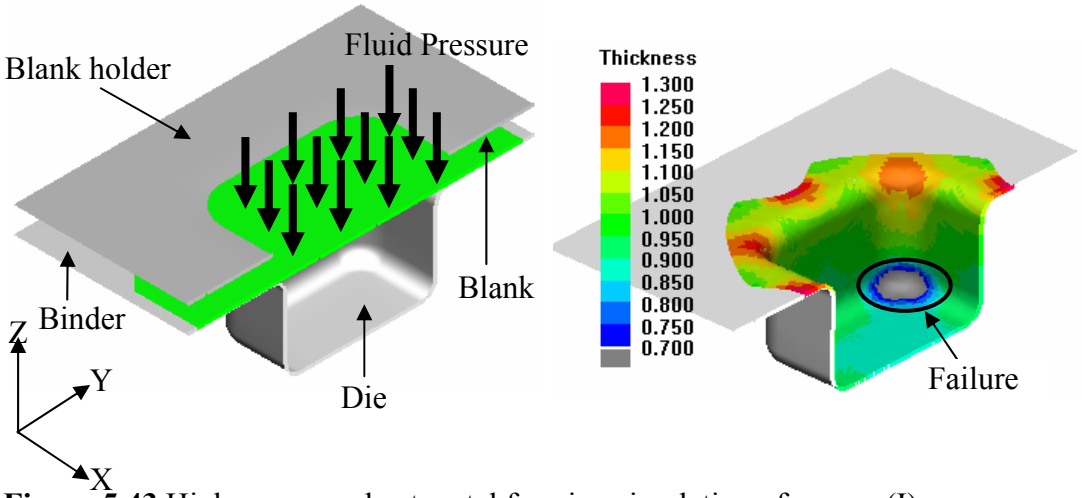


**Figure 5.43** High pressure sheet metal forming simulation of square (I) cross-section, variant 2, prismatic workpiece

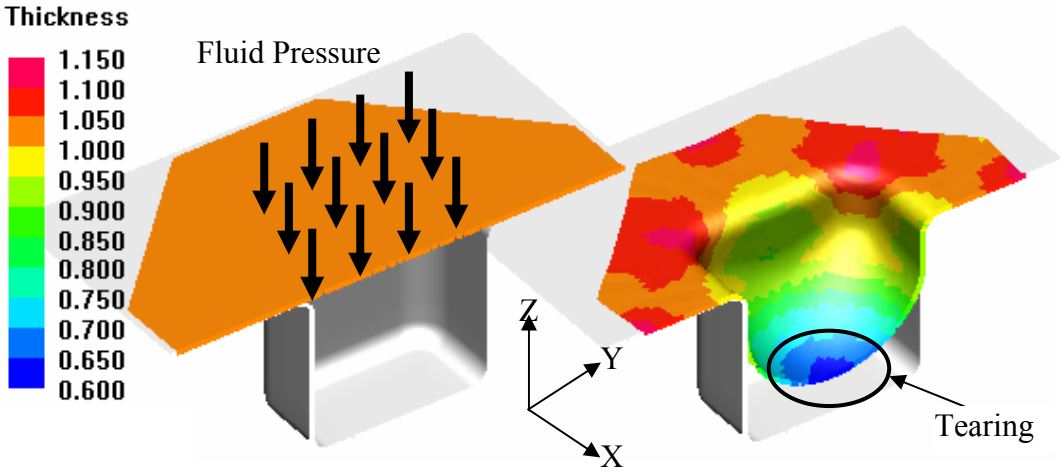


**Figure 5.44** High pressure sheet metal forming simulation of square (I) cross-section, variant 3, prismatic workpiece

## 5.8 Geometry II: Square (II) Cross-section

The last cross-section of the geometry spectrum is a square whose basic dimensions are the same with the previous cross-section (square (I)) except the corner radius, which is 37.5 mm at this time. The depths of the dies for each variant are calculated by Eq. (5.2) according to the equivalent drawing ratio defined by Eq. (5.1). Reference tool dimensions and depths of dies are given in Table 5.6 and they are used to build the punch and die meshes for the assessment simulations. Those meshes are ±0.6 mm offset from the tool reference and the clearance between the die and punch is 1.2 mm, which is 20% more than the initial blank thickness.

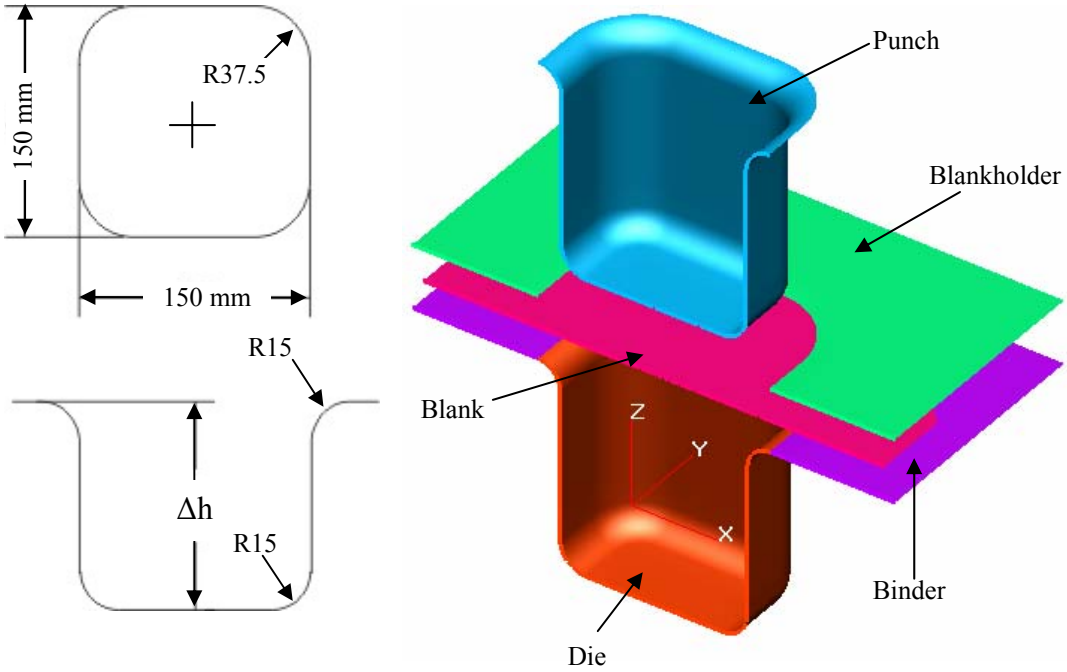


**Figure 5.45** Square (II) cross-section of geometry spectrum and tool geometry

As the optimum undeformed blank geometry, quad blank whose sharp corners are trimmed as the same amount with square (I) cross-section, is used in the assessment simulations. The dimensions are given in Table 5.6 for each variant of square (II) cross-section. All the calculations related with undeformed blank geometry and the depths of die are given Appendix E.6.

**Table 5.6** Tool reference and blank dimensions of square (II) cross-section

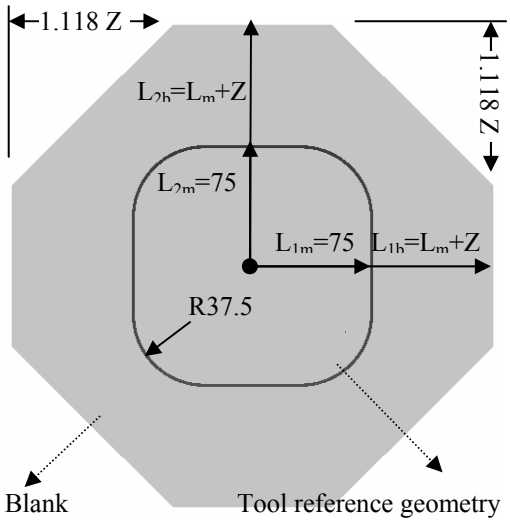


| Tool Reference Dimensions | |
|---|---|
| Mean Edge lengths ($L_{1m}$, $L_{1m}$) | 75 mm,75 mm |
| Mean Area ($A_m$) | 21292.9 mm |
| Mean Circumference ($C_m$) | 519.9 mm |

| Blank Dimensions | | | | | | |
|---|---|---|---|---|---|---|
| Var. | $\beta_{eq}$ | $A_b$ (mm²) | Z (mm) | $R_{1b}$ (mm) | $R_{2b}$ (mm) | Δh (mm) |
| 1 | 1.75 | 65210 | 61.67 | 136.67 | 136.67 | 55.84 |
| 2 | 2.00 | 85172 | 85.84 | 160.84 | 160.84 | 93.11 |
| 3 | 2.25 | 107795 | 111.23 | 186.23 | 186.23 | 135.35 |

For conventional deep drawing process (DD), three variants are separately simulated and successful results are obtained for each of them. At each variant, only depth of the die and height of the punch varied according to the corresponding equivalent drawing ratio. Figure 5.45 shows the process setup of conventional deep drawing process (DD) and Figure 5.46 shows the thickness contour of workpiece drawn into square (II) cross-section, whose die's depth is 135.35 mm (variant 3).

Maximum thinning on the workpiece shown in Figure 5.46 is about 12% and it is observed on the regions where the corner fillet and die cavity fillet are intersected. On the lateral surfaces, the average thinning is less than 10%. Although the depth of die is one of the highest in the assessment study, thickness distribution is more admissible than that of the elliptic and rectangular cross-sections. The success of the process also comes from the proper selection of undeformed blank geometry.

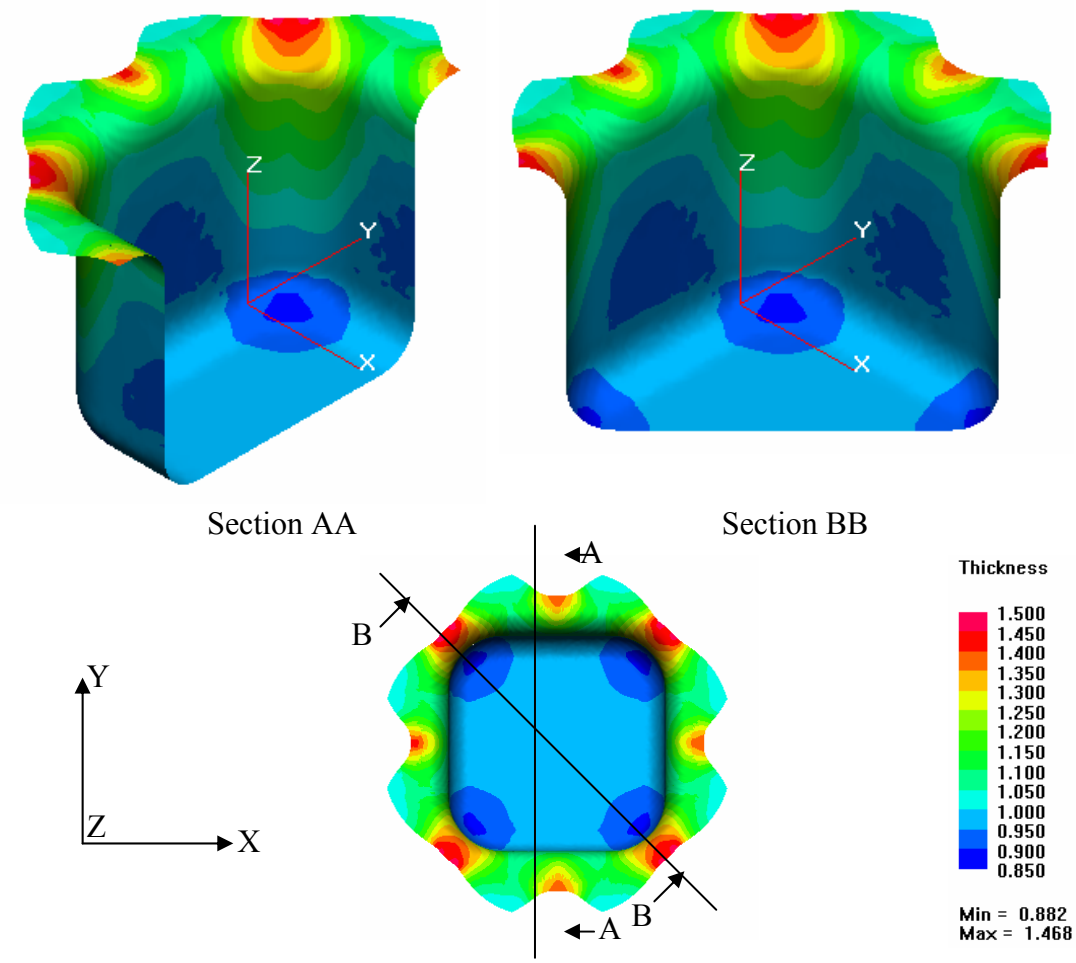


**Figure 5.46** Thickness contour of square (II) cross-section, variant 3, prismatic workpiece manufactured by conventional deep drawing process

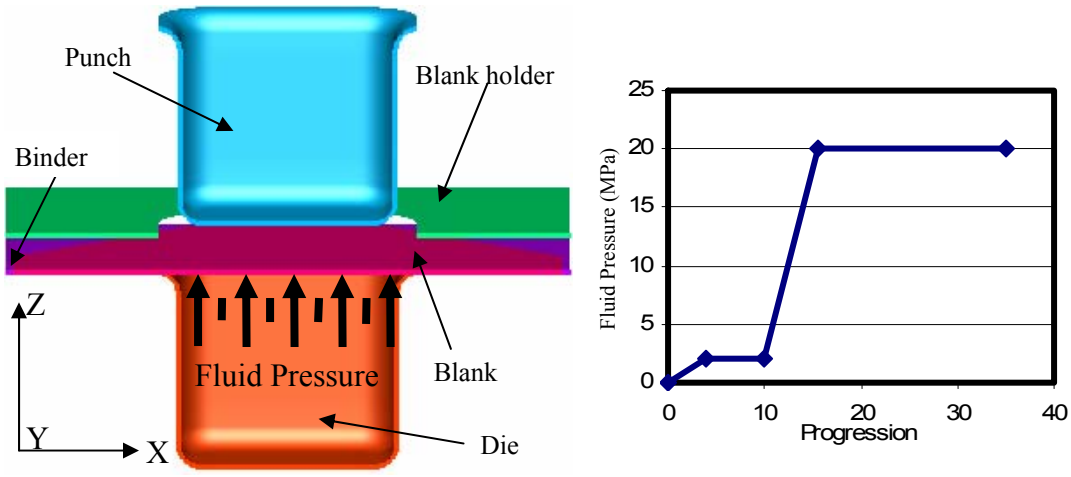


**Figure 5.47** Hydro-mechanical deep drawing (Aquadrawing) process setup and counter pressure exerted by fluid on to the workpiece

Figure 5.47 represents the tool setup of hydro-mechanical deep drawing (aquadrawing) process. Counter pressure, which is generated by the fluid medium filling the die cavity, varies from 2 MPa to 20 MPa. At the chart given in Figure 5.48, it is seen that counter pressure acting on the lower surface of workpiece allows blank to have zero thinning at the bottom of the workpiece. Thickness curve of section AA shows that blank is not deformed in thickness at the final stage of hydro-mechanical deep drawing simulation. Moreover, thickness variation curve of section CC shows that aquadrawing improves the minimum thickness of the workpieces 50% for the given geometry.

It should be also noted that friction forces decrease since the fluid medium makes the blank to lose the contact with die surface and binder. Furthermore, exerting counter pressure and pushing the blank on to the punch surface generates positive effect on the drawability of the sheet metal.

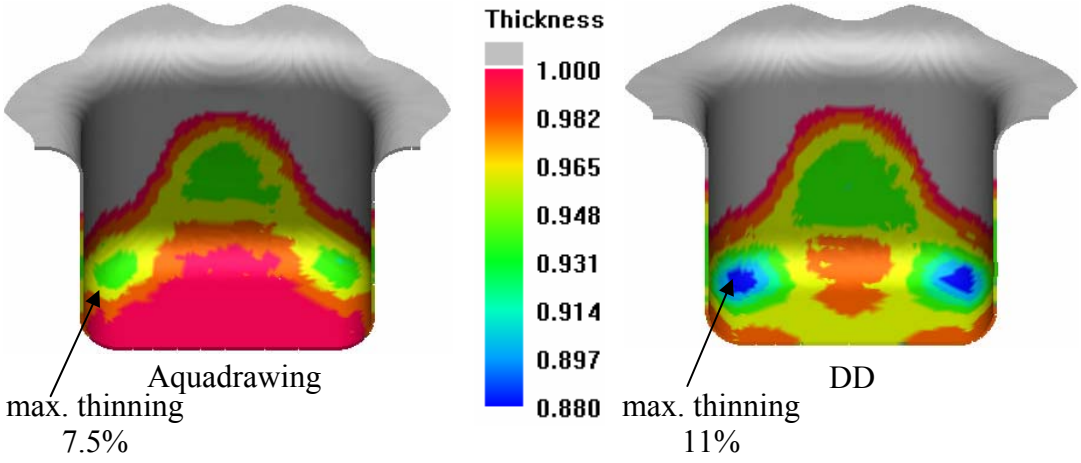


**Figure 5.48** Comparison of workpieces manufactured by hydro-mechanical deep drawing process (aquadrawing) and conventional deep drawing process (DD)

Figure 5.20 shows two workpieces of variant 3, square (II) cross-section of the spectrum, that are produced by hydro-mechanical deep drawing process and conventionally deep drawing process. It is seen that the enlargement in the bottom corner fillet of workpiece leads a reduction in the maximum thinning for both

processes. However, the influence is more significant in deep drawing processes. Compared to the previous square cross-section of geometry spectrum whose corner fillet is 25 mm, hydro-mechanically drawn workpiece exhibits 2% improvement, whereas it is 5% for conventionally drawn workpiece in the sixth cross-section.

Figure 5.20 also reveals that the difference of maximum thinning percentage of both workpieces is 3.5. Moreover, counter pressure generated by fluid medium has the bottom surface of the blank remain undeformed (thickness is 1mm). Additionally when the section CC curves of both processes are observed it is seen that section CC curve belonging to the hydro-mechanical deep drawing process is the offset of the other curve.

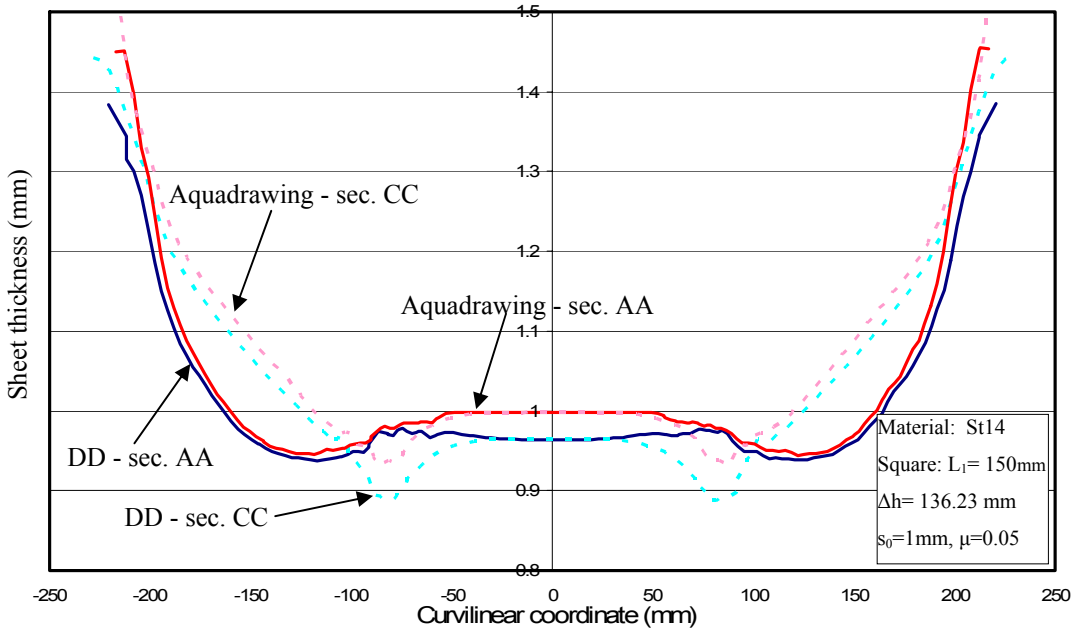


**Figure 5.49** Thickness of blank with respect to the curvilinear coordinate along the section AA and section CC of workpieces manufactured by conventional deep drawing (DD), hydro-mechanical deep drawing (aquadrawing)

As it happens in conventional deep drawing, major deformation is also governed by the punch in hydro-mechanical deep drawing process (aquadrawing). Fluid medium is present in the process setup of hydro-mechanical deep drawing process exert counter pressure in opposite direction to the punch penetration, assist the

deformation and satisfy calibration, increase the quality, and therefore widen the formability limit. In Figure 5.50, comparison of two processes is given in a different manner. At the chart, two curves that represent the minimum thickness of workpieces with respect to the drawing depth is shown. The curve belonging to the hydro-mechanical deep drawing process has constant thickness value when the drawing depth reaches to 45 mm. It means that deformation at the critical zone stops at that value. It is 80 mm for the conventional deep drawing. This improvement is the consequence of utilizing fluid medium in the process, which reduces friction forces and improves material flow.

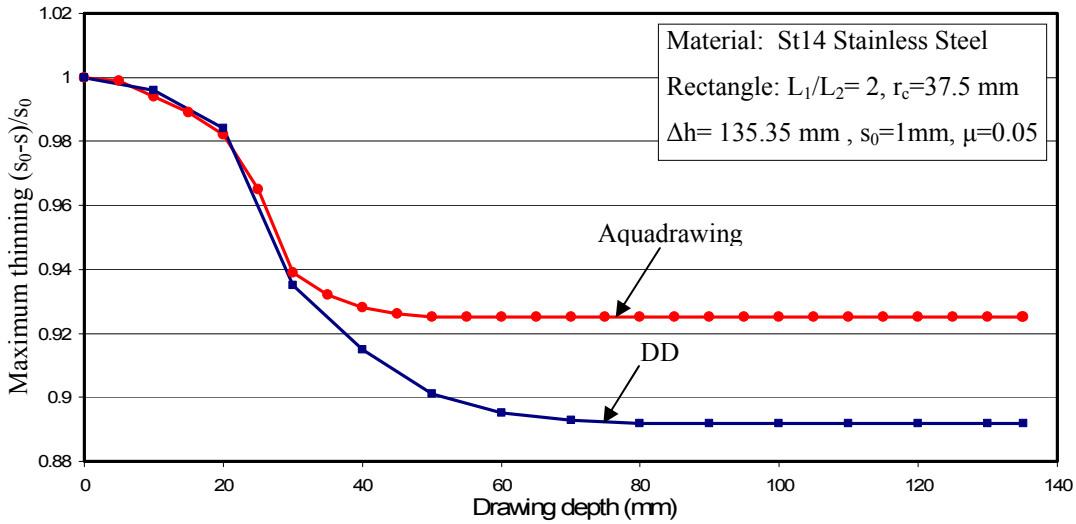


**Figure 5.50** Minimum thickness vs. drawing depth curves of workpieces produced by conventional deep drawing and hydro-mechanical deep drawing process

In the previous cross-section (square (I)) of spectrum, it is clarified that small curvatures have a significant effect in the formability of the sheet material. In the last cross-section of the study, corner fillet radius is increased to 37.5 mm and by this way, first two variants are produced within an admissible thinning range. Figures 5.51 and 5.52 show the thickness contour of workpieces. Variant 3 is again unsuccessful and extreme thinning occurs at the center of the sheet material before the blank touches to the die bottom surface (Figure 5.53).

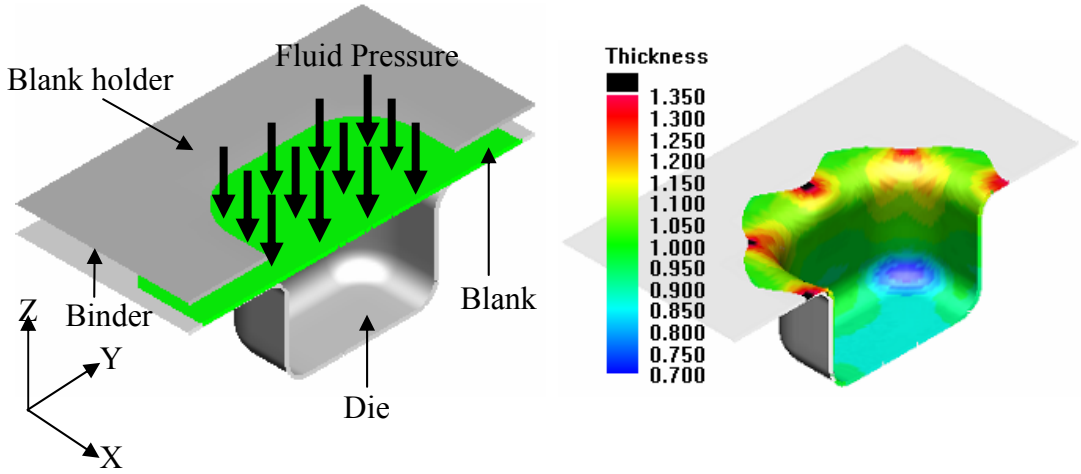


**Figure 5.51** High pressure sheet metal forming simulation of square (II) cross-section, variant 1, prismatic workpiece

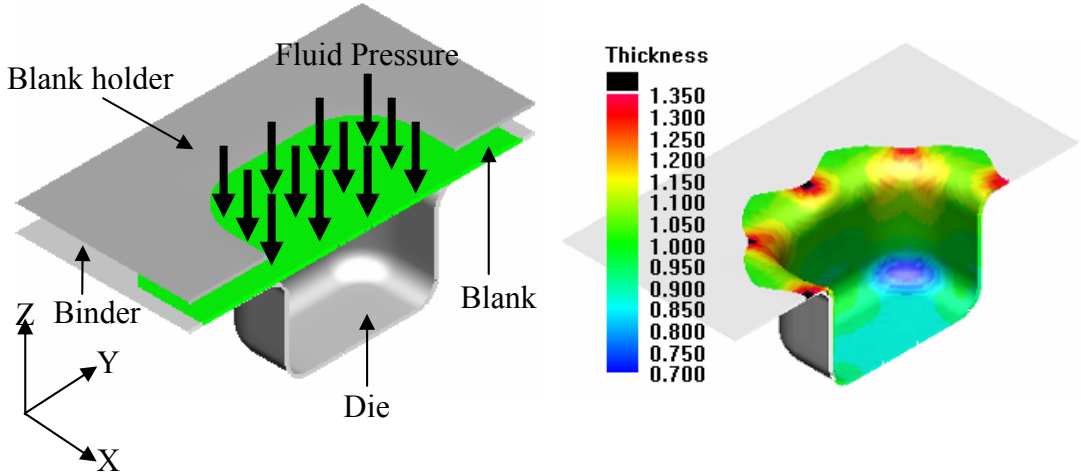


**Figure 5.52** High pressure sheet metal forming simulation of square (II) cross-section, variant 1, prismatic workpiece

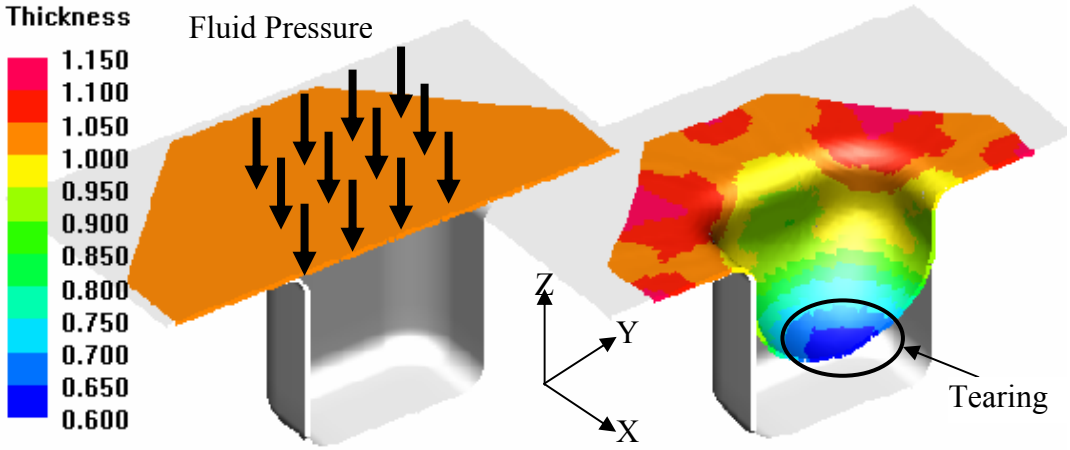


**Figure 5.53** High pressure sheet metal forming simulation of square (II) cross-section, variant 1, prismatic workpiece

## 5.9 Comparison of competing processes

In the previous sections of chapter 5, sheet materials were tried to be drawn into 18 different tools having 6 different cross-sections by using 3 sheet metal forming processes. The results of about 200 FE-simulations are used to compare the formability of competing processes on different die cross-sections and various fillet radii. In this section, the behavior of processes on each cross-section will be summarized and forming limits will be predicted.

**Circular cross-section.** Conventional deep drawing is successful in manufacturing all variants of circular cross-section cylindrical workpieces. 5 to 10 percentage thinning of blank is dominant on the bottom corner and lateral surface of product. Hydro-mechanically drawn workpiece is exposed to less thinning especially at the bottom. In high pressure sheet metal forming (HBU), the deformation starts with the bulging of the blank and finishes with the calibration of curvatures. For the circular cross-section cylindrical die having 15 mm die cavity fillet, calibration is not the limiting issue, however the workpiece having $\beta_{eq}$=2.25 fails due to high depth of the die.

**Elliptic (I) cross-section.** All processes working on elliptic cross-section whose major to minor radius ratio equal to 1.5, successfully produce the workpieces having $\beta_{eq}$=1.75, 2.00 and 2.25. The comparison of thickness distribution of workpieces along the section cuts AA and BB are given in Figure 5.15. The thickness deformation in HBU is more severe at the center of the blank than the others, whereas at ±100 mm of section BB, HBU has the highest sheet thickness value among all processes. Thinning in Aquadrawing is about 3 - 5% less than that of DD along the section cuts AA and BB.

**Elliptic (II) cross-section.** Ellipse whose major to minor radius ratio is equal to 2, is the next cross-section to be inspected. Both the conventional and hydro-mechanical deep drawing successfully manufacture all the variants of workpieces. However, high pressure sheet metal forming has difficulties in the calibration phase.

15 mm die cavity fillet is improper, especially for the higher drawing ratios. Only the workpiece, whose drawing ratio is equal to 1.75, is successfully manufactured by high pressure sheet metal forming (HBU). Figure 5.26 shows the forming limit diagram (FLD) of three workpieces ($\beta_{eq}$=2.25) manufactured by three processes. The elements that exceeds the FLC at the first quadrant, indicates the rupture of workpieces at the bottom corners.

**Rectangular cross-section** has the same aspect ratio with the previous elliptic cross-section. Furthermore, the behavior of each process is almost identical. High pressure sheet metal forming is only successful in the first drawing ratio variant of the rectangular cross-section whose cavity fillet radius is 15 mm. The effect of die cavity fillet on the formability of sheet material for high pressure sheet metal forming process is presented in Figure 5.36. As the ratio of fillet radius to the edge length exceeds the 0.8, drastic thinning exists on the bottom corners of workpiece.

**Square (I) cross-section.** The workpieces, which are manufactured by conventional deep drawing, have maximum thinning percentage of 15.8%. On the other hand, hydro-mechanical deep drawing experiences less thinning which is about 10.7%. High pressure sheet metal forming fails in the calibration phase. 25 mm corner fillet is not large enough to allow the filling of curvature before material ruptures, independent from the equivalent drawing ratio.

**Square (II) cross-section.** The corner fillet radius is increased to one-fourth (37.5 mm) of the edge length. This manipulation in the fillet dimension widens the forming window of all processes. The maximum thinning for conventional deep drawing and hydro-mechanical deep drawing is decreased to 11.9% and 7.8% respectively. The influence is more severe for high pressure sheet metal forming. It becomes possible to manufacture workpieces having equivalent drawing ratios up to 2 by the modification of the corner fillet.

Table 1 summarizes the success of each process on different die geometries for three different equivalent drawing ratios. 45 of the workpieces are successfully formed, yet 9 of them failed due to extreme thinning which is more than 30%;

therefore, necking and tearing failure modes are observed. The reason of the failure can be group into two: High depth of die or the small die curvature in the cavity.

**TABLE 5.7**. Summary of the success of the workpieces

| **Drawing Ratio ($\beta_{eq}$)** | **Depth (Δh) in mm** | **Maximum thinning (%) or failure indicator** | | |
|---|---|---|---|---|
| | | **DD** | **Aquadrawing** | **HBU** |
| ***Circle*** | | | | |
| 1.75 | 54.68 | 7.8 | 6.0 | 9.0 |
| 2.00 | 89.83 | 9.3 | 6.0 | 16.0 |
| 2.25 | 129.68 | 9.5 | 6.0 | depth of part |
| ***Ellipse (I)*** | | | | |
| 1.75 | 37.92 | 12.6 | 9.5 | 16.0 |
| 2.00 | 65.50 | 12.9 | 11.0 | 21.1 |
| 2.25 | 96.76 | 12.9 | 11.0 | 25.0 |
| ***Ellipse (II)*** | | | | |
| 1.75 | 26.57 | 9.5 | 7.0 | 22.2 |
| 2.00 | 48.80 | 13.6 | 13.0 | forming radii |
| 2.25 | 74.00 | 13.9 | 13.5 | forming radii |
| ***Rectangle*** | | | | |
| 1.75 | 28.89 | 11.1 | 9.5 | 26.1 |
| 2.00 | 53.56 | 16.0 | 15.9 | forming radii |
| 2.25 | 81.53 | 20.3 | 17.0 | forming radii |
| ***Square (I)*** | | | | |
| 1.75 | 57.38 | 15.8 | 10.7 | forming radii |
| 2.00 | 94.34 | 15.8 | 10.7 | forming radii |
| 2.25 | 136.23 | 15.8 | 10.7 | forming radii |
| ***Square (II)*** | | | | |
| 1.75 | 55.84 | 11.0 | 7.7 | 15.3 |
| 2.00 | 93.11 | 11.9 | 7.8 | 21.0 |
| 2.25 | 135.35 | 11.9 | 7.8 | depth of part |

All of the failed workpieces are attempt to be manufactured by high-pressure sheet metal forming (HBU). On the other hand, the conventional deep drawing and hydro-mechanical deep drawing were successful in the production of all examined workpieces. Hydro-mechanical deep drawing (aquadrawing) experience less thinning than the conventional deep drawing (DD) for all workpieces inspected. The difference becomes more severe as the initial flange area and drawing ratio, thus the depth of workpiece, increases since the hydro-mechanical deep drawing has a friction-reducing characteristic. Previous studies states that hydro-mechanically drawn workpieces can reach drawing ratios even equal to 3 [3, 9].

In conventional deep drawing and hydro-mechanical deep drawing, blank is drawn into the die with the solid punch. The die fillet radius and the clearance between the tools is the path followed the sheet material while flowing into the die. Therefore, the curvatures on the path have significant influence on the drawability of the sheet material. The results of numerical experiments revealed that DD and Aquadrawing can be safely used to form the sheet material up to $\beta_{eq}$=2.25 if the following die inlet fillet and die cavity fillet conditions are satisfied:

$$\frac{r_i}{R_2} \geq 0.4\,, \qquad \text{for} \quad 1.5 \leq \frac{R_1}{R_2} \leq 2 \quad \text{or} \quad 1.5 \leq \frac{L_1}{L_2} \leq 2 \tag{5.3}$$

$$\frac{r_i}{R_2} \geq 0.2\,, \qquad \text{for} \quad \frac{R_1}{R_2} < 1.5 \quad \text{or} \quad \frac{L_1}{L_2} < 1.5 \tag{5.4}$$

where

$R_1$ is the major radius of cross-section

$R_2$ is the minor radius of cross-section

$L_1$ is the half length of long edge of cross-section

$L_2$ is the half length of short edge of cross-section

$r_i$ is the radius of die inlet fillet

The geometry spectrum, size of die cavity fillets and inspected drawing ratios are quite challenging for high-pressure sheet metal forming. HBU follows quite

different path in the formation of sheet material. The process starts with the bulging of the blank. The center of the blank becomes the most deformed part of the blank, and it continues deformation until it hits to the bottom of the die. Thus, the depth of the die is one of the most dominant parameter that narrows the boundaries of the forming zone for high pressure sheet metal forming. It can be confirmed that deeper parts are not suitable to manufacture by high-pressure sheet metal forming (HBU). Figure 7 shows the forming windows of elliptic cylindrical workpiece based on depth and major radius of workpiece, as well as forming pressure.

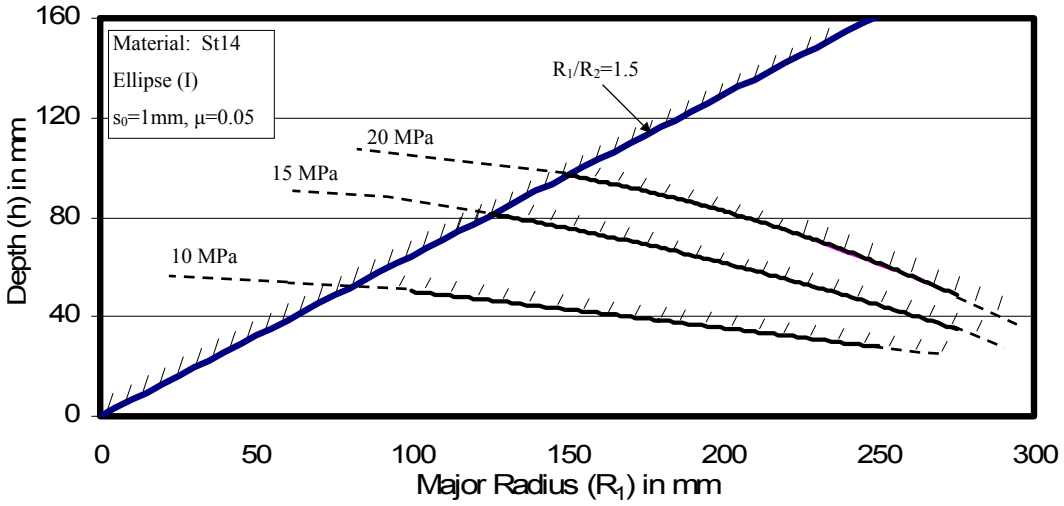


**FIGURE 5.54** Forming window of HBU for ellipse (II) cross-section

The following two equation represent the boundaries of forming windows for circular ($R_1/R_2$=1) and elliptic ($R_1/R_2$=1.5) cross-sections:

$$\frac{\Delta h}{2R_1} \le 0.865 \quad \text{for} \quad \frac{R_1}{R_2} = 1 \quad \text{and} \quad \frac{r_d}{R_2} = 0.2 \tag{5.5}$$

$$\frac{\Delta h}{2R_1} \le 0.645 \quad \text{for} \quad \frac{R_1}{R_2} = 1.5 \quad \text{and} \quad \frac{r_d}{R_2} = 0.3 \tag{5.6}$$

where $r_d$ is the radius of die cavity fillet.

Attention should be also given to the die cavity fillets. Calibration is required for the blank to fill the die cavity curvatures and taking the exact form of the die. During the calibration, internal pressures may reach up to 40 MPa. Due to this high pressure, the sheet material may be exposed to extreme thinning and thus, failure occurs. Therefore, the dimension of the curvature is the other dominant parameter influencing the formability for the high pressure sheet metal forming. Eq (5.8) gives the dimension of curvature condition for manufacturing successful cylindrical workpieces by HBU.

$$\frac{r_d}{R_2} \geq 0.8 \quad \text{for} \quad \frac{R_1}{R_2} = 2\,, \ \text{and} \quad \beta_{eq} = 2.25 \tag{5.8}$$

where $\beta_{eq}$ is equivalent drawing ratio.

Two third of the unsuccessful workpieces are prisms whose cross-section is rectangle or square. The existence of small curvatures on the die is the dominant factor influencing the formability. All unsuccessful prismatic workpieces failed due to the small ratio of die cavity fillet and corner fillet radii to the edge length except square (II) - $\beta_{eq}$=2.25 workpiece whose proportion between corner fillet and edge length is larger, yet the depth of die is high. The critical zones that cause the process to fail are bottom corners of workpiece where extreme thinning occurs during calibration. Eqns. (5.9) and (5.10) suggests the dimension of curvature conditions for prismatic workpieces, whereas Eqns. (5.11) and (5.12) gives conditions to be satisfied for producing successful prismatic products with maximum depth by HBU.

$$\frac{r_d}{L_2} \geq 0.61 \quad \text{for} \quad \frac{L_1}{L_2} = 2\,, \quad \beta_{eq} = 2.25 \quad \text{and} \quad \frac{\Delta h}{2L_1} \leq 0.544 \tag{5.9}$$

$$\frac{r_c}{L_2} > 0.\bar{3} \quad \text{for} \quad \frac{L_1}{L_2} = 1 \quad \text{and} \quad \forall\ \beta_{eq} \tag{5.10}$$

$$\frac{\Delta h}{2L_1} \le 0.193 \qquad \text{for} \quad \frac{L_1}{L_2} = 2\ , \quad \frac{r_d}{L_2} = 0.4 \tag{5.11}$$

$$\frac{\Delta h}{2L_1} \le 0.62 \qquad \text{for} \quad \frac{L_1}{L_2} \le 2\ , \quad \frac{r_c}{L_2} = 0.5 \quad \text{and} \quad \frac{r_d}{L_2} = 0.2 \tag{5.12}$$

where $L_1$, $L_2$ $r_d$ and $r_c$ is defined in Figure 8 and $\beta_{eq}$ is the equivalent drawing ratio.

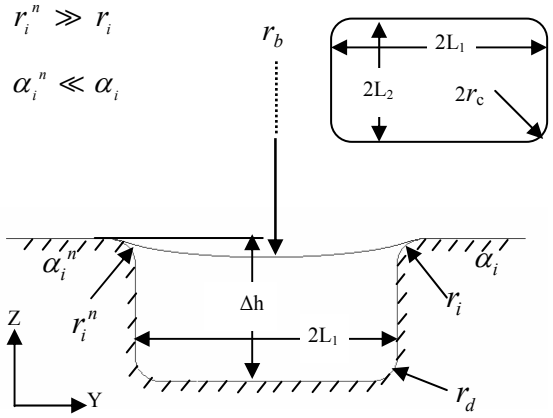


**Figure 5.55** Deformation in high pressure sheet metal forming process

The radius of die inlet fillet is less effective in the determination of forming limits of high-pressure sheet metal forming (HBU) since the bulging of sheet material automatically generates a natural fillet radius itself (Figure 8). This natural fillet radius varies as the process progresses. The initial value may be equal to one third of the edge length but it converges to real value of die fillet radius at the final stage. Therefore, the ratio of die fillet to edge length and edge length to die depth is more significant than the value of die fillet radius itself in the determination of forming limit. Moreover, the contact angle, which influences the bending/rebending deformation, is much less between the blank and die fillet, in high-pressure sheet metal forming due to bulging of sheet material.

# CHAPTER 6

# CONCLUSIONS

Due to increasing expectations, there is a strong need for sheet metal products, which are manufactured more successfully, more economically and more satisfying. To achieve those aims, various sheet metal forming processes were developed and were tried to be implemented. Detailed survey of conventional deep drawing, hydro-mechanical deep drawing, and high-pressure sheet metal forming were explained in Chapter 2. In addition, the improvements in sheet metal forming technologies necessitate the requirements of systematic researches. Therefore, this study was aimed to focus on process validation.

A spectrum consisting of six basic geometries was determined and was used to assess three sheet metal forming processes. For the assessment study, dynamic-explicit finite element analysis was employed and more than 400 numerical experiments were performed. However, the reliability and verification of the finite element simulation became more important since the assessment of sheet metal forming processes was based on the numerical experiments, hence intensive care was taken and both optimization and verification studies were performed in Chapter 4. First, the fundamental of finite element method was reviewed in Chapter 3. Then both the process and numerical parameters, which are used as the input data of the simulations, were optimized by performing precise investigations. In the optimization study, it was observed that punch velocity, element size and mesh topology, adaptive meshing and mass scaling have considerable effects on the results predicted by dynamic explicit code. The optimum parameters, which are proposed after the systematic optimization study, were first tested with the NUMISHEET benchmarks. The simulations using optimized parameters were

compared with both the experiments and simulations submitted to the benchmark. Furthermore, the results of the simulations were verified with the analytical formulations. Finally, numerical experiments simulating the high pressure sheet metal forming were compared with the experimental results so that the verification of the finite element analysis was accomplished. The comparison showed that dynamic-explicit FEM analyses simulating the drawing of steel workpieces are realistic in the determination of formability limits. On the other hand, the simulations underestimate the forming limits of aluminum workpieces unless improper material law is utilized.

Chapter 5 was dedicated to the assessment study. The results of about 200 numerical experiments were used to assess three competing processes. As a result, optimization of initial blank geometry for different type of cross-sections, determination of the drawability of sheet material into desired form, and process validations were achieved. Forming limits of each sheet metal forming processes were suggested and remarkable comments were made. The analyses revealed that depending on the product geometry and dimensional properties certain processes are more preferable for obtaining satisfactory products. Conventional deep drawing should be used to manufacture the products having drawing ratio up to 2.25 and where the mass production is required. Hydro-mechanical deep drawing is mostly suitable for the deeper products whose flange is also large, thus friction reducing effect is required. High pressure sheet metal forming should not be used for the deep products yet it is preferable for large complex spheroidal geometries. It is also unbeatable in the production of prototypes since the labor and tool costs are decreased by substituting the half of the tool with fluid medium.

As a conclusion, this study is expected to be not only valuable for understanding the forming limits capabilities of sheet metal forming processes, but also a good reference for an engineer who plans to use dynamic-explicit finite element method to simulate any engineering application.

# REFERENCES

[1] Z. Marciniak, J.L. Duncan, S. J. Hu: Mechanics of Sheet Metal Forming, Butterworth-Heinemann, London, 2002

[2] M. Kleiner: Tiefziehen, LFU-Querschnitt, Dortmund, 2004

[3] A. Wellendorf: Untersuchungen zum konventionellen und wirkmedien-basierten Umformen von komplexen Feinstblechbauteilen, Fakultät Maschinenbau Lehrstuhl für Umformtechnik Promotionvortrag, Dortmund, 2004

[4] M. Kleiner: Innenhochdruckumformung, LFU-Querschnitt, Dortmund, 2004

[5] M. Colgan, John M.: Deep Drawing Process, Journal of Material Processing Technology, 132 (2003), pp 35-47

[6] S. H. Zhang: Developments in Hydroforming, Journal of Material Processing Technology, 91 (1999), pp 236-244

[7] M. Koç, T. Altan: An Overall Review of the Tube Hydroforming (THF) technology, Journal of Material Processing Technology, 108 (2001), pp 384-393

[8] S. H. Zhang, J. Danckert: Development of Hydro-Mechanical Deep Drawing, 83 (1998), pp 14 - 25

[9] D. Banabic, H.J. Bunge, K. Pöhlandt, A.E. Tekkaya: Formability of Metallic Materials", Springer, Berlin, 2000

[10] W.I. Lankfor, S.C. Snyder, J.A. Bauscher: New Criteria for Predicting the Press Performance of Deep Drawing Sheets, Trans. ASM, 42 (1950), pp 1196-1232

[11] PAM-STAMP 2G User's Manual, ESI-Software, France, October, 2002

[12] A. E. Tekkaya: Finite Element Analysis in Solid Mechanics, Lecture Notes, Middle East Technical University, Ankara, 2002

[13] D. M. Woo,: On the Complete Solution of the Deep Drawing Problem, Int. J. Mech. Sci., 10 (1968), pp 83 - 94

[14] PAM-STAMP 2G Reference Manual, ESI-Software, France, October, 2002

[15] K. Schewizerhof, J.O. Hallquist: Explicit Integration Scheme and Contact Formulation for Thin Sheet Metal Forming In: FE-Simulation of 3D sheet metal forming processes in automotive industry. VDI-Ber. 894 (1991), 405 - 439

[16] NUMISHEET 2002 Benchmark A: Deep Drawing of Cylindrical Cup, NUMISHEET 2002, Proceedings of the Fifth International Conference and Workshop on Numerical Simulation of 3D Sheet Forming Processes, Jeju Island, Korea, October 21-25, 2002.

[17] M.W.H. Kessels, J.A.H. Ramaekers, "Dieptrekken in kort bestek (II)", Vereniging FME-CWM 1999

[18] J.A.H. Ramaekers: A Relation between the Limit-Drawing Ratio LDR and the Material Properties Strain-Hardening Exponent n and Anisotropy Factor R, Advanced Technology of Plasticity, Vol. II, Proceedings of the 6$^{th}$ ICTP, Sept. 19-24, 1999, pp. 1997-1404

[19] J. Woodthrope, R. Pearce: The Anomalous Behavior of Aluminum Sheet under Balanced Biaxial Tension, Int. J. Mech. Sci., 12 (1970), pp. 341 - 347

[20] M. Trompeter, E. Önder, W. Homberg, A.E. Tekkaya, M. Kleiner: Strategies for Material Flow Control in High Pressure Sheet Metal Forming of Large Area Parts wit Complex Geometry Details, Steel Research Int. 75 (2005)

[21] D.H. Park, S.S. Kang, S.B. Park: A Study on the Improvement of Formability for Elliptical Deep Drawing Processes, Journal of Material Processing Technology, 113 (2001), pp 662-665

[22] V. Pegada, Y. Chun, S. Santhanam: An Algorithm for Determining the Optimum Blank Shape for the Deep Drawing of Aluminum Cups, Journal of Material Processing Technology, 125-126 (2002), pp 743 - 750

[23] S. H. Kim, S. H. Kim, H. Huh: Tool Design in a Multi-Stage Drawing and Ironing Process of a Rectangular Cup with a Large Aspect Ratio Using Finite Element Analysis, Journal of Material Processing Technology, 42 (2002), pp 863 - 875

# APPENDICES

# APPENDIX A

# NUMISHEET BENCHMARK PARTICIPANTS

## A.1 Participants supplied Experiments

**Table A.1** Information about benchmark experiment 1

| **Experiment:** | AE-01 |
|---|---|
| **Benchmark participant:** | Haruyuki Konishi (Kobe Steel), Robert E Dick |
| **Address:** | 5-5 Takatsukadai 1, Nishi-ku, Kobe, 651-2271 JAPAN |
| **Email:** | konishi@afrs.kobelco.co.jp, Robert.Dick@alcoa.com |
| **Phone number:** | 81-78-992-5515 |
| **Fax number:** | 81-78-992-5517 |

**Table A.2** Information about benchmark experiment 2

| **Experiment:** | AE-02 |
|---|---|
| **Benchmark participant:** | No data is provided fo this participant and benchmark experiment |
| **Address:** | |
| **Email:** | |
| **Phone number:** | |
| **Fax number:** | |

**Table A.3** Information about benchmark experiment 3

| | |
|---|---|
| **Experiment:** | AE-03 |
| **Benchmark participant:** | L. Filice |
| **Affiliation:** | University of Calabria |
| **Address:** | Dep. of Mech. Eng. , 87036 RENDE (CS) - Italy |
| **Email:** | l.filice@unical.it |
| **Phone number:** | +39 0984 494608 |
| **Fax number:** | +39 0984 494673 |

**Table A.4** Information about benchmark experiment 4

| | |
|---|---|
| **Experiment:** | AE-04 |
| **Benchmark participant:** | Joachim Danckert |
| **Affiliation:** | Department of Production, Aalborg University |
| **Address:** | Fibigerstraede 16, DK-9220 Aalborg, Denmark |
| **Email:** | i9joach@iprod.auc.dk |
| **Phone number:** | 45 9635 8959 |
| **Fax number:** | 45 98 15 30 30 |

**Table A.5** Information about benchmark experiment 5

| | |
|---|---|
| **Experiment:** | AE-05 |
| **Benchmark participant:** | P.P. Date, Amit. M. Joshi, V. Anil Kumar. Sammeta |
| **Affiliation:** | Indian Institute of Technology, Bombay |
| **Address:** | Mech. Eng. Dept. IIT. Bombay, Powai, Mumbai-India |
| **Email:** | ppdate@me.iitb.ac.in, amitmechindia@yahoo.com |
| **Phone number:** | 91 22 576 7511 |
| **Fax number:** | 91 22 572 6875 |

**Table A.6** Information about benchmark experiment 6

| | |
|---|---|
| **Experiment:** | AE-06 |
| **Benchmark participant:** | Jonathan White*, Seung-Geun Lee*, Y.Choi*, J.K.Lee*, R.H. Wagoner** |
| **Affiliation:** | The Ohio State University, *Dept. Mech. Eng., **Dept. Mat. Sci. and Eng. |
| **Address:**<br><br>**Email:** | *209 West 18th Avenue. Columbus Ohio 43210<br>**2041 College Drive, Columbus Ohio 43210<br><br>choi.43@osu.edu, Lee.71@osu.edu |
| **Phone number:** | (614)292-7371 |
| **Fax number:** | (614)292-7369 |
| **Remarks:** | All measurements are numerical averaged values of three experiments |

**Table A.7** Information about benchmark experiment 7

| | |
|---|---|
| **Experiments:** | AE-07 |
| **Benchmark participant:** | E.H. Atzema |
| **Affiliation:** | Corus Research, development & Technology |
| **Address:** | IJTC-PRA-AUT-STP |
| **Email:** | 3H36 / 1-18; P.O. Box 10.000; 1970 CA IJmuiden; Netherlands |
| **Phone number:** | +31 2514 98524' |
| **Fax number:** | +31 2514 70432' |
| **Remarks:** | Thickness was obtained from optical surface strain measurements (PHAST tm) on the outside surface of the cup. This means the strains will be over estimated and consequently the thickness underestimated at the punch radius. The other way around at the die radius. Moreover the grid applied may influence the friction. On the aluminium the grid showed no influence on force displacement diagram, on steel a 5% increase in force was seen. |

## A.2 Participants supplied Simulations

**Table A.8** Information about benchmark simulation 1

| | |
|---|---|
| **Simulation:** | AS-01 |
| **Benchmark participant:** | João Pedro DE MAGALHÃES CORREIA, Gérard FERRON |
| **Affiliation:** | Laboratoire de Physique et Mécanique des Matériaux |
| **Address:** | I.S.G.M.P., Université de Metz, Ile du Saulcy Metz-FRANCE |
| **Email:** | pedro@lpmm.sciences.univ-metz.fr |
| **Phone number:** | 00 333 87 31 53 82 |
| **Fax number:** | 00 333 87 31 53 66 |
| **Name of the FEM code:** | ABAQUS/Explicit 5.8-15 |
| **General aspects of the code:** | commercial dynamic explicit finite element code |
| **Basic formulations:** | 1-for all the simulations, an explicit dynamic finite element analysis has been performed<br>2-the anisotropic plastic material behaviour is modelled with the model proposed by Ferron et al (1994)<br>3-as regards wrinkling analysis no wrinkling indicator has been used and no defect in the initial mesh has been introduced |
| **Element/Mesh technology:** | for the blank: 4-node, reduced integration, doubly curved shell elements (called S4R) with hourglass control, small membrane strains<br>for the tools: 4-node, bilinear quadrilateral, rigid element |
| **Number / type of elements:** | blank: 1065 elements S4R<br>die: 360 elements R3D4<br>blank-holder: 126 elements R3D4<br>punch: 324 elements R3D4<br>total number of elements: 1875 |
| **Computer used:** | HP 9000/785/J5600 2cpus (RAM: 1.5 Gb) |
| **CPU-Time: (average values)** | 2h50mm (high BHF, with punch speed=2,5 mm/s)<br>5h10mm (low BHF, H=40 mm and punch speed=1 mm/s) |
| **Remarks:** | for the 6111-T4, with a high BHF, necking occurs on the punch shoulder radius at the final stage of the deformation process. |

**Table A.9** Information about benchmark simulation 2

| | |
|---|---|
| **Simulation:** | AS-02 |
| **Benchmark participant:** | Sharvari G. Desai , P.P.Date , *K.Narasimhan |
| **Address:** | Department of Mechanical Engg, and *Department of Metullargy and Material science , IIT powai ,India . |
| **Email:** | ppdate@me.iitb.ac.in |
| **Phone number:** | 91-22-576 7511 |
| **Fax number:** | 91-22-5726875 |
| **Name of the FEM code:** | OPTRIS ,ESI ,France . |
| **General aspects of the code:** | Elasto-plastic shell element |
| **Basic formulations:** | Explicit time integration formulation |
| **Element/Mesh technology:** | Adaptive meshing |
| **Number and type of elements** | 4-node and 3-node element |
| **Computer used:** | Pentium-4 processor |
| **CPU-Time:** | 1 hour 30 min |
| **Remarks:** | enclosed separately |

**Table A.10** Information about benchmark simulation 3

| | |
|---|---|
| **Simulation:** | AS-03 |
| **Benchmark participant:** | Raghu Echempati, Ph. D., P.E. |
| **Affiliation:** | Mechanical Engineering Dept., Kettering Uni |
| **Address:** | 1700 W Third Avenue, Flint, MI 48504 (USA) |
| **Email:** | rechempa@kettering.edu |
| **Phone number:** | 810-762-7835 |
| **Fax number:** | 810-762-7860 |
| **Name of the FEM code:** | Dynaform (version 3.3)/LS-DYNA (version 960) |
| **General aspects of the code:** | Explicit Solver, 5 int. points through thickness |
| **Basic formulations:** | Quarter Model of the cup |
| **Element/Mesh technology:** | Belytschko-Tsay Material 36 in DYNA; Thin Shell elements; |
| **Number and type of elements** | # of elements 588 (Quads: 560), shell elements |
| **Computer used:** | Sun Blade 1000, 950 MHz, dual processor |
| **CPU-Time:** | 40 to 50 hours on an average using 2 CPUs |
| **Remarks:** | The results obtained at higher punch speeds match closely with the suggested upper bound speed of 50 mm/s, thus reducing the CPU time at 1,000 mm/s punch speed to less than 7 hours. |

**Table A.11** Information about benchmark simulation 4

| | |
|---|---|
| **Simulation:** | AS-04 |
| **Benchmark participant:** | Tony Chang, Wei Wang |
| **Affiliation:** | Rouge Steel Company |
| **Address:** | 3001 Miller Road, Dearborn, MI 48121 |
| **Email:** | tchang@rougesteel.com |
| **Phone number:** | 313 323 1661 |
| **Fax number:** | 313 322 4100 |
| **Name of the FEM code:** | LS-DYNA3D |
| **General aspects of the code:** | Dynamic |
| **Basic formulations:** | Explicit |
| **Element/Mesh technology:** | Generate geometry and mesh using eta/DYNAFORM based on the information in the benchmark document. |
| **Number and type of elements:** | 3449 shell elements were in the model with 1092 element initially for the blank. Adaptivity were used in the simulation. The number of elements in the blank at the end of the simulation was 9900 for high BHF case, and it was 9954 for low BHF case. |
| **Computer used:** | COMPAQ DEC/Alpha XP1000 |
| **CPU-Time:** | about 5 hours and 10 minutes for each case. |

**Table A.12** Information about benchmark simulation 5

| | |
|---|---|
| **Simulation:** | AS-05 |
| **Benchmark participant:** | Jun Park |
| **Address:** | Hibbitt, Karlsson & Sorensen, Inc.,1080 Main St. Pawtucket, RI, USA |
| **Email:** | park@hks.com |
| **Phone number:** | 401-727-4208 |
| **Fax number:** | 401-727-4208 |
| **Name of the FEM code:** | ABAQUS/Explicit |
| **Basic formulations:** | explicit time integration |
| **Element/Mesh technology:** | shell element with reduced integration |
| **Number and type of elements** | 6948 and 9278 elements for alu. and steel |
| **Computer used:** | Pentium 3, 1GHz |
| **CPU-Time:** | Dependent on problems |
| **Remarks:** | Results on only a quarter of the circle are presented in this report for both outer profile and height profile in HBHF&LBHF,respectively |

**Table A.13** Information about benchmark simulation 6

| | |
|---|---|
| **Simulation:** | AS-06 |
| **Benchmark participant:** | Wang Hua, Li Dongsheng,Zhou Xianbin,Jin Chaohai |
| **Affiliation:** | Sheet Forming Research Center<br>Beijing University Of Aeronautics & Astronautics |
| **Address:** | 704, Beijing University of Aeronautics and Astronautics, Beijing, 100083, P.R.China |
| **Email:** | LDSHXS@263.net , silente@21cn.com |
| **Phone number:** | +86-10-82317701 |
| **Fax number:** | +86-10-82317774 |
| **Name of the FEM code:** | PAM-STAMP 2000 |
| **Basic formulations:** | Dynamic Explicit,Elasto-Plastic Incremental Theory,Updated Lagrangian |
| **Element/Mesh technology:** | BT Shell Element |
| **Number and type of elements** | Al6114-T4 Blank: 8368 Elements Totally 8104 4-Node Elements with 264 3-Node Elements (local) |
| | Steel DDQ Blank: 11132 Elements Totally 10804 4-Node Elements with 328 3-Node Elements (local) |
| **Computer used (1):** | PC_PentiumII-300 For Al6114-T4 Under 50KN High BHF |
| **CPU-Time:** | 818 Minutes |
| **Computer used (2):** | PC_PentiumIII-866 For Al6114-T4 Under 10KN Low BHF |
| **CPU-Time:** | 1540 Minutes |
| **Computer used (3):** | PC_PentiumIII-550 For Steel-DDQ Under 70KN High BHF |
| **CPU-Time:** | 570 Minutes |
| **Computer used (4):** | PC_PentiumIV-1.7G For Steel-DDQ Under 10KN Low BHF |
| **CPU-Time:** | 1504 Minutes |

**Table A.14** Information about benchmark simulation 7

| | |
|---|---|
| **Simulation:** | AS-07 |
| **Benchmark participant:** | Siguang Xu, Jimmy Zhang and Chuan-Tao Wang |
| **Affiliation:** | Die Engineering Analysis Department, ,General Motors Corp. |
| **Address:** | 100 Kirts Blvd, Mail Code: 483-610-501, P.O. Box 5001, Troy, MI |
| **Email:** | chuan-tao.wang@gm.com |
| **Phone number:** | 248-696-5038 |
| **Fax number:** | 248-696-5040 |
| **Name of the FEM code:** | Ls-Dyna3d Version 960 |
| **General aspects of the code:** | 3D Dynamic explicit, elastic-plastic flow |
| **Basic formulations:** | Hill's 48 yield function, planar anisotropic, isotropic hardening |
| **Element/Mesh technology:** | B-T shell element |
| **Number / type of elements** | 23780 (aluminum)/31460(steel) elements for full model |
| **Computer used:** | Sun Blade 1000 two CPU machine |
| **CPU-Time:** | 9hrs 8min(aluminum)/16hrs 48min(steel). |
| **Remarks:** | Punch speed is scaled to 1000 mm/s |

**Table A.15** Information about benchmark simulation 8

| | |
|---|---|
| **Simulation:** | AS-08 |
| **Benchmark participant:** | J. L. Alves, M. C. Oliveira, L. F. Menezes |
| **Affiliation:** | Department of Mechanical Engineering, FCTUC, University of Coimbra |
| **Address:** | Polo II, Pinhal de Marrocos, 3030 Coimbra, Portugal |
| **Email:** | jlalves@dem.uminho.pt |
| **Phone number:** | +351 239 790700 |
| **Fax number:** | +351 239 790701 |
| **Name of the FEM code:** | DD3IMP |
| **General aspects of the code:** | Fully implicit (single iterative loop to treat non-linear elastoplasticity and contact with friction) |
| **Basic formulations:** | Elasto-plastic formulation with isotropic and kinematic hardening, Hill'48 anisotropy and an augmented Lagrangian approach to treat contact with friction (Coulomb's law); tools modelled by Bézier surfaces |
| **Element/Mesh technology:** | Isoparametric 3D brick elements with selective reduced integration technique |
| **Number and type of elements** | 8-node 3D solid FE - DDQ: 3272 FE, 6714 nodes; 6111-T4: 2168 FE, 4476 nodes. |
| **Computer used:** | Intel Xeon 1.7GHz 1GB RDRam |
| **CPU-Time:** | Earing / Wrinkling simulations: about 33 / 103 hours |
| **Remarks:** | Due to the material and part symmetries, only one quarter of the total part was simulated; sheet discretized with 3 FE layers throughout thickness |

**Table A.16** Information about benchmark simulation 9

| | |
|---|---|
| **Simulation:** | AS-09 |
| **Benchmark participant:** | Chung-Souk Han, Robert H. Wagoner |
| **Affiliation:** | The Ohio State University, Dept. Matr.Sci.&Eng. |
| **Address:** | 2041 College Road, Columbus, OH 43210, USA |
| **Email:** | wagoner@mse.eng.ohio-state.edu |
| **Phone number:** | 1-614-292-2079 |
| **Fax number:** | 1-614-292-6530 |
| **Name of the FEM code:** | SHEET-3 |
| **General aspects of the code:** | Static implicit code with N-CFS contact algorithm |
| **Basic formulations:** | 4 node shallow shell with large membrane strain |
| **Element/Mesh technology:** | 729 shell elements with 6 degrees of freedom |
| **Computer used:** | Pentium II, 450 MHz, 384 MB memory |
| **CPU-Time:** | 65293 SEC. |

**Table A.17** Information about benchmark simulation 10

| | |
|---|---|
| **Simulation:** | AS-10 |
| **Benchmark participant:** | Seung-Geun Lee, Yangwook Choi, J.K.Lee |
| **Affiliation:** | The Ohio State University |
| **Address:** | 209 West 18th Avenue. Columbus Ohio 43210 USA |
| **Email:** | choi.43@osu.edu, Lee.71@osu.edu |
| **Phone number:** | (614)292-7371 |
| **Fax number:** | (614)292-7369 |
| **Name of the FEM code:** | ABAQUS v6.21 |
| **General aspects of the code:** | EXPLICIT |
| **Element/Mesh technology:** | Reduced 4 Node Bilinear Shell Element |
| **Computer used:** | AMD Athlon 1.0GHz |
| **CPU-Time:** | 71276sec |

**Table A.18** Information about benchmark simulation 11

| | |
|---|---|
| **Simulation:** | AS-11 |
| **Benchmark participant:** | E.H. Atzema |
| **Affiliation:** | Corus Research, development & Technology |
| **Address:** | IJTC-PRA-AUT-STP 3H36 / 1-18; P.O. Box 10.000; 1970 CA IJmuiden; The Netherlands |
| **Phone number:** | +31 2514 98524' |
| **Name of the FEM code:** | DiekA |
| **General aspects of the code:** | Implicit, iterative solver, large strain formulation |
| **Basic formulations:** | Vegter yield locus Bergstrom hardening |
| **Element/Mesh technology:** | Membrane, DKT, DST elements used. Discrete Shear Triangular elements, 5 i.p. over thickness |
| **Number and type of elements** | Steel: 10191 DST + 20382 contactelements / Aluminium: 7682 DST + 15364 contact elements |
| **Computer used:** | HP 9000 / 785 (dual 8500 processor) |
| **CPU-Time:** | Steel: 1216 min. / Aluminium: 971 min. |
| **Remarks:** | Wrinkles are given around averaged profile. |

**Table A.19** Information about benchmark simulation 12

| | |
|---|---|
| **Simulation:** | AS-12 |
| **Benchmark participant:** | Siguang Xu, Ramesh Joshi, Jimmy Zhang and Chuan-Tao Wang |
| **Affiliation:** | Die Engineering Analysis Department, Metal Fabricating Division,General Motors Corp. |
| **Address:** | 100 Kirts Blvd, Mail Code: 483-610-501, P.O. Box 5001, Troy, MI 48007-5001 |
| **Email:** | chuan-tao.wang@gm.com |
| **Phone number:** | 248-696-5038 |
| **Name of the FEM code:** | Pam-Stamp 2000 |
| **General aspects of the code:** | 3D Dynamic explicit, elastic-plastic, flow Incremental theory |
| **Basic formulations:** | Hill's 48 yield function, planar anisotropic, isotropic hardening |
| **Element/Mesh technology:** | B-T shell element |
| **Number / type of elements** | 4105 (aluminum)/5065(steel) elements |
| **Computer used:** | Sun Blade 1000 two CPU machine |
| **CPU-Time:** | 4hrs 5min(aluminum)/5hrs 11min(steel). ( 2 shared memory processors, double precision) |
| **Remarks:** | one quarter of the cup is analyzed. Punch speed is scaled to 1000 mm/s |

**Table A.20** Information about benchmark simulation 13

| | |
|---|---|
| **Simlulation:** | AS-13 |
| **Benchmark participant:** | Maki Nagakura, Masato Takamura, Ohura kenichi |
| **Affiliation:** | Integrated V-CAD System Research Program<br>The Institute of Physical and Chemical Research |
| **Address:** | 2-1, Hirosawa, Wako-shi, Saitama, 351-0198, Japan |
| **Email:** | nagakura@astom.co.jp,<br>takamura@postman.riken.go.jp |
| **Phone number:** | +81(48) 467-9423 |
| **Fax number:** | +81(48) 467-8705 |
| **Name of the FEM code:** | ITAS3D |
| **General aspects of the code:** | Static-explicit FEM<br>Hill's quadratic yield function and the associative flow rule. r-minimum method to control the size of incremental step. Point data approach to describe tool geometry |
| **Basic formulations:** | Updated Lagrangian rate formulation |
| **Element/Mesh technology:** | 4-node quadrilateral degenerated shell element |
| **Number / type of elements** | Aluminium(M1) High BHF=50N : shell / 3,210 |
| | Aluminium(M1) Low BHF=10N : solid / 6,420 |
| | DDQ(M2) High BHF=70N : shell / 4,296 |
| | DDQ(M2) Low BHF=10N : solid / 8,592 |
| **Computer used:** | Pentium 4 |
| **CPU-Time:** | shell : 850min/case, solid : 4050min/case |

**Table A.21** Information about benchmark simulation 14

| | |
|---|---|
| **Simulation:** | AS-14 |
| **Benchmark participant:** | YongMing Kong, Wan Cheng, DeCai Jia |
| **Affiliation:** | Altair Engineering Ltd. (China) |
| **Address:** | Suite 305, 53 HuangPu Road, Shanghai 200080, P.R.China |
| **Email:** | kym@altair.com.cn, or yongmingkong@yahoo.com |
| **Phone number:** | 86-21-53930011 ext 204 |
| **Fax number:** | 86-21-53930859 |
| **Name of the FEM code:** | HyperForm 5.0 |
| **General aspects of the code:** | Altair HyperForm is a unique finite element based sheet metal forming simulation software solution. |
| **Basic formulations:** | Explicit dynamic solver LS-DYNA is adoptted |
| **Number / type of elements** | 4-nodes shell elements are applied, total 20353 elements are used. |
| **Computer used:** | PC with one 1.6GHz Processor and 1G RAM |
| **CPU-Time:** | 56 minutes |

**Table A.22** Information about benchmark simulation 15

| | |
|---|---|
| **Simulation:** | AS-15 |
| **Benchmark participant:** | T. Meinders |
| **Affiliation:** | University of Twente |
| **Address:** | P.O.Box 217 7500 AE Enschede |
| **Email:** | v.t.meinders@ctw.utwente.nl |
| **Phone number:** | 0031 53 489 4360 |
| **Name of the FEM code:** | Dieka |
| **General aspects of the code:** | Implicit |
| **Number / type of elements** | discrete shear triangles. Initially the simulation is started with 2372 elements, whereafter adaptive mesh refinement is applied |
| **Computer used:** | hp8000 |
| **CPU-Time:** | 1.8 hrs |
| **Remarks:** | Refinement during simulation is driven by error indicators and wrinkling indicators |

**Table A.23** Information about benchmark simulation 16

| | |
|---|---|
| **Simulation:** | AS-16 |
| **Benchmark participant:** | Adrian Banks |
| **Affiliation:** | Corus Group |
| **Address:** | Corus Research, Development & Technology, Po Box 10.000, 1970 CA IJmuiden, The Netherlands. |
| **Email:** | adrian.banks@corusgroup.com |
| **Phone number:** | +31 (0)251 491735 |
| **Fax number:** | +31 (0)251 470432 |
| **Name of the FEM code:** | Autoform, 3.14 |
| **General aspects of the code:** | Implicit, adaptive mesh. 5 layers through thickness |
| **Element/Mesh technology:** | Autoform automesh |
| **Number and type of elements** | 6257, triangular |
| **Computer used:** | HP 9000 / 785 (dual 8500 processor) |
| **CPU-Time:** | High BHF - Aluminium = 253 s ; Low BHF - Aluminium = 245 s ; High BHF - Steel = 263 s ; Low BHF - Steel = 257 s |

# APPENDIX B

# FORMING FORCE CALCULATION PROGRAM

## B.1 Program Input

*Punch Radius:* $r_p := 50$

*Die Radius:* $r_{Di} := 51.25$

*Die Fillet Radius:* $\rho_D := 9.5$

*Punch Fillet Radius* $\rho_P := 7$

*Initial Sheet Thickness:* $s_0 := 1$

*Initial Sheet Radius:* $r_{u0} := 105$

*Material Properties:* $C := 547.763$

$\varepsilon_0 := 0.008755$

$n := 0.26921$

*Anisotropy Factor:* $R_{0^\circ} := 2.16$

$R_{45^\circ} := 1.611$

$R_{90^\circ} := 2.665$

*Friction Coefficient at the Flange:* $\mu_{fl} := 0.0426$

*Friction Coefficient at the Die Fillet:* $\mu_\rho := 0.12$

*Applied Blankholder Pressure:* $P_{blh} := 2.564$

## B.2 Basic Formulation

*Clearance*

$$c := r_{Di} - r_p \qquad c = 1.25$$

*Mean Radius*

$$r_i := \frac{\left(r_p + r_{Di}\right)}{2} \qquad r_i = 50.625$$

*Drawing Ratio*

$$\beta_0 := \frac{r_{u0}}{r_i} \qquad \beta_0 = 2.074$$

*Mean Anisotropy Factor*

$$R := \frac{\left(R_{0°} + 2 \cdot R_{45°} + R_{90°}\right)}{4} \qquad R = 2.012$$

*Principal Strains*

$$i := 0, 0.1 .. \left(r_i\right) \qquad r_u(i) := r_{u0} - i$$

$$s(i) := s_0 \cdot \left(\frac{r_{u0}}{r_u(i)}\right)^{\frac{1}{R+1}}$$

$$\varepsilon_\phi(r, i) := \frac{-\left[\ln\left[\left(\frac{r_{u0}}{r}\right)^2 - \left[\left(\frac{r_u(i)}{r}\right)^2 - 1\right] \cdot \frac{s(i)}{s_0}\right]\right]}{2}$$

$$\varepsilon_z(r, i) := \ln\left(\frac{s(i)}{s_0}\right)$$

$$\varepsilon_r(r, i) := -\left(\varepsilon_\phi(r, i) + \varepsilon_z(r, i)\right)$$

*Equivalent Strain*

$$\varepsilon_{bar}(r, i) := \sqrt{\left(\frac{R + 1}{2 \cdot R + 1}\right) \cdot \left[\left(\varepsilon_\phi(r, i)\right)^2 + \left(\varepsilon_z(r, i)\right)^2 + R\left(\varepsilon_r(r, i)\right)^2\right]}$$

$$\sigma_f(r, i) := C \cdot \left(\varepsilon_0 + \varepsilon_{bar}(r, i)\right)^n$$

## B.3 Flange Deformation Force

$$K_f := 1.06 - 0.015 \cdot R$$

$$K_\sigma(i) := \frac{\sigma_f(r_i, i)}{\sigma_f(r_u(i), i)}$$

$$\beta(i) := \frac{r_u(i)}{r_i}$$

$$F_{Dfl}(i) := K_f \cdot \left( \ln\left( \frac{\beta_0}{\beta(i)} \right) + \varepsilon_0 \right)^n \cdot \left( \frac{\beta_0}{\beta(i)} \right)^{\frac{1}{R+1}} \cdot \left[ 1 - K_\sigma(i) + \left( 1 + \frac{K_\sigma(i) - 1}{1 - \frac{1}{\beta(i)}} \right) \cdot \ln(\beta(i)) \right] \left( 1 + \frac{s_0}{2 \cdot r_p} \right)$$

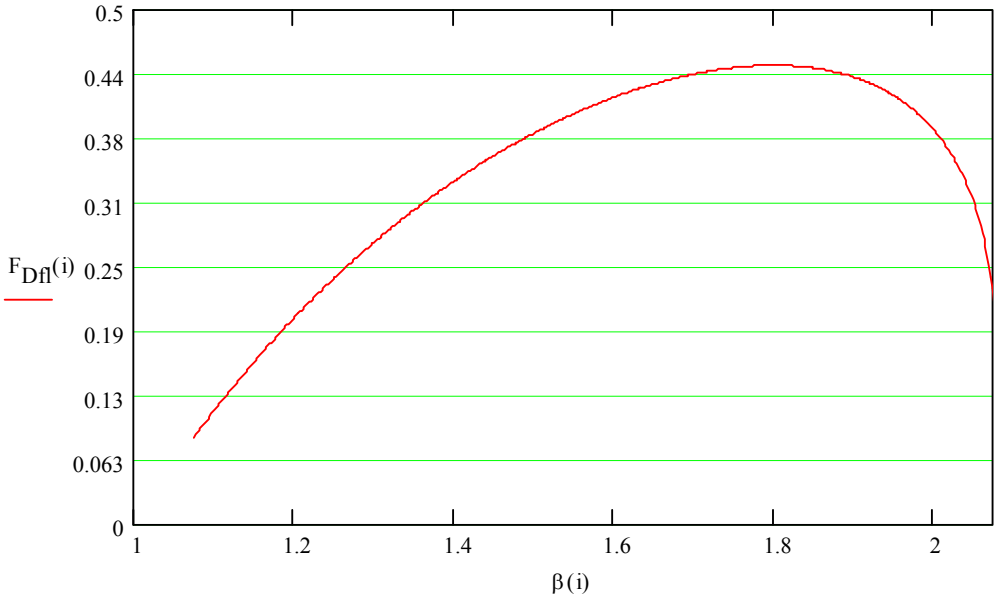


## B.4 Bending-Rebending Force

$$F_{D\rho}(i) := 0.8 \cdot \frac{\sigma_f(r_i, i)}{C} \cdot \frac{R + 1}{\sqrt{2 \cdot R + 1}} \cdot \frac{s(i)}{2 \cdot \rho_D + s(i)} \cdot \left( 1 + \frac{s_0}{2 \cdot r_p} \right)$$

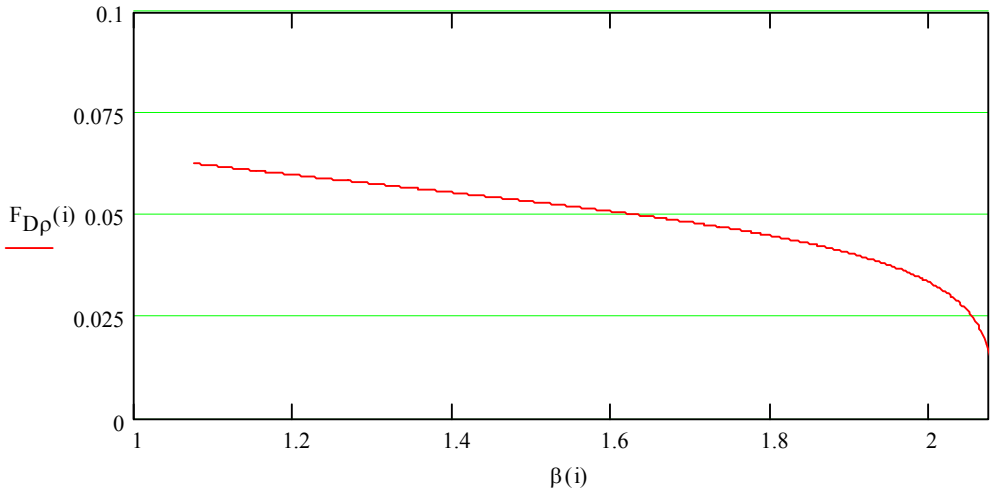


## B.5 Friction Force between Tool and Flange

$$F_{Frfl}(i) := \mu_{fl} \cdot \frac{P_{blh}}{C \cdot r_i \cdot s_0} \cdot \left[ (r_{u0})^2 - (r_{Di} + \rho_D)^2 \right]$$

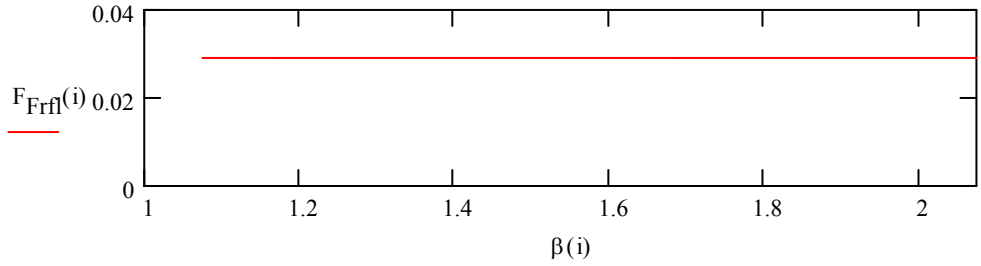

## B.6 Friction Force at Die Fillet

$$F_a(i) := F_{Dfl}(i) + F_{Frfl}(i) + \frac{1}{2}\cdot F_{D\rho}(i)$$

$$F_{Fr\rho}(i) := 1.6\cdot\mu_\rho \cdot F_a(i)$$

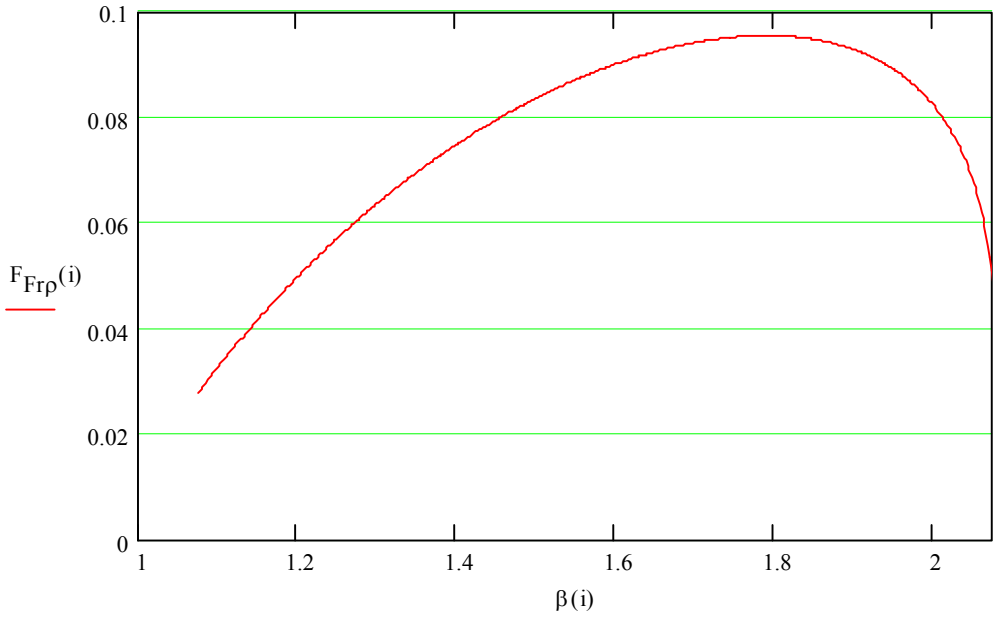


## B.7 Critical Force

$$F_C := \frac{\left(\frac{R+1}{\sqrt{2\cdot R+1}}\right)^{n+1}\cdot n^n}{\left[\left(\frac{s_0}{\rho_P}\right) + \frac{s_0}{r_p} + e^{n-\frac{\sqrt{2\cdot R+1}}{R+1}\cdot\varepsilon_0}\right]}$$

## B.8 Total Forming Force

$$F_D(i) := F_{Fr\rho}(i) + F_{Frfl}(i) + F_{D\rho}(i) + F_{Dfl}(i)$$

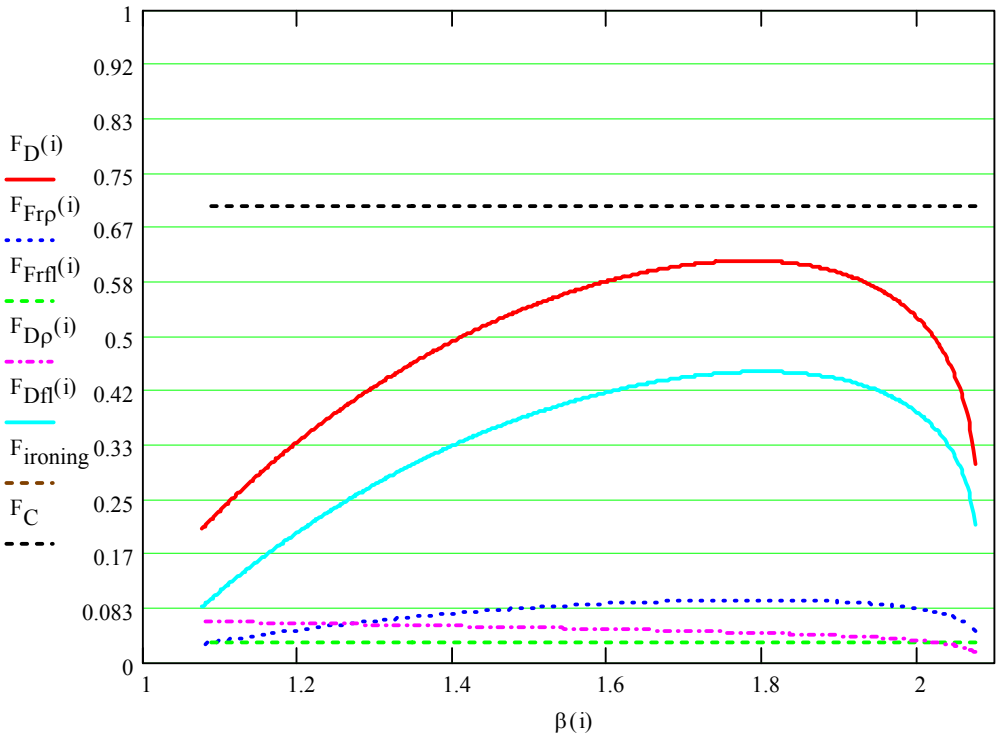

# APPENDIX C

## HBU EXPERIMENT

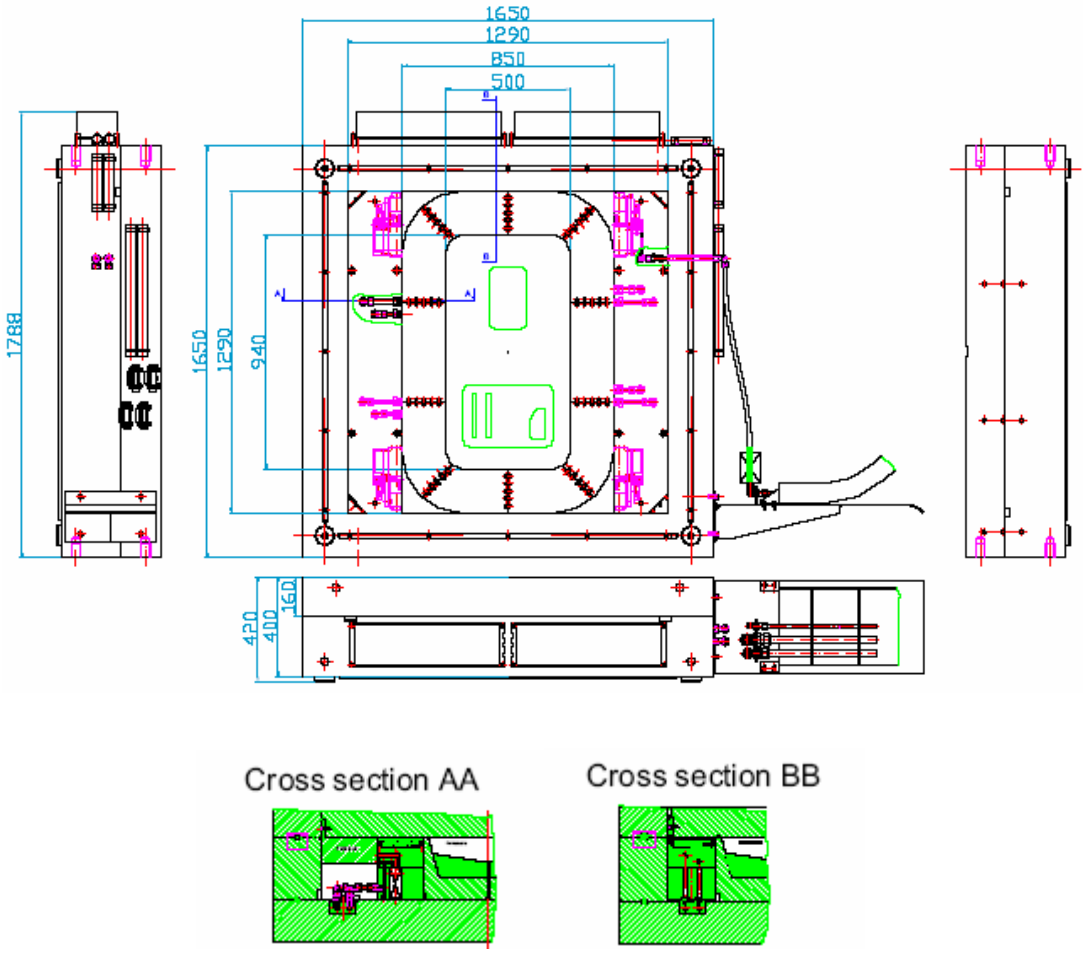


**Figure C.1** High pressure metal forming setup used in the experiment

# APPENDIX D

# MATERIAL PROPERTIES

**Table D.1** Material properties of ST14 stainless steel

| | |
|---|---|
| **E (Gpa)** | 210 |
| **ρ (kg/m$^3$)** | 7820 |
| **ν** | 0.3 |
| **R (0°)** | 1.77 |
| **R** | 1.16 |
| **R** | 1.94 |
| **FLD (strains)** | |
| -0.5 | 0.88 |
| 0.02 | 0.35 |
| 0.1 | 0.38 |
| 0.2 | 0.4 |
| 0.3 | 0.42 |
| 0.42 | 0.44 |

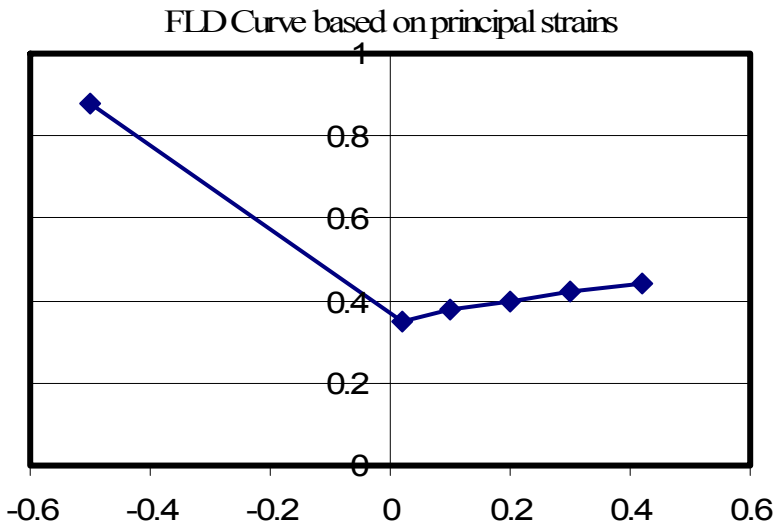

**Table D.2** Material properties of ST14 stainless steel (Flow curve)

| Plastic strain | Eq. Stress (GPa) |
|---|---|
| 0.000 | 0.228 |
| 0.057 | 0.286 |
| 0.066 | 0.296 |
| 0.076 | 0.305 |
| 0.085 | 0.313 |
| 0.094 | 0.320 |
| 0.103 | 0.327 |
| 0.112 | 0.333 |
| 0.121 | 0.338 |
| 0.129 | 0.343 |
| 0.138 | 0.348 |
| 0.147 | 0.352 |
| 0.155 | 0.356 |
| 0.164 | 0.360 |
| 0.172 | 0.364 |
| 0.181 | 0.367 |
| 0.198 | 0.374 |
| 0.298 | 0.408 |
| 0.398 | 0.433 |
| 0.498 | 0.454 |
| 0.598 | 0.472 |
| 0.698 | 0.487 |
| 0.798 | 0.501 |
| 0.898 | 0.514 |
| 0.997 | 0.526 |

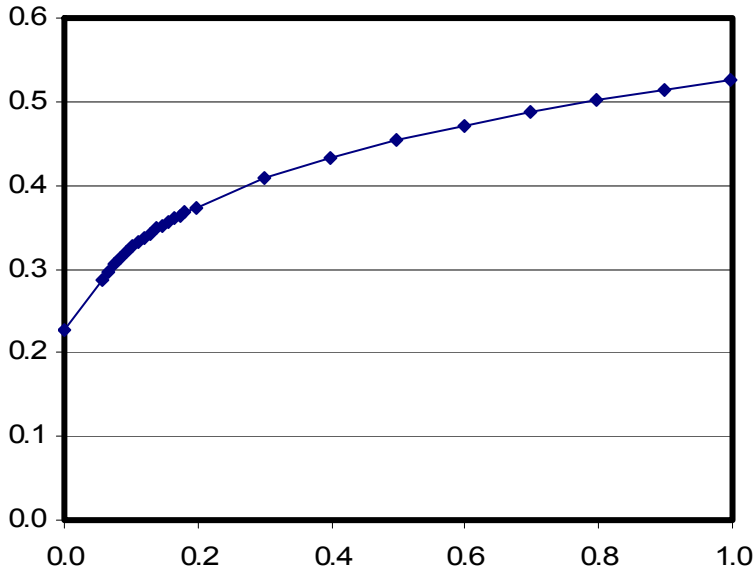

# APPENDIX E

# BLANK GEOMETRY OPTIMIZATION AND CALCULATION OF DEPTH OF DIE

## E.1 Circular Cross-Section

$R_m := 75$ mean radius of punch and die

$f := 20$ die fillet radius

$\beta_{eq} := 1.75$ drawing ratio

$A_m := R_m^{2} \cdot \pi$ mean cross sectional area

$C_m := 2 \cdot \pi \cdot R_m$ mean circumference

$C_m = 471.239$

$A_m = 17671.46$

$Z := 0$

Given

$\frac{(R_m + Z)^2 \cdot \pi}{R_m^{2} \cdot \pi} = \beta_{eq}^{2}$ flange dimension

Find(Z) = 56.25

$\Delta h := \frac{A_m \cdot \beta_{eq}^{2} - (R_m + f)^2 \cdot \pi}{C_m}$

corresponding depth of workpiece

$\Delta h = 54.677$

$\beta_{eq}$ = 2.00 → Z=75.00 mm and Δh=89.83 mm

$\beta_{eq}$ = 2.25 → Z=93.75 mm and Δh=129.68 mm

## E.2 Elliptic (I) Cross-Section

$R_{1m} := 75$ mean minor radius of punch and die

$R_{2m} := 50$ mean major radius of punch and die

$f := 20$ fillet radius

$\beta_{eq} := 1.75$ drawing ratio

$A_m := R_{1m} \cdot R_{2m} \cdot \pi$ mean cross sectional area

$C_m := 2 \cdot \pi \cdot \sqrt{\frac{R_{1m}^2 + R_{2m}^2}{2}}$ mean circumference

$C_m = 400.476$

$A_m = 1.178 \times 10^4$

$Z := 0$

Given

$\frac{(R_{1m} + Z) \cdot (R_{2m} + Z) \cdot \pi}{A_m} = \beta_{eq}^2$ flange dimension

Find(Z) = 45.392

$$h := \frac{A_m \cdot \beta_{eq}^2 - (R_{1m} + f) \cdot (R_{2m} + f) \cdot \pi}{C_m}$$

$h = 37.924$ corresponding depth of workpiece

$\beta_{eq}$ = 2.00 → Z=60.61 mm and Δh=65.50 mm

$\beta_{eq}$ = 2.25 → Z=75.85 mm and Δh=96.76 mm

## E.3 Elliptic (II) Cross-Section

$R_{1m} := 75$ mean minor radius of punch and die

$R_{2m} := 37.5$ mean major radius of punch and die

$f := 20$ fillet radius

$\beta_{eq} := 1.75$ drawing ratio

$A_m := R_{1m} \cdot R_{2m} \cdot \pi$ mean cross sectional area

$C_m := 2 \cdot \pi \cdot \sqrt{\frac{R_{1m}^2 + R_{2m}^2}{2}}$ mean circumference

$C_m = 372.547$

$A_m = 8.836 \times 10^3$

$Z := 0$

Given

$\frac{(R_{1m} + Z) \cdot (R_{2m} + Z) \cdot \pi}{R_{1m} \cdot R_{2m} \cdot \pi} = \beta_{eq}^2$ flange dimension

$\text{Find}(Z) = 38.433$

$\Delta h := \frac{A_m \cdot \beta_{eq}^2 - (R_{1m} + f) \cdot (R_{2m} + f) \cdot \pi}{C_m}$

$\Delta h = 26.57$ corresponding depth of workpiece

$\beta_{eq}$ = 2.00 → Z=51.46 mm and Δh=48.80 mm

$\beta_{eq}$ = 2.25 → Z=64.54 mm and Δh=74.00 mm

## E.4 Rectangular Cross-Section

$L_{1m} := 75$ mean long edge length of punch and die

$L_{2m} := 37.5$ mean short edge length of punch and die

$b := 25$ corner fillet radius

$f := 20$ die fillet radius

$\beta_{eq} := 1.75$ drawing ratio

$A_m := 4 \cdot L_{1m} \cdot L_{2m} - \left[ (2 \cdot b)^2 - \pi \cdot b^2 \right]$ mean cross-sectional area

$C_m := 4 \cdot \left( L_{1m} + L_{2m} \right) - 8 \cdot b + 2 \cdot b \cdot \pi$ mean circumference

$A_m = 10713.495$

$C_m = 407.08$

$Z := 0$

Given

$$\frac{4\left(L_{1m} + Z\right) \cdot \left(L_{2m} + Z\right) - 2.5 \cdot Z^2}{A_m} = \beta_{eq}^{\ 2}$$ flange dimension

$\text{Find}(Z) = 42.024$

$$\Delta h := \frac{A_m \cdot \beta_{eq}^{\ 2} - \left[ 4 \cdot \left( L_{1m} + f \right) \cdot \left( L_{2m} + f \right) - 2 \cdot f^2 \right]}{C_m}$$

corresponding depth of workpiece

$\Delta h = 28.889$

$\beta_{eq}$ = 2.00 → Z=58.73 mm and Δh=53.56 mm

$\beta_{eq}$ = 2.25 → Z=76.18 mm and Δh=81.53 mm

## E.5 Square (I) Cross-Section

$b := 25$ corner fillet radius

$f := 20$ die fillet radius

$\beta_{eq} := 1.75$ drawing ratio

$A_m := 4L_{1m}^2 - \left[4\cdot(b)^2 - \pi\cdot b^2\right]$ mean cross sectional area

$C_m := 8\cdot L_{1m} - 8\cdot b + 2\cdot b\cdot\pi$ mean circumference

$A_m = 2.196\times 10^4$

$C_m = 557.08$

$Z := 0$

Given

$\frac{4\cdot\left(L_{1m} + Z\right)^2 - 2.5Z^2}{A_m} = \beta_{eq}^2$ flange dimension

$\text{Find}(Z) = 64.277$

$\Delta h := \frac{A_m\cdot\beta_{eq}^2 - \left[4\cdot\left(L_{1m} + f\right)\cdot\left(L_{1m} + f\right) - 2\cdot f^2\right]}{C_m}$

$\Delta h = 57.376$ corresponding depth of workpiece

$\beta_{eq}$ = 2.00 → Z=89.08 mm and Δh=94.34 mm

$\beta_{eq}$ = 2.25 → Z=114.84 mm and Δh=136.23 mm

## E.6 Square (II) Cross-Section

$L_{1m} := 75$ mean edge lenght of punch and die

$b := 37.5$ corner fillet radius

$f := 20$ die fillet radius

$\beta_{eq} := 1.75$ drawing ratio

$A_m := 4L_{1m}^2 - \left[4\cdot(b)^2 - \pi\cdot b^2\right]$ mean cross sectional area

$C_m := 8\cdot L_{1m} - 8\cdot b + 2\cdot b\cdot\pi$ mean circumference

$A_m = 21292.86$

$C_m = 535.619$

$Z := 0$

Given

$$\frac{4\cdot\left(L_{1m} + Z\right)^2 - 2.5Z^2}{A_m} = \beta_{eq}^2$$ flange dimension

$\text{Find}(Z) = 61.673$

$$\Delta h := \frac{A_m\cdot\beta_{eq}^2 - \left[4\cdot\left(L_{1m} + f\right)\cdot\left(L_{1m} + f\right) - 2\cdot f^2\right]}{C_m}$$

corresponding depth of workpiece

$\Delta h = 55.841$

$\beta_{eq}$ = 2.00 → Z=85.97 mm and Δh=93.11 mm

$\beta_{eq}$ = 2.25 → Z=111.23 mm and Δh=135.35 mm